

# A MULTIFACETED EXPLORATION OF PLANETARY NEBULAE

A THESIS SUBMITTED TO THE UNIVERSITY OF MANCHESTER  
FOR THE DEGREE OF DOCTOR OF PHILOSOPHY  
IN THE FACULTY OF ENGINEERING AND PHYSICAL SCIENCES

2012

By

Lizette Guzman-Ramirez

School of Physics and Astronomy





# Contents

<b>Abstract</b>	<b>17</b>
<b>Declaration</b>	<b>18</b>
<b>Copyright</b>	<b>19</b>
<b>Acknowledgements</b>	<b>20</b>
<b>The Author</b>	<b>21</b>
Supporting Publications . . . . .	25
<b>1 Introduction</b>	<b>27</b>
1.1 Planetary Nebulae: an evolutionary phase . . . . .	27
1.2 Emission mechanisms . . . . .	29
1.2.1 Gamma Rays . . . . .	30
1.2.2 X-Rays . . . . .	30
1.2.3 Ultraviolet . . . . .	31
1.2.4 Visible . . . . .	31
1.2.5 Infrared . . . . .	32
1.2.6 Submm . . . . .	32
1.2.7 Radio . . . . .	33
1.3 Classification . . . . .	33
1.3.1 Nebular abundance . . . . .	33

## CONTENTS

1.3.2	Central star . . . . .	34
1.3.3	Morphology . . . . .	35
1.3.4	Population and distribution . . . . .	37
1.4	PNe Mysteries . . . . .	39
<b>2</b>	<b>IPHAS survey</b>	<b>41</b>
2.1	Target selection . . . . .	45
2.2	Spectroscopic follow-up . . . . .	47
2.2.1	Spectroscopy: The technique . . . . .	47
2.2.2	KPNO . . . . .	48
2.2.3	SAAO . . . . .	49
2.2.4	Data Reduction . . . . .	49
2.3	Diagnostic Diagrams . . . . .	51
2.4	Confirmed new PNe . . . . .	55
2.5	Conclusions . . . . .	66
<b>3</b>	<b>Mixed Chemistry Planetary Nebulae</b>	<b>69</b>
3.1	PNe in the Galactic Bulge . . . . .	73
3.1.1	Carbon stars in the Bulge . . . . .	73
3.2	Observations . . . . .	74
3.2.1	IR spectra from <i>Spitzer</i> . . . . .	74
3.2.2	H $\alpha$ images from the <i>HST</i> . . . . .	75
3.2.3	UV spectra from the <i>VLT</i> . . . . .	75
3.3	The mixed-chemistry problem in GBPNe . . . . .	75
3.3.1	PAHs acquired from the ISM . . . . .	76
3.3.2	Star and Nebula . . . . .	77
3.4	C-rich molecule formation in O-rich environments . . . . .	85
3.5	Origin of the PAH in Bulge PNe . . . . .	88
3.5.1	Chemical reactions . . . . .	89

3.5.2	Results . . . . .	91
3.6	Implications . . . . .	94
3.7	Conclusions . . . . .	96
<b>4</b>	<b>PAHs in PNe</b>	<b>99</b>
4.1	Observations . . . . .	101
4.1.1	VISIR photometry . . . . .	101
4.1.2	VISIR spectroscopy . . . . .	102
4.2	Results . . . . .	102
4.2.1	VISIR images . . . . .	102
4.2.2	VISIR images & spectra . . . . .	108
4.2.3	Emission lines & PAHs . . . . .	109
4.3	Discussion . . . . .	116
4.4	Conclusions . . . . .	119
<b>5</b>	<b><math>^3\text{He}^+</math> in PNe</b>	<b>121</b>
5.1	Observations using the <i>VLA</i> . . . . .	124
5.2	Results . . . . .	127
5.3	Conclusions . . . . .	133
<b>6</b>	<b>Conclusions</b>	<b>135</b>
<b>7</b>	<b>Afterthoughts</b>	<b>139</b>
<b>A</b>	<b>IPHAS object classification</b>	<b>141</b>
A.1	True PNe . . . . .	142
A.2	Possible PNe . . . . .	153
A.3	HII regions . . . . .	158
A.4	Strömgren Spheres . . . . .	164
A.5	Supernova Remnants . . . . .	165
A.6	Unclear objects . . . . .	166

## *CONTENTS*

<b>B</b>	<b>IRAF data reduction</b>	<b>179</b>
<b>C</b>	<i>Spitzer</i> spectra of GBPNe	<b>211</b>
	<b>References</b>	<b>228</b>

# List of Tables

1.1	Morphological classification of PNe. . . . .	37
1.2	Mean Galactic latitude of PNe. . . . .	38
2.1	Survey parameters . . . . .	43
2.2	Mosaics parameters . . . . .	46
2.3	PNe Morphologies . . . . .	46
2.4	PNe Morphologies sub-class . . . . .	47
2.5	PNe spectral lines . . . . .	48
2.6	Diagnostics . . . . .	56
2.6	(cont.) Diagnostics . . . . .	57
2.6	(cont.) Diagnostics . . . . .	58
2.7	Classification . . . . .	58
2.8	New IPHAS PNe . . . . .	64
2.9	Classification of new PNe . . . . .	65
2.10	Missing PNe . . . . .	66
3.1	Galactic Bulge PNe . . . . .	78
3.2	Model parameters for the PN M1-31 . . . . .	86
3.3	Example of model reactions of different types. . . . .	91
4.1	VISIR/VLT observations log . . . . .	105
4.2	Emission line and PAHs intensities . . . . .	114
4.3	Emission lines and PAHs intensities (scaled to the GB) . . . . .	116

## *LIST OF TABLES*

5.1	<i>VLA</i> observations log. . . . .	124
5.2	<i>VLA</i> Observations Parameters. . . . .	126
5.3	PNe abundances . . . . .	130

# List of Figures

1	Montage of Planetary Nebulae . . . . .	26
1.1	The Dumbbell Nebula, Messier 27. Image taken from the HST im- age gallery <a href="http://opposite.stsci.edu/pubinfo/pr/97/pn/photo-gallery.html">http://opposite.stsci.edu/pubinfo/pr/97/pn/photo-gallery.html</a>	27
1.2	Hertzsprung-Russell diagram . . . . .	29
1.3	CSPN . . . . .	35
1.4	Morphology classification . . . . .	37
1.5	PNe distribution I . . . . .	38
1.6	PNe distribution II . . . . .	39
2.1	Planetary Nebula NGC 6781 . . . . .	41
2.2	IPHAS IDR sky coverage . . . . .	43
2.3	Tiling configuration . . . . .	44
2.4	Diagnostic diagrams (Sabbadin et al. 1977) . . . . .	53
2.5	Diagnostic diagrams (Riesgo & López 2006) . . . . .	54
2.6	Diagnostic Diagram 1 . . . . .	59
2.7	Diagnostic Diagram 2 . . . . .	59
2.8	Diagnostic Diagram 3 . . . . .	59
2.9	True PN . . . . .	60
2.10	Possible PN . . . . .	60
2.11	HII region . . . . .	60
2.12	Strömgren sphere . . . . .	61
2.13	SNR . . . . .	61

## LIST OF FIGURES

2.14	Unclear object . . . . .	61
2.15	Galactic distribution of PNe . . . . .	62
2.16	Galactic distribution of PNe (16-23hrs) . . . . .	62
2.17	Fit of the Galactic distribution of PNe . . . . .	65
3.1	Colour-colour diagram . . . . .	69
3.2	Mixed-chemistry . . . . .	72
3.3	Correlation morphology-PAHs . . . . .	80
3.3	(cont.) Correlation morphology-PAHs . . . . .	81
3.3	(cont.) Correlation morphology-PAHs . . . . .	82
3.3	(cont.) Correlation morphology-PAHs . . . . .	83
3.3	(cont.) Correlation morphology-PAHs . . . . .	84
3.4	<i>Spitzer</i> spectrum of the PN M1-31 . . . . .	87
3.5	Temperature as a function of visual extinction . . . . .	90
3.6	Abundances for O, C, C <sup>+</sup> and CO . . . . .	92
3.7	Abundances of C <sub>2</sub> H, C <sub>8</sub> H, and C <sub>23</sub> H <sub>2</sub> . . . . .	93
4.1	The <i>VLT</i> . . . . .	99
4.2	VISIR image of Cn1-5 . . . . .	103
4.3	VISIR image of M1-25 . . . . .	103
4.4	VISIR image of H1-61 . . . . .	104
4.5	VISIR image of Hb6 . . . . .	104
4.6	VISIR image of M3-15 . . . . .	104
4.7	VISIR image of Th3-4 . . . . .	105
4.8	VISIR image of H1-23 . . . . .	106
4.9	VISIR image of H1-40 . . . . .	106
4.10	VISIR image and spectra of M1-31 . . . . .	110
4.11	VISIR image and spectra of M1-40 . . . . .	111
4.12	VISIR image and spectra of M3-38 . . . . .	112
4.13	VISIR and <i>Spitzer</i> spectra . . . . .	113



4.14	Line ratios correlation . . . . .	115
4.15	Size vs $H_2$ . . . . .	117
4.16	$H_2$ vs $11.3\mu m$ . . . . .	117
4.17	$H_2$ vs $T_{\text{eff}}$ . . . . .	117
5.1	The <i>VLA</i> . . . . .	121
5.2	$^3\text{He}$ predictions and observations . . . . .	123
5.3	$^3\text{He}$ predictions for low mass stars . . . . .	125
5.4	Line images . . . . .	128
5.5	$^3\text{He}/\text{H}$ abundance . . . . .	132
A.1	PN 00:13:33 +67:18:03 . . . . .	142
A.2	PN 01:31:09 +61:22:58 . . . . .	142
A.3	PN 14:40:30 -52:34:51 . . . . .	143
A.4	PN 16:23:17 -31:44:57 . . . . .	143
A.5	PN 18:34:38 +00:08:03 . . . . .	143
A.6	PN 18:42:11 +00:50:31 . . . . .	144
A.7	PN 18:53:21 +05:56:41 . . . . .	144
A.8	PN 18:58:15 +07:37:53 . . . . .	144
A.9	PN 19:01:15 +11:41:47 . . . . .	145
A.10	PN 19:04:54 +10:18:01 . . . . .	145
A.11	PN 19:05:12 +16:13:47 . . . . .	145
A.12	PN 19:05:43 +11:00:18 . . . . .	146
A.13	PN 19:10:01 +14:22:03 . . . . .	146
A.14	PN 19:10:22 +11:05:38 . . . . .	146
A.15	PN 19:10:27 +03:40:46 . . . . .	147
A.16	PN 19:12:55 +14:32:48 . . . . .	147
A.17	PN 19:21:52 +13:52:23 . . . . .	147
A.18	PN 19:21:53 +14:30:56 . . . . .	148
A.19	PN 19:28:37 +24:50:24 . . . . .	148

## LIST OF FIGURES

A.20 PN 19:35:32 +11:21:15 . . . . .	148
A.21 PN 19:42:26 +21:45:21 . . . . .	149
A.22 PN 19:44:00 +17:09:01 . . . . .	149
A.23 PN 19:45:10 +27:09:29 . . . . .	149
A.24 PN 19:48:52 +22:25:16 . . . . .	150
A.25 PN 19:51:26 +26:58:39 . . . . .	150
A.26 PN 19:52:09 +27:18:30 . . . . .	150
A.27 PN 19:54:36 +31:33:26 . . . . .	151
A.28 PN 20:00:18 +36:59:34 . . . . .	151
A.29 PN 20:05:22 +36:59:43 . . . . .	151
A.30 PN 20:09:32 +37:31:18 . . . . .	152
A.31 PN 23:27:12 +65:09:18 . . . . .	152
A.32 PN 23:44:03 +60:32:42 . . . . .	152
A.33 PN 00:00:21 +57:22:07 . . . . .	153
A.34 PN 00:51:23 +63:10:59 . . . . .	153
A.35 PN 16:46:45 -38:37:00 . . . . .	154
A.36 PN 18:20:44 -12:47:52 . . . . .	154
A.37 PN 18:26:03 -10:11:39 . . . . .	154
A.38 PN 18:45:05 +00:11:58 . . . . .	155
A.39 PN 18:57:37 +02:03:40 . . . . .	155
A.40 PN 19:02:28 +02:07:22 . . . . .	155
A.41 PN 19:11:17 +10:37:34 . . . . .	156
A.42 PN 19:17:16 +03:34:47 . . . . .	156
A.43 PN 19:48:14 +28:07:29 . . . . .	156
A.44 PN 19:59:19 +31:25:34 . . . . .	157
A.45 PN 23:40:09 +61:16:01 . . . . .	157
A.46 PN 00:00:43 +67:10:12 . . . . .	158
A.47 PN 00:05:35 +66:03:16 . . . . .	158
A.48 PN 00:44:56 -73:10:11 . . . . .	159

## *LIST OF FIGURES*

A.49 PN 01:00:35 +60:51:19 . . . . .	159
A.50 PN 01:01:33 +60:54:25 . . . . .	159
A.51 PN 01:02:35 +60:54:18 . . . . .	160
A.52 PN 01:08:24 +60:32:41 . . . . .	160
A.53 PN 01:48:27 +62:54:41 . . . . .	160
A.54 PN 02:53:40 +60:30:15 . . . . .	161
A.55 PN 02:59:09 +60:19:02 . . . . .	161
A.56 PN 16:19:16 -52:34:51 . . . . .	161
A.57 PN 19:07:07 +04:23:16 . . . . .	162
A.58 PN 19:48:53 +18:10:21 . . . . .	162
A.59 PN 20:13:38 +33:15:12 . . . . .	162
A.60 PN 22:41:37 +58:42:27 . . . . .	163
A.61 PN 23:56:09 +66:52:05 . . . . .	163
A.62 PN 00:15:19 +61:14:59 . . . . .	164
A.63 PN 23:53:04 +62:46:32 . . . . .	164
A.64 PN 23:01:35 +58:40:07 . . . . .	165
A.65 PN 23:11:35 +61:38:29 . . . . .	165
A.66 PN 18:26:23 -10:29:47 . . . . .	166
A.67 PN 18:28:01 -10:14:09 . . . . .	166
A.68 PN 18:28:29 -09:06:12 . . . . .	167
A.69 PN 18:32:09 -09:39:06 . . . . .	167
A.70 PN 18:51:41 -30:03:37 . . . . .	167
A.71 PN 18:52:10 -30:40:23 . . . . .	168
A.72 PN 18:52:39 -30:09:16 . . . . .	168
A.73 PN 18:52:50 -29:56:32 . . . . .	168
A.74 PN 18:52:54 -30:00:20 . . . . .	169
A.75 PN 18:53:14 -30:09:14 . . . . .	169
A.76 PN 18:53:16 +00:00:30 . . . . .	169
A.77 PN 18:53:18 -30:13:43 . . . . .	170

## LIST OF FIGURES

A.78 PN 18:53:29 -29:38:23 . . . . .	170
A.79 PN 18:54:07 -30:39:20 . . . . .	170
A.80 PN 18:54:11 -30:23:19 . . . . .	171
A.81 PN 18:54:24 -30:25:10 . . . . .	171
A.82 PN 18:54:29 -30:37:41 . . . . .	171
A.83 PN 18:54:30 -30:11:22 . . . . .	172
A.84 PN 18:54:39 -29:54:18 . . . . .	172
A.85 PN 18:54:41 -30:20:36 . . . . .	172
A.86 PN 18:54:56 -30:14:08 . . . . .	173
A.87 PN 18:55:07 -30:40:03 . . . . .	173
A.88 PN 18:55:16 -30:36:18 . . . . .	173
A.89 PN 18:55:39 -29:55:57 . . . . .	174
A.90 PN 18:55:40 -30:16:32 . . . . .	174
A.91 PN 18:55:44 -30:12:26 . . . . .	174
A.92 PN 18:57:52 -30:32:00 . . . . .	175
A.93 PN 18:57:57 -30:10:08 . . . . .	175
A.94 PN 19:03:25 +10:44:58 . . . . .	175
A.95 PN 19:03:47 +05:09:36 . . . . .	176
A.96 PN 19:04:12 +10:31:32 . . . . .	176
A.97 PN 19:48:46 +18:15:18 . . . . .	176
A.98 PN 23:17:35 +63:45:06 . . . . .	177
A.99 PN 23:18:36 +64:04:06 . . . . .	177
A.100PN 23:29:07 +59:34:30 . . . . .	177
C.1 PN G000.0 -06.8 . . . . .	212
C.2 PN G000.1 +04.3 . . . . .	212
C.3 PN G000.3 +01.5 . . . . .	212
C.4 PN G000.8 +01.3 . . . . .	213
C.5 PN G001.2 +01.2 . . . . .	213

# LIST OF FIGURES

C.6	PN G001.3 +00.9 . . . . .	213
C.7	PN G002.2 -09.4 . . . . .	214
C.8	PN G002.8 +01.7 . . . . .	214
C.9	PN G003.1 +02.9 . . . . .	214
C.10	PN G003.6 +03.1 . . . . .	215
C.11	PN G004.0 -03.0 . . . . .	215
C.12	PN G004.9 +04.9 . . . . .	215
C.13	PN G005.2 +04.2 . . . . .	216
C.14	PN G005.9 -02.6 . . . . .	216
C.15	PN G006.1 +08.3 . . . . .	216
C.16	PN G006.4 +02.0 . . . . .	217
C.17	PN G006.5 -03.1 . . . . .	217
C.18	PN G006.8 +04.1 . . . . .	217
C.19	PN G007.2 +01.8 . . . . .	218
C.20	PN G008.2 +06.8 . . . . .	218
C.21	PN G008.3 +01.1 . . . . .	218
C.22	PN G011.9 +04.2 . . . . .	219
C.23	PN G012.2 +04.9 . . . . .	219
C.24	PN G331.3 -12.1 . . . . .	219
C.25	PN G345.0 -04.9 . . . . .	220
C.26	PN G345.2 -08.8 . . . . .	220
C.27	PN G348.4 -02.8 . . . . .	220
C.28	PN G349.8 -00.3 . . . . .	221
C.29	PN G352.6 +00.1 . . . . .	221
C.30	PN G354.5 +03.3 . . . . .	221
C.31	PN G355.6 -02.7 . . . . .	222
C.32	PN G355.7 -03.5 . . . . .	222
C.33	PN G355.9 -02.3 . . . . .	222
C.34	PN G355.9 +03.6 . . . . .	223

## *LIST OF FIGURES*

C.35 PN G356.5 -02.3 . . . . .	223
C.36 PN G356.5 -03.6 . . . . .	223
C.37 PN G356.9 +04.4 . . . . .	224
C.38 PN G357.6 +01.7 . . . . .	224
C.39 PN G358.2 +04.2 . . . . .	224
C.40 PN G358.3 +03.0 . . . . .	225
C.41 PN G358.7 -05.2 . . . . .	225
C.42 PN G359.1 -01.7 . . . . .	225
C.43 PN G359.2 +01.2 . . . . .	226
C.44 PN G359.3 -01.8 . . . . .	226
C.45 PN G359.4 -00.8 . . . . .	226
C.46 PN G359.7 -02.6 . . . . .	227
C.47 PN G359.8 +02.4 . . . . .	227

# The University of Manchester

ABSTRACT OF THESIS submitted by Lizette Guzman-Ramirez  
for the Degree of Doctor of Philosophy and entitled  
“A Multifaceted Exploration of Planetary Nebulae”, November 2012.

This thesis analyses and proposes solutions for the following PNe mysteries:

- 1. The missing PNe population.** 100 new objects were spectroscopically observed and analysed using the INT Photometric H $\alpha$  Survey (IPHAS). 32 are PNe, 13 are possible PNe and the rest are HII regions, SNR and unclear objects. The new PNe were within the inner parts of the galactic plane. The IPHAS survey has been the deepest survey done in H $\alpha$ , and revealed objects never seen before.
- 2. The mixed chemistry in Galactic Bulge PNe.** These GBPNe are the end-products of low-mass stars (and therefore expected to be O-rich) and belong to a metal rich population. These PNe present dual-dust chemistry, with the presence of PAHs (carbon-rich) and crystalline silicates (oxygen-rich) in their spectra. This thesis analysed 40 Galactic Bulge PNe and found a strong correlation between intensity of the PAH bands and morphology, notably a massive torus. This torus provides the dense irradiated environment needed to form the PAHs. Follow-up observations using VISIR revealed a dense dusty tori in 11 PNe. PAHs are present in the outer edges of these tori, whereas ionised material is located within the dusty tori.
- 3. The  $^3\text{He}$  problem.** Using the *VLA* we observed three PNe, upper-limits of their  $^3\text{He}$  abundances were estimated. The resulting evolution of  $^3\text{He}$  is only consistent with the values determined in pre-solar material and the ISM, if the PNe observed represent only 4% of the population of low-mass stars, and the remaining 96% have undergone enhanced  $^3\text{He}$  depletion.

# Declaration

No portion of the work referred to in this thesis has been submitted in support of an application for another degree or qualification of this or any other university or other institution of learning.



# Copyright

The author of this thesis (including any appendices and/or schedules to this thesis) owns certain copyright or related rights in it (the “Copyright”) and she has given The University of Manchester certain rights to use such Copyright, including for administrative purposes. Copies of this thesis, either in full or in extracts and whether in hard or electronic copy, may be made only in accordance with the Copyright, Designs and Patents Act 1988 (as amended) and regulations issued under it or, where appropriate, in accordance with licensing agreements which the University has from time to time. This page must form part of any such copies made. The ownership of certain Copyright, patents, designs, trade marks and other intellectual property (the “Intellectual Property”) and any reproductions of copyright works in the thesis, for example graphs and tables (“Reproductions”), which may be described in this thesis, may not be owned by the author and may be owned by third parties. Such Intellectual Property and Reproductions cannot and must not be made available for use without the prior written permission of the owner(s) of the relevant Intellectual Property and/or Reproductions. Further information on the conditions under which disclosure, publication and commercialisation of this thesis, the Copyright and any Intellectual Property and/or Reproductions described in it may take place is available in the University IP Policy (see <http://www.campus.manchester.ac.uk/medialibrary/policies/intellectual-property.pdf>), in any relevant Thesis restriction declarations deposited in the University Library, The University Library’s regulations (see <http://www.manchester.ac.uk/library/aboutus/regulations>) and in The University’s policy on presentation of Theses.

# Acknowledgements

I want to thank my family first of all, not only I wouldn't be here without them, but they have been the most supportive people I could have ever dreamed of. Thank you mum, dad, sister, Eduardo and the little one that just arrived to the family (Michelle).

My supervisor has been my main scientific motivation in these 4 years. Thank you for all the time and effort you put into this research. Also a big thank you to you and your family that always made me feel welcomed.

During these 4 years, there are people that have always been there for me. These people I call my adopted family, people that filled the holes of being away from home. Thank you all, for sharing some parts of your life with me and teaching me so much about life, love and most importantly for all the laughs. My adopted family from SLP: Naye, Sara, Jimena, familia Gallegos, David, Chuy, Memo, Paco, and Alex. My adopted family from Morelia: Pau, familia Perezgil, Pepe, Migue, Luis, Susana, Enrique, R2D2, and Paco. And my adopted family from Manchester: Citla, Yayis, David, Edna, Mau, Myri, Christina, Laura, Kerry, Claire, Mareike, Jen, Libby, Christina, Jonsy, Amy, Steffania, Captain America, Mark, Mike, Bill, Iain, Mels, Adam, Jaime, Sam, and Evan.

Last but not least I want to thank the DJ's that made my 4 PhD-years loads more fun; Tiesto, Gareth Emery, Ferry Corsten, Above and Beyond, Calvin Harris, Sasha, Chris Lake and of course the amazing SHM. To them and to the best crew to go dancing with: Neil, Andrey, Scott and Matt, thank you.

# The Author

The author was born in May 1984 in Saltillo, Coahuila, Mexico. She studied an MSc in Astronomy and Astrophysics at the Centre for Radioastronomy and Astrophysics at the UNAM University in Mexico. She graduated in August 2007. Spent 2008 writing-up papers as a follow-up from her MSc and applying for funding to do a PhD abroad. At the beginning of 2009 she started a PhD at the Jodrell Bank Centre for Astrophysics, for which this thesis is submitted.

*To my family and  
my adopted family.*

*I find hope in the darkest of days, and focus on the brightest.*

*I do not judge the Universe.*

Dalai Lama

*Listen up, maggots. You are not special. You are not a beautiful or unique snowflake.*

*You're the same decaying organic matter as everything else.*

Tyler Durden, Fight Club



# Supporting Publications

**$^3\text{He}$  in planetary nebulae: The problem persists**, Guzman-Ramirez, L., Pineda, J., Zijlstra, A. A., Stancliffe R., Karakas, A., in preparation.

**PAHs Formation in O-rich Galactic Bulge Planetary Nebulae**, Guzman-Ramirez, L., Lagadec, E., Zijlstra, A. A., Gesick, K., in preparation.

**Discovery of planetary nebulae using predictive diagnostics established solely from mid-infrared properties**, Parker, Q. A., Cohen, M., Stupar, M., Frew, D. J., Green, A. J., Bojicic, I., **Guzman-Ramirez, L.**, Sabin, L., Vogt, F., 2012, MNRAS, arXiv:1208.4164.

**Carbon enrichment of the evolved stars in the Sagittarius dwarf spheroidal**, McDonald, I., White, J. R., Zijlstra, A. A., **Guzman Ramirez, L.**, Szyszka, C., van Loon, J. Th., Lagadec, E., Jones, O., 2012, MNRAS, arXiv:1209.2563.

**A distance estimate based on angular expansion for the planetary nebula NGC 6881**, **Guzman-Ramirez, L.**, Gomez, Y., Loinard, L., Tafuya, D., 2011, MNRAS, 414, 3129

**Carbon chemistry in Galactic bulge planetary nebulae**, **Guzman-Ramirez, L.**, Zijlstra, A. A., Nchumn, R., Gesicki, K., Lagadec, E., Millar, T. J., Woods, Paul M., 2011, MNRAS, 414, 1667

**Disk evaporation in a planetary nebula**, Gesicki, K., Zijlstra, A. A., Szyszka, C., Hajduk, M., Lagadec, E., **Guzman Ramirez, L.**, 2010, A&A, 514, 54

**Expansion Parallax of the Planetary Nebula IC 418**, **Guzman, L.**, Loinard, L., Gomez, Y., Morisset, C., 2009, AJ, 138, 46

**Ionization-bounded and Density-bounded Planetary nebulae**, Rodriguez, L. F., Gomez, Y., **Guzman, L.**, 2009, RMxAA, 45, 85

**Expansion Parallax for the Compact Planetary Nebula M2-43**, **Guzman, L.**, Gomez, Y., Rodriguez, L. F. 2006, RMxAA, 42, 127



Figure 1: Montage of PNe observed with the HST. Images taken from the HST image gallery <http://oposite.stsci.edu/pubinfo/pr/97/pn/photo-gallery.html>



# Chapter 1

## Introduction

### 1.1 Planetary Nebulae: an evolutionary phase

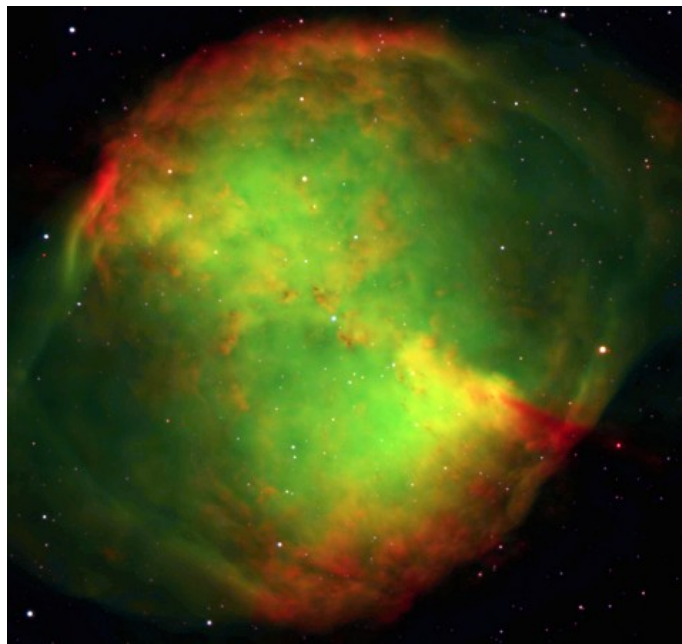


Figure 1.1: The Dumbbell Nebula, Messier 27. Image taken from the HST image gallery <http://oposite.stsci.edu/pubinfo/pr/97/pn/photo-gallery.html>

The Dumbbell Nebula, also known as Messier object number 27 (Figure 1.1) was the first planetary nebula (PN) ever observed. It was found in 1764 by Charles Messier. The name planetary nebulae (PNe) was coined by William Herschel, who thought

## 1: INTRODUCTION

they resembled the greenish disk of a planet. They were later distinguished from other galactic diffuse nebula by the fact that PN have round structures and were often associated with a central star. In 1864, William Huggins was the first person to take a spectrum of a PN (NGC 6543) and found that the spectrum was dominated by emission lines and not a continuum spectrum as for stars. Spectroscopic observations of the nebula led to the discovery that emission lines in planetary nebulae (PNe) are broad, or even split. Charles Perrine in 1929 first correctly interpreted this as the expansion of the nebula. The dynamical lifetime of a PN was then estimated to be  $\sim 10^4$  yr, using an average size of 0.3 pc and an expansion velocity of  $30 \text{ km s}^{-1}$  (Kwok 2000).

In 1956 I. S. Shklovsky compared the expansion velocities of PN with the escape velocities of red giants to argue that PN are the ejected atmospheres of red giants. With a lifetime of  $2 \times 10^4$  yr and the total number of PN in the galaxy being  $6 \times 10^4$ , he estimated that the PN formation rate is 3 per year. Because this is the same number of stars leaving the main sequence, he suggested that most low-mass stars will go through the PN stage. In 1968 Minkowski & Osterbrock supported Shklovsky's scenario adding the fact that the radial velocities of PNe in the Galaxy resemble those of the red giants.

Now we know that PNe form at the end phase of stellar evolution. Stars with mass less than about  $8 M_{\odot}$  eject almost all of their mass in a phase of catastrophic mass loss. Such stars live most of their lives on the Main Sequence, where the energy source is hydrogen fusion. On having finished this phase the star evolves rapidly, creating a convective photosphere. A pulsational instability produces a surrounding shell of dust and molecular gas. During this stage, known as the Asymptotic Giant Branch (AGB) phase, the star can lose between 20 and 80% of its mass, reaching mass loss rates of up to  $10^{-4} M_{\odot} \text{ yr}^{-1}$ . The remaining core of the star ceases nuclear burning and becomes a hot white dwarf (WD). The ejecta briefly become ionised, before dispersing and merging into the interstellar medium. The ionised phase is visible as a planetary nebula (Pottasch 1984). Such a complete evolution track is shown in Figure 1.2 for an initial stellar mass of  $2 M_{\odot}$  (Herwig 2005).

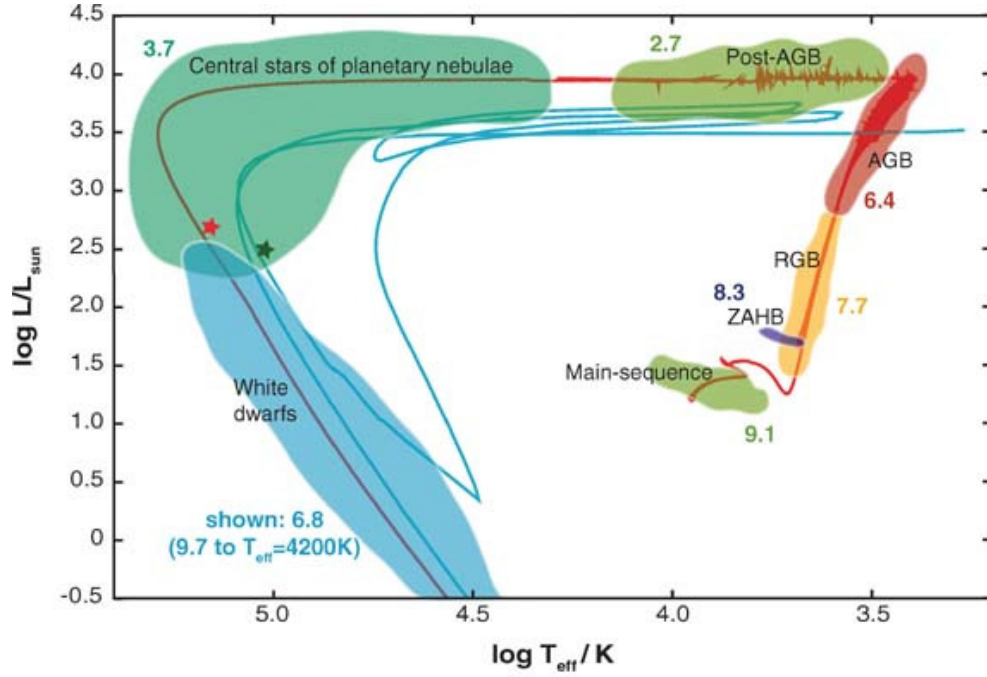


Figure 1.2: The Hertzsprung-Russell diagram, evolutionary track for a  $2 M_{\odot}$  star. The model uses solar metallicity, the blue track shows a born-again evolution (triggered by a very late thermal pulse) of the same mass, however shifted for clarity. The red and green stars mark the position of the observed central stars of planetary nebulae PG 1159-035 and NGC 6853 respectively. The number labels indicate the log of the approximate duration of each phase (Herwig 2005). Image taken from the same paper.

The mass loss from stars is important to the evolution of the host galaxy. In the Galaxy, around half the interstellar medium (ISM) is such recycled stellar gas. The ejecta are enriched with the products of nuclear burning: much of the carbon comes from this source, and most of the interstellar dust is formed in these ejecta. PNe are ideal objects for studying dust formation and evolution that will enrich the ISM. Dust and carbon are essential to the formation of planets and life (Tielens 2005).

## 1.2 Emission mechanisms

Planetary Nebulae, composed of a hot white dwarf (WD) and the ionised nebula around it, radiate across all the electromagnetic spectrum. The temperature of different re-

## 1: INTRODUCTION

gions of PN range from  $\sim 10\text{K}$  in the molecular gas,  $\sim 100\text{K}$  in the dust component,  $\sim 10,000\text{K}$  in the ionised gas,  $\sim 100,000\text{K}$  in the atmosphere of the central star, and  $\sim 1,000,000\text{K}$  in the shocked stellar wind bubble. Correspondingly, all states of matter from solid, molecular, atomic and ionic forms are present. The radiation from the central star interacts with all these different forms of matter and is reprocessed into emission covering the entire electromagnetic spectrum, making PNe some of the most interesting objects to observe (Kwok 2000).

### 1.2.1 Gamma Rays

Planetary Nebulae have not yet been observed to emit gamma rays. White dwarves on the other hand might be able to produce enough energy that can reach the gamma-ray regime. It is still under investigation, but Kashiyama & Ioka (2010) proposed the possibility of white dwarves to be a new candidate for high energy emitting sources. A double degenerate white dwarf binary merges into a white dwarf pulsar with rotational energy ( $\sim 10^{50}\text{erg}$ ) comparable to a neutron star. They theorise that the white dwarf pulsars can produce up to  $\sim 10\text{TeV}$  gamma rays.

### 1.2.2 X-Rays

Over the past decade, about a dozen nearby Galactic PNe were found to be sources of X-ray emission. This emission can be produced by multiple mechanisms;

- Photospheric emission from the central star. The hot star ( $T_{\text{eff}} > 100,000\text{K}$ ) is expected to produce energies of about  $\ll 0.5\text{keV}$ .
- Emission from shock-heated gas in the interiors of PN, this is generated by the interaction of the fast stellar wind with the previous slow AGB wind.
- Shock-heated gas in bow-shocks formed by collimated outflows or jets trespassing onto the AGB wind at velocities  $\geq 300\text{kms}^{-1}$ .
- Coronal emission from a late-type dwarf companion.

X-ray imaging satellites like *Chandra* and *XMM-Newton* have provided compelling observational evidence of these emission (Guerrero et al. 2004). PNe have been observed to show diffuse x-ray emission, confined within the innermost nebular shell, the so called “hot-bubble” (Kastner et al. 2012). A few PNe have been found to show a hard X-ray excess. This could be a hint of the presence of binary companions and/or accretion processes associated with the central star of the PNe (Kastner 2007). The hard X-rays might arise from accretion onto a compact, hot companion (Kastner & Soker 2003) or from the corona of a late-type companion that has been “re-born” via accretion of AGB wind material (Jeffries & Stevens 1996).

### 1.2.3 Ultraviolet

Central stars of planetary nebula (CSPN) have high temperatures and emit most of their fluxes in the UV. Satellites like the International Ultraviolet Explorer (*IUE*) have been used to analyse the spectra of the central star of PNe. The UV spectrum between 1000 and 2000Å contains P-Cygni-type profiles of resonance lines of several ions of C, N, O, Si, S, P, which remain strong until far out in the wind, as well as hundreds of strongly wind-contaminated lines of FeIV, FeV, FeVI, CrV, NiIV, ArV and ArVI. All these lines are used to measure the density and velocity structure of the atmospheric outflow, that will yield the fundamental stellar parameters (Kaschinski et al. 2012).

### 1.2.4 Visible

Unlike stars which show continuous spectra, the optical spectra of PNe are dominated by emission lines. Line emission occurs when electrons in the atoms make a transition from one bound electronic state to another bound state at a lower energy. The UV photons from the central star will ionise the atoms in the nebula. The electrons ejected in the ionisation process provide a pool of kinetic energy for the collisional excitation of the heavy atoms (C, N, O, etc.). Spontaneous emissions from various excited states of different atoms and ions are responsible for the rich emission-line spectrum seen in the visible (Kwok 2000). The first comprehensive spectroscopic survey of PNe was carried out by Acker and Stenholm between 1984 and 1991 (Acker et al. 1992). Over  $\sim 1000$

## 1: INTRODUCTION

PNe were observed in the 4,000–7,400Å wavelength range at a resolution of  $\sim 10\text{\AA}$ . The excitation class, electron temperature, electron density, and the absolute  $H\beta$  fluxes were calculated for a large number of PNe (Acker et al. 1991).

### 1.2.5 Infrared

In the near-infrared, the major absorption processes are bound-free (ionisation) and free-free (when an electron travels close to an ion, accelerates and emits a pulse). Dust becomes the dominant emission mechanism in the mid- to far-infrared. The radiation from the dust component usually peaks beyond  $20\mu\text{m}$ , where the Earth's atmosphere is opaque, this is the reason why observations using satellites were needed to observe the dust component in PN. Observations using the Infrared Astronomical Satellite (*IRAS*) found that PNe dust temperatures range from 40 to 240K. Dust features were also identified: a family of emission bands at 3.3, 6.2, 7.7, 8.6 and  $11.3\mu\text{m}$  was first detected in a young carbon-rich PN, these bands are now identified as vibrational modes of polycyclic aromatic hydrocarbon molecules (PAHs) (Allamandola et al. 1989).

### 1.2.6 Submm

In the submillimetre regime the main emission mechanism comes from transitions between rotational and vibrational states of molecules. Large surveys of emission from the carbon monoxide (CO) molecule and other molecules show that evolved stars are losing mass in the form of stellar winds at relatively low outflow speeds. This wind creates several shells in the nebula, these shells are being observed in the submm wavelengths allowing the study of photochemistry in these environments; the shell kinematics give us an examination of the evolutionary history of the star during its transition to the PN stage, since the molecular shell was emitted during the AGB phase and therefore contains information about that phase (Jaminet et al. 1992). The measurement of the shell masses of a large number of planetary nebulae, coupled with an examination of their luminosities and galactic kinematics, should allow a good value to be set for the upper progenitor mass limit for a white dwarf stars, or, conversely, for the lower mass limit for supernova progenitors.

### 1.2.7 Radio

In the radio domain, free-free is the dominant emission mechanism in PN. PN have been extensively observed in radio wavelengths since the beginning of radio astronomy (Terzian 1966). In the 1980's, The Very Large Array (*VLA*) made radio surveys of PN, which produced better positions, fluxes and angular sizes for several hundred PN (Gathier et al. 1983; Kwok 1985; Zijlstra et al. 1989; Aaquist & Kwok 1990a, 1991; Kwok & Aaquist 1993). Radio photometric observations have been used to derive properties of the nebula. The total flux of free-free emission can be used to calculate the ionised mass ( $M_i$ ) of the PN.

## 1.3 Classification

In general, PN can be classified depending on their nebular chemical abundance, their central star and/or their morphology. Most of these classifications have been done in the UV and optical regime. Using spectroscopy in the UV we can classify the central star; with spectroscopy in the optical we observe the intensities of some of the main elements of the nebula, which are used to calculate the PN chemical abundances. Also in the optical using imaging (mainly  $H\alpha$  and  $[OIII]$ , or more filters if possible) a morphological classification can be done. Since imaging only give us a 2D representation of the PN, there is a risk that orientation effects can lead to the wrong classification.

### 1.3.1 Nebular abundance

In 1978, Manuel Peimbert classified PNe based on their chemical nebular abundance and other characteristics. He defined the classification as:

- Type I sources are He- and N-rich, filamentary structures, and low mean heights above the Galactic mid-plane. They are likely to be associated with the highest mass progenitor of all. Progenitor masses must exceed  $\sim 2.4M_{\odot}$  (Peimbert & Serrano 1980; Calvet & Peimbert 1983).

## 1: INTRODUCTION

- Type II sources have lower abundances and larger mean heights  $\langle z \rangle \sim 150 \text{ pc}$ . These correspond to PNe in the solar neighbourhood. Their progenitors have masses of  $\sim 1.5 M_{\odot}$ , this correspond to intermediate Population I objects. Most PNe are Type II.
- Type III belong to the Galactic thick disk, and have large peculiar velocities,  $\delta v > 60 \text{ km s}^{-1}$ . Due to their kinematics characteristics they are expected to be Fe-poor.
- Type IV sources are those that belong to the halo. They show an slight deficiency of He relative to other PNe.
- Type V sources are located in the Galactic Bulge (Perinotto 1991).

### 1.3.2 Central star

Spectra of the central star of a planetary nebula (CSPN) can be divided into two main groups: those showing H-rich atmospheres and those with H-poor atmospheres. About 10% of the group of H-poor CSPN have central stars with Wolf-Rayet (WR) spectra. Their spectra share a common classification as WR stars (massive stars) because they both show an emission-line spectra from an expanding H-poor stellar wind. These central stars have strongly enhanced C and He, but little or no H in their atmosphere, and are the low mass counterparts to the population I Wolf-Rayet stars. To avoid confusion for the spectral type of the central star in PNe it is common to use square brackets [WC]. Here the C means that the star is dominated by C and deficient in N; for stars deficient in C [WN] is used. The formation of H-poor central stars is probably related to a thermal pulse either at the very end of the AGB or during the young PN phase. H-rich layers may be removed due to efficient mixing and subsequent nuclear burning. It is unclear at present which mechanism (post-AGB pulse or very late thermal pulse) dominates the formation rate of PNe with [WC] central stars.

Figure 1.3 shows two spectra taken using the Ultraviolet and Visual Echelle Spectrograph (UVES) instrument on the Very Large Telescope (*VLT*). One can clearly see



the difference between the H-poor central star of the PN M3-15, classified as a [WC5] and the H-rich central star of Th3-4 (Guzman-Ramirez et al. 2011).

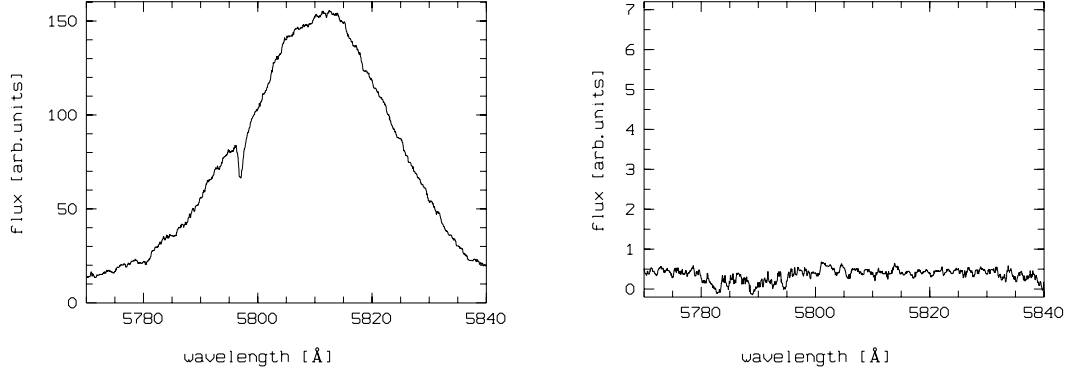


Figure 1.3: UVES spectrum of the central star of the PN M3-15 (left), showing the broad emission of the CIV line at 5800/5811 Å classified as [WC5]. The central star of the PN Th3-4 (right) shows no emission lines.

### Formation of a Wolf-Rayet type central star

De Marco & Soker (2002) proposed the spiralling-in of a companion as a formation mechanism for a Wolf-Rayet type central star in PNe. This process starts when a low-mass companion enters a common envelope phase with the AGB progenitor, enhances the mass-loss rate, and is then destroyed. Its dense material collides with the core and forms an accretion disk, causing extra mixing between the core and the envelope material, turning the star to a C-rich star and then to a H-deficient one through dredge-up, due to shear instabilities induced by the accretion disk. They conclude that planets with mass of  $0.001\text{--}0.1 M_{\odot}$  may survive evaporation until they reach the core of the AGB star, where they may form disks after being tidally destroyed.

#### 1.3.3 Morphology

The 2D morphology of a large number of PNe in the Galaxy has been observed. Most PNe appear to possess bipolar, round and elliptical morphologies. But of course all these morphological classes are blurred by projection effects, and more importantly, they can depend on the emission line used for making the image. Images obtained

## 1: INTRODUCTION

using [NII] and [OI] filters appear edge-brightened, while images taken with [OIII] and H $\alpha$  filters seem to arise in the nebular interior (Balick & Frank 2002). Phillips (2003) studied the relation between elemental abundance of PNe and their morphology, finding the following:

- Round sources are associated with low abundances of heavy elements (low metallicity). This suggests that the progenitors of these objects are of relatively low mass. The same study showed that PNe with circular morphology tend to have high Galactic latitudes.
- Bipolar PNe are concentrated towards low galactic latitudes. They are mostly associated with higher abundances, suggesting they arise from higher-mass progenitors. Most of Type I PNe are bipolar, showing high N, C and He abundances.
- Elliptical sources showed to be distributed over the entire abundance range of elements (N, O, Ne, Ar, Cl, S, C and He) leading to the conclusion that they arise from progenitors of all masses. These PNe are mostly found at high Galactic latitudes, as are round PNe.

There are also micro-structures observed in a lot of PNe, like ansae (or Fast, Low Ionisation Emission Regions (FLIERs)), minor lobes, point symmetry outflows, central obscuring waist, clumps and tails (Sahai et al. 2007).

Figure 1.4 shows some examples for the main different morphologies observed in PNe. NGC 246 is classified as round, NGC 650 is a clearly bipolar PN and NGC 6565 shows an elliptical morphology. (The images were taken from the PNIC: Planetary Nebula Image Catalogue<sup>1</sup>).

To date there are  $\sim 3,000$  known PNe, roughly half of which have been morphologically classified in different catalogues. The classification statistics of Corradi & Schwarz 1995a; Manchado 2004; Parker et al. 2006; Miszalski et al. 2008 are summarised in Table 1.1.

---

<sup>1</sup><http://www.astro.washington.edu/users/balick/PNIC/> (Balick 2007)

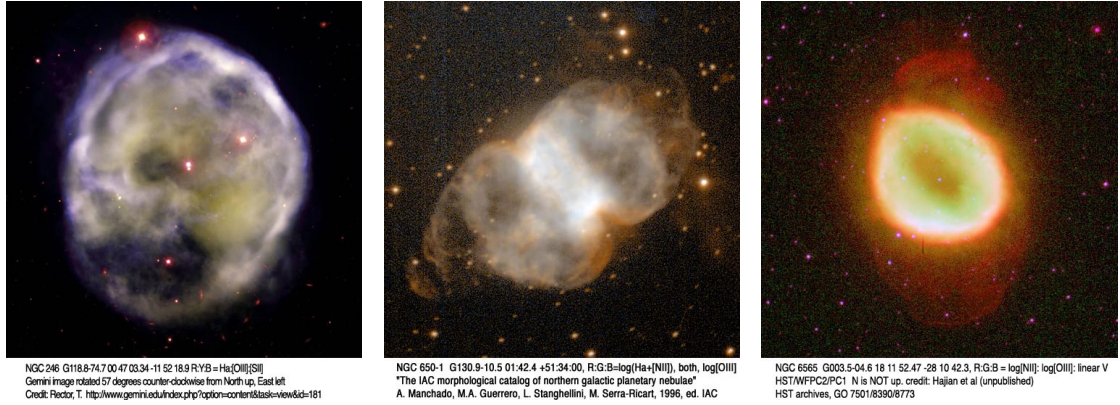


Figure 1.4: PNe morphologies; circular NGC246 (left), bipolar NGC650 (middle) and elliptical NGC6565 (right). The images were taken from the PNIC: Planetary Nebula Image Catalogue (Balick 2007).

Table 1.1: Morphological classification of PNe.

Shape	Corradi, R <sup>1</sup> total sample of 359	Manchado, A <sup>2</sup> total sample of 255	MASH <sup>3</sup> total sample of 905
Elliptical	64%	58%	55%
Bipolar	14%	17%	10%
Round	N/A	25%	28%
Irregular	18%	N/A	4%
Point symmetric	4%	N/A	N/A

<sup>1</sup>Corradi & Schwarz (1995a), <sup>2</sup> Manchado (2004),

<sup>3</sup>Parker et al. (2006); Miszalski et al. (2008)

### 1.3.4 Population and distribution

The PNe population of the Galactic Disc has been estimated by Zijlstra & Pottasch (1991). Assuming a scale length of the disk of 3.5 kpc; that the relative number of PN is independent of position in the Galaxy; and using a distance to the Galactic centre of 7.8 kpc, the number of PN is  $23,000 \pm 6,000$ . Frew & Parker (2006) found that the total number of PNe (including the Galactic Bulge) is  $28,000 \pm 5000$ . Using stellar population synthesis models (for PNe with radii  $< 0.9$  pc), Moe & De Marco (2006) calculated that there should be  $46,000 \pm 13,000$  PNe in our Galaxy. All of these estimates far exceed the number of confirmed PNe. This is attributed to a combination of heavy obscuration by dust in the Galactic plane and the diversity in observed PN properties (angular extent, surface brightness and morphology). Table 1.2 shows the mean

## 1: INTRODUCTION

Galactic latitude  $|b|$  for the different morphologies observed in the latest catalogues, presented in section 1.3.3. As for the scale height  $\langle z \rangle$  they all agree that round PNe extend up to  $\sim 600$ pc, elliptical PNe  $\sim 280$ pc and that bipolar PNe are very concentrated towards the Galactic Disc at  $\langle z \rangle \sim 100$ pc. This implies that bipolar PNe come from a more massive population of stars compared to round and elliptical.

Table 1.2: Mean Galactic latitude of PNe.

Shape	Corradi <sup>1</sup>	Manchado <sup>2</sup>	MASH <sup>3</sup>
	$ b $	$ b $	$ b $
Elliptical	$9^\circ$	$5^\circ$	$3.5^\circ$
Bipolar	$3^\circ$	$2^\circ$	$2.5^\circ$
Round	N/A	$8^\circ$	$4.05^\circ$
Irregular	$4^\circ$	N/A	$3.23^\circ$

<sup>1</sup>Corradi & Schwarz (1995a), <sup>2</sup> Manchado (2004),

<sup>3</sup>Parker et al. (2006); Miszalski et al. (2008)

Figures 1.5 and 1.6 show the distribution of PNe in the Galaxy in Galactic coordinates, equatorial coordinates, their Galactic longitude, and Galactic latitude. The distribution in Galactic longitudes is more or less symmetrical. The concentration towards the Galactic equator is very high, 84% of them are located at  $|b| \pm 10^\circ$  (Kohoutek 2001).

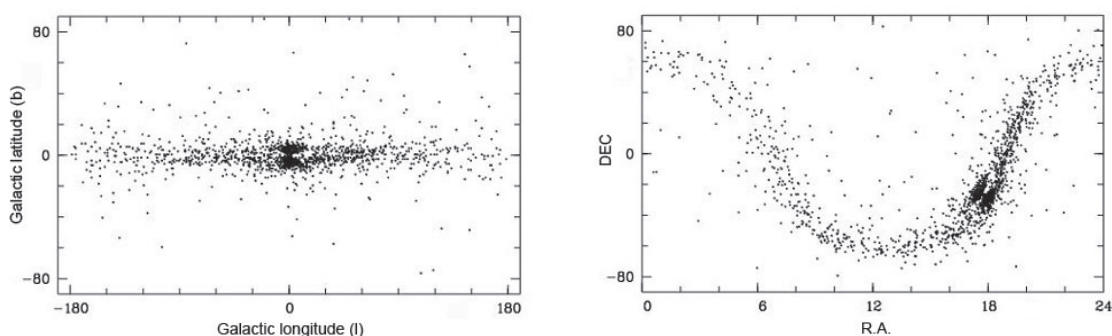


Figure 1.5: Distribution of known planetary nebulae in Galactic coordinates (left) and equatorial coordinates (right) (Kohoutek 2001).

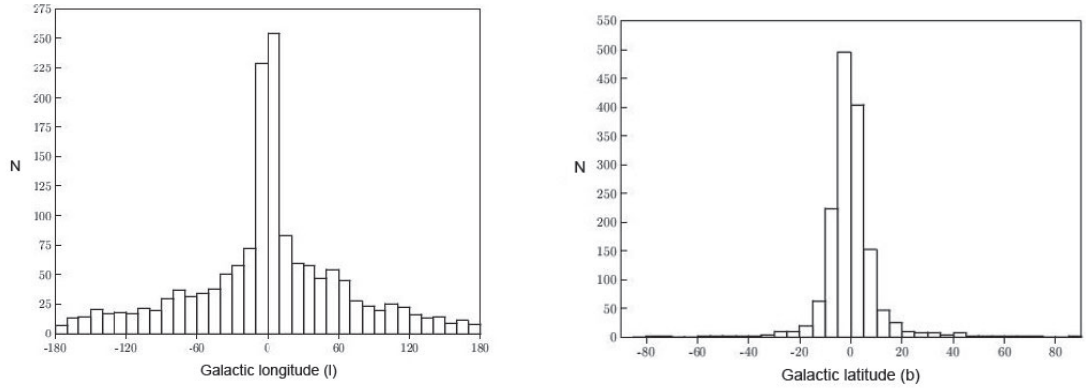


Figure 1.6: Distribution of known planetary nebulae according to their Galactic longitude (left) and their Galactic latitude (right) (Kohoutek 2001).

## 1.4 PNe Mysteries

- **Missing PNe.** The detection of PNe is affected by interstellar extinction. More evolved PNe have very low surface brightness, making them hard to detect, very distant PNe could be unresolvable. In crowded areas like the Galactic plane it is hard to detect them due to confusion effects.
- **Physical properties.** Luminosity function and abundances are generally based on nearby or very bright (young) PNe. This is because these analyses require an accurate distance and many spectral lines that can only be observed in very bright objects due to the sensitivity limit of the telescopes to date.
- **Morphology.** One of the main paradigms in the PNe community is to identify if there is a single unified model that can explain the large-scale shapes of post-AGB and PNe, or if there is more than one process that affects shaping. As shown in Fig.1.4, bipolar PNe present disks and tori: the formation mechanism of these structure is still an open question.
- **Mixed-chemistry.** Observations of Galactic Disk PNe using the Infrared Space Observatory (*ISO*) showed C-rich dust (PAHs) nested inside a shell of O-rich dust (amorphous and/or crystalline silicates). In PNe with late Wolf-Rayet type central stars the mixed-chemistry phenomena is attributed to the presence of

## 1: INTRODUCTION

old oxygen-rich material in a circumstellar disk, with the PAHs forming in a more recent carbon-rich outflow. This phenomena has been also observed in Galactic Bulge PNe (GBPNe); contrary to Galactic Disk PNe, GBPNe are not expected to experience a carbon-rich outflow. The mixed chemistry phenomenon occurring in the GBPNe is best explained through hydrocarbon chemistry in an UV-irradiated, dense torus. As mentioned in the above mystery, the formation and evolution of these tori in PNe is still far from being understood. Please refer ahead to discussion of C- and O-rich PNe in Chapters 3 and 4.

- **$^3\text{He}$  problem.** According to stellar evolution models, low-mass stars ( $M < 2.5M_{\odot}$ ) are the net producers of  $^3\text{He}$ . There are only a few PNe that have been detected to harbour  $^3\text{He}$ , but their abundances agree with the stellar evolution models. When stellar production is included in models for the chemical evolution of the Galaxy, no agreement between the observed (HII regions and ISM) and predicted  $^3\text{He}$  abundances can be found. Standard evolution models predict that: (1) the protosolar  $^3\text{He}/\text{H}$  value should be less than what is found in the present ISM; (2) the  $^3\text{He}/\text{H}$  abundance should grow with source metallicity; and (3) there should be a  $^3\text{He}/\text{H}$  abundance gradient in the Galactic Disk with the highest abundances occurring in the highly-processed inner Galaxy. None of these predictions have been confirmed by observations.

The aim of this thesis is to analyse and solve some of the mysteries of PNe presented above. In Chapter 2, newly confirmed PNe were found using the INT Photometric  $\text{H}\alpha$  Survey (IPHAS). The complete list of  $\text{H}\alpha$  images and its corresponding spectra are presented in Appendix A. Chapter 3 presents the mixed chemistry phenomena observed in a sample of 40 Galactic Bulge PNe. As with the optical data, the list of *Spitzer* spectra is given in Appendix C. Chapter 4 shows the spatially resolved emission of PAH features observed in O-rich GBPNe and describes a correlation found between the  $\text{H}_2$  line ( $12.4\mu\text{m}$ ) and the effective temperature of its central star. Chapter 5 shows upper limits of the  $^3\text{He}$  abundance in a sample of 3 PNe. In Chapter 6 the main conclusions are presented and Chapter 7 is full of afterthoughts and future work.

## Chapter 2

### IPHAS survey



Figure 2.1: Planetary Nebula NGC 6781. Image based on data obtained as part of the INT Photometric H-Alpha Survey of the Northern Galactic Plane, prepared by Nick Wright, Harvard-Smithsonian Center for Astrophysics, on behalf of the IPHAS Collaboration.

The Isaac Newton Telescope (INT) Photometric H $\alpha$  Survey (IPHAS) of the northern Galactic plane (Drew et al. 2005) is an imaging survey using the Wide Field Camera

(WFC) on the INT.

The imaging in broad-band Sloan  $r'$  and  $i'$  filters, accompanying narrow-band  $H\alpha$  filter ( $\lambda_c = 6568\text{\AA}$ ,  $\text{FWHM} = 95\text{\AA}$ ) observations, reaches to at least a magnitude of  $r' = 20$ . One of the survey's main aims is to identify large numbers of objects in the important short-lived phases of stellar evolution.  $H\alpha$  traces ionised gas of assorted nebulae such as HII regions, planetary nebulae, Wolf-Rayet nebulae and supernova remnants. The survey covers the entire northern Galactic plane in the Galactic latitude range  $-5^\circ \leq b \leq +5^\circ$ , a total sky area of  $1800\text{deg}^2$ .

The initial data release (IDR) (González-Solares & et al. 2008) contains  $1600\text{ deg}^2$  of imaging data in three bands covering the northern Galactic plane at latitudes  $|b| < 5^\circ$  and longitudes  $30^\circ \leq l \leq 220^\circ$ . Fig. 2.2 shows the distribution in the sky. The area observed was divided into fields corresponding to the coverage of the WFC. Fields have been defined in a diagonal rather than rectangular geometry in order to take advantage of the L shape of the detector configuration allowing for a 5% overlap between adjacent pointings. Fig. 2.3 provides an example of the observation configuration. Gaps between detectors are typically 20 arcsec. Therefore the area not observed in each pointing due to the gaps is about  $12\text{ arcmin}^2$  (i.e.  $\sim 1\%$ ). In order to cover the chip gaps and bad columns each “field” is observed in pairs which are referred to as “on” and “off” positions with an offset of 5 arcmin west and 5 arcmin south between the pointings. Most of the objects are thus observed twice. Field pairs are observed consecutively in the three bands before moving to the next field pair in order to minimise the effects of photometric variability. Each field pair is assigned an identification which is referred to as “field number”. The overall survey properties and quality of the data are summarised in Table 2.1. The exposure time for each filter is 30 s in  $r'$  (except in the first year of observations, 2003, when it was 10 s), 10 s in  $i'$  and 120 s in  $H\alpha$ .

Once the raw data was obtained, it was processed in a pipeline specially designed by Irwin & Lewis (2001) for the WFC. The data is first debiased, bad pixels and columns are flagged and recorded in confidence maps which are used during catalogue generation. The CCDs are found to have significant non linearities so a correction using



Table 2.1: Survey parameters and IDR quality summary.

Parameter	Value
Telescope	2.5-m Isaac Newton Telescope, La Palma
Instrument	Wide Field Camera
Field of view	0.29 deg <sup>2</sup> (per pointing)
Detector scale	0.33 arcsec pixel <sup>-1</sup>
Total area of survey	~1800 deg <sup>2</sup>
Total area in IDR	~1600 deg <sup>2</sup>
Area included in the PhotoObjBest catalogue	~1000 deg <sup>2</sup>
Number of unique objects in the full catalogue	~200 000 000
Number of unique objects in the PhotoObjBest catalogue	~90 000 000
Filters	$r'$ , $i'$ , H $\alpha$
Exposure time	30 s ( $r'$ ), 10 s ( $i'$ ), 120 s (H $\alpha$ )
FWHM (median)	1.3 arcsec ( $r'$ ), 1.2 arcsec ( $i'$ ), 1.3 arcsec (H $\alpha$ )
Magnitude limit (Vega, $5\sigma$ )	21.8 ( $r'$ ), 20.2 ( $i'$ ), 20.6 (H $\alpha$ )
Astrometry	<0.1 arcsec (based on 2MASS)

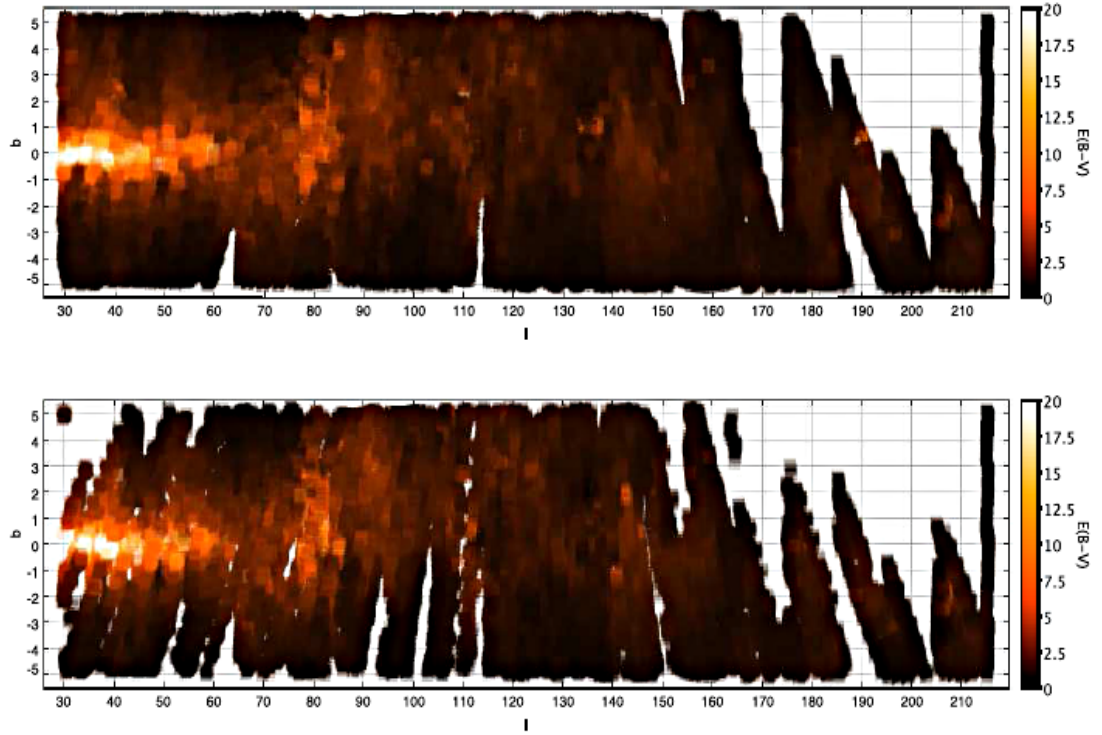


Figure 2.2: IPHAS IDR sky coverage in Galactic coordinates (degrees). The top figure displays the coverage of the full release and the bottom one the coverage of the PhotoObjBest best observations subset. Brightness indicates the total line-of-sight reddening as computed from the Schlegel et al. (1998) dust maps using 4 pixel interpolation.

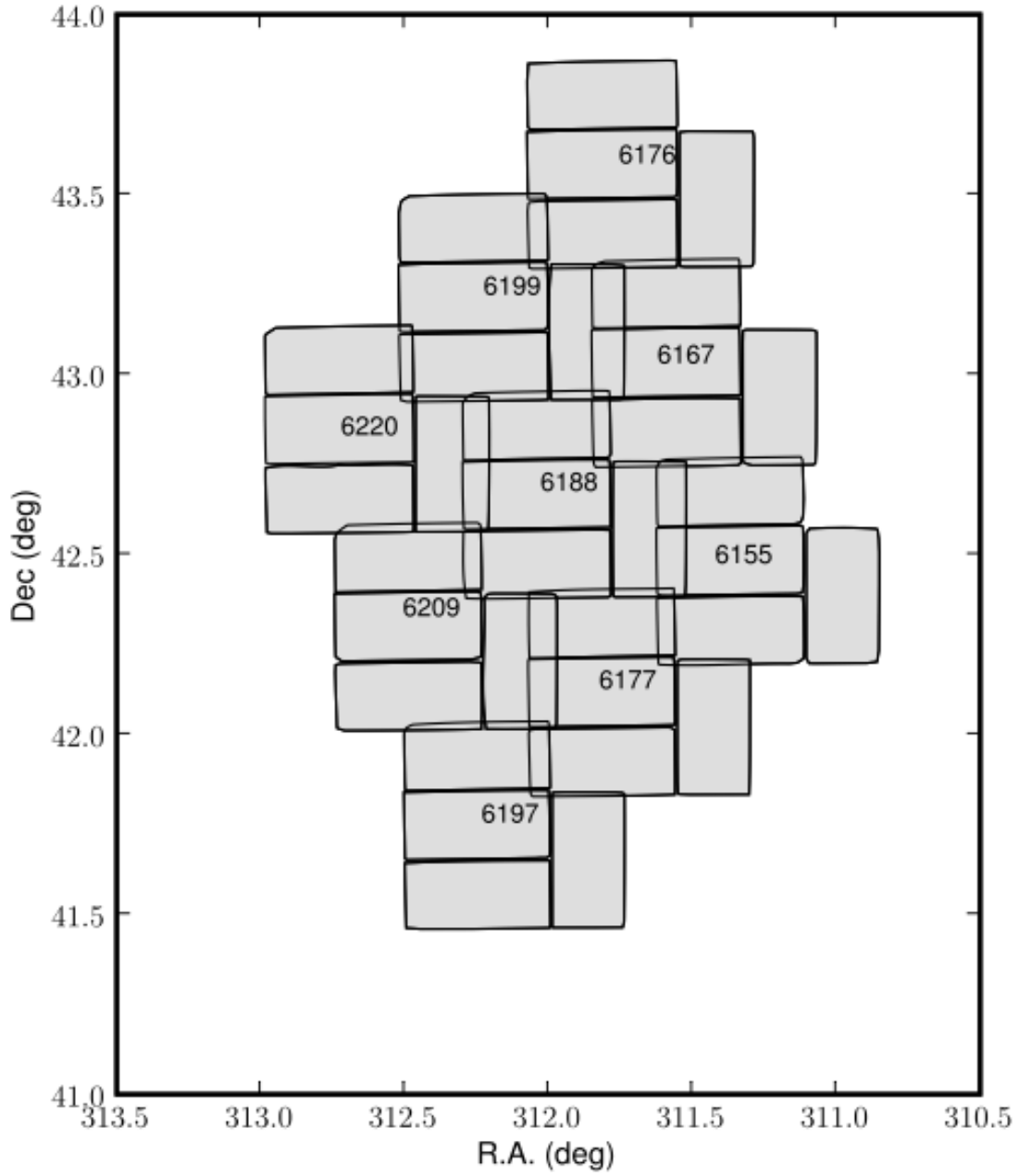


Figure 2.3: Tiling configuration of  $3 \times 3$  pointings covering an area of  $\sim 2 \text{ deg}^2$ . Chips are outlined in black. Field numbers are also shown.

look-up-tables is applied to all data. Flatfield images in each band are constructed by combining multiple sky flats obtained in bright sky conditions during twilight. Master fringe frames are created by combining all the science exposures for each band and used to correct the images ( $i'$  band). Finally an astrometric solution is applied which results

in an internal astrometric precision better than 100mas over the whole WFC array. The data is photometrically calibrated using a series of Landolt standard stars. Data from non photometric nights are flagged by the pipeline and each area is calibrated using the overlap regions ( $\sim 10\%$ ) between pointings. A number of key quality control performance measures are extracted on a nightly basis from the generated object catalogues. These indicators include instrumental information such as sky brightness, image quality (ellipticity, FWHM) and throughputs from extraction of standard star fluxes and comparison with known zero point data. After the quality control, all the point sources in the fields are measured (position and magnitude) and catalogued by the pipeline.

## 2.1 Target selection

The Northern Galactic Plane was divided into  $2\text{deg}^2$   $\text{H}\alpha$ - $r$  (continuum removal) regions in order to create mosaics. The extended nebulae were searched for via visual inspection of those maps. To create the mosaics, the  $\text{H}\alpha$  and the  $r$  images have to be selected, including the off-set observations corresponding to the same centre coordinates to fill the inter-chip gaps on the WFC. The next step is to set the quality parameters of the PostgreSQL database, generated automatically from the FITS headers of the pipeline object catalogues.<sup>1</sup> Table 2.2 presents the list of parameters used to create the frames used. Two binning systems were applied:

- 15 pixels  $\times$  15 pixels, this corresponds to 5 arcsec binning with the WFC (1 pixel represents 5 arcsec on the sky). This binning is used to resolve low surface brightness objects, this makes the shape (outflows, ansae, clumps, tail) of the nebulae more pronounced. This parameter set is used to detect objects with sizes greater than 3–4 arcmin. The different types of morphology are described in Chapter 1 Section 1.3.3.

---

<sup>1</sup>Wide Field Survey: Final Data Products <http://www.ing.iac.es/PR/newsletter/news9/science2.html>

- 5 pixels  $\times$  5 pixels, this corresponds to 1.7 arcsec binning with the WFC (1 pixel represents 1.7 arcsec on the sky). This binning is used to detect intermediate size nebulae with sizes between 15 arcsec to 2–3 arcmin.

Table 2.2: The parameters used to retrieve these mosaics are the following.

Search box	120 arcmin
Filters	H $\alpha$ ,r
Sky level	< 600 (in H $\alpha$ )
Ellipticity	< 0.3
Seeing	< 5 arcsec
Magnitude limit	> 18
Binning	15 and 5 pixels

The list of PNe candidates that we followed-up spectroscopically comes from the catalogue for extended nebulae. All were found by visual search at 15 and 5 pixels binning (L. Sabin, PhD Thesis, 2008). The classification as candidate PN was based mainly on the morphology. PNe are known for their symmetrical shapes: bipolar, elliptical, round, point-symmetric. The 120s exposure in H $\alpha$  only give us a first estimate of the shape of the PN. Table 2.3 and 2.4 presents a list of the main morphological classification used for these objects, using sub-classes in the cases where more structures were observed.

Table 2.3: Morphological classification of the PN candidates.

Main class
B – Bipolar
E – Elliptical
I – Irregular
M – Multipolar
R – Round

Table 2.4: Morphological sub-classification of the PN candidates.

Sub-class
a – ansae
d – disk
Ms – Multiple shells
r – ring(s)
t – torous

## 2.2 Spectroscopic follow-up

### 2.2.1 Spectroscopy: The technique

Spectroscopy is the best tool to characterise an astronomical object: it allows us to derive its chemical signature, temperature, density and velocity. The PN optical spectrum is dominated by emission lines. The high temperatures of the central star of PNe (30,000K to 100,000K) creates a UV radiation field that ionises the nebula. Once the atoms recombine they emit photons that we observe as emission lines.

Also for recombination lines, the density of the nebula provides the necessary conditions for transitions within the same electronic configuration to occur. These transitions violate the LS coupling selection rules. In light atoms (generally  $Z < 30$ ), electron spins  $s_i$  interact among themselves so they combine to form a total spin angular momentum  $S$ . The same happens with orbital angular momenta  $l_i$ , forming a total orbital angular momentum  $L$ . The interaction between the quantum numbers  $L$  and  $S$  is called RussellSaunders coupling or LS coupling. Transitions for which the selection rule that the spin does not change is violated is a result of the failure of LS coupling, these are called forbidden transitions. These transitions are perfectly possible but occur at a lower rate. Forbidden emission lines have only been observed in extremely low-density gases and plasmas, under such conditions, once an atom or molecule has been excited for any reason into a meta-stable state, then it is almost certain to decay by emitting a forbidden-line photon. Since meta-stable states are rather common, forbidden transitions account for a significant percentage of the photons emitted by the low density gas in PNe (Stanton 1973).

The emission lines coming from these transitions are distinguished from the normal

transitions by square-brackets, like [OIII]. These transitions dominate the emission line spectrum of a PN and they are a good marker to differentiate them from other H $\alpha$  emitters. Table 2.5 lists the element and wavelength of the main spectral lines observed in PN.

Table 2.5: Main spectral lines observed in PNe.

Element	Laboratory wavelength ( $\text{\AA}$ )
H $\delta$	4101.7
H $\gamma$	4340.5
H $\beta$	4861.3
[OIII]	4958.9
[OIII]	5006.8
[OI]	5577.4
[NII]	6548.1
H $\alpha$	6562.8
[NII]	6583.6
[SII]	6717.0
[SII]	6731.3

IPHAS provides the largest, least biased and most homogeneous PNe candidate list ever assembled in the Northern Galactic plane and over the widest evolutionary range with which to attack our key science aims: the missing population of PNe in the inner regions of the plane, their morphology, sizes and chemical abundances. IPHAS gives us a realistic opportunity to significantly improve the population statistics for this important class of objects. In the framework of the IPHAS survey, a spectroscopic follow-up was undertaken. The main immediate objective is to confirm their nature as planetary nebulae, vital before any further study can be made, with emphasis on the more evolved/extended examples. In this thesis we carried out observations with the following telescopes:

### 2.2.2 KPNO

Kitt Peak National Observatory (KPNO) is part of the National Optical Astronomy Observatory (NOAO). The 2.1m telescope has a Pyrex primary mirror. Its fast focal ratio, f/2.6, allowed a relatively fast Cassegrain focus. For the follow-up observations

the GoldCam Spectrograph was used. The 2.1-m GoldCam spectrometer offers resolutions from 300 to 4500 using a variety of gratings.

The observations were taken as part of the 2009B-0267 (PI Albert Zijlstra) program. The settings for these observations used the grating 240, centred at 5500Å which gives a coverage of 3040Å with a dispersion of 1.52 (Å/pixel) giving us a resolution of 4.1Å.

### 2.2.3 SAAO

The South African Astronomical Observatory (SAAO) is the national centre for optical and infrared astronomy in South Africa. It is a facility of the National Research Foundation under the Department of Science and Technology. The 1.9m telescope was built by Grubb Parsons in 1938-48 for the Radcliffe Observatory, Pretoria. It has a 2-pier asymmetrical mounting. All observing is done with the telescope East of the polar axis. The Cassegrain focus of the telescope is f/18,  $\sim 6$  arcsec/mm.

The settings for these observations used two gratings:

- (1) Grating 7, has a dispersion of 210Å/mm, a coverage of 4200Å with a blaze of 4600Å giving us a resolution of 5Å.
- (2) Grating 5, has a dispersion of 50Å/mm, a coverage of 800Å with a blaze of 6800Å giving us a resolution of 1Å.

The observations were taken as part of the quarter Jul-Sep 2010 (PI Quentin Parker).

### 2.2.4 Data Reduction

All the spectra were reduced using the IRAF packages. In Appendix B the complete data reduction process is presented. The main tasks used were:

- 1. Remove the overscan area.** This area is typically 32 columns at the right edge of the frames that has the electronic pedestal level, this was subtracted from all the frames and then chopped off to leave only the region with useful data. This step trims-off the overscan area and also the first and last few rows and columns of the frames.
- 2. Subtract the bias.** These are zero seconds integration exposures that will give

you the red-noise<sup>2</sup> of your instrument. Generally a few bias frames are taken, averaged and then subtracted from the data-frames.

**3. Divide by the normalised flats.** Flat field exposures are used to remove pixel-to-pixel variations across the chip. Usually dome flats (exposures of a quartz lamp illuminating the spectrograph slit) will suffice to remove the pixel-to-pixel response of the CCD.

**4. Remove bad columns.** In the case of having one or a few columns where the sensitivity of the chip is below the average or even zero, it is important to remove these columns from your data. The way it works is averaging the data obtained in the columns right next to the damaged column.

**5. Remove cosmic rays.** For long integration time exposures, cosmic rays become a big problem. In the case of PNe, the integration exposures were around 30min, therefore cosmic rays removal was mandatory. The software used to do this is called L.A. Cosmic. It detects round, single (or a few) pixels high intensities and removes them from the frames.

**6. Wavelength calibration.** For the wavelength calibration ARC frames were taken after every object. The ARC frames will determine the dispersion solution. Using the dispersion solution, the object spectrum will be put on a linear wavelength scale by interpolating to a constant delta wavelength per pixel.

**7. Background subtraction.** Usually using a few rows of sky above and below the object signal will be enough to average the sky background and subtract it from the object data. In this manner sky lines will be removed.

**8. Flux calibration.** After applying the response correction, the flux calibration can be done when a spectrophotometric standard star was observed, it is then used to calibrate the spectrum to real flux units.

Once the spectra is wavelength and flux calibrated, the measurements of the line intensities were made using the IRAF package (gaussian fit). It applies a gaussian fit to the line and gives you the peak flux of each line and the frequency at which it was

---

<sup>2</sup>When the range of time-correlations in the noise is such that the power spectrum follows a power law with a negative spectral index, then the noise process is referred to as red-noise.



observed. These intensities were then used to calculate the intensity ratios between  $H\alpha$ , [NII], and [SII].

## 2.3 Diagnostic Diagrams

Spectroscopically PNe can still be confused with other astronomical objects. The astronomical significance of the  $H\alpha$  spectral line emission is that it both traces diffuse ionised nebulae and is prominent in the spectra of pre- and post-main sequence stars. The main  $H\alpha$  emitters found in the IPHAS survey are: diffuse nebulae, emission line stars, galaxies, Herbig-Haro objects, HII regions, supernova remnants (SNR), symbiotic stars and planetary nebulae. Therefore is important to remark the main characteristics of the different objects. For the specific case of the sources analysed in this thesis, the main objects found were:

- **Planetary Nebulae.** The [OIII] emission line is normally about 3 to 5 times brighter than the  $H\alpha$  line.
- **HII regions.** In the case of HII regions the intensity of the [NII] and [OIII] lines depend on the temperature of the central star. The principal differentiator is the [NII]/ $H\alpha$  ratio, if it is lower than 0.7 it may be an indication of HII nature of its nebulosity, grater than 0.7 it means it could be a PN, SNR or a Population I Wolf-Rayet nebula, because it indicates N-enhancement (Kennicutt et al. 2000).
- **Supernova Remnants.** They normally have very little continuum emission. Their main difference is that they show very strong [SII], [OI] and [OIII] lines.
- **Strömgren Sphere.** They are spheres of ionised hydrogen (HII) around a young star of the spectral classes O or B. They are also known as ionisation bounded

compact HII regions but HII regions could be instructed fully ionised, density bounded features that appear as wisps and filaments. They look like PNe in  $H\alpha$ , but their spectra do not exhibit [OIII] emission.

The diagnostic diagrams are based on the fact that different nebulae show different line ratios varying as a function of their internal physical processes, like photoionisation or shock excitation, and evolutionary stage. For example, SNR generally present low  $H\alpha$ /[NII] and  $H\alpha$ /[SII] line ratios compared to HII regions, as they are shock-excited instead of photoionised like the latter ones. Sabbadin et al. (1977) intending to classify the nebula Sharpless 176, presented a plot of the ratio  $H\alpha$ /[NII] versus the ratio 6717/6731 of [SII], which is a density indicator. For a better constraint they also plotted the  $H\alpha$ /[NII] ratio versus the  $H\alpha$ /[SII] ratio and also the  $H\alpha$ /[SII] versus the 6717/6731 ratios observed in SNR, HII regions and PN (see Fig. 2.4). The variation of these intensity ratios is a function of the evolutionary stage of the object. Recently Riesgo & López (2006) presented diagnostic diagrams of electron density-excitation for a sample of 613 PNe. These diagrams provide a good representation of the range of physical conditions, indicated by the emission line ratios of  $\log([H\alpha]/[SII])$  versus  $\log([H\alpha]/[NII])$ ,  $\log([H\alpha]/[SII])$  versus [SII]  $\lambda 6717/6731$ , and  $\log([H\alpha]/[NII])$  versus [SII]  $\lambda 6717/6731$  (see Fig. 2.5). For both diagrams the data on HII regions are taken from Kaler (1976) and the data on SNR are from Daltabuit et al. (1976); Sabbadin & D’Odorico (1976); Dopita (1976).

These methods were adapted as an extra criterium in this thesis to classify the objects observed. Table 2.6 lists the line intensity ratios of all the objects observed (100 in total). Column one has the coordinates of each object, column two and three show the line intensity ratios of the  $H\alpha$  versus [NII] and [SII] respectively, column four has the ratio between the [SII] doublet  $\lambda 6717/6731$  and column five has the classification status (true PN, possible PN, HII, SNR, Strömgren sphere, and unclear). Using these tables the diagnostic diagrams were produced for these objects. Figure 2.8 presents these diagnostic diagrams for all the objects analysed; the oval shows the PNe bound-

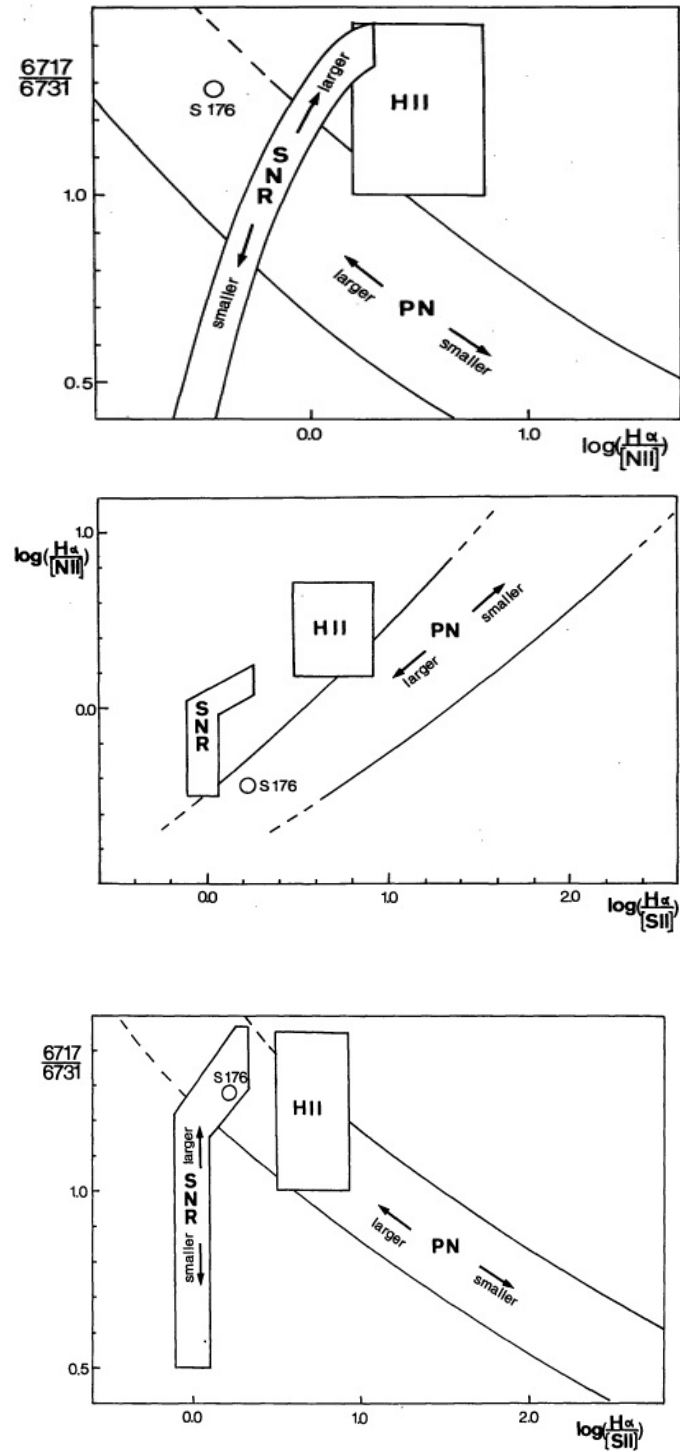


Figure 2.4: Diagnostic diagrams from Sabbadin et al. (1977).

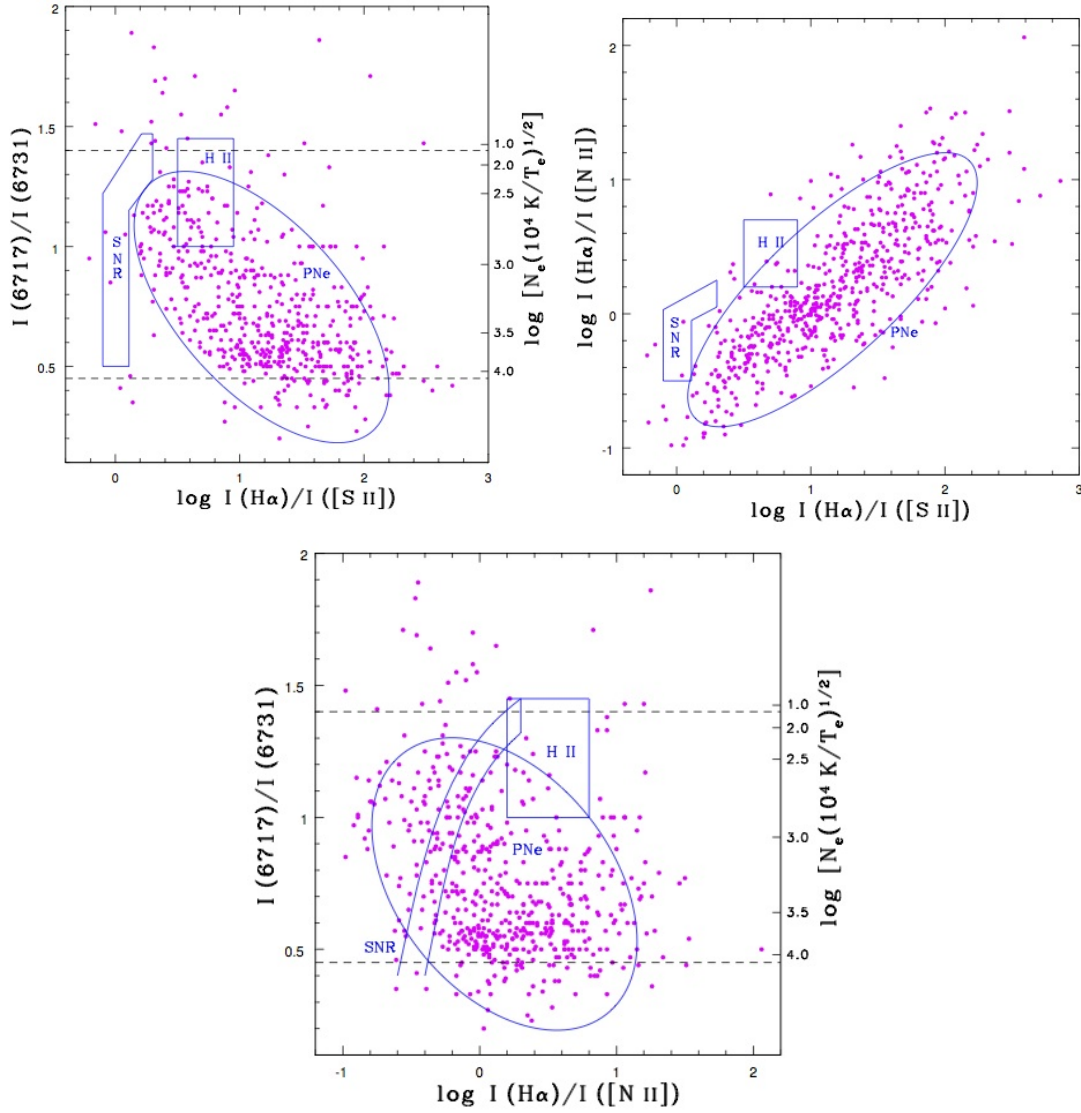


Figure 2.5: Diagnostic diagrams from Riesgo & López (2006).

aries, the box represents the HII regions location and the L-shaped box is where the SNR should fall in these diagrams. It is clear in the Figure that a lot of PNe seem to be clustered towards the SNR boxes, this could be due to the fact that some of the objects are high excitation PNe, show higher metallicity or their progenitor mass is higher.

The classification was made using the diagnostic diagrams, by analysing each spectra and combining it with the  $H\alpha$  image. Figures 2.9 to 2.14 show examples of a true

PN, a possible PN, an HII region, an Strömgren sphere, a supernova remnant and an unclear object. In the images we can see the morphology of PNe is mainly compact and bright, sometimes resolved as a ring. In the case of HII regions they are mostly diffuse objects. For the Strömgren spheres they look like PNe, but they do not exhibit [OIII] emission. The supernova remnants are diffuse but they have very intense high excitation lines, due to shocks. As for the unclear objects, some of them do not show any lines, which could be due to various reasons, probably the target was out of the slit, or the object is not bright enough to show emission lines. There are a few objects that show the  $H\alpha$  line only, they could be  $H\alpha$  emitting stars, but were not subject to further investigation.

## 2.4 Confirmed new PNe

The 100 objects observed are listed in Table 2.6. In Table 2.7 the summary of the objects classification is shown. True and possible PNe represent 45% of the complete sample of objects observed, followed by unclear objects that represent the 35% of the sample. Most of the unclear objects were observed in very crowded areas, making difficult to make sure that the object was in the slit of the spectrograph, also in some of the nights the seeing was higher than 3, making it difficult for the instrument to detect the signal from the object.

Appendix A presents all the images and their corresponding spectrum observed for the 100 objects. They are classified as shown in Table 2.7. True PNe are presented first, then possible PNe, HII regions, Strömgren spheres, SNRs and unclear objects at the end. They all conserved their PNe candidate name, therefore they are labeled PN and then their coordinates.

In Figures 2.15 and 2.16 a comparison of Galactic PNe and the new PNe is presented. The top panel shows the distribution of Galactic PNe over all longitudes and only  $|b| < 5^\circ$ . The bottom panel represents PNe in the area covered by the IPHAS survey in longitude and latitude analysed in this chapter ( $16 < l < 23$ hrs and  $|b| < 5^\circ$ ). One of the main goals of the IPHAS survey was to find the obscured population of PNe

Table 2.6: Line intensity ratios for all the objects observed as part of the follow-up IPHAS project. Main lines to identify the true identity of a PN. Column one has the  $\alpha$ ,  $\delta$  (J2000) of each object, column two and three show the line intensity ratios of the H $\alpha$  versus [NII] and [SII] respectively, column four has the ratio between the [SII] doublet and column five has the classification status (true PN, possible PN, HII, SNR, Strömgren sphere, and unclear).

PN	$\log(\text{H}\alpha/[\text{NII}])$	$\log(\text{H}\alpha/[\text{SII}])$	[6717/6731]	Classification
00:00:21.402 +57:22:07.15	0.53	0.71	2.19	Possible PN
00:00:43.240 +67:10:12.50	0.28	0.76	0.98	HII
00:05:35.348 +66:03:16.57	0.36	0.66	1.59	HII
00:13:33.330 +67:18:03.30	-0.39	0.98	2.08	True PN
00:15:19.529 +61:14:59.03	0.58	0.77	1.22	Strömgren Sphere
00:44:56.000 -73:10:11.00	0.01	0.07	1.21	HII
00:51:23.246 +63:10:59.07	0.34	0.33	1.72	Possible PN
01:00:35.331 +60:51:19.53	0.68	0.8	1.52	HII
01:01:33.966 +60:54:25.12	0.86	0.87	2.2	HII
01:02:35.765 +60:54:18.92	0.7	1.5	1.01	HII
01:08:24.867 +60:32:41.69	1.08	0.76	2.26	HII
01:31:09.090 +61:22:58.69	1.39	1.19	0.51	True PN
01:48:27.130 +62:54:41.80	0.53	0.89	1.02	HII
02:53:40.670 +60:30:15.69	0.29	0.76	0.96	HII
02:59:09.000 +60:19:02.00	0.46	1.07	1.06	HII
14:40:30.000 -52:34:51.00	0.1	1.45	1.34	True PN
16:19:16.000 -52:34:51.00	1.38	0.89	1.04	HII
16:23:17.000 -31:44:57.00	0.07	0.29	0.74	True PN
16:46:45.000 -38:37:00.00	-0.07	-0.01	1.07	Possible PN
18:20:44.000 -12:47:52.00	-0.28	-0.66	3.01	Possible PN
18:26:03.000 -10:11:39.00	-0.34	0.96	0.62	Possible PN
18:26:23.000 -10:29:47.00	0.02	-0.19	1.22	Unclear
18:28:01.000 -10:14:09.00	0.02	-0.04	2.99	Unclear
18:28:29.000 -09:06:12.00	-0.65	-0.64	2.15	Unclear
18:32:09.000 -09:39:06.00	-0.61	-0.96	0.66	Unclear
18:34:38.710 +00:08:03.70	1	1.64	1.3	True PN
18:42:11.390 +00:50:31.70	1.52	3.82	0.02	True PN
18:45:05.230 +00:11:58.60	1.26	1.17	2.88	Possible PN
18:51:41.000 -30:03:37.00	-0.1	0.02	1.01	Unclear
18:52:10.000 -30:40:23.00	-0.02	0.01	1.04	Unclear
18:52:39.000 -30:09:16.00	-0.21	-0.09	0.79	Unclear
18:52:50.000 -29:56:32.00	-0.11	-0.14	1.45	Unclear
18:52:54.000 -30:00:20.00	-0.09	0.47	0.52	Unclear
18:53:14.000 -30:09:14.00	-0.07	0.08	1	Unclear
18:53:16.000 +00:00:30.00	-0.01	0.01	1.31	Unclear
18:53:18.000 -30:13:43.00	0	0	1.33	Unclear
18:53:21.760 +05:56:41.90	1.21	2.04	4.18	True PN
18:53:29.000 -29:38:23.00	0.07	-0.04	0.8	Unclear
18:54:07.000 -30:39:20.00	0.03	0.08	1.14	Unclear
18:54:11.000 -30:23:19.00	-0.04	0.07	0.89	Unclear

Table 2.6: (cont.) Line intensity ratios for all the objects observed as part of the follow-up IPHAS project. Main lines to identify the true identity of a PN. Column one has the  $\alpha$ ,  $\delta$  (J2000) of each object, column two and three show the line intensity ratios of the H $\alpha$  versus [NII] and [SIII] respectively, column four has the ratio between the [SII] doublet and column five has the classification status (true PN, possible PN, HII, SNR, Strömgren sphere, and unclear).

PN	$\log(\text{H}\alpha/[\text{NII}])$	$\log(\text{H}\alpha/[\text{SII}])$	[6717/6731]	Classification
18:54:24.000 -30:25:10.00	-0.15	-0.08	1.14	Unclear
18:54:29.000 -30:37:41.00	0	0.03	0.97	Unclear
18:54:30.000 -30:11:22.00	0.01	0.13	0.64	Unclear
18:54:39.000 -29:54:18.00	-0.09	0.06	0.59	Unclear
18:54:41.000 -30:20:36.00	-0.02	0.06	1.15	Unclear
18:54:56.000 -30:14:08.00	-0.06	-0.11	1.18	Unclear
18:55:07.000 -30:40:03.00	-0.05	0.01	0.86	Unclear
18:55:16.000 -30:36:18.00	-0.01	0.04	1.25	Unclear
18:55:39.000 -29:55:57.00	0.05	0.2	0.72	Unclear
18:55:40.000 -30:16:32.00	-0.3	0.14	0.7	Unclear
18:55:44.000 -30:12:26.00	0.35	0.24	0.74	Unclear
18:57:37.000 +02:03:40.00	0.13	0.09	0.91	Possible PN
18:57:52.000 -30:32:00.00	0.13	0.41	1.16	Unclear
18:57:57.000 -30:10:08.00	-0.15	-0.25	1.34	Unclear
18:58:15.852 +07:37:53.47	0.04	0.95	1.17	True PN
19:01:15.597 +11:41:47.65	0.67	1.04	0.98	True PN
19:02:28.000 +02:07:22.00	-0.02	0.77	0.16	Possible PN
19:03:25.000 +10:44:58.00	-0.02	0.01	0.64	Unclear
19:03:47.000 +05:09:36.00	0	-0.03	0.9	Unclear
19:04:12.000 +10:31:32.00	0.01	0.09	1.21	Unclear
19:04:54.000 +10:18:01.00	0.14	1.85	0.58	True PN
19:05:12.452 +16:13:47.55	0.48	0.69	1.05	True PN
19:05:43.843 +11:00:18.55	4.12	2.13	0.79	True PN
19:07:07.000 +04:23:16.00	0.49	-0.23	0.65	HII
19:10:01.000 +14:22:03.90	-0.16	0.77	1.05	True PN
19:10:22.104 +11:05:38.49	1.54	1.6	0.81	True PN
19:10:27.000 +03:40:46.00	0.10	0.74	1.35	True PN
19:11:17.000 +10:37:34.00	-0.15	-1.77	1.86	Possible PN
19:12:55.483 +14:32:48.10	-0.08	1.26	0.83	True PN
19:17:16.408 +03:34:47.34	0.19	0.24	0.95	Possible PN
19:21:52.039 +13:52:23.19	-0.17	1.48	1.59	True PN
19:21:53.942 +14:30:56.21	-0.2	0.82	0.44	True PN
19:28:37.759 +24:50:24.82	0.15	1.15	1.86	True PN
19:35:32.100 +11:21:15.70	1.94	2.33	0.83	True PN
19:42:26.150 +21:45:21.73	-0.29	1.07	0.86	True PN
19:44:00.000 +17:09:01.00	0.66	1.31	0.96	True PN
19:45:10.651 +27:09:29.52	-0.35	1.27	1.38	True PN
19:48:14.980 +28:07:29.60	0.43	0.66	1.14	Possible PN
19:48:46.000 +18:15:18.00	0.1	0.09	0.98	Unclear
19:48:52.000 +22:25:16.00	-0.27	0.54	1.10	True PN

## 2: IPHAS SURVEY

Table 2.6: (cont.) Line intensity ratios for all the objects observed as part of the follow-up IPHAS project. Main lines to identify the true identity of a PN. Column one has the  $\alpha$ ,  $\delta$  (J2000) of each object, column two and three show the line intensity ratios of the H $\alpha$  versus [NII] and [SII] respectively, column four has the ratio between the [SII] doublet and column five has the classification status (true PN, possible PN, HII, SNR, Strömgren sphere, and unclear).

PN	$\log(\text{H}\alpha/[\text{NII}])$	$\log(\text{H}\alpha/[\text{SII}])$	[6717/6731]	Classification
19:48:53.738 +18:10:21.10	0.46	0.74	1.18	HII
19:51:26.570 +26:58:39.30	-0.14	0.65	1.05	True PN
19:52:09.130 +27:18:30.90	0.22	1.77	0.54	True PN
19:54:36.449 +31:33:26.39	-0.17	1.66	0.97	True PN
19:59:19.070 +31:25:34.30	0.27	0.73	0.8	Possible PN
20:00:18.726 +36:59:34.58	0.48	1.27	1.64	True PN
20:05:22.130 +36:59:43.60	-0.21	0.68	1.1	True PN
20:09:32.890 +37:31:18.30	1.59	2.15	1.35	True PN
20:13:38.600 +33:15:12.50	0.07	1	0.91	HII
22:41:37.610 +58:42:27.80	1.31	1.32	1.44	HII
23:01:35.021 +58:40:07.39	0.14	0.35	1	SNR
23:11:35.600 +61:38:29.60	0.35	0.43	0.67	SNR
23:17:35.930 +63:45:06.40	1.19	1.35	1.04	Unclear
23:18:36.340 +64:04:06.40	0.9	1.26	1.17	Unclear
23:27:12.660 +65:09:18.70	-0.06	0.52	1.41	True PN
23:29:07.040 +59:34:30.40	1.21	1.16	1.13	Unclear
23:40:09.851 +61:16:01.74	0.55	0.7	1.48	Possible PN
23:44:03.000 +60:32:42.00	0.27	0.92	1.57	True PN
23:53:04.778 +62:46:32.35	-0.08	-0.04	1.02	Strömgren sphere
23:56:09.068 +66:52:05.47	0.36	0.64	1.66	HII

Table 2.7: Summary of the classification of the 100 objects observed.

Classification	Number of objects
True PN	32
Possible PN	13
HII Region	16
Strömgren sphere	2
SNR	2
Unclear	35

in the inner parts of the centre of the Galaxy. The two plots presented here show that the IPHAS survey has significantly increased the number of PNe in the inner plane of the Milky Way.

Table 2.8 lists the morphology observed in all the new and possible PNe found. Table 2.9 shows a summary of the morphologies encountered. Round PNe is the most observed shape. One of the IPHAS survey intentions was to find old and extended PNe. On the contrary to what has been observed in other surveys, as it is shown in Table



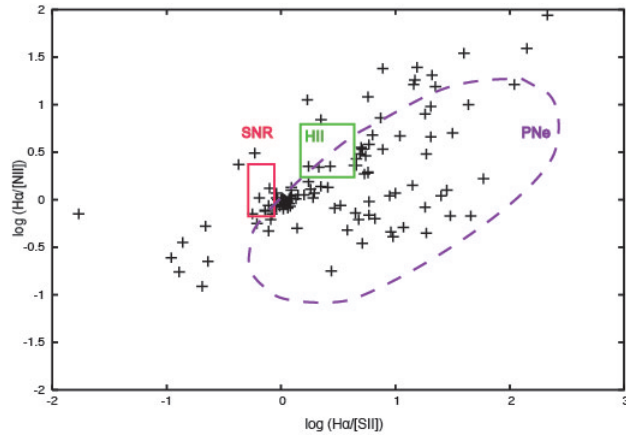


Figure 2.6: Line intensity ratio of  $H\alpha/[SII]$  versus  $H\alpha/[NII]$

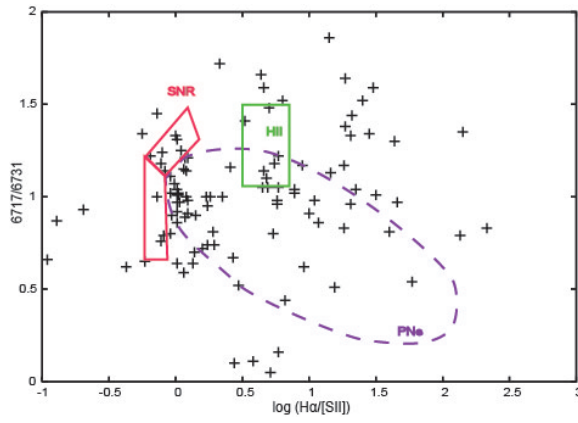


Figure 2.7:  $H\alpha/[SII]$  versus the  $[SII]$  doublet  $\lambda 6717/6731$

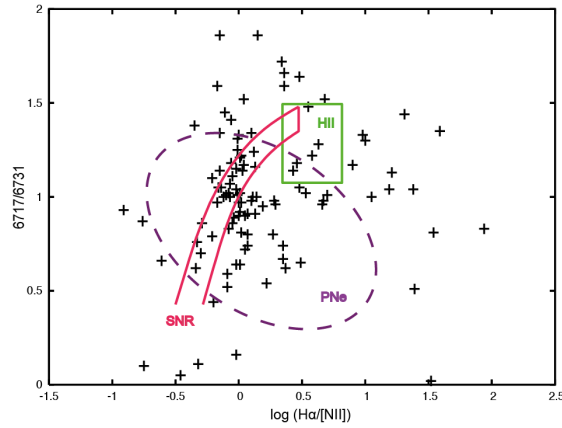


Figure 2.8:  $H\alpha/[NII]$  versus the  $[SII]$  doublet  $\lambda 6717/6731$

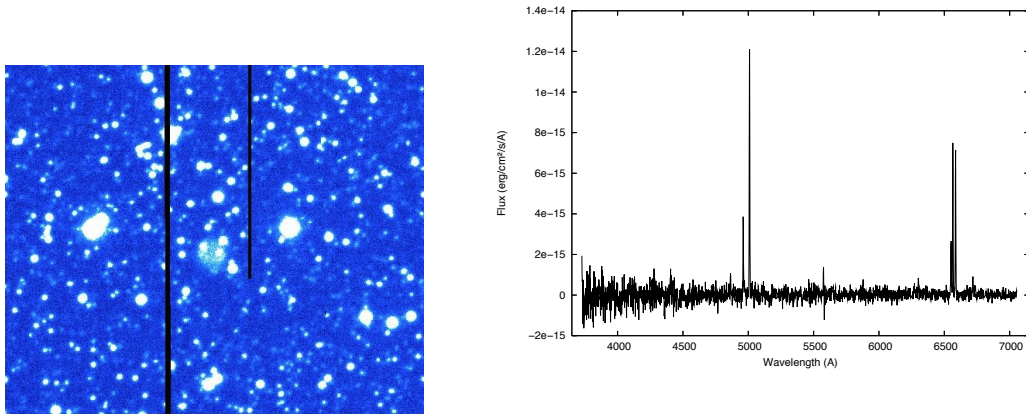


Figure 2.9: True planetary nebula (PN 19:10:27 +03:40:4)

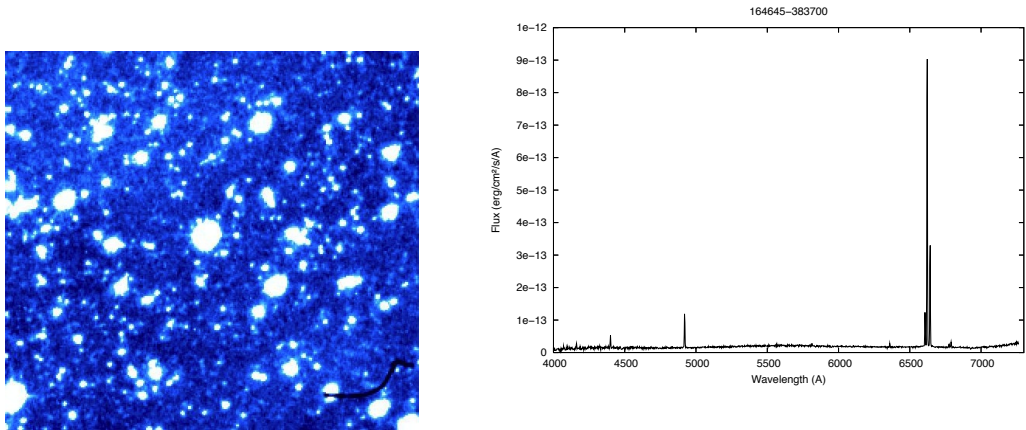


Figure 2.10: Possible planetary nebula (PN 16:46:45 -38:37:00)

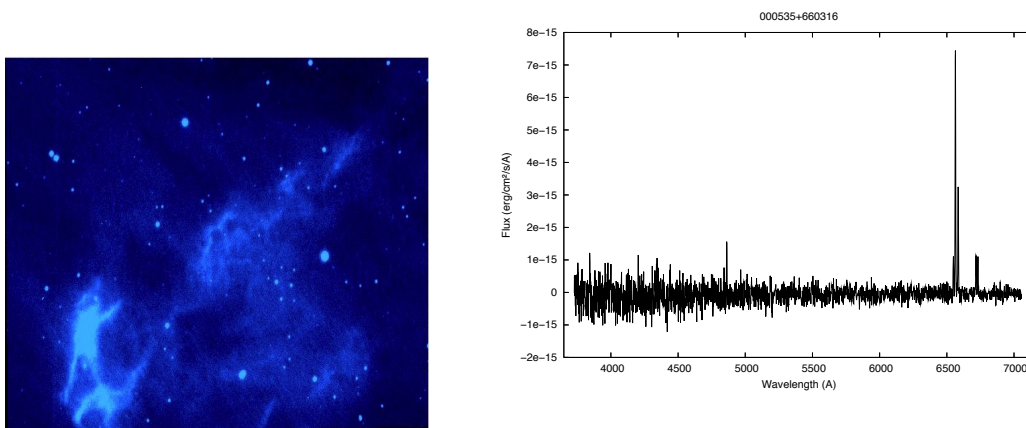


Figure 2.11: HII region (00:05:35 +66:03:16)

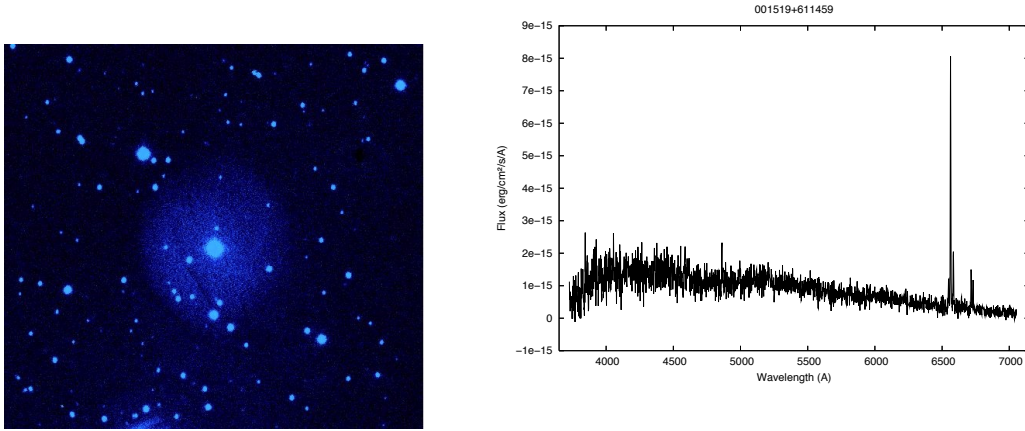


Figure 2.12: Strömgren sphere (00:15:19 +61:14:59)

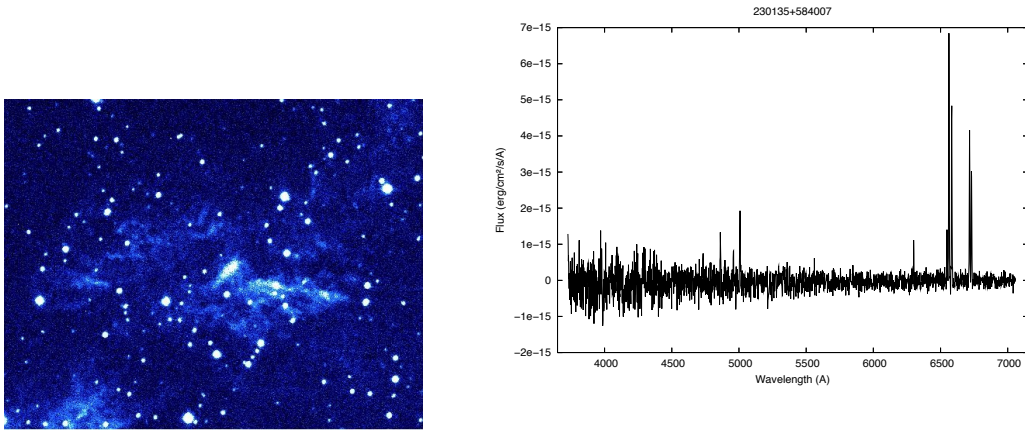


Figure 2.13: Supernova remnant (23:01:35 +58:40:07)

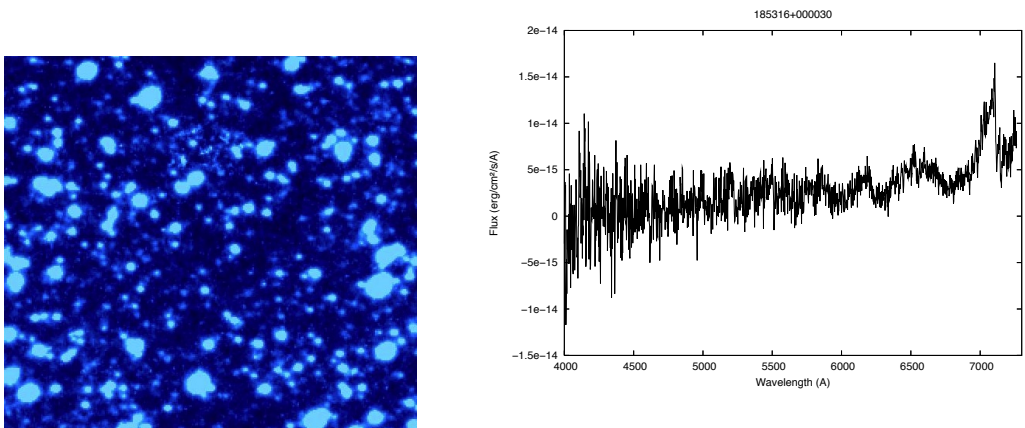


Figure 2.14: Unclear object (18:53:16 +00:00:30)

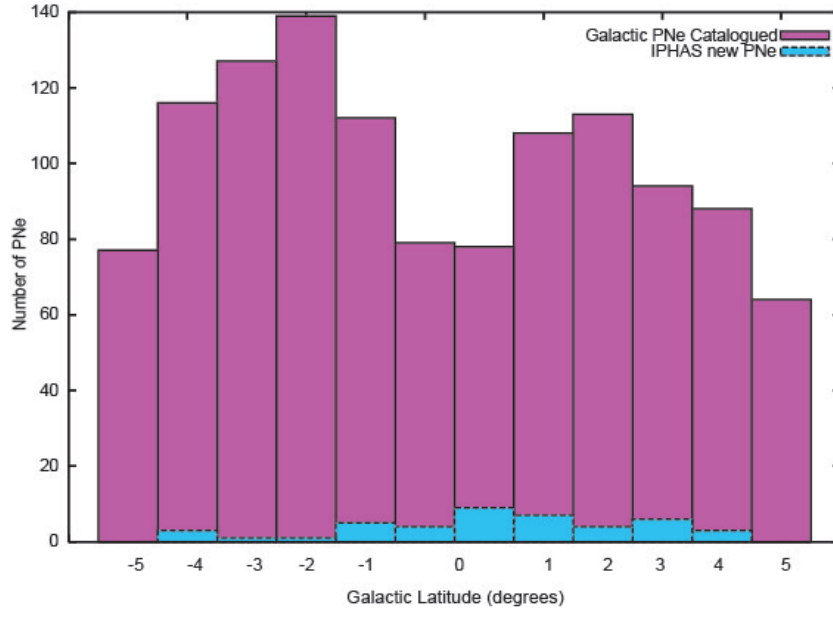


Figure 2.15: Galactic distribution of PNe from the Acker catalogue (pink) compared to the new and possible PNe from the IPHAS survey (blue).

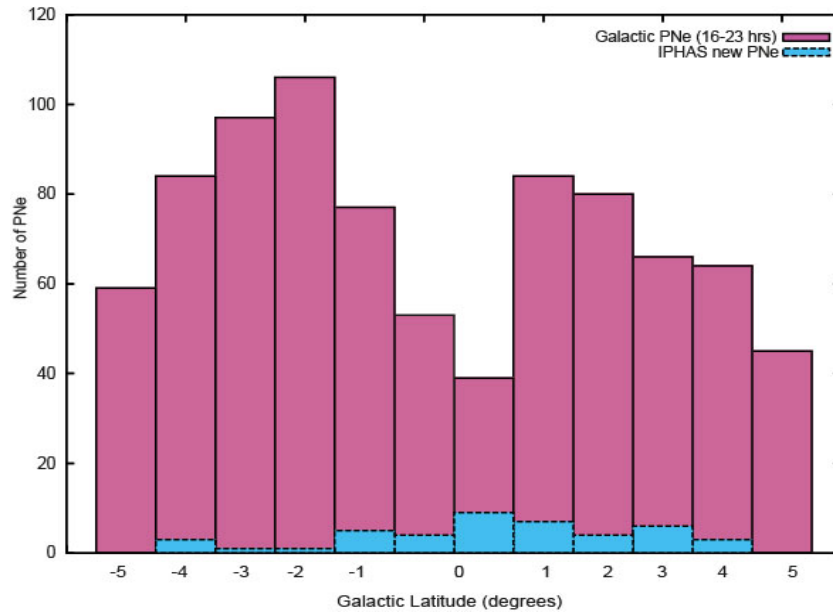


Figure 2.16: Galactic distribution of PNe from the Acker catalogue only in the range of  $16 < l < 23$ hrs and  $|b| < 5^\circ$  (pink) compared to the new and possible PNe from the IPHAS survey (blue).

2.8, 62% of the new confirmed PNe are round. As it is shown in Table 1.1 (Chapter 1) the dominant shape in PNe is elliptical, then round and then bipolar. The reason why this study shows that the dominate shape is round, comes from the fact that we are observing more evolved and fainter PNe.

Soker (2006) predicted that very deep observations will detect more faint PNe, most of which will be round. He calculated that there is indeed a hidden PN population, defined as PNe that originate from AGB stars and are now ionised by the same central stars but that are much too faint to be detected. They are formed from stars that did not go through a final intensive mass-loss rate episode at the end of their AGB phase, most likely because they did not interact with a stellar companion, a brown dwarf, or a massive planet. Reexamining the PN formation rate, their results indicate the formation rate of PNe to be roughly equal to the WD formation rate (Liebert et al. 2005). If this result holds, then they conclude that the hidden PN population comprises  $\sim 60\%$ – $70\%$  of all PNs. These are mostly, but not solely, round PNs.

We confirm the hidden population of PNe found by us to be mostly round.

For the new and possible PNe their morphology, [OIII] intensity and position in the sky was investigated. The [OIII] line in PNe is one of the main lines for its identification. In Table 2.8 the [OIII] line is present in 35 of them (out of 45) where the line intensity ranges from  $2 \times 10^{-16}$  to  $7 \times 10^{-12}$  erg/cm<sup>2</sup>/s/Å. We compare these line intensities with HII regions. For the HII regions the [OIII] line is present only in 3 objects (out of 16) with an intensities range from  $6.8 \times 10^{-15}$  to  $1 \times 10^{-14}$  erg/cm<sup>2</sup>/s/Å. For most of our targets PNe show brighter [OIII] than HII regions.

We used the Galactic distribution of PNe in the range of  $16 < l < 23$ hrs and  $|b| < 5^\circ$  to estimate the missing population of PNe. Using a Gaussian fit to the population. Figure 2.17 shows the Gaussian fit obtained. Using this fit we estimated that the number of missing PNe in this region is 201 PNe, of which we found 43 new PNe. This correspond to a total of 21.3% of the missing population of PNe. In Table 2.10 we present the estimated number of PNe calculated using the Gaussian fit, the number of PNe found and the percentage that they represent. The main contributions of new

## 2: IPHAS SURVEY

Table 2.8: Characteristics of new and possible PNe found in the IPHAS survey. Column one presents the R.A. and DEC coordinates, column 2 describes their morphology and in column 3 the [OIII] line intensity is presented.

PN	Classification	Size (arcsec)	[OIII] Flux (erg/cm <sup>2</sup> /s/Å)
00:00:21.402 +57:22:07.15	Bipolar	16.3	2.7e-15
00:13:33.330 +67:18:03.30	Bipolar	16.4	3e-15
00:51:23.246 +63:10:59.07	Irregular	26	2e-16
01:31:09.090 +61:22:58.69	Round	26.2	2.15e-15
14:40:30.000 -52:34:51.00	Elliptical	32.7	7e-12
16:23:17.000 -31:44:57.00	Bipolar	147.2	1e-14
16:46:45.000 -38:37:00.00	Round	16.3	–
18:20:44.000 -12:47:52.00	Round	13	–
18:26:03.000 -10:11:39.00	Round	13	–
18:34:38.710 +00:08:03.70	Round	13	7.8e-14
18:42:11.390 +00:50:31.70	Round	13	5e-15
18:45:05.230 +00:11:58.60	Round	9.8	–
18:53:21.760 +05:56:41.90	Round	6.5	3e-15
18:57:37.000 +02:03:40.00	Elliptical	16.3	–
18:58:15.852 +07:37:53.47	Round	9.8	1e-15
19:01:15.597 +11:41:47.65	Round	32.7	6.5e-15
19:02:28.000 +02:07:22.00	Bipolar	32.7	3e-15
19:04:54.000 +10:18:01.00	Bipolar	19.6	2.8e-13
19:05:12.452 +16:13:47.55	Round	59	3.3e-15
19:05:43.843 +11:00:18.55	Round	9.8	1.5e-15
19:10:01.000 +14:22:03.90	Round	13	3.6e-14
19:10:22.104 +11:05:38.49	Round	13	1.2e-14
19:10:27.000 +03:40:46.00	Bipolar	13	1.2e-14
19:11:17.000 +10:37:34.00	Round	5	–
19:12:55.483 +14:32:48.10	Round	9.8	3.2e-15
19:17:16.408 +03:34:47.34	Round	16.3	–
19:21:52.039 +13:52:23.19	Elliptical	16.3	1.9e-15
19:21:53.942 +14:30:56.21	Elliptical	16.3	–
19:28:37.759 +24:50:24.82	Bipolar	13	9.7e-15
19:35:32.100 +11:21:15.70	Round	9.8	2.7e-14
19:42:26.150 +21:45:21.73	Bipolar	19.6	3e-15
19:44:00.000 +17:09:01.00	Elliptical	19.6	2.4e-13
19:45:10.651 +27:09:29.52	Elliptical	9.8	1.8e-15
19:48:14.980 +28:07:29.60	Round	6.5	–
19:48:52.000 +22:25:16.00	Round	23	3e-13
19:51:26.570 +26:58:39.30	Round	6.5	2.5e-15
19:52:09.130 +27:18:30.90	Round	9.8	2.5e-15
19:54:36.449 +31:33:26.39	Round	13	3e-14
19:59:19.070 +31:25:34.30	Irregular	6.5	–
20:00:18.726 +36:59:34.58	Round	30	1.9e-13
20:05:22.130 +36:59:43.60	Bipolar	13	2.5e-15
20:09:32.890 +37:31:18.30	Round	9.8	1.5e-14
23:27:12.660 +65:09:18.70	Round	19.6	5e-15
23:40:09.851 +61:16:01.74	Round	16.3	–
23:44:03.000 +60:32:42.00	Round	23	4.5e-15

Table 2.9: Summary of the classification of the new and possible PNe from the IPHAS survey.

Classification	Number of objects
Round	28
Elliptical	6
Bipolar	9
Irregular	2

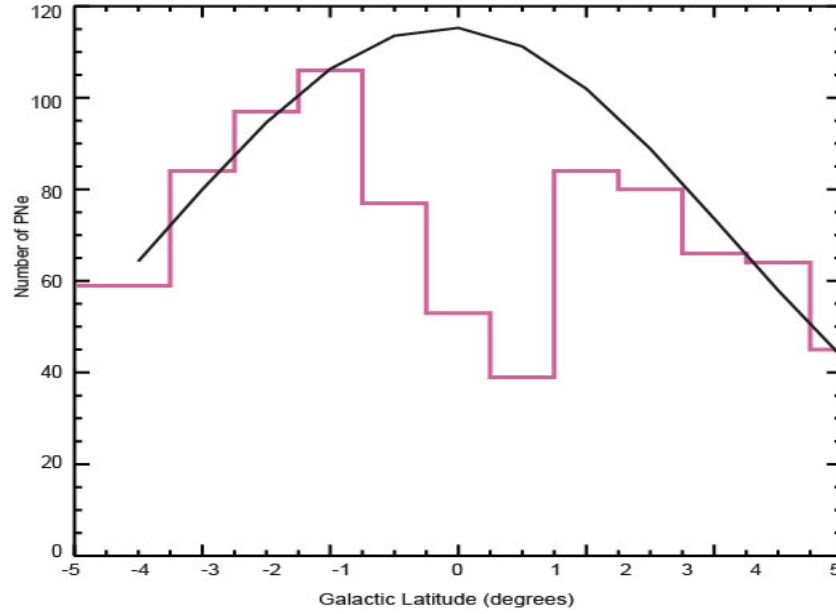


Figure 2.17: Galactic distribution of PNe then form the Acker catalogue only in the range of  $16 < l < 23$ hrs and  $|b| < 5^\circ$  (pink). Gaussian fit for the complete population of PNe (black).

PNe are found to at  $b=4$  and  $b=-4$ , but we also made a big contribution of new PNe in the inner plane ( $b=2$ ). From the fit we obtained that the biggest contribution of missing PNe is concentrated at  $b=0$ , where we only contributed  $\sim 10\%$  of new PNe. A second gaussian fit was made adding the new PNe found in this thesis. Using the new fit, we calculated that the missing PNe are still obscured or too faint to be detected ( $b=0,1$ ) and that the number of PNe missing in the range of  $16 < l < 23$ hrs and  $|b| < 5^\circ$ , is 180.

Only for comparison purposes an exponential fit was also performed, due to the fact that the density of the gas in the inner parts of the Galactic Disk follows an exponential function. But the fit we obtained predicts only 108 Missing PNe, almost half of the

Table 2.10: Estimated number of missing PNe. The last column represent the percentage of new PNe detected in each galactic latitude.

Galactic latitude (b)	Total PNe	Missing PNe	New PNe	%
5	45	-1	0	0
4	64	-5	3	60
3	66	9	6	66
2	80	10	4	40
1	84	19	7	36.8
0	92	135	13	9.62
-1	77	36	5	13.8
-2	106	0	1	0
-3	97	-3	1	33.3
-4	84	-4	3	75
-5	59	5	0	0
Total	854	201	43	21.3

predictions using a gaussian fit.

## 2.5 Conclusions

The main conclusions of this Chapter are presented in the following list:

- The aim of this Chapter was to present newly confirmed PNe. Using the INT Photometric H $\alpha$  Survey (IPHAS) the PNe candidates list was used for an spectroscopic follow-up program. Using the 1.9m telescope at SAAO and the 2.1m telescope at KPNO we were able to observe 100 targets.
- To classify each object, their spectra was carefully analysed, the H $\alpha$  image helped to differentiate between other objects and also diagnostic diagrams were used.
- We confirmed 32 new planetary nebulae and 13 possible planetary nebulae. Out of a 100 targets that makes a 45% success rate.
- Analysing the new and possible PNe, it was found that the IPHAS survey in the region observed for this thesis ( $16 < l < 23$ hrs and  $|b| < 5^\circ$ ) was able to find the obscured population of PNe in the inner parts of the plane of the Galaxy.



- The morphology of these new and possible PNe was studied, it was found that round PNe is the most observed shape. The round PNe represent 62% of all of them.
- The [OIII] line is present in 35 (out of 45) of the PNe, where the line intensity ranges from  $2 \times 10^{-16}$  to  $7 \times 10^{-12}$  erg/cm<sup>2</sup>/s/Å. For most of our targets PNe show brighter [OIII] than HII regions.
- Using a Gaussian fit to the Galactic distribution of PNe in the range of  $16 < l < 23$ hrs and  $|b| < 5^\circ$ , we estimated the missing population of PNe population. We contributed a 21.3% of the missing population of PNe. The main contributions of new PNe are found to at  $b=4$  and  $b=-4$ , but we also made a big contribution of new PNe in the inner plane ( $b=2$ ). A second gaussian fit was made adding the new PNe found in this thesis. The missing PNe are still obscured or too faint to be detected ( $b=0,1$ ) and the number of PNe missing in the range of  $16 < l < 23$ hrs and  $|b| < 5^\circ$ , is 180.

Following the mysteries found in PNe in the next chapter, a chemical analysis of an older population of PNe is presented. These PNe are located in the Galactic Bulge. Their chemical differences compared to the PNe observed in the Galactic Disk make them a very distinct population of PNe.



## Chapter 3

# Mixed Chemistry Planetary Nebulae

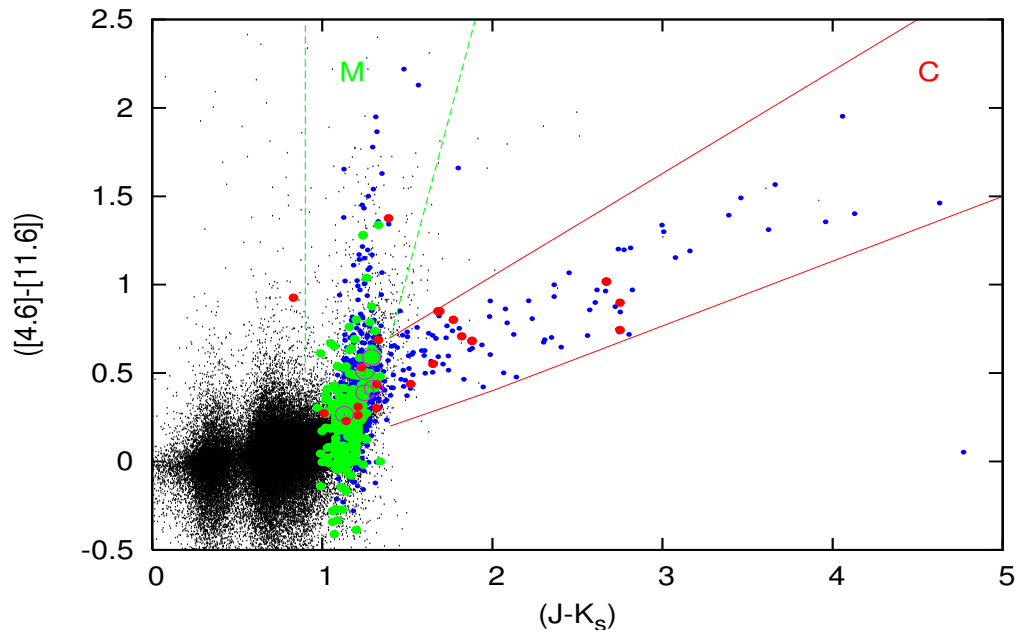


Figure 3.1: 2MASS–WISE colour-colour diagram of the Sgr dSph. Black points show the entire 2MASS–WISE cross-correlated catalogue brighter than  $K_s = 11.22$  mag. Small, blue dots denote the subset of colour-selected AGB Sgr dSph stars; red dots denote observed carbon stars; green dots denote observed M-type stars. The lines mark the approximate locations of the carbon-dust-producing and silicate-dust-producing evolutionary tracks (McDonald et al. 2012).

Observationally there is a clear dichotomy between oxygen- and carbon-rich stars. From the primordial abundances, stars start being oxygen dominated. In the evolutionary sequence stars of low and intermediate mass may evolve from being oxygen-rich to being carbon-rich, a change reflected in the chemical composition of the stellar wind.

The change occurs in the AGB phase, when carbon produced by He-burning is brought to the surface by processes in the stellar interior thereby increasing the C/O ratio until it exceeds unity and a carbon star is formed. This is the so-called third dredge-up (Herwig 2005). The process depends on stellar mass: Vassiliadis & Wood (1993) showed the third dredge up occurs if the core mass of the star  $M_{cs} > 1.5 M_{\odot}$ .

Carbon-rich dust species tend to have significantly higher opacities than oxygen-rich species, meaning that stellar outflows can be driven more effectively. Of particular importance for the historical enrichment of the ISM, in our own and other galaxies, is the variation of the onset and length of this carbon-rich phase with metallicity and initial stellar mass. Only some stars become carbon-rich: low-mass stars do not dredge up sufficient carbon to become carbon-rich, while high-mass stars undergo hot-bottom burning via the CNO cycle, which reduces the carbon abundance in the dredged-up layers, limiting surface carbon enrichment (Lattanzio et al. 1996). A good way to identify C-stars in a galaxy is using colour-colour diagrams. As an example, Figure 3.1 shows a colourcolour diagram incorporating both the 2MASS and WISE (Cutri & IPAC/WISE Science Data Center Team 2012) data. These colours have been chosen so that the heavily-reddened carbon stars, which usually display very red colours at almost all near- and mid-infrared wavelengths, lie off to the right of the diagram, as indicated by the solid red lines. Meanwhile, the oxygen-rich giants have blue (J–Ks) colours due to the lack of dust opacity, but large ([4.6]–[11.6]) colours thanks to the 10 $\mu$ m silicate feature, as indicated by the dashed green lines. This diagram appears to separate the different stellar types reasonably well (McDonald et al. 2012).

In other words theoretically, stars with masses less than  $1.5 M_{\odot}$  will never become C-rich stars. This predicts a clear distinction, with some (lower-mass) stars showing oxygen-rich and some (higher-mass) stars carbon-rich ejecta. In the molecular ejecta, the CO molecule locks away the less abundant element, leaving the remaining free O or

C to drive the chemistry and dust formation. Oxygen-rich shells are characterised by silicate dust, while carbon-rich shells show carbonaceous dust and Polycyclic Aromatic Hydrocarbon (PAH) emission bands.

Unexpectedly Zijlstra et al. (1991) firstly observed the mixed-chemistry phenomena when the [WC11] PN IRAS07027-7934 with strong PAH emission bands at 6.2, 7.7, 8.6, and 11.3  $\mu\text{m}$ , was found to also harbour a 1.6GHz OH maser line. This transition requires long path lengths at moderate temperatures, while PAH emission bands require a strong UV field, telling us that the O-rich material is in the outer regions and the C-rich material needs to be closer to the star.

After this, observations made with *ISO* uncovered several further cases, where PAH emission in PNe occurred together with emission bands of silicates at 23.5, 27.5, 33.8, and 10 $\mu\text{m}$ . Figure 3.2 shows the spectra of the planetary nebulae He 2-113 and BD+30 3639. In the left side the PAHs emission bands at 3.3, 6.2, 7.7, 8.6, and 11.3 $\mu\text{m}$  (marked with red arrows) are present. At longer wavelengths the emission from crystalline silicates at 23.5, 27.5, and 33.8 $\mu\text{m}$  is found (marked with blue arrows) (Waters et al. 1998). CDP -56°8032 was also found to harbour PAHs and emission bands of silicates. All three objects belong to the late [WC] type central stars of PNe.

De Marco & Soker 2002 explored the evolution of [WC] type central stars of PNe, different hypotheses that could explain the simultaneous existence of C- and O-rich particles around C-rich stars are:

- A recent thermal pulse has converted an O-rich outflow to one that is C-rich. The O-rich grains are expected to be further out and cooler than the C-rich particles. Such transition occur only once during the lifetime of a star, thus the probability to observe a sufficiently recent O-rich to C-rich transition by the PNe is expected to be low. IRAS 07027- 7934 is a candidate for a [WC] type central star which can only have formed through a fatal thermal pulse (FTP) scenario. The FTP scenario correspond to a very recent evolution from the AGB, where the nebula is very dense and compact. An accretion scenario could explain the link between dense, compact nebula and the peculiar evolution, in such model, the PAH molecules could in fact form in the accreting gas, where the CO is

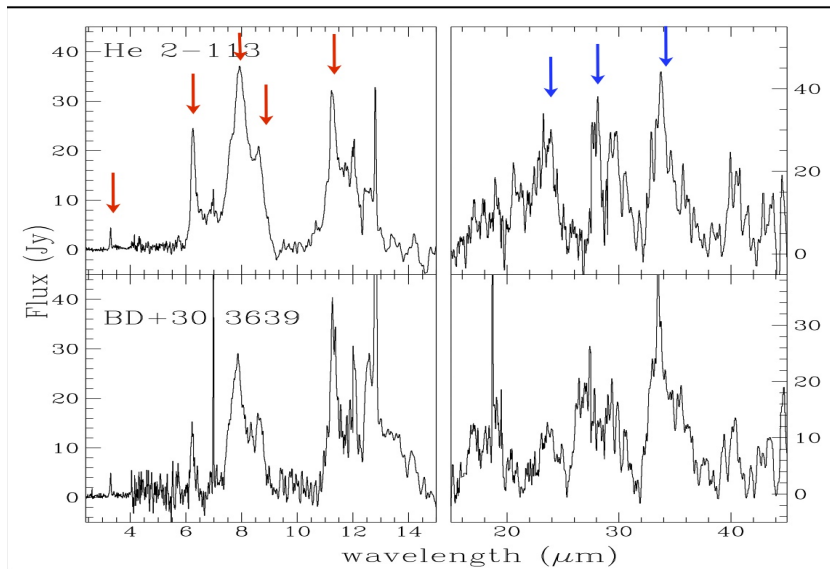


Figure 3.2: Spectra of the planetary nebulae He 2-113 (top) and BD+30 3639 (bottom) showing the PAHs emission bands at 3.3, 6.2, 7.7, 8.6, and 11.3  $\mu\text{m}$  (marked with red arrows). While at longer wavelengths the emission from crystalline silicates is present (marked with blue arrows) (Waters et al. 1998).

dissociated.

- The silicate grains are in orbit around the system and existed well before the current evolutionary phase. Barnbaum et al. (1991) proposed that C stars showing silicate emission are binaries containing a disk in which O-rich grains have accumulated during an earlier evolutionary phase.
- An alternative possibility for the grains, is if they reside in a Kuiper belt or inner Oort comet cloud around the star, the interaction of cometary nuclei in such a belt with mass outflow and ionisation front from the PN might provide the conditions needed to liberate the small particles that are required in order to explain the observed far-infrared (FIR) silicate and ice bands

After analysing all these possibilities they conclude that the apparent correlation between the presence of crystalline silicate grains around PNe and the presence of both PAHs and [WC] type central star seems to implicate a chemistry change between an O- and a C-rich AGB outflow as the cause. It is thought that such objects may be one result of helium shell flashes in low-intermediate-mass stars on the AGB, a helium shell

flash may have ejected or ingested essentially all the remaining H-rich outer envelope, resulting then H poor, like late [WC] type central star PNe (Cohen et al. 1999, 2002).

However, the opposite case has also been observed, when weak PAH emission has been seen in some clearly oxygen-rich objects, such as NGC 6302 and Roberts 22 (Zijlstra et al. 2001). PAH bands have been detected in S-type AGB stars, with C/O ratios close to, but below, unity (Smolders et al. 2010). Cohen & Barlow (2005) have shown that some PAH emission can occur at C/O ratios as low as 0.6.

## 3.1 PNe in the Galactic Bulge

The Galactic Bulge (GB) is the spheroidal component at the centre of the Milky Way, its mass is about 4 times smaller than the disk and 16 times larger than the halo. The bulge seems to have been passively evolving for the last  $\sim 10$  Gyr, hence it is the ideal fossil probe of Galaxy formation (Zoccali & Minniti 2009). Planetary Nebulae in the Galactic Bulge have been studied for a while, simply because they are at a fixed distance, making it easier to derive their abundances, kinematics and age. PNe have been used to trace the Bulge dynamics, due to their brightness.

Gutenkunst et al. (2008) and Perea-Calderón et al. (2009) showed that the mixed-chemistry phenomenon is widespread among the Galactic Bulge Planetary Nebulae (GBPNe). Their *Spitzer* observations show that the simultaneous presence of oxygen- and carbon-rich features is common, and is not restricted to objects with late/cool [WC] type stars.

### 3.1.1 Carbon stars in the Bulge

Based on a near IR colour magnitude diagram, Zoccali et al. (2003a) calculated that the age for the bulk of bulge stars is  $\sim 10$  Gyr, with no trace of an intermediate or young population. Uttenthaler et al. (2012) observed 45 AGB stars in the GB and they are all O-rich. There is also evidence that 4 out of a sample of 27 objects were detected to show technetium (Tc), which is an evidence of third dredge-up (Uttenthaler et al. 2008). But according to Azzopardi et al. (1988) the few AGB carbon stars in the Bulge

do not originate from third dredge-up. The traditional explanation relating the mixed chemistry to a recent evolution towards carbon-star is unlikely for the Bulge objects, as these old, low-mass stars are not expected to show third dredge-up, and therefore should not show enhanced C/O ratios. Different explanations are needed.

## 3.2 Observations

Perea-Calderón et al. (2009) revised the mixed chemistry in 21 Galactic Bulge PNe, out of a total sample of 26, using *Spitzer Space Telescope* spectra. We (Guzman-Ramirez et al. 2011) retrieved and re-reduced these 21 *Spitzer* spectra. Also included is the PN H2-20 from Gutenkunst et al. (2008), and a further 18 PNe in the GB for which spectroscopic data was found in the *Spitzer* archive, yielding a total sample of 40.

### 3.2.1 IR spectra from *Spitzer*

All the spectra were taken with the Infrared Spectrograph (IRS) (Houck et al. 2004). The spectra cover a range between 5.2–37.2 $\mu\text{m}$  by using the Short-Low (SL: 5.2–14.5 $\mu\text{m}$ ;  $64 < R < 128$ ), Short-High (SH: 9.9–19.6 $\mu\text{m}$ ;  $R \sim 600$ ) and Long-High (LH: 18.7–37.2 $\mu\text{m}$ ;  $R \sim 600$ ) modules. The data were retrieved from the *Spitzer* Science Centre Data Archive using Leopard (program # 3633). The *Spitzer* IRS Custom Extractor (SPICE) was used to do the extraction of the spectra for each nod position from the 2D images. All spectra were cleaned for bad data points, spurious jumps and glitches, and then they were combined and merged to create a single 5–37 $\mu\text{m}$  spectrum. Flux offsets between different wavelengths ranges were not corrected but these are minor. Offsets can be caused by the fact that the different wavelength ranges use different slits, and our objects have sizes similar to or larger than the slit widths. The *Spitzer* samples were mostly selected based on known IRAS 12 $\mu\text{m}$  flux. The complete sample of the *Spitzer* spectra is presented in Appendix C.



### 3.2.2 H $\alpha$ images from the *HST*

Twenty-two of the objects were included in an Hubble Space Telescope (*HST*) Snapshot survey of 37 Galactic Bulge PNe (proposal 9356, PI Albert Zijlstra). The WFPC2 images were taken in three different filters, H $\alpha$ , V, and [OIII], with typical exposure times of  $2 \times 100$  sec, 60 sec and  $2 \times 80$  sec, respectively. The objects were placed on the CCD of the Planetary Camera (PC) with a pixel scale of  $0''.0455$ . Pipe-line reduced images were retrieved. Only the H $\alpha$  images are used here.

The target selection for the original *HST* observation was based on a catalogued diameter less than  $5''$ . It included a few objects without a known size. Other than this, the target selection was random among the known PNe in the direction of the Bulge. The fact that so many of the *Spitzer* sample were included in the *HST* observations indicate that the *Spitzer* target selection indirectly also made use of the diameter. The overlap in selection reflects the brighter infrared emission from compact nebulae.

### 3.2.3 UV spectra from the *VLT*

Echelle spectra were obtained for the 22 objects using the ultraviolet and visual echelle spectrograph (UVES) of the *VLT*. An exposure time of 600 sec was used. The spectra cover the wavelength range from 3300 to 6600 Å, with a resolution of 80,000. These spectra were used to investigate the nature of the central stars, based on the presence of stellar emission lines.

## 3.3 The mixed-chemistry problem in GBPNe

Explanation relating the mixed chemistry to a recent evolution towards carbon-star is unlikely for the Bulge objects, as mentioned before, they are not expected to show third dredge-up, and therefore should not show enhanced C/O ratios. To solve the mixed-chemistry phenomena in GBPNe, two main hypotheses were considered; (1) an external cause, where the PAHs come from the ISM, and (2) internal causes, implying the formation of the PAHs inside the nebula.

### 3.3.1 PAHs acquired from the ISM

PAHs could be present in an oxygen-rich environment if they are acquired from the ISM. This can be done by gathering interstellar PAHs through the “wall” where the expanding nebula collides with the ISM, creating a stationary shock (Wareing et al. 2007), in which the interaction region is dominated by ISM material. As the Bulge PNe have a high velocity dispersion with respect to the ISM, the “wall” is expected to be close to the nebula, and one-sided.

To test this hypothesis, the spatial location of the PAH emission bands was compared, at 6.2 and 11.3 $\mu\text{m}$ , to that of the 12.8 $\mu\text{m}$  [Ne II] emission line. The 12.8 $\mu\text{m}$  [Ne II] emission line comes from the ionised region, so the position of the line traces the position of the PN and is not affected by extinction. On the other hand, if the PAHs have been swept up from the ISM, then their physical position would not be at the same position as the PN (or the [Ne II] for this case) so there should be an offset in their positions. This was done for 40 objects in the sample. The peak of the [Ne II] line and the 11.3 $\mu\text{m}$  PAH feature were measured using the SH part of the spectrum. It is important to mention that not all the interaction zones of moving stars will be displaced from the central star, they could be superimposed based on viewing angle, but better resolution is needed to address this fact.

In a few cases evidence for an offset was found. In PN Hb4, the faint 11.3 $\mu\text{m}$  feature is offset by about 6'' from the [Ne II] 12.80 $\mu\text{m}$  emission line. In M2-14, the faint 11.3 $\mu\text{m}$  emission is offset by 4'' from the [Ne II] line. We also found an offset of 2'' between the [Ne II] line and the PAH band at 11.3 $\mu\text{m}$  in the case of H1-16, H1-50, H2-20, M1-40 and Cn1-5. These smaller offsets may not be real, as the resolution at the position of the peak of the line and the feature is about 2''. Hb4 provides the strongest case for a spatial offset. However, as shown in Table 3.1, it has at best weak evidence for mixed chemistry.

Thus, there are only a few potential cases where interaction with the ISM, or other forms of ISM confusion, may contribute to the PAH features. In the large majority of cases, the dust and PAH features are co-located and centred on the nebula. In these cases the mixed chemistry is likely to have an internal origin, related solely to the star

and its ejecta.

### 3.3.2 Star and Nebula

Table 3.1 lists the 40 PNe analysed, it is in order of PAH strength, where the PAH strength is defined as the peak line flux of the  $7.7\mu\text{m}$  PAH band. From H2-18 (006.3+04.4) onward, no  $7.7\mu\text{m}$  emission feature is detected. Both PAH and silicate bands were identified. PAHs bands were seen in all objects, except for 5 objects where only very faint  $11.3\mu\text{m}$  and/or  $7.7\mu\text{m}$  bands and no other features were seen. Silicate emission was seen in 34 PNe. Evidence for mixed chemistry (both PAH and silicate emission) was found in 30 PNe, where those with dubious PAH bands were excluded.

Table 3.1 shows that the mixed chemistry phenomenon is not limited to emission-line objects, objects that show emission lines in their spectra, either [WC] objects or weak emission line objects (wels) (cf. Górny et al. 2010). In our sample of 30 mixed chemistry PNe, 10 have emission-line stars and 20 do not. In the rejected sample of 10 PNe, 4 have emission-line stars and 6 do not. This confirms that in the Bulge, there is no clear relation between mixed chemistry and class of central star. However, among the mixed chemistry objects, there is a strong tendency for the emission line stars to have the strongest  $7.7\mu\text{m}$  band. Thus, although the mixed chemistry is itself independent of the stellar class, it is amplified by emission-line stars.

In Figure 3.3 we show the *Spitzer* spectra, *HST* images, and the UVES spectra for each of the 22 GBPNe.

#### Infrared spectra

The *Spitzer* spectra are shown in the left-most panels of Figure 3.3. The vertical red lines indicate the wavelength of PAH bands: 6.2, 7.7, 8.6 and  $11.3\mu\text{m}$ . Only the short wavelength region (SL and HL) is shown. Offsets between the different spectral segments are visible in three cases.

Th 3-4 (PN G354.5+03.3), H 1-46 (PN G358.5-04.2), and Th 4-1 (PN G 007.5+04.3) show a strong broad band at  $10\mu\text{m}$ , interpreted as silicate emission. In all three cases, the peak is shifted to longer wavelengths, beyond  $10\mu\text{m}$ . In the classification scheme of

### 3: MIXED CHEMISTRY PLANETARY NEBULAE

Table 3.1: Galactic Bulge PNe. Column 3 and 4 list the identified bands in the IRS spectra. Col. 5 lists the peak line flux of the 7.7 $\mu$ m PAH band. Col. 6 indicate whether the star has emission lines [WC] or is of weak emission-line (wels) type. A star in Col. 3 indicates that the PAH bands are very faint and may be in some doubt. Mixed-chemistry objects are those unstarred objects which do not have “none” in col. 4 (30 in total).

PN G Name	Name	PAHs ( $\mu$ m)	Silicates ( $\mu$ m)	7.7 $\mu$ m (mJy)	Star
008.3-01.1	M 1-40	6.2, 7.7, 11.3	27.5, 33.8	400	wels
002.2-09.4	Cn 1-5	6.2, 7.7, 11.3	27.5, 33.8	280	[WC4]
356.8+03.3	Th 3-12	6.2, 7.7, 8.6, 11.3	33.8	180	
006.5-03.1	H 1-61	6.2, 7.7, 11.3	27.5, 33.8	150	wels
006.4+02.0	M 1-31	6.2, 7.7, 11.3	10, 27.5, 33.8	140	wels
357.1-04.7	H 1-43	6.2, 7.7, 8.6, 11.3	10, 27.5, 33.8	130	[WC11]
007.2+01.8	Hb 6	6.2, 7.7, 11.3	27.5, 33.8	120	
358.7+05.2	M 3-40	6.2, 7.7, 8.6, 11.3	27.5, 33.8	111	
356.5-02.3	M 1-27	6.2, 7.7, 11.3	27.5	100	[WC11]
004.9+04.9	M 1-25	6.2, 7.7, 11.3	27.5, 33.8	90	[WC6]
359.3-01.8	M 3-44	6.2, 7.7, 11.3	27.5, 33.8	80	[WC11]
358.9+03.4	H 1-19	6.2, 7.7, 8.6, 11.3	27.5, 33.8	80	
000.1+04.3	H 1-16	6.2, 7.7, 11.3	27.5, 33.8	80	
352.6+03.0	H 1-8	6.2, 7.7, 8.6, 11.3	27.5, 33.8	70	
003.1+03.4	Hen 2-263	6.2, 7.7, 8.6, 11.3	23.5, 27.5, 33.8	60	
354.5+03.3	Th 3-4	6.2, 7.7, 8.6, 11.3	10, 27.5, 33.8	60	
359.9-04.5	M 2-27	6.2, 7.7, 11.3	27.5, 33.8	60	wels
000.0-06.8	Hen 2-367	6.2, 7.7, 11.3	27.5, 33.8	60	
351.9-01.9	K 5-4	6.2, 7.7, 8.6, 11.3	none	50	
356.9+04.4	M 3-38	6.2, 7.7, 11.3	27.5, 33.8	50	
002.8-01.7	H 2-20	6.2, 7.7, 11.3	27.5, 33.8	40	
006.8+04.1	M 3-15	6.2, 7.7, 11.3	27.5, 33.8	20	[WC5]
007.5+04.3	Th 4-1	7.7, faint 11.3	10, 27.5, 33.8	20	
358.5-04.2	H 1-46	7.7, 11.3	10, 27.5, 33.8	18	
004.0-03.0	M 2-29	7.7, 8.6, 11.3	none	10	
355.9+03.6	H 1-9	7.7, 8.6	none	10	
357.2+02.0	H 2-13	faint 7.7, 11.3	33.8	8	
001.2+02.1	Hen 2-262	faint 6.2, 7.7, 8.6, 11.3	33.8	8	
004.1-03.8	KFL 11	faint 7.7, 8.6, 11.3	33.8	5	
003.1+02.9	Hb 4	faint 7.7 and 11.3 (*)	27.5, 33.8	5	[WC4]
002.9-03.9	H 2-39	faint 7.7 (*)	23.5, 27.5, 33.8	1	
006.3+04.4	H 2-18	11.3	33.8	0	
003.6+03.1	M 2-14	faint 11.3 (*)	27.5, 33.8	0	wels
356.5-03.6	H 2-27	faint 11.3 (*)	none	0	[WC11]
358.5+02.9	Al 2-F	faint 11.3 (*)	33.8	0	
008.6-02.6	MaC 1-11	faint 8.6, 11.3	33.8	0	
006.1+08.3	M 1-20	6.2, 8.6, 11.3	none	0	[WC8]
005.9-02.6	MaC 1-10	11.3	33.8	0	
008.2+06.8	Hen 2-260	8.6	none	0	
359.7-02.6	H 1-40	6.2, 11.3	10, 27.5, 33.8	0	

Sloan & Price (1998), they are of type SE4/5. The  $13\mu\text{m}$  feature typically associated with the reddest silicates (SE1-4) in AGB stars, is not present in our objects. Perea-Calderón et al. (2009) show three more objects with silicate emission without PAH features; these also have reddish silicates, and are of type SE5-6, without a  $13\mu\text{m}$  feature. The redshifting of the silicate emission may be attributed to large dust grains.

## Morphology

*HST* images of 22 objects were used to study their morphology. The  $\text{H}\alpha$  *HST* images are shown in the middle panels of Figure 3.3, again in the order listed above (of decreasing PAH strength). The arrows indicate the orientation of the image and the bar indicates the spatial scale. The images are displayed using an “asinh” scale to enhance the contrast and to better see the faintest structures. Note that the images of different objects are not to the same spatial or intensity scale.

A few further images are available in the literature. M1-40 has a diameter of  $20''$  (Schwarz et al. 1992) and is therefore likely a foreground nebula. Cn1-5 has a similar-sized halo (Corradi et al. 2003) and also is probably not in the Bulge. M1-25 was imaged by Aaquist & Kwok (1990b) who find a torus with diameter  $1.7''$ . Hb 6 and Hb 4 are also not expected to be in the Bulge as their radio fluxes are too high (Zijlstra et al. 1989; Aaquist & Kwok 1990b).

## Emission-line stars

The right-most panels of these figures show the UVES spectra located around the strong stellar emission C IV-5800/5811Å. This line is an indicator for [WC] type central stars. The y-axis scale is the same for all panels, except for two objects with strong emission lines. In the case of H1-43 (PN G357.1-04.7) the stellar broad line C III at 5696Å together with the nebular narrow line of [NII] at 5755Å is presented. The UVES spectra confirm the classification of Górny et al. (2004) but do not reveal any further emission-line stars.

The most important aspect of Figure 3.3 is the predominance of a very specific

### 3: MIXED CHEMISTRY PLANETARY NEBULAE

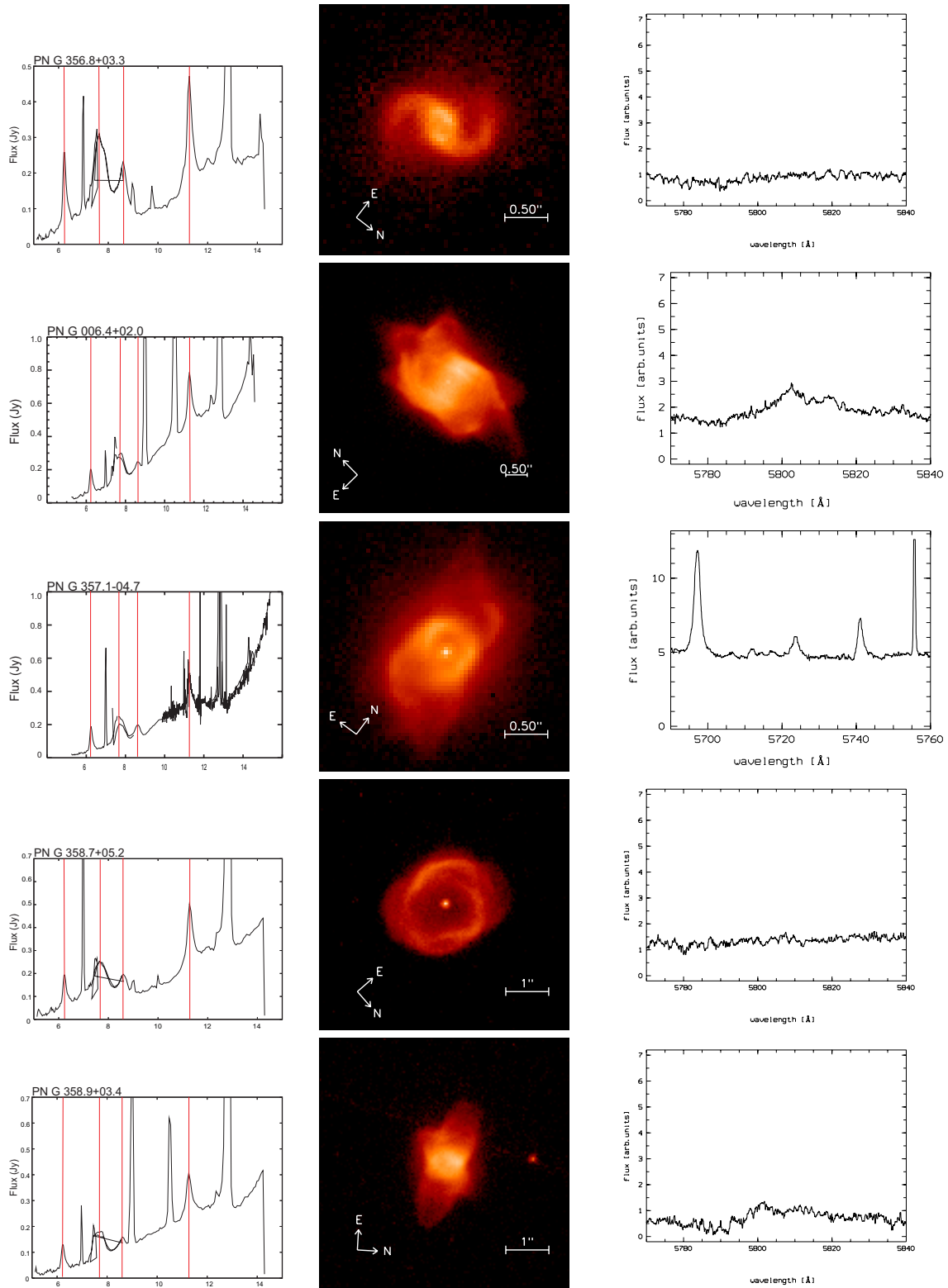


Figure 3.3: Correlation image showing in the first column the IR *Spitzer* spectrum, showing the short wavelength region, the vertical red lines show the PAH bands. In the second column is the corresponding *HST* image and in the third column shows a part of the UVES spectrum.

### 3.3: THE MIXED-CHEMISTRY PROBLEM IN GBPNE

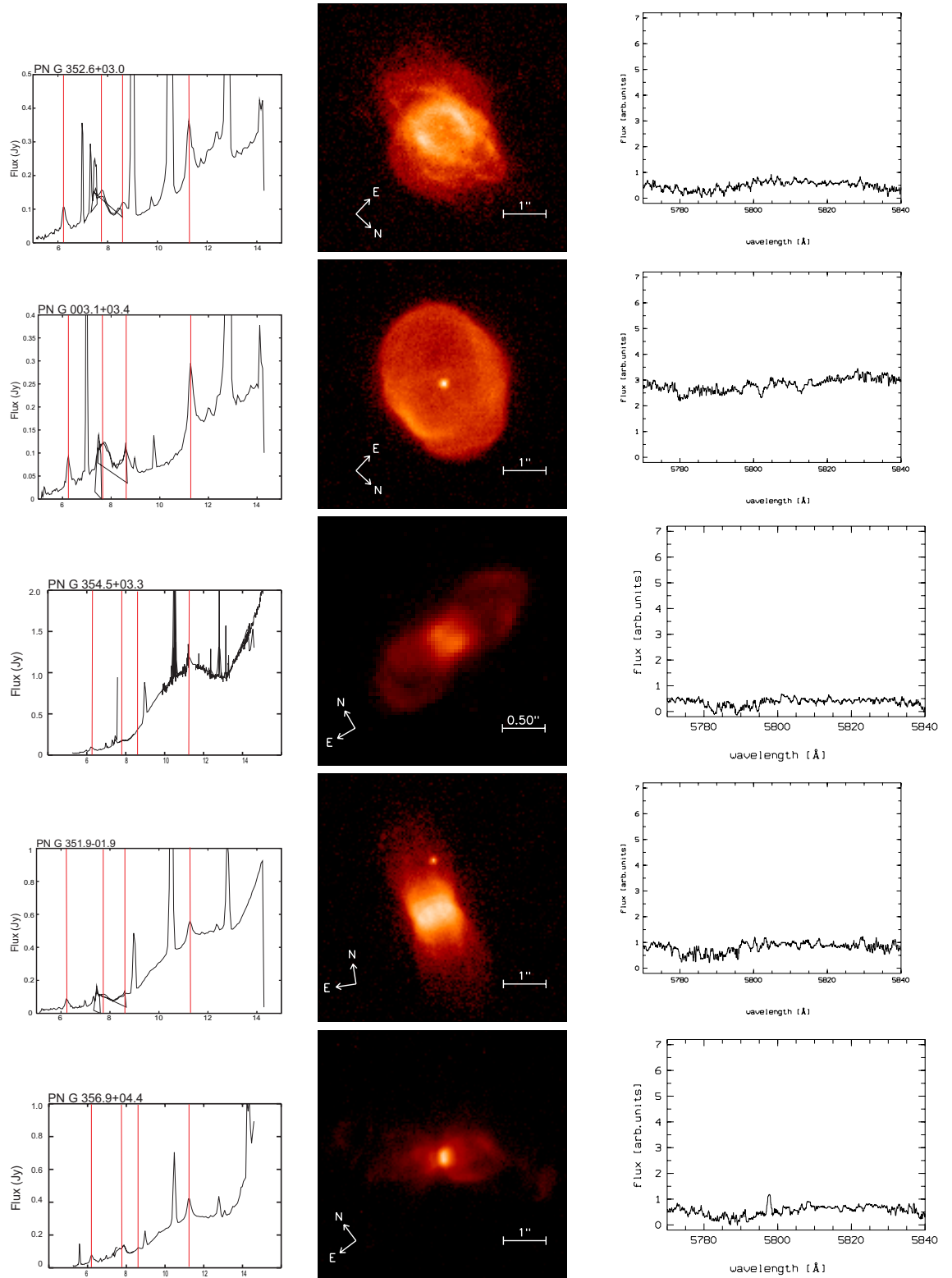


Figure 3.3: (cont.) Correlation image showing in the first column the IR *Spitzer* spectrum, showing the short wavelength region, the vertical red lines show the PAH bands. In the second column is the corresponding *HST* image and in the third column shows a part of the UVES spectrum.

### 3: MIXED CHEMISTRY PLANETARY NEBULAE

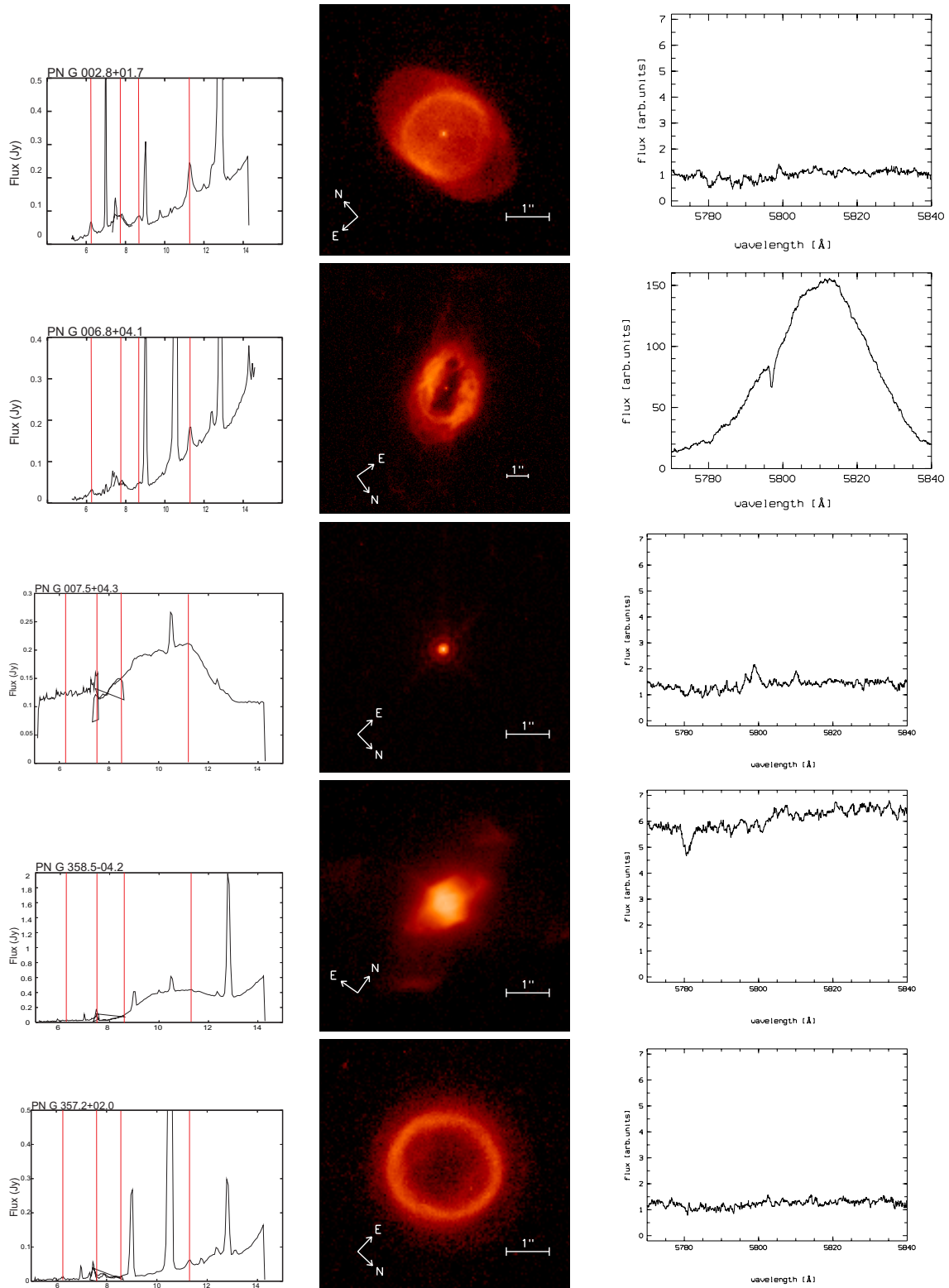


Figure 3.3: (cont.) Correlation image showing in the first column the IR *Spitzer* spectrum, showing the short wavelength region, the vertical red lines show the PAH bands. In the second column is the corresponding *HST* image and in the third column shows a part of the UVES spectrum.



### 3.3: THE MIXED-CHEMISTRY PROBLEM IN GBPNE

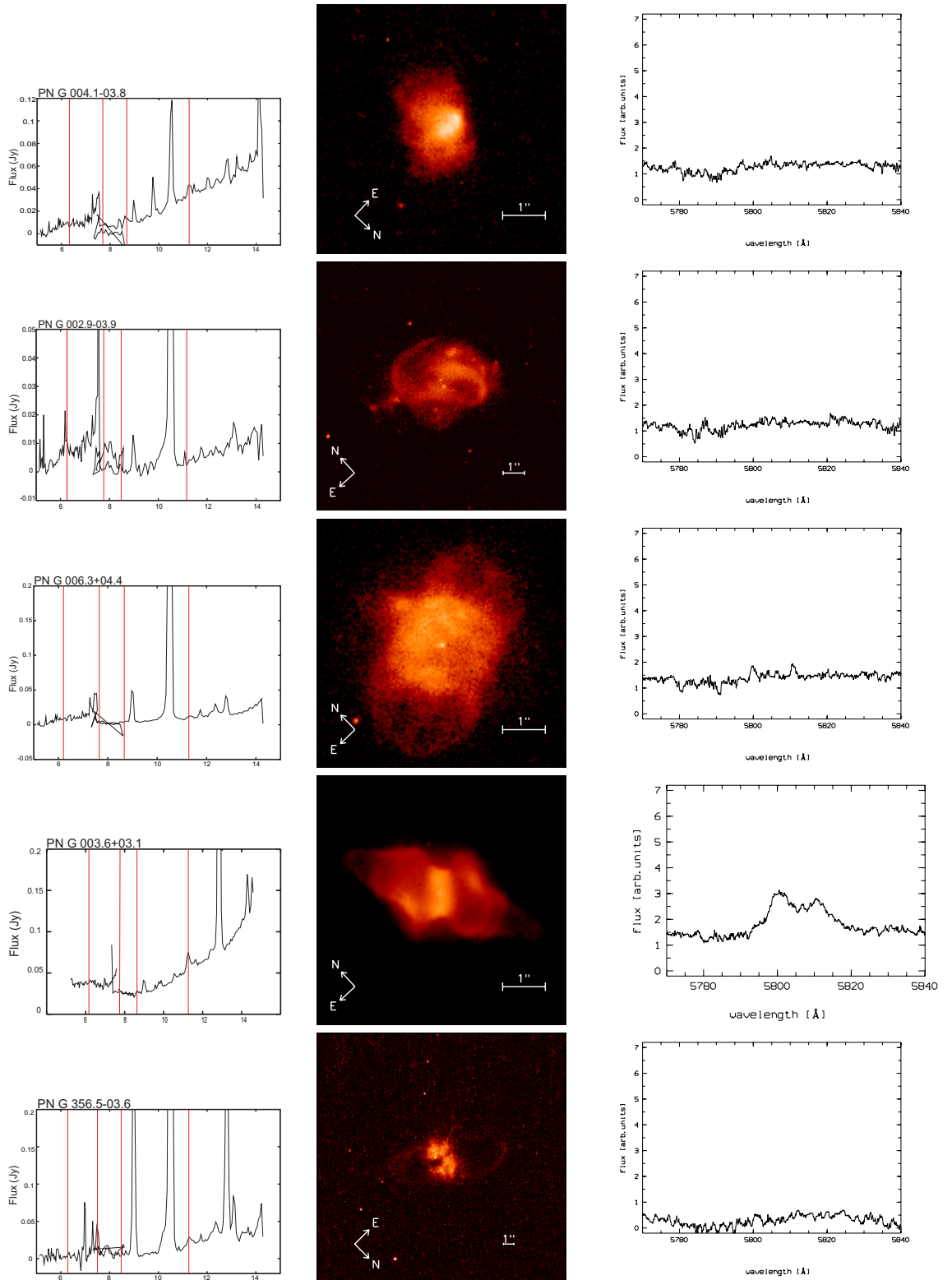


Figure 3.3: (cont.) Correlation image showing in the first column the IR *Spitzer* spectrum, showing the short wavelength region, the vertical red lines show the PAH bands. In the second column is the corresponding *HST* image and in the third column shows a part of the UVES spectrum.

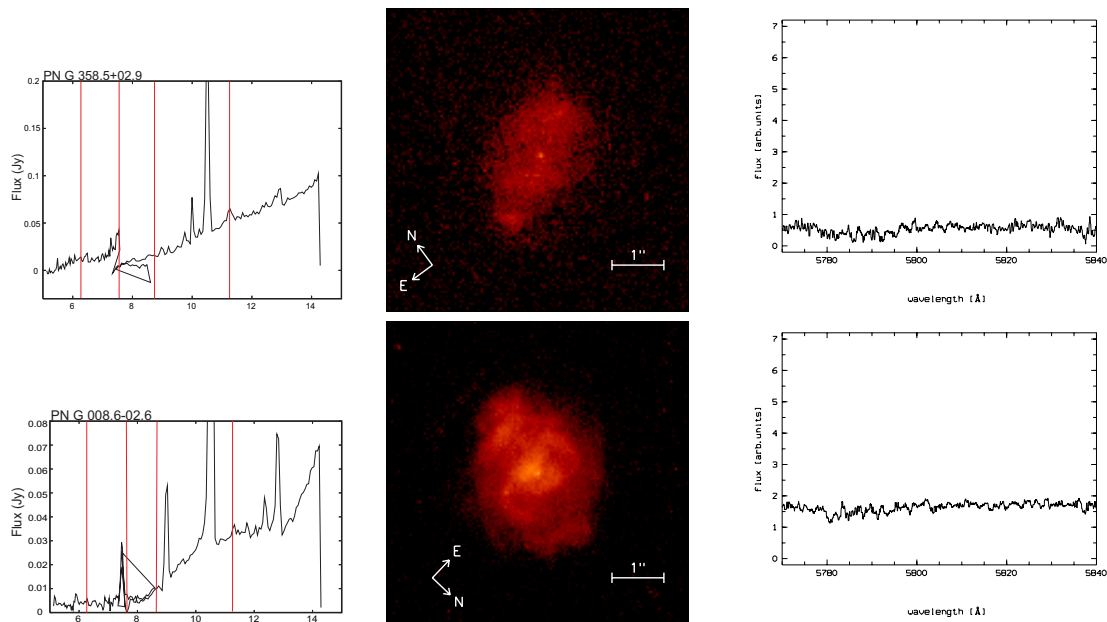


Figure 3.3: (cont.) Correlation image showing in the first column the IR *Spitzer* spectrum, showing the short wavelength region, the vertical red lines show the PAH bands. In the second column is the corresponding *HST* image and in the third column shows a part of the UVES spectrum.

morphology: a dense torus with bipolar or multipolar flows. This appears to correlate well with the PAH band strength. In a few cases the torus appears to be seen pole-on (PN G358.7+05.2 and PN G002.8+01.7), but in other cases the structure is easily visible. The confining tori have a range of sizes but are always well defined. The objects without  $7.7\mu\text{m}$  feature, towards the end of the sequence, tend to show less structured morphologies. The clearest exceptions to the rule are PN G003.6+03.1 which has no  $7.7\mu\text{m}$  detection (and has a relatively large torus) and PN G003.1+03.4 which does not show elongated lobes, possibly because of viewing angle. It was noted that one of the three silicate objects (PN G007.5+04.3) is unresolved by *HST* and is extremely compact.

This type of morphology is not the most common in the Galaxy; most PNe are round or elliptical. In the IAC morphological catalogue (Manchado et al. 1996), only 10 bipolar/quadrupolar nebulae are present among 240 objects. Corradi & Schwarz (1995) find that 15% of Galactic PNe are bipolar. Zijlstra (2007) finds 40% of compact Bulge PNe are bipolar or related. This is in contrast to our 70%.

It was concluded that the mixed chemistry phenomenon is strongly related to morphology, or the presence of a torus. There is no clear relation to the central star, apart from a possible amplification of the PAH bands by emission-line stars.

### 3.4 C-rich molecule formation in O-rich environments

To test if the dust spectra can be related to the presence of a torus, we model the *Spitzer* spectrum for the representative PN M1-31 (PN G006.4+02.0), using the MC3D (MonteCarlo 3-D) program (Wolf et al. 1999). PAHs were not incorporated in this model but only used astronomical silicate as the dust component as our aim is to reproduce the shape of the continuum due to emission from these dust grains.

The model has 6 main parameters that can be adjusted to arrive at the best fit. Other parameters were kept fixed: an effective temperature of the star of 57,000K was used, a luminosity of 6,500L<sub>⊙</sub> (Gesicki & Zijlstra 2007), an inclination of the disk of 90 degrees (edge-on), with the distance to the Galactic Bulge taken as 8.5kpc (Schneider & Buckley 1996). Test calculations were performed for a range of inclinations, but we found that this parameter has a limited effect on the result, because of the limited opacity at 10μm of the torus.

The Monte Carlo simulation calculates the radiative transfer for 100 wavelength points between 10<sup>-3</sup> and 10<sup>3</sup>μm, to calculate the dust temperature. It then uses 29 wavelengths between 1 and 53μm to calculate the SED.

The main parameters are: the inner radius of the torus ( $R_{in}$ ), the outer radius ( $R_{out}$ ), the dust mass ( $M_{dust}$ ), the exponent of the power law describing the density in the midplane ( $r^{-\alpha}$ ), flaring ( $r^{\beta}$ ) and the scale height at 100AU from  $R_{in}$ , ( $h_0$ ) (Wood et al. 1998) Equations 3.1 and 3.2 shows the density profile used for the calculations in the models. The fitted inner radius of the torus, of 5000 AU, is in good agreement with that measured from the *HST* image (0.55'' which at 8.5kpc is 4600AU).

$$\rho(r, z) = \rho_0 \left( \frac{R_{\star}}{r} \right)^{\alpha} \exp \left[ -\frac{1}{2} \frac{Z}{h(r)} \right], \quad (3.1)$$

Table 3.2: Model parameters for the PN M1-31

$R_{\text{in}}[\text{AU}]$	$R_{\text{out}}[\text{AU}]$	$M_{\text{dust}}(\text{M}_{\odot})$	$\alpha$	$\beta$	$h_0[\text{AU}]$
$5000 \pm 100$	$50000 \pm 1000$	$5.5 \times 10^{-3}$	$2.5 \pm 0.1$	$2 \pm 0.1$	$500 \pm 50$

The errors in the parameters correspond to an accuracy of the model of 10%.

where

$$h(r) = h_0 \left( \frac{r}{R_{\star}} \right)^{\beta}. \quad (3.2)$$

In Fig 3.4, we plot the *Spitzer* spectrum and the MC3D model. A good fit is obtained, with the model reproducing the steep onset of the continuum at  $14\mu\text{m}$ . The model is a little below the measured flux at shorter wavelengths, which may be due to a contribution from PAH or a very small grain continuum emission. A model with a mixture of silicate and carbon dust was also calculated, but it did not reproduce the longer wavelength continuum as well, predicting too much flux longward of  $24\mu\text{m}$ . The best fit obtained for the parameters is listed in Table 3.2.

The inner radius fits the *HST* image well but is relatively far from the star. This indicates that the fitted component is the expanding torus, and not a Keplerian disc. The model scale height is derived very close to the inner edge of the torus (100AU outside of the inner radius of 5000AU) where it is 10% of the radius, i.e. a thin torus. The flaring increases as  $r^2$  and at the outer edge of the model, the height is equal to the radius. The *HST* image suggests a thickness of the torus which is intermediate between these values. The dust mass indicates a gas mass of around  $0.1 \text{ M}_{\odot}$  (for an assumed gas-to-dust ratio of 200). The ionised mass has been estimated as  $0.29 \text{ M}_{\odot}$  (Gesicki & Zijlstra 2007). This suggests that the modelled torus accounts for a large fraction of the nebular mass.

The calculation shows that the dust continuum emission can be explained as arising from the dense torus using oxygen-rich dust (silicate) to explain the SED: there is no significant carbonaceous component. The fitted torus is large and massive. This is a significant finding, as the traditional model for mixed chemistry poses a long-lived, compact oxygen-rich disc. Such a disc is in Keplerian rotation. Waters et al. (1998) observed in the Red Rectangle a low-mass disc of 500-2000AU in size. Chesneau et al.

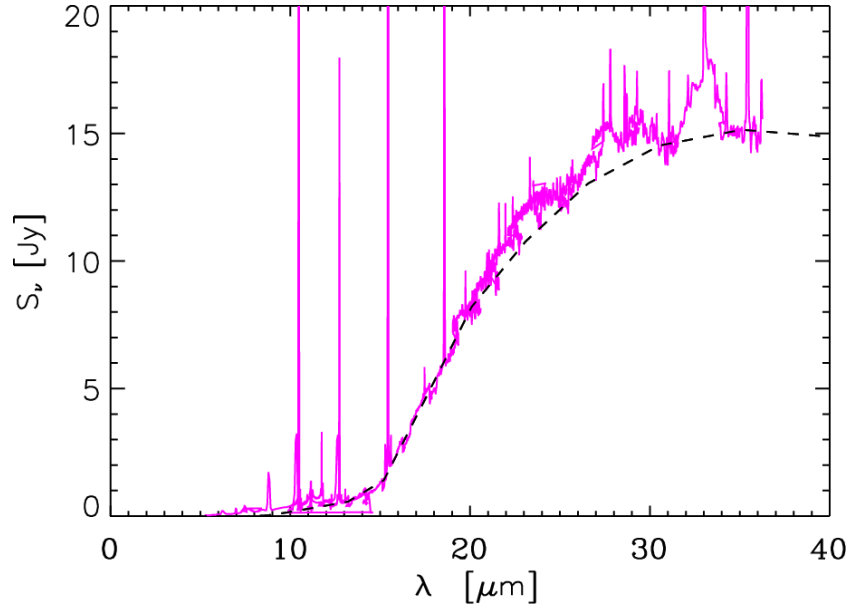


Figure 3.4: The *Spitzer* spectrum of the PN M1-31. The dashed black line is the model calculated using the MC3D code.

(2007) observed a disc size of 9-500AU in Mz-3 with a dust mass of  $1 \times 10^{-5} M_{\odot}$ . No evidence was found for such a component for M1-31.

In the traditional stellar evolution model, the silicates were ejected  $> 10^5$ yr ago, with the star subsequently becoming carbon-rich prior to the ejection of the main nebula (Habing 1996). In contrast, the torus of M1-31 is part of the main nebula and ejected  $< 10^4$  yr ago: at this time the ejecta were oxygen-rich. The mixed chemistry phenomenon is therefore unlikely to be related to the star becoming carbon-rich, as the chances of this occurring over such a short time scale are low, whereas the occurrence of mixed chemistry appears to be relatively common in GBPNe.

Interestingly, the two brightest PAH emitters in the mixed-chemistry sample, M1-40 and Cn1-5, are foreground nebulae. These are emission-line stars for which the traditional model of a long-lived disc may hold, similar to objects such as IRAS 07027-7934 and the Red Rectangle. The mixed chemistry nebulae in the Bulge are a population which is distinct from these disc objects, with a different origin of the mixed chemistry.

### 3.5 Origin of the PAH in Bulge PNe

The previous analysis shows that the mixed-chemistry Bulge nebulae are likely oxygen-rich. This is consistent with expectations based on the stellar population in the Bulge. The Bulge is believed to contain a 10 Gyr old population, with little or no trace of younger stars (Zoccali et al. 2003b), although recently, some indications have been found for a younger, highly metal-rich population (Bensby et al. 2010).

Carbon stars originate from third dredge-up, which requires a minimum stellar mass of  $M_i > 1.5 M_\odot$  (Vassiliadis & Wood 1993). It is not expected to occur in 10 Gyr old populations. Furthermore, at high metallicity the formation of carbon stars is inhibited by the large oxygen abundance which needs to be overcome by the primary carbon. Carbon stars are rare in the inner Galaxy (Le Bertre et al. 2003) and absent in the Galactic Bulge (Feast 2007), consistent with this expectation.

This strengthens the case that the mixed chemistry is occurring in oxygen-rich gas, expelled by oxygen-rich stars.

A strong correlation between mixed chemistry and morphology was found, specifically, the presence of a massive torus. This indicates that the chemical pathway to the PAH molecules occurs within their high density regions. These tori remain molecular for some time after the ionisation of the nebula has started, due to the trapping of the ionisation front and due to the shielding effects of the dust column density (Woods et al. 2005). Micro-structures like clumps also play an important role in shielding the molecules from the UV radiation. A mini PDR (photon-dominated region) is expected in these molecular regions (Phillips et al. 2010), slowly being overrun by the advancing ionisation front.

A mini-PDR within a dense torus is a plausible location for the PAH formation. In interstellar clouds, PAH emission is often associated with PDR regions (Joblin et al. 2010; Kassis et al. 2006). It is unclear whether PAHs form in these regions or whether they become visible due to UV excitation. In our objects, because of the close relationship between morphology and PAHs, it seems likely they form in the regions where they are observed.

In AGB stars, the dichotomy between O-rich and C-rich chemistry can be broken,

as is shown by the observation of hot water in the carbon stars IRC +10 216 (Decin et al. 2010; Neufeld et al. 2011; Cernicharo et al. 2011). This may be due to collisional destruction of CO in the shocks (Duari et al. 1998) or interstellar UV photons (Agundez et al. 2010a). The latter authors find that for O-rich circumstellar envelopes, the penetration of interstellar UV photons into the inner layers leads to the formation of molecules such as CH<sub>4</sub> and HCN with abundances relative to H<sub>2</sub> in the range of 10<sup>-8</sup> to 10<sup>-7</sup>. This chemistry is initiated by CO dissociation; the dissociation energy of CO is 11.1 eV.

### 3.5.1 Chemical reactions

Here whether a C-rich chemistry can be similarly driven by UV photons penetrating the dense, oxygen-rich torus is investigated. The penetration is limited by the dust extinction: in our *HST* image, internal extinction is clearly visible in M3-38 (PN G356.9+04.4) which has the most compact torus.

Our model, which contains gas-phase chemistry only, is based on that of Ni Chuimin (2009) (see also Millar et al. 2007), developed for conditions in PDR regions. It uses an extrapolation of the Meudon 2006 PDR chemistry code (Le Petit et al. 2006), and assumes a semi-infinite and constant-density slab with a density of  $2 \times 10^4 \text{ cm}^{-3}$ , UV radiation enhanced by a factor of 60 over the average interstellar field, treats thermal balance self-consistently, and contains a mixture of reactions extrapolated from the Meudon chemical files and also the UDFA 2006 (Woodall et al. 2007)<sup>1</sup>, Rate 99 (Le Teuff et al. 2000) and Ohio State OSU-03<sup>2</sup> databases. In Figure 3.5 the behaviour of the temperature against  $A_V$  is shown. As expected, the temperature does not vary much between the three models with each displaying an increase in cooling by atomic O as its abundance increases. Formation and destruction of large hydrocarbon chains, that is with more than 4 carbon atoms, of the form C<sub>n</sub>H<sub>m</sub>, ( $n \leq 23$ ,  $m \leq 2$ ) and their associated ions were added. This resulted in a chemical network of 269 species connected by about 3500 reactions involving ion-neutral and neutral-neutral collisions, photodissociation and photoionisation, dissociative and radiative recombination with

---

<sup>1</sup><http://www.udfa.net>

<sup>2</sup><http://www.physics.ohio-state.edu/~eric/research.html>

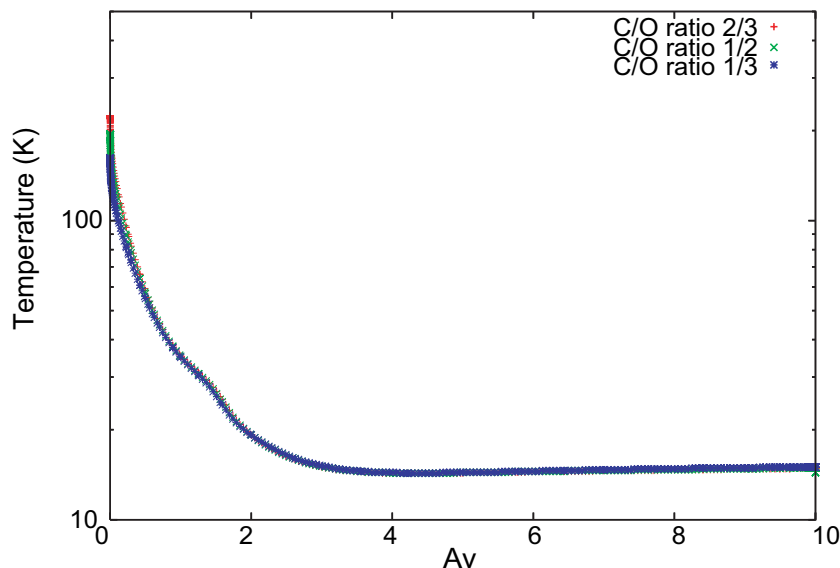


Figure 3.5: Temperature as a function of visual extinction in our three models. The temperature is calculated self-consistently in the constant-density slab.

electrons and radiative association reactions. The goal of the models is to study the abundances of large hydrocarbons. The specific formation of benzene rings (Woods et al. 2002, 2003) and PAHs is not included, but cyclisation is assumed to be possible for chains of 23 carbon atoms. Laboratory spectroscopy has shown that this does not yet happen spontaneously for chains of 13 carbon atoms (Giesen 1994).

The elemental carbon abundance is kept constant at the standard value of  $1.32 \times 10^{-4}$  relative to the total hydrogen abundance (Savage & Sembach 1996) while the elemental oxygen abundance is varied to give a range of C/O values of 2/3, 1/2 and 1/3.

The formation pathways for the carbon chain species in the chemical model include neutral-neutral C atom reactions, radiative association reactions with carbon atoms, and ion-molecule reactions with  $C^+$ . Destruction of these chains occur in reactions with oxygen atoms ( $O + C_n$ ), photodissociation and photoionisation, dissociative recombination and electronic recombination reactions (Table 3.3). The oxygen-destruction reaction rates are adopted and extrapolated from the Meudon 2006 chemistry (Le Petit et al. 2006). The oxygen destruction rates for  $C_2$  and  $C_4$  are assumed to be reasonably fast ( $1.5 \times 10^{-11}$  and  $10^{-10} \text{ cm}^3 \text{ s}^{-1}$ , respectively), while the reaction with  $C_3$  is assumed to have an energy barrier (Woon & Herbst 1996).



Table 3.3: Example of model reactions of different types.

oxygen destruction	$O + C_n \rightarrow C_{n-1} + CO$	Meudon
neutral-neutral	$C + C_nH \rightarrow C_{n+1} + H$	UDFA
neutral-neutral	$C + C_nH_2 \rightarrow C_{n+1}H + H$	UDFA
radiative association	$C + C_n \rightarrow C_{n+1} + h\nu$	Meudon
radiative association	$C + C_nH \rightarrow C_{n+1}H + h\nu$	Meudon
ion-molecule	$C^+ + C_nH \rightarrow C_{n+1}^+ + H$	OSU-03

Example reactions of various types included in the model are listed in Table 3.3. The last column shows the source of the adopted rate coefficients, either from the Meudon model, the UDFA, or OSU-03 databases.

### 3.5.2 Results

If PAH emission does originate from the torus and is not swept-up interstellar gas as is indicated by our observations, then it is valid to consider whether the PAH themselves can be formed in this oxygen-rich, UV-irradiated environment. Since there is no detailed chemical kinetic model for PAH formation, this hydrocarbon chemistry could be used as a proxy for PAH formation, noting that even the presence of abundant hydrocarbons in a PDR would not necessarily prove that PAHs are formed in the same environment.

The PDR model calculations show that the chemistry first tends towards complexity around the  $C^+/C/CO$  transition at  $A_V \sim 1.4$  mag. This transition is seen in Fig. 3.6 which plots the abundances of O, C,  $C^+$  and CO as a function of  $A_V$ . As expected, only O shows a difference between the three models, for the other species the results for the model with  $C/O = 1/2$  were the only ones plotted.

Figure 3.7 shows the calculated fractional abundances (relative to  $H_2$ ) for the molecules  $C_2H$ ,  $C_8H$  and  $C_{23}H_2$ , respectively, as function of  $A_V$ , which measures depth into the slab, and  $C/O$  ratio.

Two hydrocarbon peaks are seen, one at  $A_V \sim 1.5$ , and one at  $A_V \sim 4-6$ . The first peak occurs in the region in which  $C^+$  and  $H_2$  are abundant with the hydrocarbon chemistry initiated by the  $C^+-H_2$  radiative association reaction. Subsequent reactions with C and  $C^+$  form  $C_2H$ .  $C_2H$  is the main seed molecule for the formation of larger hydrocarbons, as it is in the carbon-rich envelope of IRC+10216 (Millar et al. 2001),

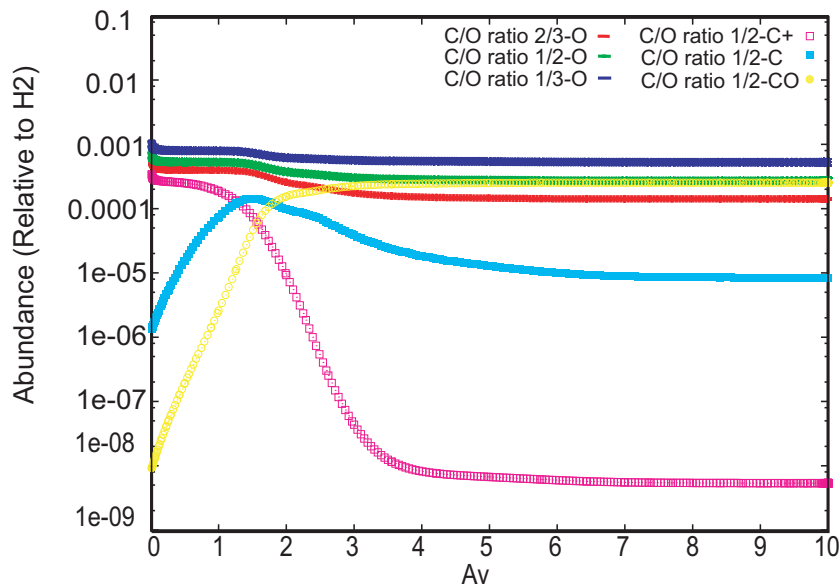


Figure 3.6: Calculated abundances for O, C,  $C^+$  and CO for the three models with varying C/O ratios. Only the O atom abundance varies, other abundances are almost identical in the models and are shown here for the case of  $C/O = 1/2$ .

and reactions continue to build up to  $C_8H$ , although large(r) hydrocarbons are not highly abundant at low extinction.

The second peak, at higher  $A_V \sim 4 - 6$ , occurs where atomic carbon becomes abundant and drives chemistry through proton transfer with  $H_3^+$  to form  $CH^+$  which subsequently reacts with  $H_2$  to form simple hydrides. Here the chemistry produces a surprisingly large abundance of the biggest hydrocarbons in the model.

Oxygen atom destruction reactions are the dominant loss of larger hydrocarbons at high  $A_V$  where there is little  $C^+$ . The reaction rates of  $C_2H$  and C with O are rather uncertain: they differ by an order of magnitude between the UDFA and the Meudon chemical models. However, because of the importance of O, the abundances depend on the C/O ratios: models with less O produce higher abundances of large hydrocarbons. The difference amplifies for the larger molecules: whereas for  $C_2H$  and  $C_8H$  the difference in abundance between  $C/O=1/3$  and  $2/3$  is within an order of magnitude, for  $C_{23}H_2$  it is four orders of magnitude. Even a small increase in the C/O ratio makes a large difference here.

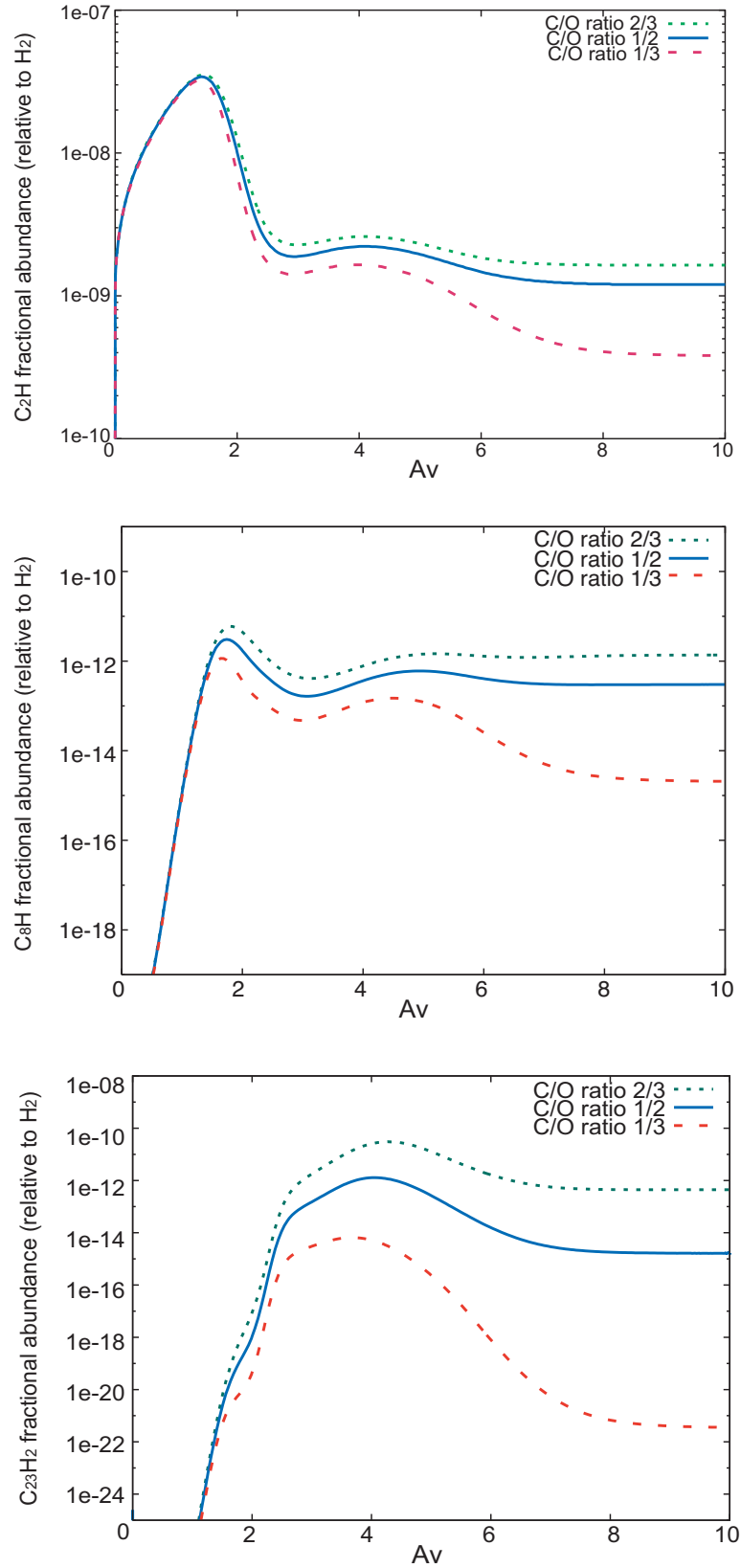


Figure 3.7: Calculated abundances (relative to  $H_2$ ) for varying C/O ratios for  $C_2H$  (top),  $C_8H$  (middle), and  $C_{23}H_2$  (bottom).

### 3.6 Implications

Under the assumptions of the chemical model, it is clear that larger hydrocarbons can form within oxygen-rich environments. It is assumed here that a mechanism exists to convert these long linear hydrocarbon chains into PAH molecules. Such a discovery is surprising, but clues have been previously found in the inner regions of oxygen-rich stars, where small carbon-bearing molecules have been observed, and explained by means of shock chemistry (Cherchneff 1995) or penetration of UV photons (Agundez et al. 2010b). Furthermore, in the oxygen-rich environment of a protoplanetary disc, Woods & Willacy (2007) showed that benzene and large polyynes of up to  $C_8H_2$  can form through ion-molecule chemistry in suitably dense conditions, where cosmic- and X-rays provide a source of ionisation. In this latter model, in the ISM (McEwan et al. 1999), and in proto-PNe with carbon-rich tori (Woods et al. 2002, 2003) closure of the aromatic ring occurs through the reaction of small ( $C_{2...4}H_{3...5}^{(+)}$ ) hydrocarbons, which are not included in our model due to the simple nature of the Meudon chemistry (Table 3.3). However, these small hydrocarbons are typically formed by the destruction of larger polyynes, and through reaction with atomic carbon, which are abundant in the chemical model. Once this first aromatic ring closure has occurred, subsequent aromatic growth is rapid in comparison (Cherchneff et al. 1992; Wang & Frenklach 1994).

If it is assumed that the underlying abundance distribution of hydrocarbon chains is related to that of PAHs, then some inferences on the properties of PAH emission in the Galactic Bulge PNe can be made. First, a reasonable extinction is needed. At low  $A_V$  ( $<2$ ), where carbon is ionised, the abundances of the longest chains are strongly suppressed by photodissociation and photoionisation. This still allows for the formation of shorter linear hydrocarbons, but PAH formation is not expected. Efficient PAH formation requires sufficient extinction to render carbon neutral and to minimise the effects of photodestruction. The optimum extinction in our model is around  $A_V \sim 4$ . At even higher extinction, carbon is locked up in CO and fewer of the longest hydrocarbon chains form, although intermediate chains ( $C_8H$ ) still form.

In order to generate sufficient reactive C and  $C^+$  UV photons are required to dissociate CO contained in the dense molecular torus. Thus, the central star needs to be

hot enough to generate these photons. Our models use a radiation field of 60 times the interstellar radiation field which corresponds to a star of spectral type B, or temperature around 15 000K. This suggests that the PAHs will not form until the star is hot enough to begin to ionise the nebula. By this time, the nebula will have expanded and the extinction has dropped considerably.

The need for the torus may therefore be to provide an irradiated region dense enough to allow a photon-dominated chemistry, in a nebula old enough to allow for an ionising star. Such a requirement would explain the close relation between PAH emission in oxygen-rich PNe, and the presence of a dense torus. This same relation also holds in non-Bulge PNe, e.g. NGC 6302 and Roberts 22 (Zijlstra et al. 2001). Clumps inside the torus may also play a very important role in shielding the molecules from the UV radiation of the central star. Studies of clumps in PNe have revealed that molecules do survive from the ABG to the PNe phase (Redman et al. 2003).

The predicted abundances show a strong dependence on C/O ratio (Fig. 3.7). This may explain the finding of Cohen & Barlow (2005) that PAH emission at lower C/O ratio is faint. An increase in the C/O ratio, even if it remains below unity, would benefit PAH formation. But such an increase is not expected in Bulge PNe which may not experience carbon dredge-up.

Finally, even though this model goes some way to explaining the observed mixed chemistry, it remains unexplained why PNe with [WC] type central stars would have stronger PAH emission. Part of this correlation may be due to the fact that the brightest objects in Table 3.1 contain some foreground nebulae. However, even excluding these, it still appears that the emission-line stars dominate the top end of the Table.

Two possible explanations can be envisaged. First, the stellar winds may inject some carbon into the surrounding nebulae. This would locally enhance the C/O ratio, and increase the PAH formation rate.

The second explanation could be related to the energy deposition by the stellar wind into the nebula. Gesicki et al. (2006) showed that nebulae around [WC] type central stars are turbulent indicating that some energy deposition into the nebulae occurs, for instance from the stellar wind. The turbulence may aid in dissociating CO, or more likely, causes compressed regions with a larger range of extinctions. The second

explanation appears more plausible. However, the relation between stellar winds and PAH emission needs to be studied further.

Finally it was noted that the  $A_V$  in Figures 3.6 and 3.7 is time-dependent. As the torus expands, the extinction drops. The local conditions thus evolve from right to left in the Figures. This predicts two layers within the torus, one with the smaller hydrocarbons at  $A_V \sim 1.5$  and one with PAHs at  $A_V \sim 4$ , which are both moving inward into the torus as the nebula evolves. This makes the layer at lower extinction, with shorter hydrocarbons, a product of the destruction of the PAHs by the increasing UV radiation field. If the PAHs are more UV-stable than the largest chains in the model, then PAHs could be present at lower extinction than predicted here.

## 3.7 Conclusions

The main conclusions of this Chapter are summarised in the following list:

- Observations of 40 PNe towards the Galactic Bulge were analysed using the IRS instrument on board *Spitzer*. It was found that 30 of them present a mixed chemistry phenomenon. From these 40 PNe *HST* observations of 22 were used to analyse their morphology.
- A strong correlation was found between strength of the PAH bands and morphology, in particular, the presence of a massive torus. Data from *VLT/UVES* was also used to study their central stars. No correlation was found between the classification of the central star and the mixed chemistry phenomenon, although PNe with emission line stars (wels or [WC]) tend to have stronger PAHs emission. This could be related to carbon injection or energy deposition by the wind into the nebula, enhancing PAH formation.
- The *Spitzer* spectrum was modelled for the representative PN M1-31. The SED can be explained using oxygen-rich (silicate) dust. The fitted torus is large and massive, with a size of 5000-50000AU and a mass of  $5 \times 10^{-3} M_{\odot}$ . Because of the age of the torus of M1-31 ( $< 10^4$ yr) the mixed chemistry phenomenon is unlikely to be related to a change of composition of the stellar ejecta over time. Such a

change would be unexpected in the Bulge population (which does not show third dredge-up), and would be very rare over such a short period in any case, whereas the occurrence of mixed chemistry appears to be relatively common.

- For the chemical analysis of the PAH formation in an oxygen-rich environment, the gas-phase models from Ní Chuimín (2009) were used. These are an extrapolation of the Meudon 2006 PDR chemistry code to include the chemistry of large hydrocarbons. They cover a range of  $A_V$  and C/O ratios of 1/3, 1/2 and 2/3. Although the models do not include PAH formation, it shows that large hydrocarbons can form in oxygen-rich environments and that their abundances can be relatively large in moderately shielded regions. The model predicts two layers, one at  $A_V \sim 1.5$  where small hydrocarbons form from reactions with  $C^+$ , and one at  $A_V \sim 4$ , where larger chains (and by implication, PAHs) form from reactions with neutral, atomic carbon.
- The torus observed in all of the PNe that present the mixed chemistry phenomenon could provide the dense, irradiated environment needed to form the PAHs detected.

The complete list of the *Spitzer* spectra is displayed in Appendix C. The whole spectrum is presented on the left and its corresponding short-wavelength region of the spectra on the right side (for the PAHs emission bands to be clearer). After these findings, a sample of PNe were selected to be observed with the *VLT* imager and spectrometer for mid-infrared (VISIR). This instrument has enough resolution to identify the spatial position of the PAH bands in these PNe, therefore we were able to test our theory of the formation of PAHs in the tori of these PNe. The result of this research is presented in Chapter 4.





# Chapter 4

## PAHs in PNe



Figure 4.1: The very large telescope (VLT) located at Paranal, Chile (Credit: G.Gillet/ESO).

According to our current understanding of stellar evolution, all stars with main sequence mass in the range  $1\text{--}8M_{\odot}$  evolve via the asymptotic giant branch (AGB) phase to the planetary nebula stage (PN). As they ascend the AGB, their mass-loss rate increases from solar-like values ( $10^{-14} M_{\odot}\text{yr}^{-1}$ ) up to  $10^{-4} M_{\odot}\text{yr}^{-1}$ . Dust grains and molecules, predominantly CO, condense within their winds, forming substantial circumstellar envelopes detectable in the infrared and millimetre domains. Dredge-up of newly synthesised carbon and s-processed elements affects the chemistry of the envelope. As the CO molecule is very stable, the chemistry in the AGB shell is determined by

the C/O ratio. If  $C/O < 1$  then all the carbon is trapped in CO, and the chemistry is dominated by oxygen components. Silicate dust forms, with spectral signatures at 9.8 and 18  $\mu\text{m}$ . If  $C/O > 1$  then carbon dominates the chemistry and the main observed dust features are amorphous carbon (which has no spectral feature), SiC (11.3  $\mu\text{m}$ ), and complex hydrocarbons, including PAHs and fullerenes (Cami et al. 2010). Stars begin their life with  $C/O < 1$  and are thus oxygen rich. In intermediate-mass AGB stars, the dredge up of carbon can raise C/O above unity to form a carbon star. A drastic change in the dust and molecular composition thus occurs. At the end of the AGB phase the stars becomes hotter, the envelope becomes detached and ionised by the central star and shines as a Planetary Nebula.

A recent mid-infrared spectroscopic survey of Planetary Nebulae (Perea-Calderón et al. 2009) in the Galactic Bulge has provided some surprising results. They observed 26 PNe in the Bulge and found that 21 of them showed a dual-dust chemistry, with the presence of PAHs (carbon-rich) and crystalline silicates (oxygen-rich) in their spectra. This had already been observed in a few PNe with [WC]-type central stars which have little or no H in their atmospheres (Waters et al. 1998), thought to be a rare event relating to the mixing of carbon-rich ejecta into a pre-existing oxygen-rich shell. But in the Galactic Bulge, this dual-dust chemistry is observed in PNe with ordinary central stars and is present in a large fraction of the PNe envelopes observed with *Spitzer*.

Perea-Calderón et al. (2009) proposed that this dual-dust chemistry is due to a recent change of chemistry in the envelope of these low mass, high metallicity population of PNe. But the probability to observe a large number of such stars just during their short transition phase between O-rich and C-rich is almost zero, and in fact Bulge stars are too low mass to undergo carbon dredge-up and so do not experience this transition. It is much more likely that the hydrocarbons form from dissociation of CO molecules. Further analysis made by Guzman-Ramirez et al. (2011) of a sample of 40 Galactic Bulge planetary nebulae (GBPNe) showed that the mixed chemistry phenomenon is seen in 30 nebulae. HST images and UVES spectra showed that the mixed chemistry is not related to the presence of emission-line or [WC] stars, as it is in the Galactic disk population instead a strong correlation is found with morphology, and the presence of a dense torus. The mixed chemistry phenomenon occurring in the GBPNe is best

explained through hydrocarbon chemistry in an UV-irradiated, dense torus.

PNe in the Bulge are the end-products of low-mass stars (and therefore expected to be O-rich) and belong to a metal rich population. The high rate of bulge PNe with mixed chemistry detected with *Spitzer* clearly deserves further investigation. A sample of 11 PNe were selected to be observed with the *VLT* imager and spectrometer for mid-infrared (VISIR). This instrument has enough resolution to identify the spatial position of the PAH bands in these PNe, therefore we were able to test our theory of the formation of PAHs in the tori of these PNe.

## 4.1 Observations

The observations were performed using the ESO mid-infrared instrument VISIR (Lagage et al. 2004) installed on UT3 at the VLT (Paranal, Chile). This instrument composed of an imager and a long-slit spectrometer covering several filters in N (8-13 $\mu$ m) and Q (16-24 $\mu$ m) atmospheric windows.

### 4.1.1 VISIR photometry

The pixel scale we used is 0".0755 and the field of view 19".2 $\times$ 19".2. The observations were done using the normal VISIR imaging mode, using the standard chopping and nodding technique to remove the sky background. We used a perpendicular chop-throw of 10". In this mode, all the frames taken at a given chopping position are co-added immediately at the end of the exposure. The detector integration time (DIT) for a single frame is typically of the order of 10/20ms. To reduce the data, we used the standard ESO pipeline Gasgano (version 3.4.4). This pipeline applies flat field correction, bad pixels removal, source alignment and co-addition of the frames for each filter. To improve the spatial resolution of the reduced images, we used the Richardson-Lucy deconvolution algorithm (Richardson 1972), using standard stars observed shortly before or after the observations as a measure of the point spread function (PSF) and typically 30 iterations. Images were obtained with three filters: PAH1, PAH2, and SIV ( $8.59 \pm 0.42\mu$ m, 11.25

$\pm 0.59\mu\text{m}$ , and  $10.49 \pm 0.16\mu\text{m}$ , respectively). Finally, according to the ESO manual<sup>1</sup> systematic uncertainties of VISIR photometric data are of the order of 10% for PAH1 and PAH2. The PAH1 filter's transmission covers the  $8.6\mu\text{m}$  PAH feature, SIV the SIV emission line and PAH2 the  $11.3\mu\text{m}$  PAH feature. As most of our objects are red, the PAH1 images are very noisy or the object is barely detected, except for four compact sources. To determine the spatial location of the  $11.3\mu\text{m}$  PAH feature and the [SIV] emission line, we built two-colour images for each object. In these images, red represents the [SIV] emission (ionised material) and green the  $11.3\mu\text{m}$  feature (PAHs). Zones in yellow contain emissions from both ionised material and PAHs.

### 4.1.2 VISIR spectroscopy

We also performed VISIR low-resolution spectroscopy ( $R \sim 350$  at  $10\mu\text{m}$ ) of three PNe, M1-31, M1-40 and M3-38 from  $9.0$  to  $13.46\mu\text{m}$  split in three filters of the N band, centred at  $9.8$ ,  $11.4$  and  $12.4\mu\text{m}$ . We used standard stars observed shortly before or after the observations to correct our spectra from telluric absorption. Extraction of the spectra, wavelength calibration, telluric lines correction, and flux calibration were then carried out using the IDL reduction package mentioned above. The long-slit spectrograph gave us an spatially resolved 2D spectra for each object, from which we extracted the PAHs features, the [SIV] emission line and the continuum. We were able to analyse and compare their spatial extension for the three objects. The observations were carried out on under the program ID 087.D-0270 , PI Eric Lagadec. Table 4.1 presents the log of the observations.

## 4.2 Results

### 4.2.1 VISIR images

**Cn1-5** (PN G002.2-09.4) A torus is clearly seen in all the images, even if the emission is very weak in the bluest filter, PAH1. The observed morphologies are however slightly different. The PAH2 image displays an elliptical envelope, with a bright equatorial

---

<sup>1</sup>[www.eso.org/sci/facilities/paranal/instruments/visir/doc](http://www.eso.org/sci/facilities/paranal/instruments/visir/doc)

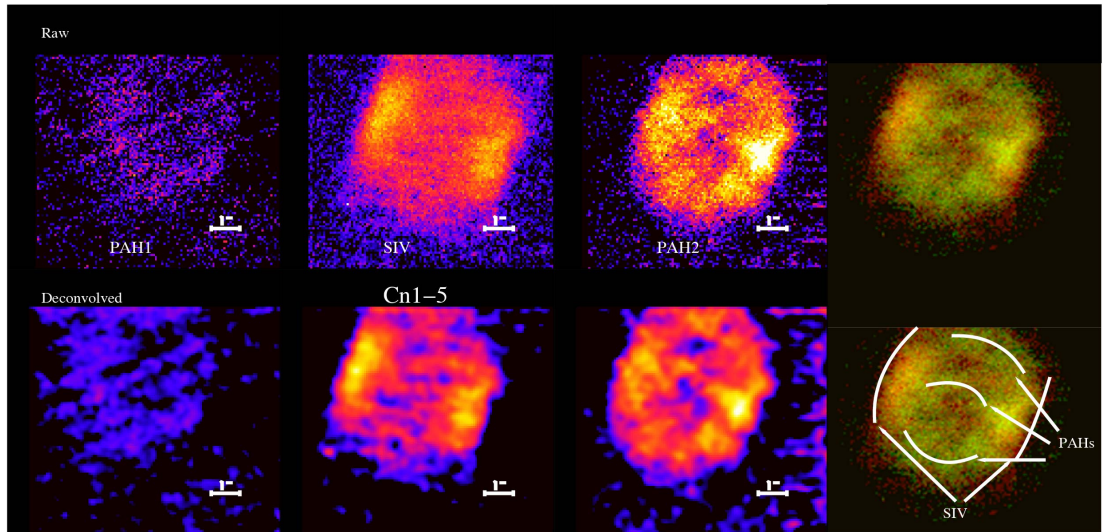


Figure 4.2: VISIR observations of Cn1-5 at 8.59 (PAH1), 10.49 (SIV) and 11.25 $\mu$ m (PAH2). North is up and East is left. The upper images are the original, while the lower panel display the images deconvolved using a Richardson-Lucy algorithm. The right part of the figure displays a two-colour image made combining images obtained in the PAH2 filter (green) and SIV (red). The region in yellow thus contain emission from both filters.

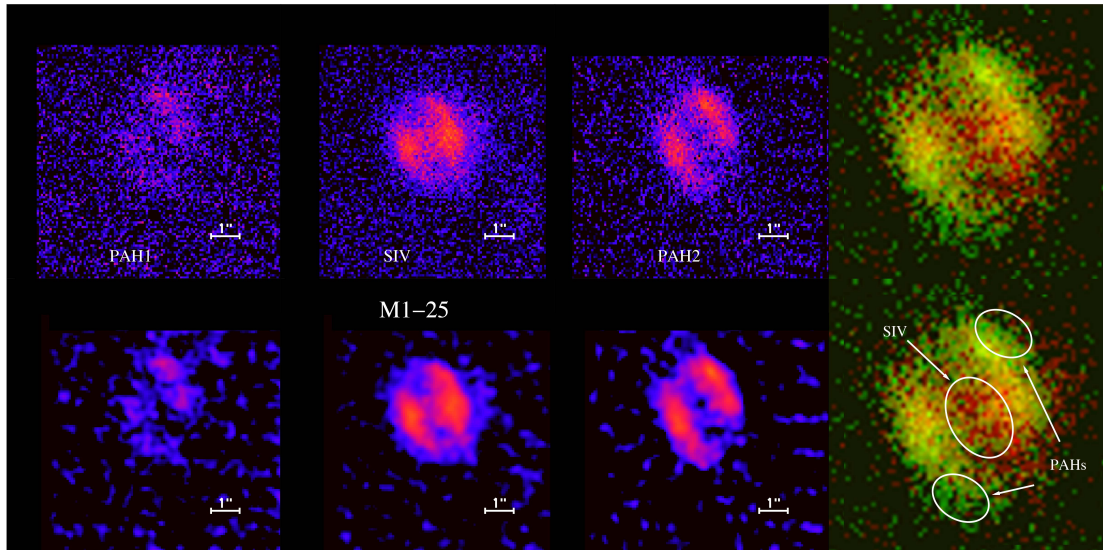


Figure 4.3: Same as Fig. 4.2, for M1-25.

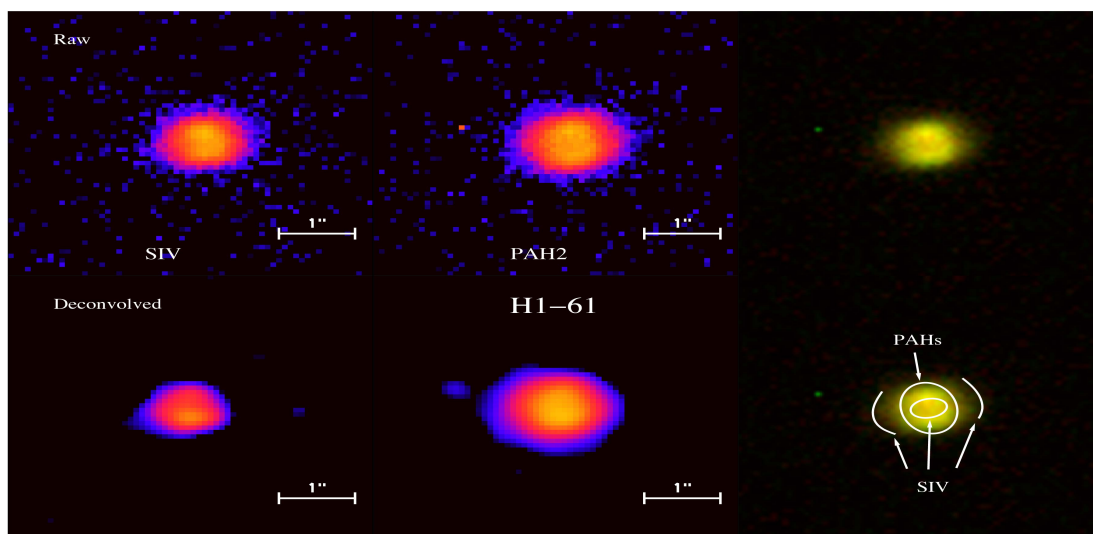


Figure 4.4: VISIR observations of H1-61 at 10.49 (SIV) and 11.25 $\mu$ m (PAH2). North is up and East is left. The upper images are the original, while the lower panel display the images deconvolved using a Richardson-Lucy algorithm. The right part of the figure displays a two-colour image made combining images obtained in the PAH2 filter (green) and SIV (red). The region in yellow thus contain emission from both filters.

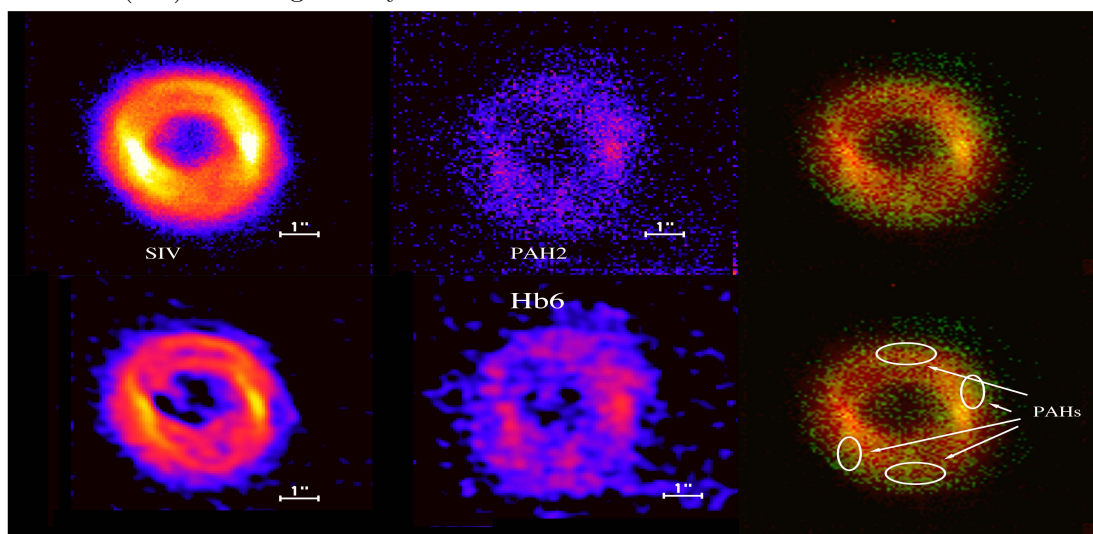


Figure 4.5: Same as Fig. 4.4, for Hb6.

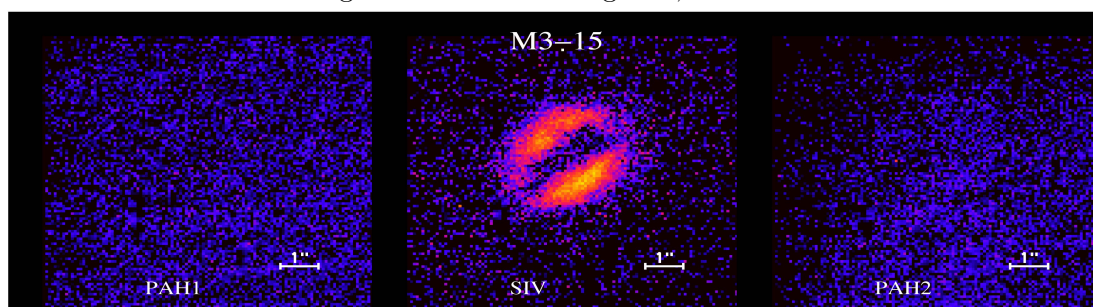


Figure 4.6: VISIR observations of M3-15 at 8.59 (PAH1), 10.49 (SIV) and 11.25 $\mu$ m (PAH2). North is up and East is left. The images are the original without deconvolution.



Table 4.1: Log of the VISIR/VLT observations.

Name	PNG Name	IRAS 12 $\mu$ m flux Jy	Imaging/Spectroscopy	Filter	Integration time s
Cn1-5	002.2 -09.4	1.69	Imaging	PAH1	300
			"	PAH2	1200
			"	SIV	1200
M1-25	004.9 +04.9	0.78	Imaging	PAH1	1200
			"	PAH2	1200
			"	SIV	1200
M1-31	006.4 +02.0	1.17	Imaging	PAH2	240
			"	SIV	240
			Spectrum	N	600
H1-61	006.5 -03.1	1.02	Imaging	PAH2	240
			"	SIV	240
M3-15	006.8 +04.1	0.53	Imaging	PAH1	240
			"	PAH2	240
			"	SIV	120
Hb6	007.2 +01.8	1.88	Imaging	PAH2	240
			"	SIV	240
M1-40	008.3 -01.1	2.70	Imaging	PAH2	960
			"	SIV	480
			Spectrum	N	600
Th3-4	354.5 +03.3	1.30	Imaging	PAH1	120
			"	PAH2	120
			"	SIV	120
M3-38	356.9 +04.4	1.20	Imaging	PAH1	120
			"	PAH2	120
			"	SIV	120
			Spectrum	N	360
H1-43	357.1 -04.7	0.49	Imaging	PAH1	240
			"	PAH2	240
			"	SIV	480
H1-40	359.7 -02.6	2.38	Imaging	PAH1	120
			"	PAH2	60
			"	SIV	120

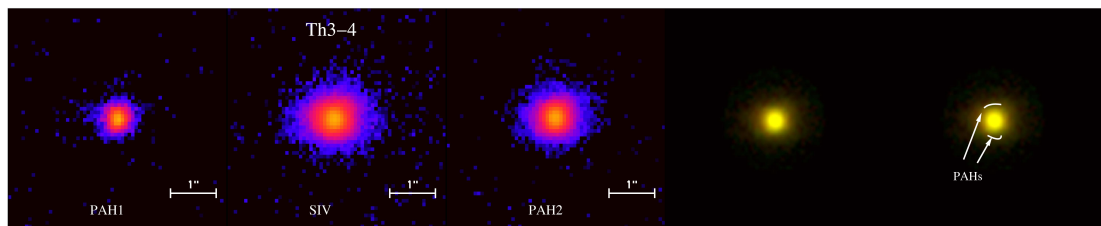


Figure 4.7: VISIR observations of Th3-4 at 8.59 (PAH1), 10.49 (SIV) and 11.25 $\mu$ m (PAH2). North is up and East is left. The images are the original without deconvolution. The right part of the figure displays a two-colour image made combining images obtained in the PAH2 filter (green) and SIV (red). The region in yellow thus contain emission from both filters.

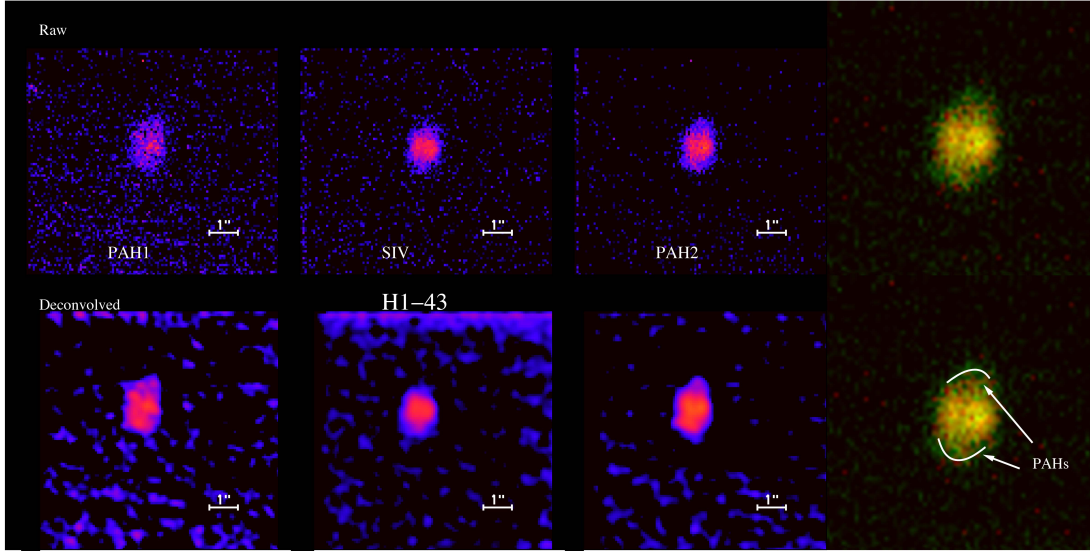


Figure 4.8: Same as Fig. 4.2, for H1-43.

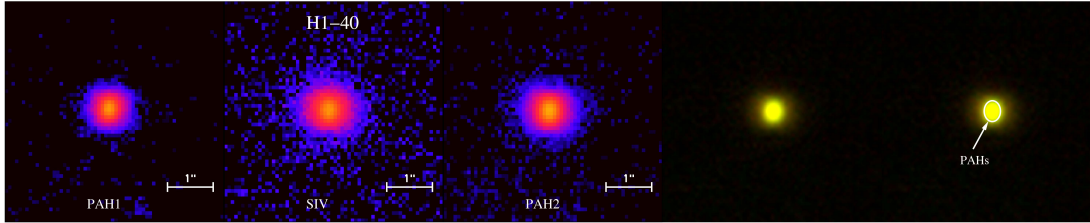


Figure 4.9: Same as Fig. 4.7, for H1-40.

lane, while the SIV image shows a more rectangular morphology. The bright equatorial lane seen in PAH2 indicates that part of the PAHs are located on the torus. The two colour images confirm this, as we see that the PAHs are concentrated in an equatorial lane joining both sides of the torus. PAHs are also seen in two regions parallel to this equatorial lane, north and south of it respectively.

VISIR images of **M1-25** (PN G004.9 +04.9) also show the presence of an equatorial torus, with an envelope elongated in a direction perpendicular to this torus. As the object is very red, it is barely detected in the bluest filter (PAH1). The two colour image show that the ionised material is more concentrated toward the core of the equatorial torus. PAHs seem to be more concentrated toward the outer edges of the torus.

VISIR images of **H1-61** (PN G006.5 -03.1) show the presence of an equatorial torus with extended emission in the direction perpendicular to the torus. The two colour image seems to indicate that the ionised material is more present in the outflow



and the inner parts of the torus, while the PAHs seem to be present at the outer edge of the torus.

**M3-15** (PN G006.8+04.1) was only detected in the SIV filter. This is due to the fact that the SIV emission line in this object is much brighter than the PAHs. The projection of a torus seen almost edge-on is clearly visible. Its morphology lead us to dub this object the *Kiss Nebula*.

**Hb6** (PN G007.2+01.8) display a doughnut-like shape in both SIV and PAH2 filters. The deconvolved image (bottom-left) shows a double ring-like morphology with the SIV brightest emission coming from the region between the two rings. The brightest emission parts of the nebula are located at the edges of this elliptical structure. This could be the projection of a torus. Due to the weakness of the target in the PAH2 filter, it is difficult to clearly locate the PAHs, but four *bright* zones are seen at both edge of the torus and above and under the equatorial plane of the nebula. Interestingly, these two latest regions appear to be where the SIV emission is weaker.

**Th3-4** (PN G354.5+03.3) The VISIR images show the presence of a compact torus with an equatorial plane along a position angle (P.A.) very close to zero. The SIV image shows an envelope elongated in a direction perpendicular to that torus. This is not seen in PAH1 and PAH2, and could be due to the lower intensity of the PAHs with respect to the [SIV] line.

VISIR images of **H1-43** (PN G357.6 +01.7) also reveal the presence of an equatorial torus with extended emission in the perpendicular direction. The source is also very red, and is barely detected in PAH1. The source is very compact, but the two colour image indicates that PAHs are more abundant outside the torus, in a direction perpendicular to its equatorial plane.

The images of **H1-40** (PN G359.7-02.6) show a morphology very similar to that of Th3-4, with a very compact central torus and an elongation perpendicular to this torus, better seen in the SIV filter. The two colour image indicates that the ionised material is present in the outflow (perpendicular to the torus), where PAHs are not seen. PAHs seem to be present at the edge of the compact torus.

### 4.2.2 VISIR images & spectra

In Figure 4.10, 4.11 and 4.12 we present on the top, the VISIR observations of M1-31, M1-40 and M3-38 at 8.59 (PAH1), 10.49 (SIV) and 11.25 $\mu$ m (PAH2). North is up and East is left. The upper images are the original images, while the lower lines display the images deconvolved using a Richardson-Lucy algorithm (for M3-38 we did not performed the deconvolved algorithm). The right part of the figure displays a two-colour image made combining images obtained in the PAH2 filter (green) and SIV (red). The region in yellow contains emission from both filters spatially resolved emission from the 11.3 and 11.7 $\mu$ m PAHs band and the [SIV] emission line for the PNe. On the bottom we show the VISIR spectroscopic observation of each object. The long-slit spectrograph gave us an spatially resolved 2D spectra, we performed a cut along the spatial direction of the VISIR spectra for the corresponding PNe. Emission of the 11.3 $\mu$ m PAH band (green), the [SIV] emission line (red) and the continuum (black) is presented.

The VISIR images of **M1-31** (PN G006.4+02.0) display a compact torus seen almost edge-on, with extended material in a direction perpendicular to the torus. The two-colour image indicates that PAHs are present at the edge of the torus and in the outflows. For this PN the P.A. of the slit was 85° (almost perpendicular to the outflows). We can clearly see that the emission of the PAHs for the PN M1-31 comes from a broader region compared to the [SIV] line. This confirms that, as seen in the two-colour image, the PAHs are present at the outer edges of the torus (see Figure 4.10).

The VISIR images of **M1-40** (PN G008.3-01.1) reveal a torus seen close to face on and many asymmetric structures around the clumpy central torus. Extended emission is seen in a direction perpendicular to the torus, and also parallel to it. The two-colour image indicates that the ionised material is present at the inner edge of the torus and PAHs at the outer edges. In the slit profile we can see the double peak due to the morphology of the object. The P.A. of the slit for this PN is at 31° (crossing the torus in a direction perpendicular to the outflows). One can see the PAHs emission comes from the outer edges of the torus, and the SIV from the inner parts of the torus,

agreeing with the two-colour image (see Figure 4.11).

**M3-38** (PN G356.9+04.4) is a very compact PN with a central torus and emission in a direction perpendicular to this torus. The two-colour image indicates that the PAHs and the ionised material come from similar regions. The source is very compact and barely resolvable, making the interpretation of the spectrum difficult. The slit profile shows the the PAHs seem to be in a slightly more compact region than the ionised region (see Figure 4.12).

In Fig. 4.13 we present on the right side the VISIR spectra of the PNe M1-31, M1-40, and M3-38 where the absolute filter transmission curves for the PAH1, SIV and PAH2 filters were over plotted (dashed pink line). In the left panel we compare the *Spitzer* and VISIR spectra with the emission line and PAH bands identification.

The spectrum of M1-31 shows the PAH features at 11.3 and 11.7 $\mu$ m, and the H<sub>2</sub> line at 9.6 and 12.4 $\mu$ m. The spectrum for the PN M1-40 has the emission line [ArV] meaning that this is a high-excitation PN. This PN has PAHs features at 11.3 and 11.7 $\mu$ m and H<sub>2</sub> is present at 9.6 and 12.4 $\mu$ m. M3-38 is also a high-excitation PN, as its spectrum shows the emission line [ArV]. The spectrum also shows an excess in the continuum that could not be subtracted, this is due to the very broad silicate feature at 10 $\mu$ m. It also presents the H<sub>2</sub> emission line at 9.6 and 12.4 $\mu$ m.

### 4.2.3 Emission lines & PAHs

Using the *Spitzer* spectra analysed in Chapter 3, we measured the peak flux of the emission lines [SIV] centred at 10.51 $\mu$ m, [NeII] centred at 12.81 $\mu$ m and [NeIII] centred at 15.6 $\mu$ m, as well as the integrated flux of the PAH feature at 11.3 $\mu$ m and the H<sub>2</sub> line at 12.4 $\mu$ m. In Table 4.2 we show the values of these lines and the PAH features. In the same Table we present the measured size (in arcseconds) of each PNe and its effective temperature (in K).

Trying to find a diagnostic of the ionisation state of emission-line objects, Groves et al. (2008) found a strong correlation between the [SIV]/[NeII] versus the [NeIII]/[NeII] emission lines ratios. The authors were looking for a ground-based technique to analyse the ionisation state of astronomical objects. They found a very strong correlation be-

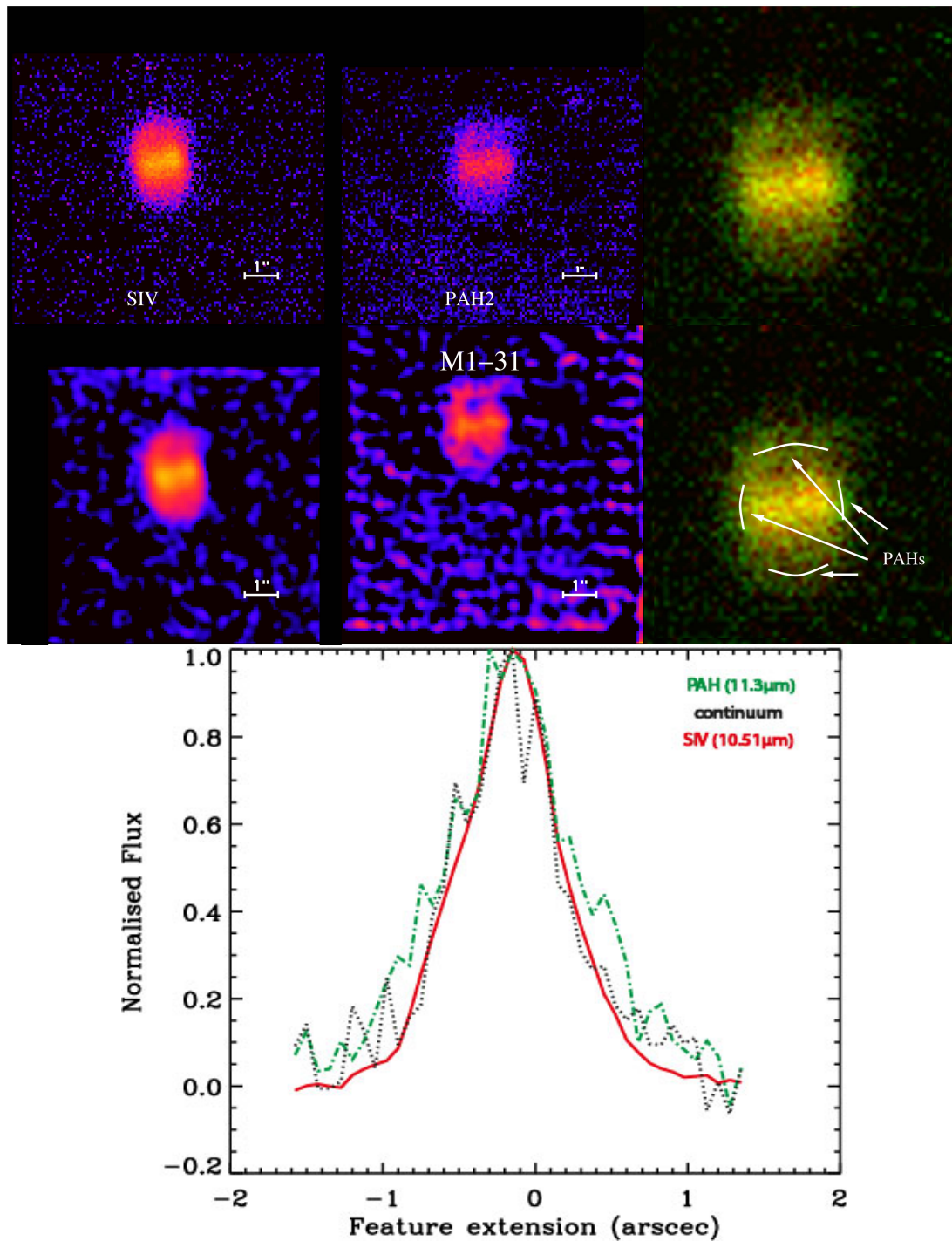


Figure 4.10: The top panel shows the VISIR observations of M1-31 at 10.49 (SIV) and 11.25  $\mu\text{m}$  (PAH2). North is up and East is left. The upper images are the originals, while the lower lines display the images deconvolved using a Richardson-Lucy algorithm. The right part of the figure displays a two-colour image made combining images obtained in the PAH2 filter (green) and SIV (red). The region in yellow contains emission from both filters. On the bottom panel a cut along the VISIR spatially resolved 2D spectra is presented. Emission of the 11.3  $\mu\text{m}$  PAH band (green), the [SIV] emission line (red) and the continuum (black) is shown.

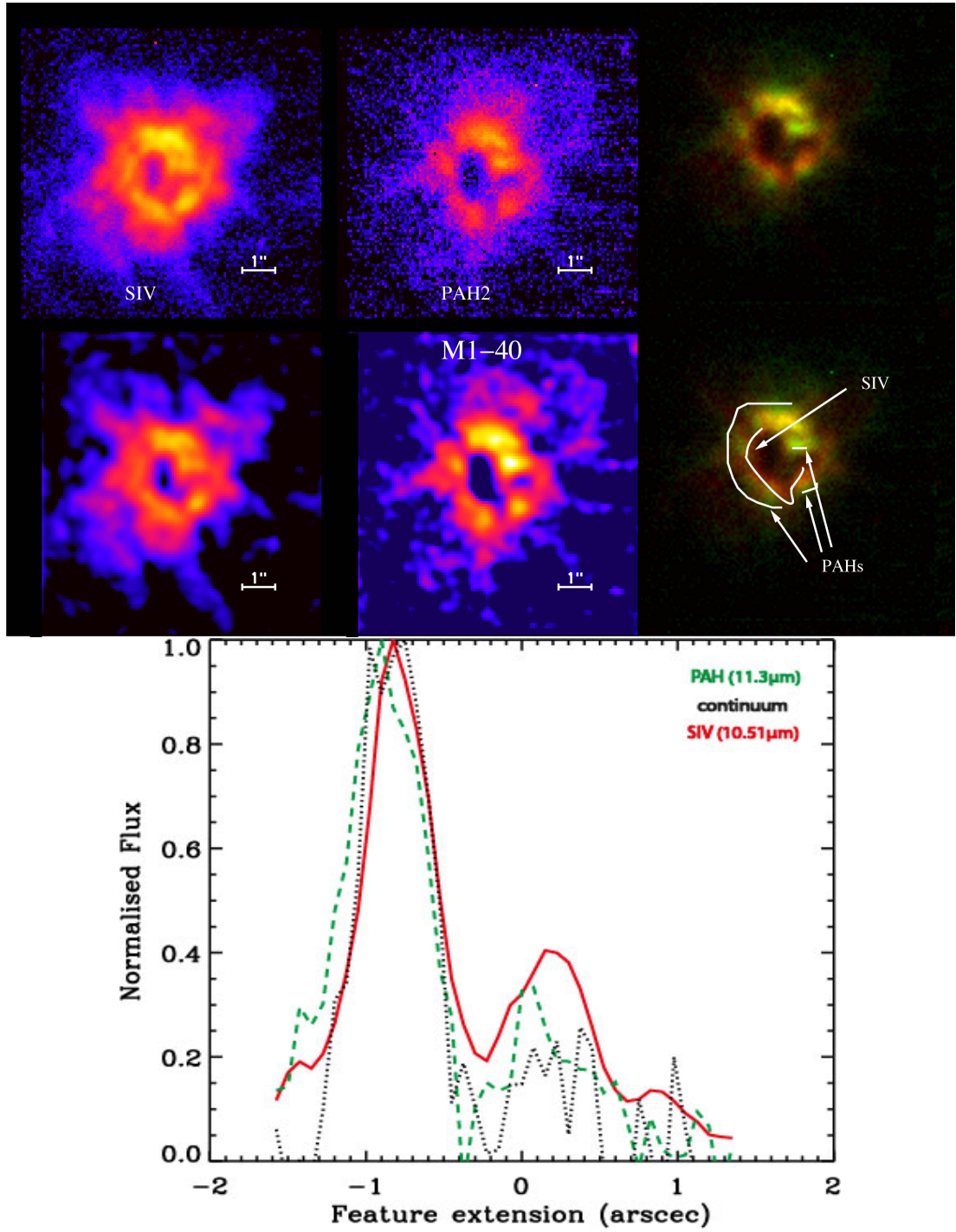


Figure 4.11: Same as Figure 4.10 for M1-40.

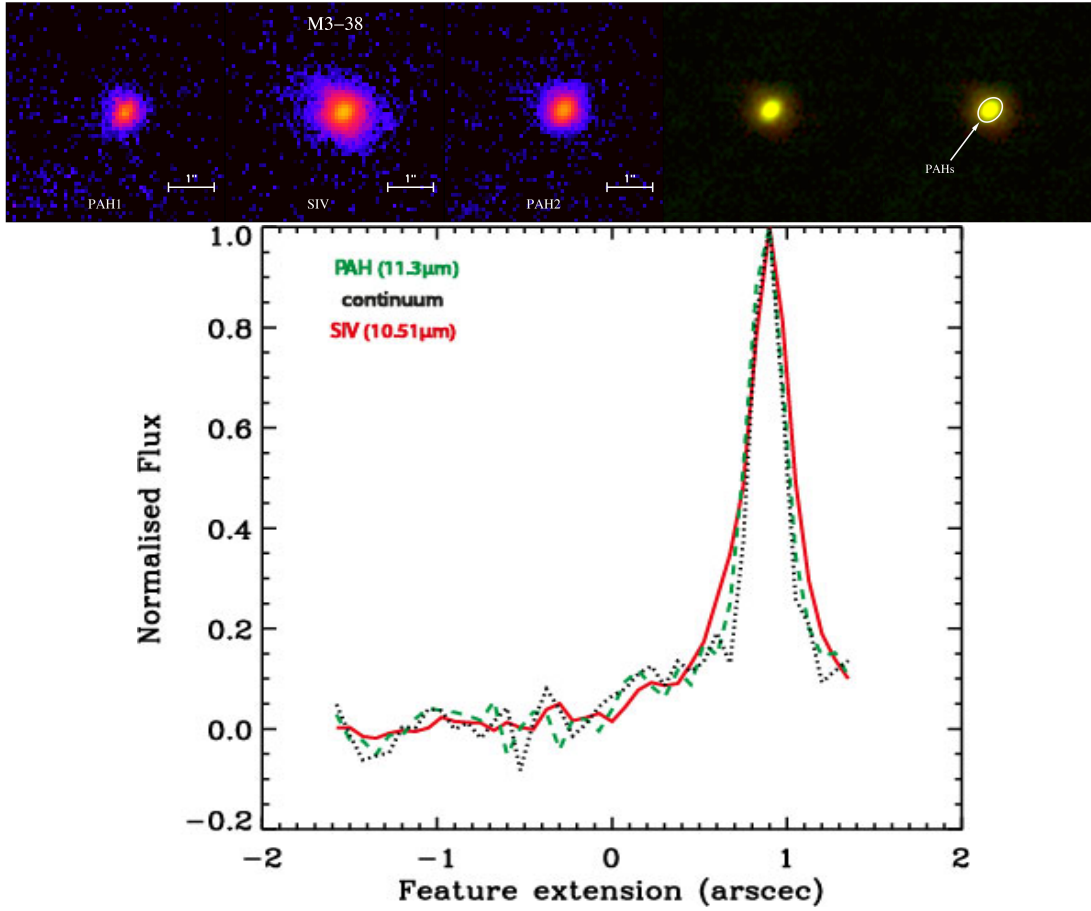


Figure 4.12: The top panel shows the VISIR observations of M3-38 at 8.59 (PAH1), 10.49 (SIV) and 11.25 μm (PAH2). North is up and East is left. The right part of the figure displays a two-colour image made combining images obtained in the PAH2 filter (green) and SIV (red). The region in yellow contains emission from both filters. On the bottom panel a cut along the VISIR spatially resolved 2D spectra is presented. Emission of the 11.3 μm PAH band (green), the [SIV] emission line (red) and the continuum (black) is shown.

tween the [SIV]/[NeII] and [NeIII]/[NeII] ratios, with a linear fit of  $\log([\text{NeIII}]/[\text{NeII}]) = 0.81\log([\text{SIV}]/[\text{NeII}]) + 0.36$ , accurate to a factor of two over four orders of magnitude in the line ratios. This correlation was observed for Galactic and extragalactic HII regions, ultra luminous infra-red galaxies (ULIRGs), active galactic nuclei (AGN), Galactic and extragalactic planetary nebulae (PNe), starburst galaxies and blue compact dwarfs (BCDs).

For the 11 objects presented here, their line intensities were measured and they were plotted in the same manner. The correlation is presented in Figure 4.14. To



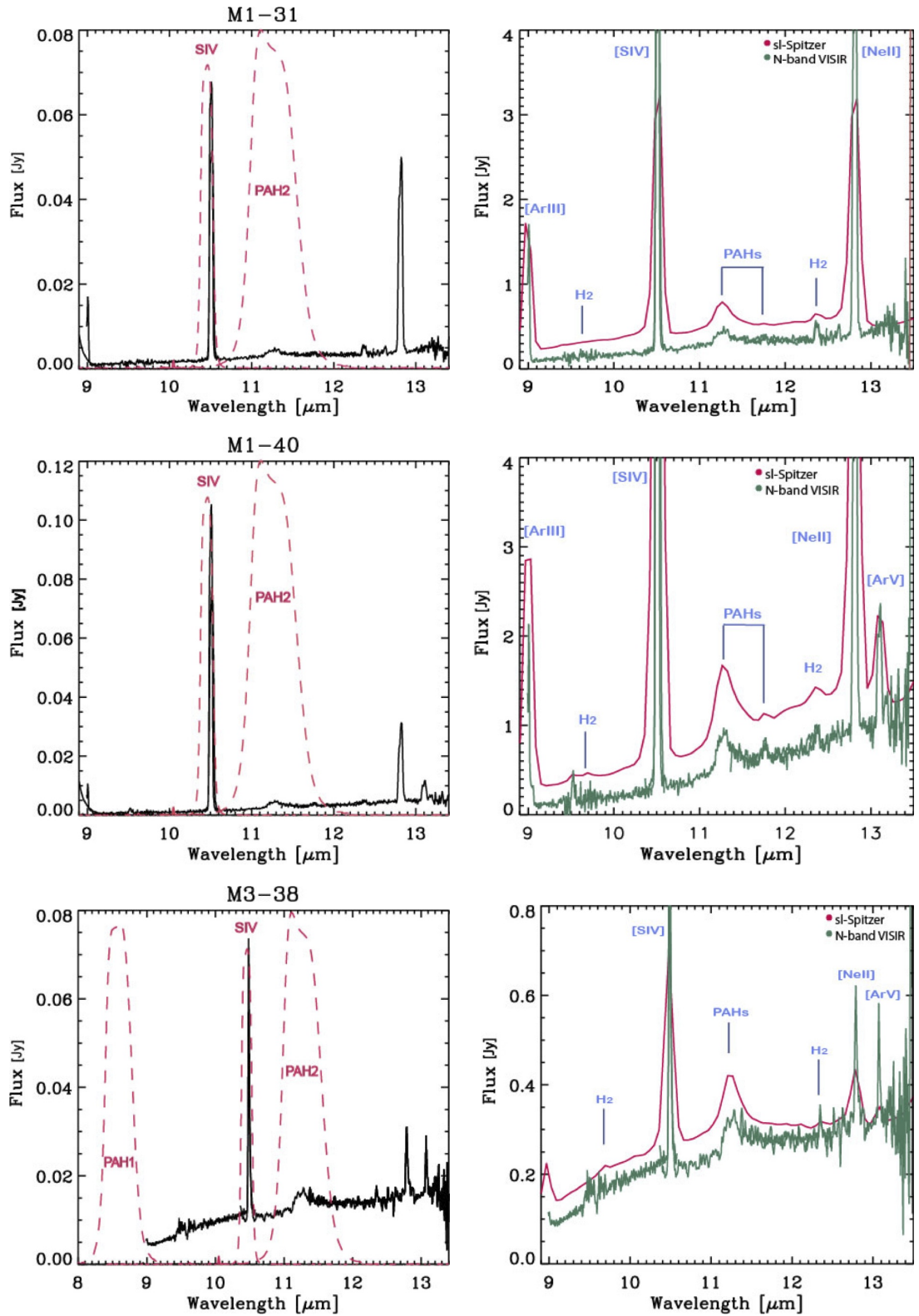


Figure 4.13: The left panel shows the VLT-VISIR N-band spectrum of the PNe M1-31, M1-40 and M3-38 with the absolute filter transmission curves for the PAH1, SIV, and PAH2 filters over plotted in the spectra (dashed pink line). The right panel shows VLT and *Spitzer* spectrum over plotted and the line and PAH bands identification.

Table 4.2: Emission line intensities and integrated flux for the 11.3 $\mu$ m PAH band and the H<sub>2</sub> line (12.4 $\mu$ m). Size of each PN and the effective temperature of its central star is also presented.

Name	PNG Name	11.3 $\mu$ m Jy	H <sub>2</sub> Jy	Size arcsec	$\log([\text{SIV}]$ / $[\text{NeII}]$ )	$\log([\text{NeIII}]$ / $[\text{NeII}]$ )	$\log(T_{\text{eff}})$ K
Cn1-5	002.2 -09.4	1.76	0.15	5	-0.07	0.84	5.04 <sup>1</sup>
M1-25	004.9 +04.9	0.69	0.09	3	-1.39	0.87	4.62 <sup>2</sup>
M1-31	006.4 +02.0	1.33	0.12	1.6	0.14	0.98	4.76 <sup>2</sup>
H1-61	006.5 -03.1	1.48	0.07	1.4	-1.22	0.11	—
M3-15	006.8 +04.1	0.22	0.09	3	0.66	1.35	4.92 <sup>3</sup>
Hb6	007.2 +01.8	0.50	0.33	5	1.03	1.45	4.84 <sup>4</sup>
M1-40	008.3 -01.1	3.63	0.28	3.5	0.35	0.82	5.15 <sup>2</sup>
Th3-4	354.5 +03.3	0.52	0.14	1.2	0.63	1.45	4.68 <sup>3</sup>
M3-38	356.9 +04.4	0.64	0.02	1.1	0.45	1	5.09 <sup>5</sup>
H1-23	357.6 +01.7	0.74	0.03	1.1	-1.61	—	4.26 <sup>2</sup>
H1-40	359.7 -02.6	0.69	0.09	1.2	0.12	0.84	4.85 <sup>6</sup>

<sup>1</sup>Acker & Neiner (2003), <sup>2</sup>Gesicki & Zijlstra (2007), <sup>3</sup>(Gesicki, priv. comm), <sup>4</sup>Phillips (2003),  
<sup>5</sup>(Gesicki, 2012 subm.) <sup>6</sup>Gesicki & Zijlstra (2000)

compare the GBPNe line intensities with all the other emission-line objects, we used the data kindly provided by the first author of the above mentioned paper (see references therein). We find that the  $[\text{SIV}]/[\text{NeII}]$  -  $[\text{NeIII}]/[\text{NeII}]$  correlation also works for PNe in the Galactic Bulge. As predicted by photoionisation theory, higher ionisation leads to higher values for both ratios. Is interesting to mention that even though GBPNe follow the same correlation, they all seem to be dominant in the upper part of the plot, in fact, this is true also for Galactic PNe, although they present the same slope, they seem to have higher values of  $[\text{NeIII}]/[\text{NeII}]$  ratio.

Using the values in Table 4.2 we compared the PAH integrated flux (at 11.3 $\mu$ m) and the H<sub>2</sub> line (at 12.4 $\mu$ m) with the PNe size in arcseconds, the central start effective temperature, and the  $[\text{SIV}]$ ,  $[\text{NeII}]$ ,  $[\text{NeIII}]$  emission lines. Figure 4.15 displays the plot of the size of the PNe versus its H<sub>2</sub> (12.4 $\mu$ m) emission line. In panel (a) we clearly see that the 3 objects away from the trend are the non-GB PNe. In this panel, despite a certain scattering, we can clearly see that the PNe Hb6, M1-40 and Cn1-5 are far from where we find all of the others PNe. This lead us to conclude that they were at a different distance, not in the GB. As Guzman-Ramirez et al. (2011) mentioned, these PNe are found at distances much closer than the GB. According to Phillips & Márquez-Lugo (2011) Hb6 is at a distance of 2.5 kpc, Cn1-5 at 4.5 kpc and M1-40 at



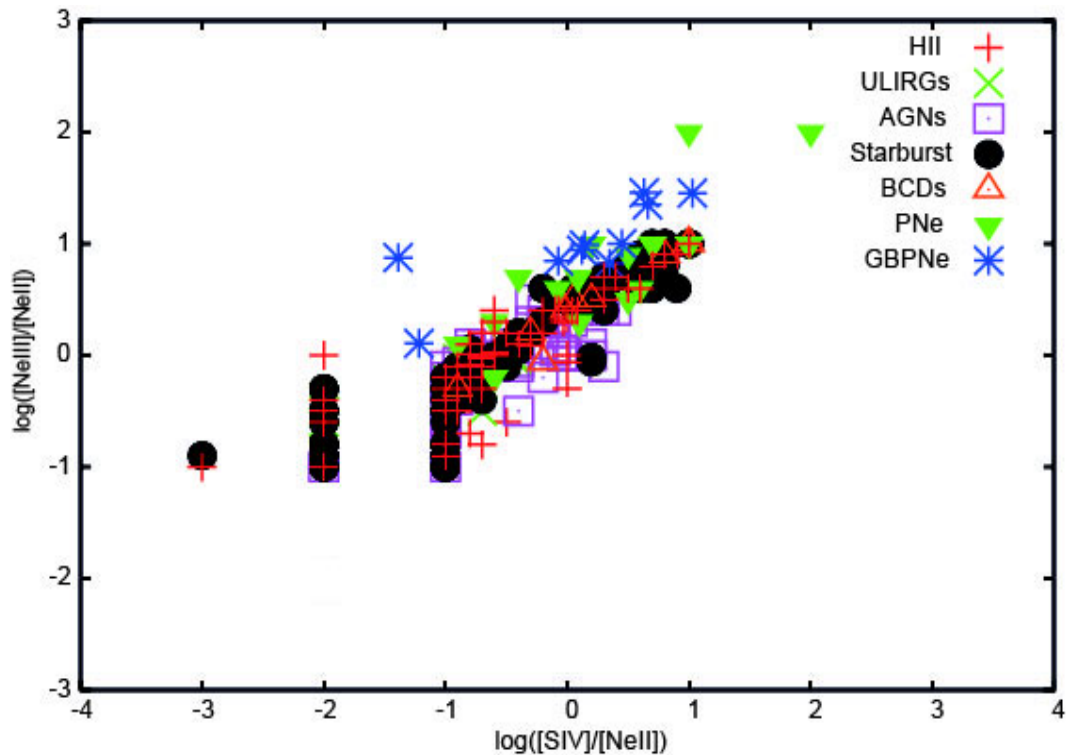


Figure 4.14:  $[SIV]/[NeII]$  -  $[NeIII]/[NeII]$  correlation for Galactic Bulge Planetary Nebulae (GBPNe).

2.8 kpc. We scaled their sizes and surface brightness to the distance to the Bulge (8.5 kpc), so that we could compare their intensities and sizes to the other PNe. Table 4.3 shows the same values presented in table 4.2 but in this case we scaled the PNe Hb6, Cn1-5 and M1-40 to be in the GB. Using these values we plotted Figure 4.15 panel (b). We can see that in general PNe from the GB have stronger  $12.4\mu\text{m}$   $H_2$  emission lines compared to the non-GB ones.

In Figure 4.16 we present different relations. Panel (c) shows the  $H_2$  ( $12.4\mu\text{m}$ ) line versus the  $11.3\mu\text{m}$  PAH band, this panel presents the same effect that Figure 4.15 shows for the non-GBPNe; so in panel (d) we scaled their distances. The main finding is that in general PNe in the GB tend to have higher emission of the  $H_2$  ( $12.4\mu\text{m}$ ) line than the PNe in the Disk.

On the other hand in Figure 4.17 we present the  $11.3\mu\text{m}$  PAH band and the  $H_2$  ( $12.4\mu\text{m}$ ) line versus the effective temperature of the central star. Panel (e) shows

Table 4.3: Same as Table 4.2 but with Hb6, Cn1-5 and M1-40 fluxes and sizes scaled as if they were in the Galactic Bulge (8.5 kpc).

Name	PNG Name	11.3 $\mu$ m Jy	H <sub>2</sub> Jy	Size arcsec	log([SIV] /[NeII])	log([NeIII] /[NeII])	log( $T_{\text{eff}}$ ) K
Cn1-5	002.2 $-09.4$	0.56	0.05	1.78	-0.07	0.84	5.04
M1-25	004.9 $+04.9$	0.69	0.09	3	-1.39	0.87	4.62
M1-31	006.4 $+02.0$	1.33	0.12	1.6	0.14	0.98	4.76
H1-61	006.5 $-03.1$	1.48	0.07	1.4	-1.22	0.11	–
M3-15	006.8 $+04.1$	0.22	0.09	3	0.66	1.35	4.92
Hb6	007.2 $+01.8$	0.05	0.03	1.5	1.03	1.45	4.84
M1-40	008.3 $-01.1$	0.46	0.03	1.9	0.35	0.82	5.15
Th3-4	354.5 $+03.3$	0.52	0.14	1.2	0.63	1.45	4.68
M3-38	356.9 $+04.4$	0.64	0.02	1.1	0.45	1	5.09
H1-23	357.6 $+01.7$	0.74	0.03	1.1	-1.61	–	4.26
H1-40	359.7 $-02.6$	0.69	0.09	1.2	0.12	0.84	4.85

that the PAH emission band at 11.3 $\mu$ m does not correlate with the temperature of the central star, while in the case of panel (f) there is a clear correlation between the H<sub>2</sub> (12.4 $\mu$ m) line and its central star effective temperature. This suggest that the H<sub>2</sub> line is being radiatively excited in all these objects, instead of being excited by shocks. It is also important to notice that we did not observe a correlation between the H<sub>2</sub> line and the PAH band, implying that they come from different regions of the nebula. Because of the correlation found between the temperature of the central star and the H<sub>2</sub> (12.4 $\mu$ m) line, we can infer that the region were the H<sub>2</sub> lies should be close to the central star, while the PAHs reside in an outer region.

### 4.3 Discussion

Our observations confirm the very tight correlation between dual chemistry and the presence of a dense dusty torus in Galactic Bulge PNe, as seen by Guzman-Ramirez et al. (2011). By combining narrow band images centred on PAHs and SIV, it demonstrates that the PAHs are located at the outer edges of the dense dusty tori for the PNe Cn1-5, M1-25, H1-61, Hb6, H1-43, M1-31, and M1-40. For the case of Th3-4, H1-40, and M3-38 they are barely resolved, from the combined images we can see that maybe some of the PAH emission comes from the outer edge of the torus, but is not very clear. Using the spatially resolved spectra, we can see that for the case of M3-38 the PAHs

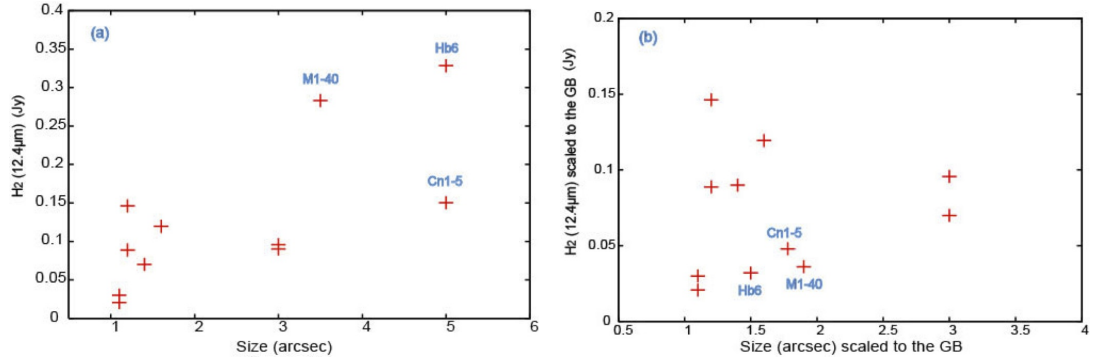


Figure 4.15: Size of the PNe in arcseconds versus its H<sub>2</sub> emission line's strength (12.4μm). In panel (a) we clearly see that the 3 objects away from the trend are the non-GB PNe. In panel (b) we corrected their distances and we can see that in general PNe from the GB have stronger H<sub>2</sub> (12.4μm) emission compared to the non-GB ones.

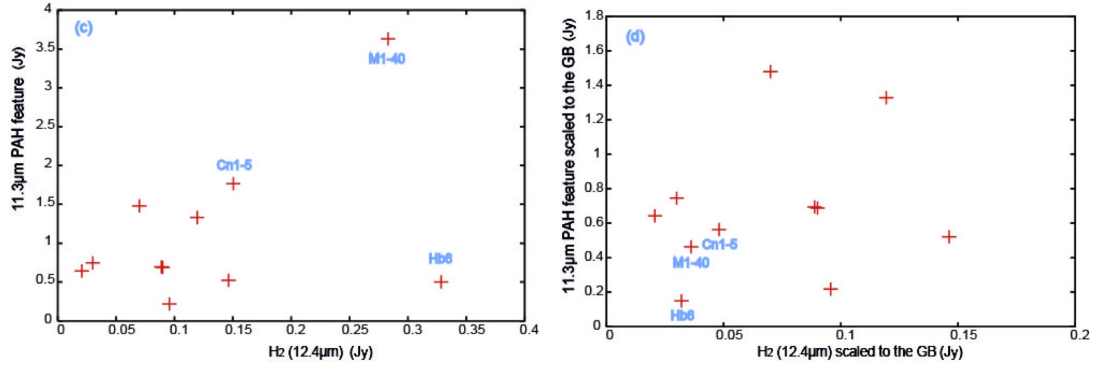


Figure 4.16: Panel (c) shows the H<sub>2</sub> emission line's strength at 12.4μm compared with the 11.3μm PAH band. Panel (d) shows the same emission features but using the scaled values for the PNe Hb6, Cn1-5 and M1-40 as if they were in the GB (8.5 kpc).

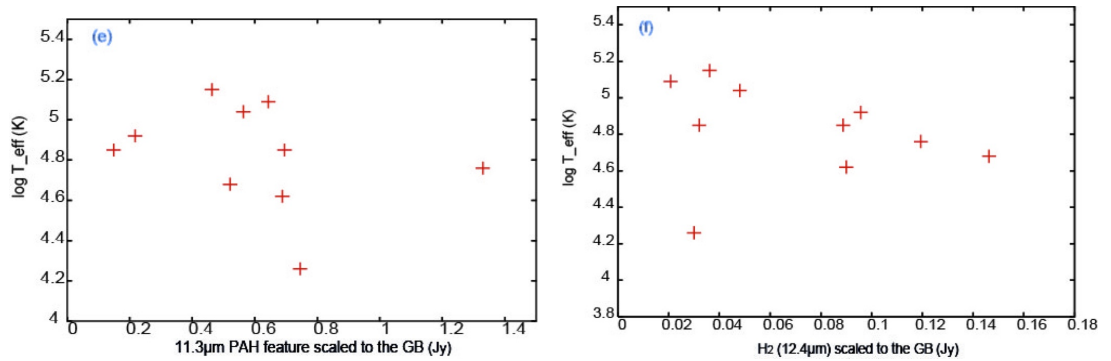


Figure 4.17: Panel (e) shows the integrated flux of the 11.3μm PAH band versus the effective temperature of the central star. No correlation is seen. For panel (f) we present the strength of the H<sub>2</sub> emission line at 12.4μm versus the effective temperature of the central star. A weak correlation is seen where the H<sub>2</sub> decreases when the temperature of the central star increases.

seem to be coming from a more compact region than the ionised region.

For the rest of the sources, the ionised material is present in the inner part of these tori and in outflows perpendicular to it. This is a strong confirmation of the model predictions by Guzman-Ramirez et al. (2011). We predicted that long carbonaceous carbon chains would form on the surface of dense structures when CO was photodissociated by a strong radiation field. Perea-Calderón et al. (2009) proposed that the dual chemistry in GBPNe was due to a recent thermal pulse, which made the star turn from oxygen-rich to carbon-rich. If that was the case we would expect to see carbon-rich material in the inner parts of the nebula. This is only seen in M3-38, for all the other sources, this is clearly not the case.

We have also shown no clear correlation between the  $[\text{SIV}]/[\text{NeII}]$  or  $[\text{NeIII}]/[\text{NeII}]$  emission lines ratio and the  $11.3\mu\text{m}$  PAH feature. This indicates that the ionised material and the PAHs come from different regions, as expected from the model proposed by Guzman-Ramirez et al. (2011).  $\text{H}_2$  has been observed in more than 70 PNe, these observations indicate that the objects have in general a high or moderate N/O abundance ratio and bipolar morphology. The detections include young and evolved PNe, suggesting that the molecule can survive over significant fraction of the lifetime of a PN (Kimura et al. 2012).

A weak correlation is seen where the  $\text{H}_2$  decreases when the temperature of the central star increases meaning that the  $\text{H}_2$  is being radiatively excited in all these PNe and is not excited by shocks. The mixed-chemistry objects we observed in the Galactic bulge are thus distinct from other dual dust chemistry objects such as the Red Rectangle (Waters et al. 1998) and the PNe with WC central stars (Waters et al. 1998). These objects are carbon-rich and display oxygen features from earlier mass-loss, when the star was still oxygen-rich. The oxygen-rich material in these objects is thought to be present in a large disc, while the PAHs should be present in the outflows. The GBPNe are a distinct population of dual dust chemistry objects, as they are still clearly oxygen-rich. The observation we present thus confirms that carbon-rich material, which are the building block of life, can be formed even in oxygen-rich environments.

## 4.4 Conclusions

The main conclusions of this Chapter can be summarised as follows:

- Emission of the PAH features at  $8.6\mu\text{m}$  and  $11.3\mu\text{m}$  and the [SIV] line were imaged using the VISIR instrument in the *VLT*. We find a dense dusty tori in the 11 objects we observed. The ionised [SIV] material is located inside the dusty tori, while the PAHs are present at the outer edges of these tori. This confirms that the PAHs formation is just outside the ionised zone, therefore it must be due to the photodissociation of CO.
- After measuring the line intensities. The [SIV]/[NeII] - [NeIII]/[NeII] correlation is observed for all the PNe, higher ionisation leads to higher values for both ratios.
- Using the *Spitzer* spectra we measure the  $11.3\mu\text{m}$  PAH integrated flux and the  $12.4\mu\text{m}$   $\text{H}_2$  line. Once we compare them, we confirmed that the PNe Cn1-5, M1-40 and Hb6 are not within the Galactic Bulge. This was also observed when we plotted the size of the PNe versus its  $12.4\mu\text{m}$   $\text{H}_2$  emission line.
- The [SIV]/[NeII] emission lines ratio does not correlate with the  $11.3\mu\text{m}$  PAH feature, neither does the [NeIII]/[NeII] emission lines ratio. This shows that they do not come from the same region. We expect the emission lines to come from the inside of the PDR region, where the elements can recombine. While the PAHs are just outside this region, where some UV-photons penetrate and dissociate CO, the free C then will aggregate, leading to the formation of the PAHs.
- A weak correlation is seen where the  $\text{H}_2$  decreases when the temperature of the central star increases. This means that the  $\text{H}_2$  is being radiatively excited in all these PNe and is not excited by shocks.



# Chapter 5

## $^3\text{He}^+$ in PNe



Figure 5.1: The Very Large Array (VLA) located at the National Radio Astronomy Observatory in Socorro, New Mexico, USA (Credit: J. Marvil)

The cosmic abundance of the  $^3\text{He}$  isotope has important implications for many fields of astrophysics. It impacts stellar evolution, chemical evolution and cosmology. The present interstellar  $^3\text{He}$  abundance, as per all the light elements, comes from a combination of Big Bang Nucleosynthesis (BBN) and stellar nucleosynthesis (Wilson & Rood 1994). HII regions are young objects compared with the age of the Galaxy, so they represent the zero-age objects. Their  $^3\text{He}$  abundance is the result of  $13.7 \times 10^9$  yr of Galactic chemical evolution. Any hydrogen-burning zone of a star with a temperature range from  $4 \times 10^6 \text{K}$  to  $7 \times 10^6 \text{K}$  will produce  $^3\text{He}$  via the  $p$ - $p$  chain. Stars with masses  $< 2.5 M_{\odot}$  are the net producers of  $^3\text{He}$ . For these stars,  $p$ - $p$  burning is rapid enough to produce D *in situ*, and enable the production of  $^3\text{He}$  ( $\text{D} + \text{p} \rightarrow ^3\text{He} + \gamma$ ). More massive

stars are dominated by CNO burning; although they do produce some  $^3\text{He}$  via the  $p$ - $p$  chain in their outer zones, it is not enough to offset the  $^3\text{He}$  destruction in the interior zones (Dearborn et al. 1986). Therefore PNe evolved from stars with masses  $<2.5M_{\odot}$  should be substantially enriched in  $^3\text{He}$ . PNe  $^3\text{He}$  abundances are important tests of stellar evolution theory (Bania et al. 2010).

Galli et al. (1995) presented “The  $^3\text{He}$  Problem”. According to standard models of stellar nucleosynthesis there should be a  $^3\text{He}/\text{H}$  abundance gradient in the Galactic Disk with the highest abundances occurring in the highly-processed inner Galaxy, the  $^3\text{He}/\text{H}$  abundance should grow with source metallicity and the protosolar  $^3\text{He}/\text{H}$  value should be less than what is found in the present ISM. After more than 30 years of effort, observations of the abundance of  $^3\text{He}$  in HII regions are inconsistent with these expectations (Rood et al. 1979; Bania et al. 2007).

The abundance of  $^3\text{He}$  can only be derived from measurements of the hyperfine transition of  $^3\text{He}^+$  which has a rest frequency of 8.665 GHz. Detecting  $^3\text{He}^+$  in PNe challenges the sensitivity limits of all existing radio telescopes. The detection of  $^3\text{He}$  in any PN will require  $^3\text{He}/\text{H} \sim 10^{-4}$ , which is the abundance predicted by standard stellar models. After an intense search of  $^3\text{He}$  in PNe, the results are still unclear. Bania et al. (2010) observed a sample of 12 PNe.  $^3\text{He}$  was detected in only 2 of them. NGC 3242 was observed with Effelsberg a 100m dish from the Max Planck Institute for Radio Astronomy (MPIfR) and the NRAO 140-foot telescopes, however the observations are inconsistent with each other, implying a  $^3\text{He}/\text{H}$  abundance that is  $\sim 25\%$  of the  $10^{-4}$  abundance predicted. For the case of J320,  $^3\text{He}$  was detected at a  $4\sigma$  level with the NRAO VLA. Composite  $^3\text{He}^+$  average spectrum for 6 PNe (NGC 6543, NGC 6720, NGC 7009, NGC 7662, and IC 289), using Effelsberg, Arecibo and *GBT* observations, consistently show  $^3\text{He}^+$  emission at the  $\sim 1\text{mK}$  level.

The  $^3\text{He}$  problem is illustrated in Fig. 5.2 (taken from Galli 2004), where the direct predictions are shown by the upper line, while the circles show current measurements. The solar system abundance ratio  $^3\text{He}/\text{H}$  is approximately  $1.6 \times 10^{-5}$ , measured by ULYSSES and GALILEO spacecraft. ISM values of  $^3\text{He}$  measured in HII regions are in the same range. These  $^3\text{He}$  abundances are at least two orders of magnitude different from what it is observed in PNe.



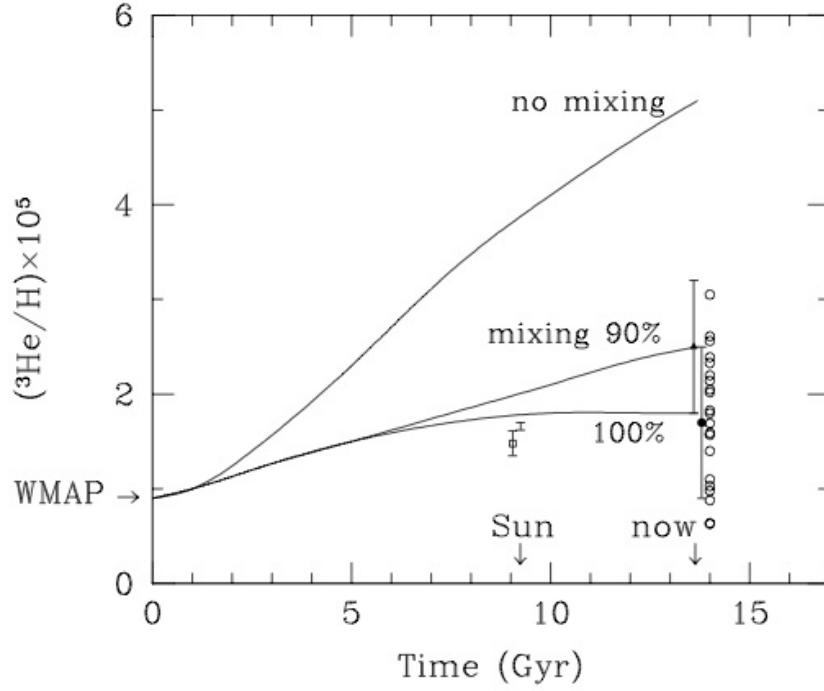


Figure 5.2: Evolution of  $^3\text{He}/\text{H}$  in the solar neighbourhood, computed without extra mixing (upper curve) and with extra mixing in 90% or 100% of stars  $M < 2.5M_{\odot}$  (lower curves). The two arrows indicate the present epoch and the time of formation of the solar system 4.55 Gyr ago. Symbols and error bars show the  $^3\text{He}/\text{H}$  value measured in: meteorites (empty squares); Jupiter's atmosphere (errorbar); the local ionised ISM (filled triangle); the local neutral ISM (filled circle); and the sample of HII regions (empty circles). Figure from Galli (2004)

For the  $^3\text{He}$  problem to be solved, it will require that the vast majority of low-mass stars fail to enrich the ISM. One suggestion to solve this is adding extra mixing in the red giant branch (RGB) stage. This extra mixing adds to the standard first dredge-up to modify the surface abundances. Eggleton et al. (2006) showed that mixing in the surface convective zone of low-mass stars in the RGB phase is extended below the classical convective limit and that it is very fast compared with the nuclear time scales of either the hydrogen-burning shell or the  $^3\text{He}$ -burning shell. Their model estimated that as the H-shell burns outwards the  $^3\text{He}$  will be destroyed. Although low-mass stars do produce considerable amounts of  $^3\text{He}$  on the main sequence phase, this will be all destroyed by the substantially deeper mixing they expect to occur in the red giant

Table 5.1: *VLA* observations log.

Date	PNe	R.A.	DEC	Observed $\nu$ (MHz)
13-12-2009	NGC 6572	18:12:06.36	+06:51:13.01	8665.6132
15-12-2009	IC 418	05:27:28.20	-12:41:50.26	8662.6338
26-12-2009	NGC 7009	21:04:10.87	-11:21:48.25	8666.0602

More observations were obtained for the same sources but due to the lack of calibrators or bad data they were not considered for this analysis.

branch phase. These same results estimate that while 90% of the  ${}^3\text{He}$  is destroyed in  $1\text{M}_{\odot}$  stars, only 40-60% is destroyed in a  $2\text{M}_{\odot}$  star model, depending on the speed of mixing. For stars above  $4\text{M}_{\odot}$ , the bottom of the convective envelope is hot enough for nuclear burning (hot bottom burning). This leaves a mass range around  $2\text{M}_{\odot}$  which is still expected to contribute to  ${}^3\text{He}$  enrichment. Recent observations of Smiljanic et al. (2009) have further complicated the issue: they found a few  $2.5\text{--}4\text{M}_{\odot}$  stars with low  ${}^{12}\text{C}/{}^{13}\text{C}$  ratios, where CN-processed material has been brought from the H-shell to the envelope. Extra mixing mechanisms do not appear to operate in these stars, and additional mechanisms are assumed. Whether these would affect  ${}^3\text{He}$  is not known.

Figure 5.3 shows the predictions. The upper curves show the predicted  ${}^3\text{He}$  abundances in the stellar atmospheres in models without any extra mixing. The vertical-barred section shows the predictions with extra mixing, with the largest reduction at  $1\text{M}_{\odot}$ . The horizontal lines show the cosmological abundance.

## 5.1 Observations using the *VLA*

Motivated by this problem, three planetary nebulae were observed using the NRAO *VLA* in D configuration. Table 5.1 describes the targets and the log of the observations. In Table 5.2 the parameters of the observations are presented.

The data was edited and reduced using the Common Astronomy Software Applications (CASA) package. The calibration technique was slightly different for every object.

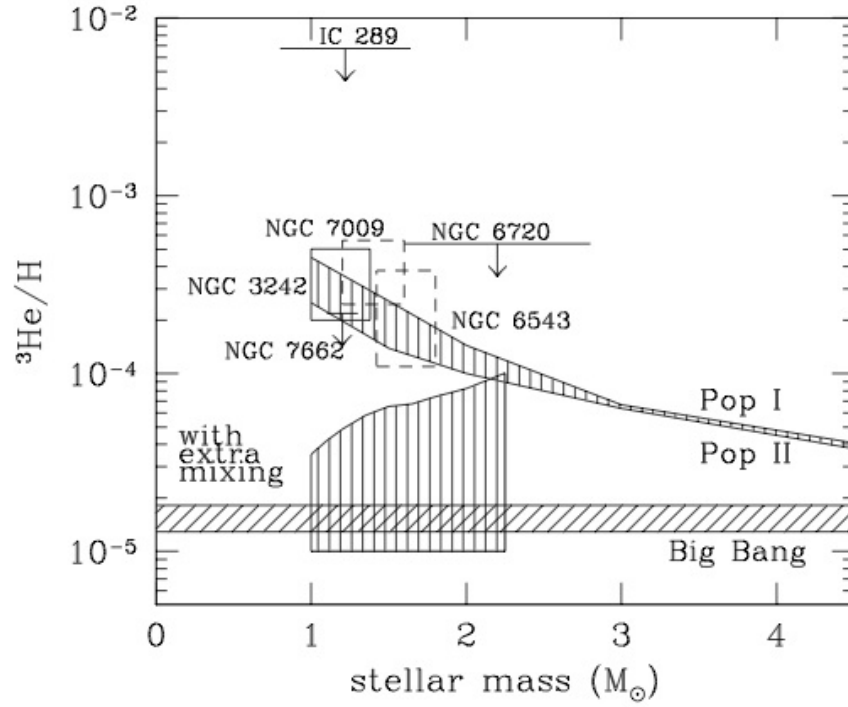


Figure 5.3: Predicted and measured  $^3\text{He}$  abundances in low mass stars. The upper curves show the predicted  $^3\text{He}$  abundances in the stellar atmospheres in models without any extra mixing. The vertical-barred section shows the predictions with extra mixing, with the largest reduction at  $1M_{\odot}$ . The horizontal lines show the cosmological abundance. Figure from Galli (2004)

- **IC 418.** For this source the phase calibrator (B0609-157) was used as a bandpass calibrator. The integration time was averaged every hour to get the bandpass solutions. The calibrator B0137+331 was used to calibrate the intensity scale. The continuum intensity of this source was sufficient to perform the standard self-calibration technique. The self-calibration algorithm was applied to the continuum after the standard phase and bandpass calibration.

Three loops of self-calibration were applied, the first 2 were only in phase, using the complete time interval for the first one and then a solutions interval of 300s. After this a self-calibration in amplitude and phase was applied using 150s for the solutions interval. Once this was obtained these solutions were applied to the line data, the continuum was subtracted and the clean image was created.

Table 5.2: VLA Observations Parameters.

Parameters	IC418	NGC 6572	NGC 7009
Date	Dec, 2009	Dec, 2009	Dec, 2009
Total observed time (hr)	6	6.2	4.6
Configuration	D	D	D
R.A. (J2000)	05:27:28.20	18:12:06.36	21:04:10.8
DEC (J2000)	-12:41:50.26	+06:51:13.01	-11:21:48.25
FWHM of primary beam (arcmin)	5.4	5.4	5.4
Size of the PNe (arcsecs)	$30 \times 6$	$18.9 \times 6.9$	$12 \times 7$
FWHM of synthesised beam (arcsec)	13	9	9
Total bandwidth (MHz)	6.152	6.152	6.152
Number of channels	62	62	62
LSR central velocity ( $\text{kms}^{-1}$ )	62.0	-8.7	-46.6
Spectral resolution ( $\text{kms}^{-1}$ )	3.378	3.378	3.378
Flux density calibrator	0137+331	1331+305	1733-130
Phase calibrator	0609-157	1751+096	2136+006
Line channel rms (mJy/beam)*	1	0.4	0.8
Continuum rms (mJy/beam)	2.0	1.53	1.3

\*Continuum subtracted

- **NGC 6572.** For this source the phase calibrator (B1751+096) was used as a bandpass calibrator; the integration time was averaged every hour to get the bandpass solutions. The calibrator B1331+305 was used to calibrate the intensity scale. The continuum intensity of this source was sufficient to perform the standard self-calibration technique. The self-calibration algorithm was applied after the standard phase and bandpass calibration.

Several loops of self-calibration were applied. The first 4 were only in phase, changing the solutions interval from using the complete integration time up to intervals of 21s. After this a self-calibration in amplitude and phase was applied three times, also changing the intervals of the solutions, starting using 150s. Ultimately the best result for the self-calibration was obtained using a solution interval of 21s in phase only and a solution interval of 30s for the amplitude and phase. Once this was obtained these solutions were applied to the line data, the continuum was subtracted and the clean image was created.

- **NGC 7009.** For this source also the phase calibrator (B2136+006) was used as a bandpass calibrator; the integration time was averaged every hour to get

the bandpass solutions. The same calibrator was used to calibrate the intensity scale. For this data set, a flux calibrator was not observed. But as mentioned in Table 5.1 there were more observations taken for these sources. In the case of NGC 7009 a day before of the observations analysed here a flux calibrator was observed; this was used to calibrate the phase calibrator (same for both observations) and the flux obtained was imposed into the phase calibrator for the data set used here. Therefore the same calibrator was used as a phase, bandpass and amplitude calibrator. For this source a self-calibration technique was applied, but it did not improve the data. Therefore the image and spectrum presented here were made using only the standard calibration. Once this was obtained these solutions were applied to the line data, the continuum was subtracted and the clean image was created.

The continuum images are completely limited by the finite dynamic range of the strong continuum emission and thus are not limited by thermal fluctuations. The line data, after subtraction of the continuum, are limited by thermal noise. This explains why the continuum rms values are larger than the line data values (see Table 5.2).

## 5.2 Results

The result of the observations are presented in Figure 5.4, showing the emission cube with the continuum subtracted. As a reference the emission of the continuum is over plotted in red contours. The spectrum presented on the right of every image is the emission coming from the centre of the contours, where the emission of the line should be. The  $^3\text{He}^+$  line was not detected for any of the objects, therefore only upper limits for the density values were calculated. We used a  $3\sigma$  level of the rms as an upper limit for the three sources.

## 5: $^3\text{He}^+$ IN PNE

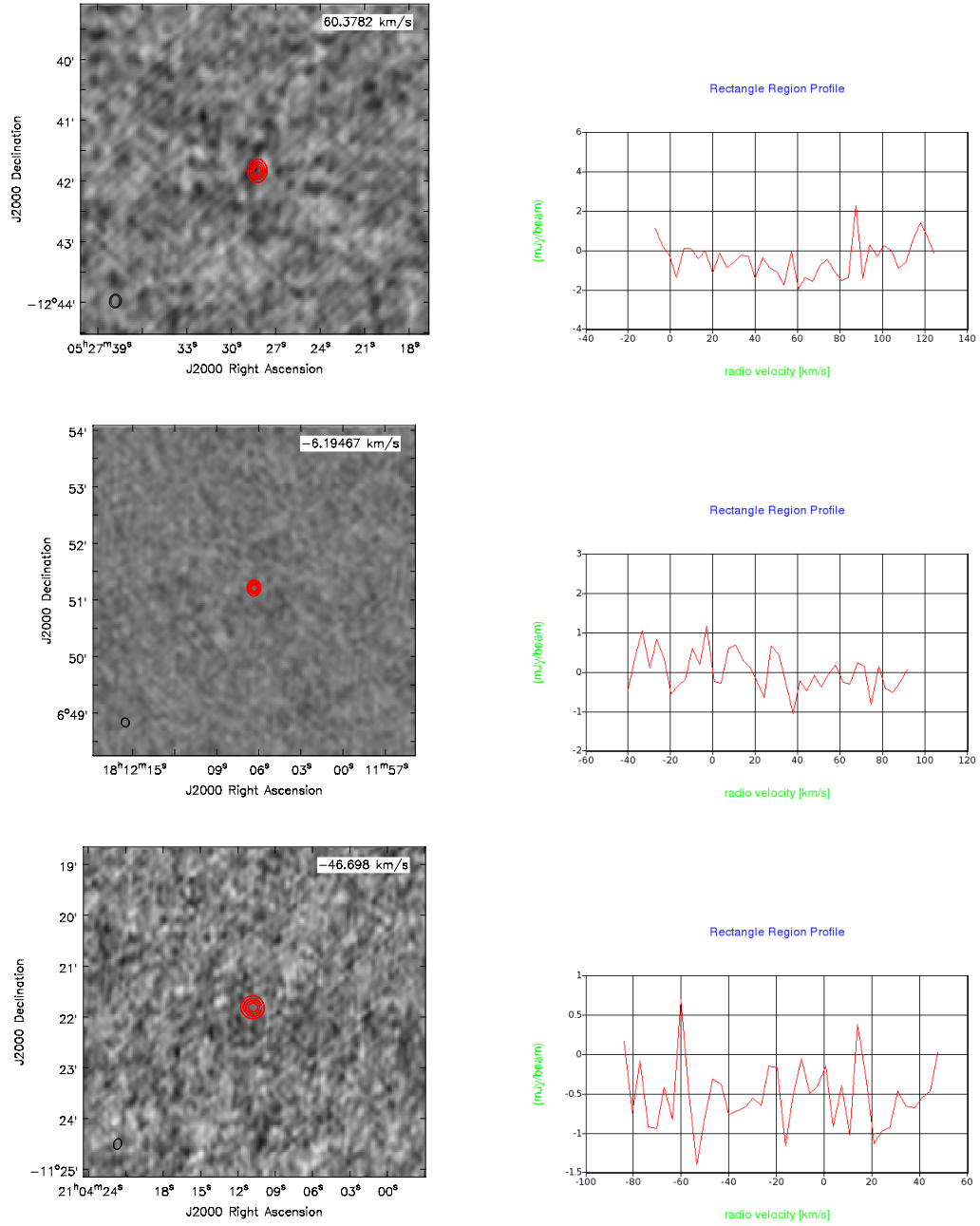


Figure 5.4: VLA observations of IC 418 (top), NGC 6572 (middle), and NGC 7009 (bottom). On the left side the image shows the emission of the source, continuum subtracted. The red contours in the centre show the position of the continuum emission for each source. On the right side is the spectrum of the source. The  $^3\text{He}^+$  line should be at  $62\text{km s}^{-1}$  for IC 418, at  $-8.7\text{km s}^{-1}$  for NGC 6572 and at  $-46.6\text{km s}^{-1}$  for NGC 7009.

The  $^3\text{He}^+$  column density can be obtained using:

$$N(^3\text{He}^+) = \frac{g_l + g_u}{g_u} \frac{8\pi k\nu^2}{hc^3 A_{ul}} \int T_B(v) dv, \quad (5.1)$$

where  $g_u = 1$  is the  $g$  value or magnetic moment of the upper state,  $g_l = 3$  is the  $g$  value or magnetic moment of the lower state,  $A_{ul} = 1.95436 \times 10^{-12} \text{s}^{-1}$  (Gould 1994), and  $T_B(v)$  is the brightness temperature profile of the line. For a gaussian line profile,

$$\int T_B(v) dv = 1/2 \sqrt{\frac{\pi}{\ln 2}} T_B^0 \Delta v, \quad (5.2)$$

where  $T_B^0$  is the brightness temperature at the centre of the line and  $\Delta v$  is the full width at half power. The brightness temperature  $T_B^0$  is related to the observed beam-averaged brightness temperature  $T_L$ , by (Rood et al. 1995)

$$T_B^0 = T_L \frac{\theta_b^2 + \theta_s^2}{\theta_s^2}, \quad (5.3)$$

where  $\theta_b$  and  $\theta_s$  are the beam and source angular radii.

The number of  $^3\text{He}^+$  atoms per unit volume,  $n(^3\text{He}^+)$ , can be obtained by dividing the column density  $N(^3\text{He}^+)$  by the averaged optical path,  $\langle \Delta s \rangle$ , through the source. Representing a PN as a homogeneous sphere of radius  $R = \theta_s D$ , where  $D$  is the distance, the optical path at a position angle  $\theta$  is  $\Delta s(\theta) = 2\sqrt{R^2 - (\theta D)^2}$ , and the optical path averaged on the source results  $\langle \Delta s \rangle = \pi R/2 = \pi \theta_s D/2$ .

The expression for  $n(^3\text{He}^+)$  is then

$$n(^3\text{He}^+) = 8 \sqrt{\frac{\pi}{\ln 2}} \frac{g_l + g_u}{g_u} \frac{k\nu^2}{hc^3 A_{ul}} \frac{\theta_b^2 + \theta_s^2}{D\theta_s^3} T_L \Delta v. \quad (5.4)$$

Rearranging Equation 5.4 and using the numerical values, the final expression can be presented as follows,

$$n(^3\text{He}^+) = 22.7 \left( \frac{T_L}{\text{mK}} \right) \left( \frac{\Delta v}{\text{kms}^{-1}} \right) \left( \frac{D}{\text{kpc}} \right)^{-1} \left( \frac{\theta_s}{''} \right)^{-3} \left( \frac{\theta_b}{41''} \right)^2 \left( 1 + \frac{\theta_s^2}{\theta_b^2} \right) \text{cm}^{-3} \quad (5.5)$$

Table 5.3 shows the calculated  $^3\text{He}^+$  density for the three sources. The distance

Table 5.3: Parameters used to calculate the  ${}^3\text{He}$  abundance in the PNe.

PNe	D (kpc)	M $M_{\odot}$	$T_L$ (mK)	$\Delta v$ ( $\text{kms}^{-1}$ )	$n(\text{H}^+)$ ( $\text{cm}^{-3}$ )	$n({}^3\text{He}^+)$ ( $\text{cm}^{-3}$ )	${}^3\text{He}^+/\text{H}^+$ ( $10^{-3}$ )
IC 418	1.3	1.7	271	30	$3 \times 10^3$	$< 12.99$	$< 4.33$
NGC 6572	1.2	1.0	150	15	$22 \times 10^3$	$< 5.38$	$< 0.24$
NGC 7009	1.2	1.4	465	43	$3.62 \times 10^3$	$< 29.85$	$< 8.24$

values used were 1.2kpc for NGC 7009 (Galli et al. 1997), 1.2kpc for NGC 6572 (Hajian et al. 1995) and 1.3kpc for IC 418 (Guzmán et al. 2009). To calculate the abundance we need to divide by the  $\text{H}^+$  density. The values presented in Table 5.3 were taken from Galli et al. (1997); Balser et al. (2006); Morisset & Georgiev (2009) for NGC 7009, NGC 6572 and IC 418 respectively. The  $\text{H}^+$  abundance is derived from the thermal free-free bremsstrahlung radio continuum emission, and is proportional to the square of the density. To obtain these values, the PNe were modelled using a numerical code, called NEBULA for the case of NGC 6572 and NGC 7009 (Balser et al. 1997). This code calculates the radio recombination line and continuum emission from an ionised plasma. The modelled nebulae are composed solely of hydrogen and helium. The numerical grid uses a three-dimensional Cartesian coordinate system that allows for the specification of a completely arbitrary density and ionisation structure. For the case of IC 418 its  $\text{H}^+$  abundance was modelled using Cloudy\_3D (Morisset 2006).

Once we calculated the  ${}^3\text{He}^+/\text{H}^+$  abundance, we can compare the values with the theoretical calculations and the stellar models predictions. Figure 5.5 shows a revised version of Figure 5.3 using the  ${}^3\text{He}$  abundance in PNe from Balser et al. (1997), the mass estimates from Galli et al. (1997). The curves labelled as Pop I and II show the standard abundance of  ${}^3\text{He}$  taken from Weiss et al. (1996). The blue curve labelled ExtraMix represents the results of stellar nucleosynthesis calculations using deep mixing by Boothroyd & Sackmann (1999). Stellar models using thermohaline mixing are also shown using the light-blue line (R. Stancliffe, priv. communication, 2012). The Big Bang line is the primordial value of  ${}^3\text{He}/\text{H}$ , and the abundances of  ${}^3\text{He}$  for the PNe calculated in this work are also presented. For all the  ${}^3\text{He}^+/\text{H}^+$  values calculated and taken from the literature it has been assumed that  ${}^3\text{He}/\text{H} \simeq {}^3\text{He}^+/\text{H}^+$  (Balser et al. 1994). The three objects analysed here are each marked with a red arrow, indicating



they are upper limits. The horizontal bar at the top of the arrow corresponds to the error in the mass estimates. These estimations agree very well with the estimations made before, and for IC 418 and NGC 7009 the values are consistent with the Population I and II theoretical predictions. For IC 418, this is the first upper limit calculation and it agrees with the stellar model predictions. For NGC 7009 a  ${}^3\text{He}/\text{H}$  abundance of  $< 8.24 \times 10^{-3}$  was calculated. Previous observations of this source gave estimates of  $< (5.8-31) \times 10^{-4}$ . In the case of NGC 6572 the abundance calculated is lower than the theoretical models predict. An upper limit for this PNe was calculated by Balser et al. (2006): the value they estimate is  $< 10^{-3}$ . We found an upper limit of  $< 2.4 \times 10^{-4}$ . As mentioned before for all the cases we assumed that  ${}^3\text{He}^+/\text{H}^+ = {}^3\text{He}/\text{H}$ , this implies that all the He inside the  $\text{H}^+$  region is singly ionised, but if the nebula were to have some ionisation structure (some He is either neutral or doubly ionised) then the  ${}^3\text{He}^+$  intensity will require higher  ${}^3\text{He}/\text{H}$  abundances in order to reproduce the observed  ${}^3\text{He}^+$  intensity. It is possible that NGC 6572 has such an ionisation structure, if this is the case then we expect that its  ${}^3\text{He}^+/\text{H}^+$  abundance to be higher.

In the same Figure 5.5 the models for extra mixing processes is also presented. The most extensive calculations are those from Boothroyd & Sackmann (1999). The detailed calculations indicate that the mass dependence of the destruction of  ${}^3\text{He}$  is very strong, and the resulting abundance decreases sharply for masses below  $\sim 2.5 M_{\odot}$ . It is clearly seen in this Figure that the observed PNe have not suffered any depletion. Almost all of the PNe are more than a factor of  $\sim 2$  above the non-standard curve (the Extramix predictions). To conclude, these upper limit observations do not support the conjecture of enhanced  ${}^3\text{He}$  depletion in all low-mass stars.

Newer stellar models from Lagarde et al. (2012) analyse the evolution of  ${}^3\text{He}$  and its destruction due to the effects of thermohaline instability and rotation-induced mixing. Their models show that thermohaline mixing can induce significant depletion of  ${}^3\text{He}$  in low- and intermediate-mass stars. Although these stars remain the net producers of  ${}^3\text{He}$ , their contribution to the Galactic evolution of this element is highly reduced compared to classical theory. It is claimed in their paper that thermohaline mixing is the only physical mechanism known so far able to solve the so-called “The  ${}^3\text{He}$  Problem”. Importantly, its inhibition by a fossil magnetic field in red giant stars that

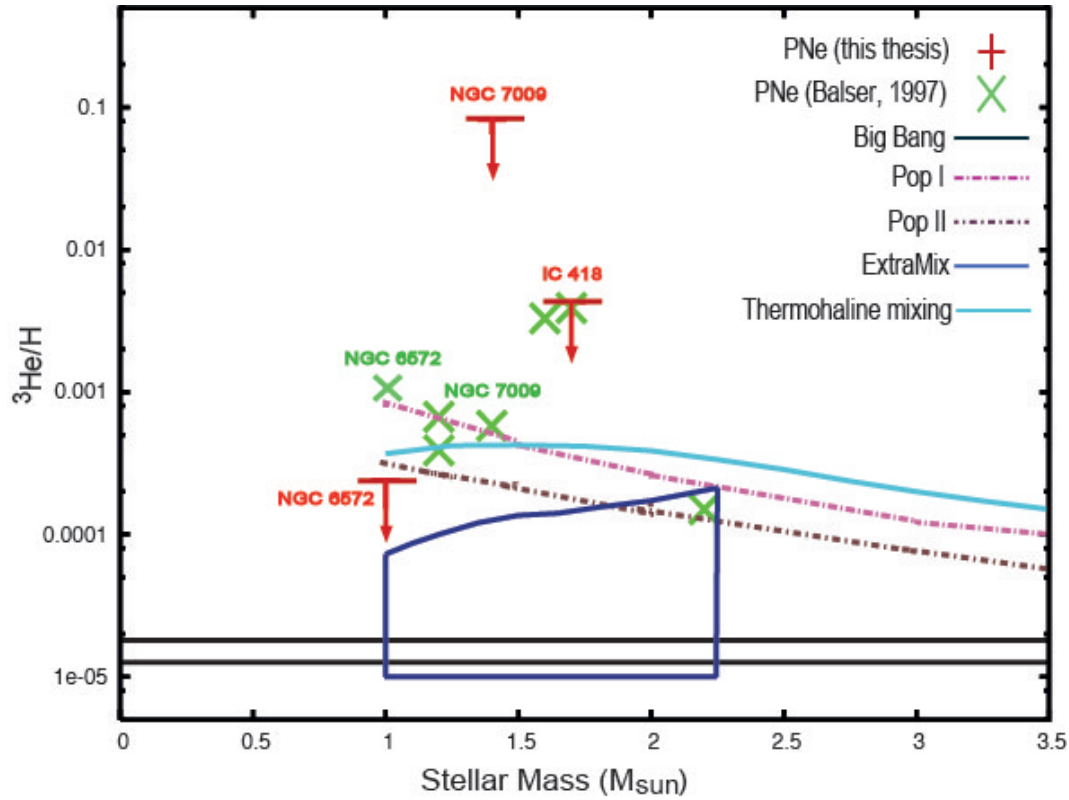


Figure 5.5: Abundance of  $^3\text{He}/\text{H}$  versus main-sequence masses. The green symbols represent the sample of PNe from Balser et al. (1997), using the mass estimates from Galli et al. (1997). The curves as Pop I and II show the standard abundance of  $^3\text{He}$  taken from Weiss et al. (1996). The blue curve labelled ExtraMix represents the results of stellar nucleosynthesis calculations using deep mixing by Boothroyd & Sackmann (1999). The light-blue curve represent the stellar models using thermohaline mixing (R. Stancliffe, priv. communication, 2012). The Big Bang line is the primordial value of  $^3\text{He}/\text{H}$ .

are descendants of Ap stars does reconcile the measurements of  $^3\text{He}/\text{H}$  in Galactic HII regions with high values of  $^3\text{He}$  in a few PNe. These stellar models using thermohaline mixing are also represented in Figure 5.5 (light-blue line). These models were computed only for stars at the first thermal pulse, with masses between  $1\text{--}3.5M_{\odot}$  in steps of  $0.25M_{\odot}$ , and for  $Z=0.02$  (R. Stancliffe, priv. communication, 2012).

## 5.3 Conclusions

Upper-limits for the  $^3\text{He}$  abundance of three PNe has been estimated using the  $^3\text{He}^+$  emission line observed with the *VLA* towards the PNe IC 418, NGC 6572 and NGC 7009. These results give broad support to the hypothesis that  $^3\text{H}$  is not destroyed in stars and survives the PN phase.

In total two strong detections and six upper limits of the  $^3\text{He}$  abundance on PNe have been reported in the literature, including this work, and are consistent with standard stellar evolution calculations. They are more than an order of magnitude larger than what is found in any HII region (Balser et al. 1997), the local ISM (Gloeckler & Geiss 1996) or the proto-solar system (Geiss 1993). For the values obtained in PNe the  $^3\text{He}$  abundances are consistent with the standard models that  $^3\text{He}$  is produced in significant quantities by stars of  $1\text{--}2M_{\odot}$  and that PNe with progenitors in that mass range should have  $^3\text{He}/\text{H} \sim \text{few} \times 10^{-4}$ . This means that there is at least some stellar production of  $^3\text{He}$ . In order to understand the chemical evolution of the Galaxy, it is crucial we understand the contribution of PNe to the  $^3\text{He}$  abundance. Chemical evolution models started including only processed primordial deuterium (D) as a source of  $^3\text{He}$  synthesis in low mass stars. But even without including any stellar production of  $^3\text{He}$ , these models showed that  $^3\text{He}/\text{H}$  increases with time (Vangioni-Flam et al. 1994).

Because the abundance of  $^3\text{He}$  in HII regions, the ISM and the proto-solar system is much lower than predicted, new chemical models were proposed. These models include non convective mixing processes that either prevent the buildup of  $^3\text{He}$  on the main-sequence or destroys  $^3\text{He}$  along the upper red giant branch (Boothroyd & Sackmann 1999; Lagarde et al. 2012). Confronting these new models that are consistent with HII regions, ISM and proto-solar  $^3\text{He}$  abundance are the observations of PNe.

The resulting evolution of  $^3\text{He}$  is only consistent with the values determined in pre-solar material and the ISM if more than 96% of the whole population of stars with mass below  $\sim 2.5M_{\odot}$  have undergone enhanced  $^3\text{He}$  depletion. This means that unless the sample of PNe observed so far represent the 4% of stars that can produce  $^3\text{He}$ , leading to the  $^3\text{He}$  abundances observed (which is unlikely), the solution to “The  $^3\text{He}$  Problem” lies elsewhere.



# Chapter 6

## Conclusions

This thesis intends to analyse some of the most important issues in the planetary nebulae field. Once we understood this issues, a lot of effort was put into trying to solve some of them. There were mainly three mysteries in PNe tackled in this thesis and they are presented in the following list:

- **The missing PNe.**

Newly confirmed PNe were found using the INT Photometric H $\alpha$  Survey (IPHAS). Using the 1.9m telescope at SAAO and the 2.1m telescope at KPNO we were able to spectroscopically observe 100 targets. To classify each object, their spectra was carefully analysed. The H $\alpha$  image helped to differentiate between some objects; also diagnostic diagrams were used. We found 32 new planetary nebulae and 13 possible planetary nebulae. Out of a 100 targets that makes a 45% success rate. From these new PNe, the IPHAS survey in the region observed for this thesis ( $16 < l < 23$ hrs and  $|b| < 5^\circ$ ) was able to find the obscured population of PNe in the inner parts of the centre of the Galaxy. The dominant morphology of these new and possible PNe was found to be round. The round PNe represents 62% of all of them. Also as predicted, the [OIII] line for most of our true PNe targets show brighter [OIII] than HII regions. This line is present in 35 (out of 45) of the PNe, where the line intensity ranges from  $2 \times 10^{-16}$  to  $7 \times 10^{-12}$  erg/cm<sup>2</sup>/s/Å. Using a Gaussian fit to the Galactic distribution of PNe in the range of  $16 < l < 23$ hrs and  $|b| < 5^\circ$ , we estimated the missing population of PNe population. We

contributed a 21.3% of the missing population of PNe. A second gaussian fit was made adding the new PNe found in this thesis. The missing PNe are still obscured or too faint to be detected ( $b=0,1$ ) and the number of PNe missing in the same  $l$  and  $b$  is 180.

- **Formation of C-rich molecules in O-rich PNe.**

The mixed-chemistry phenomenon in Galactic Bulge PNe seems to be well correlated with the PNe morphology. A strong correlation was found between strength of the PAH bands and morphology, in particular, the presence of a massive torus. A chemical analysis of the PAH formation in an oxygen-rich environment was studied using the Meudon 2006 PDR chemistry code. Although the model does not include PAH formation, it shows that large hydrocarbons can form in oxygen-rich environments and that their abundances can be relatively large in moderately shielded regions. The model predicts two layers, one at  $A_V \sim 1.5$  where small hydrocarbons form from reactions with  $C^+$ , and one at  $A_V \sim 4$ , where larger chains (and by implication, PAHs) form from reactions with neutral, atomic carbon.

After these findings, a sample of PNe were selected to be observed with the *VLT* imager and spectrometer for mid-infrared (VISIR). The emission of the PAHs in these 11 PNe were spatially resolved. In almost all the cases the PAH emissions come from a dense/compact region (torus) in the centre of the PNe. This confirms that the PAHs formation must be due to the photodissociation of CO.

The line intensities of [SIV], [NeII] and [NeIII] were measured. The [SIV]/[NeII] emission line ratio does not correlate with the PAH (11.3 $\mu$ m) feature, neither does the [NeIII]/[NeII] emission lines ratio. This indicates that they do not come from the same region. We expect the emission lines to come from the inside of the PDR region, where the elements can recombine, while the PAHs are just outside this region, where some UV-photons penetrate and dissociate CO, the free C then will aggregate, leading to the formation of the PAHs.

We do not find a correlation between the  $H_2$  and the PAHs, indicating that

they come from the different regions. Also there was no correlation between the 11.3 $\mu\text{m}$  PAH feature and the temperature of the central star. On the contrary a strong correlation between the 12.4 $\mu\text{m}$   $\text{H}_2$  line and the temperature of the central star was found. The hotter the star, the less  $\text{H}_2$  is detected. This suggests that the  $\text{H}_2$  is being radiatively excited in all these PNe and is not excited by shocks.

- **“The  $^3\text{He}$  Problem”.**

Although better constraints were found for the upper-limits of the abundance of  $^3\text{He}$  in PNe, “The  $^3\text{He}$  Problem” is still an unsolved problem. Observations of the  $^3\text{He}^+$  emission line using the *VLA* towards the PNe IC 418, NGC 6572 and NGC 7009 were used to obtain upper-limits for their  $^3\text{He}$  abundance. For the values obtained in PNe it looks like the  $^3\text{He}$  abundances are consistent with the standard models, in which  $^3\text{He}$  is produced in significant quantities by stars of 1–2 $M_\odot$  and that PNe with progenitors in that mass range should have  $^3\text{He}/\text{H} \sim \text{few} \times 10^{-4}$ . To understand the chemical evolution of the Galaxy, we need to understand the contribution of PNe in the  $^3\text{He}$  abundance. Because the abundance of  $^3\text{He}$  in HII regions, the ISM and the proto-solar system is much lower than what is predicted, new chemical models were proposed. The resulting evolution of  $^3\text{He}$  can be consistent with the values determined in pre-solar material and the ISM if 96% of the population of stars with mass below  $\sim 2.5M_\odot$  has undergone enhanced  $^3\text{He}$  depletion. This implies that unless the combined sample of PNe that has been observed so far is very atypical, the solution to the “The  $^3\text{He}$  Problem” lies elsewhere.

## *6: CONCLUSIONS*



# Chapter 7

## Afterthoughts

Surveys like IPHAS were intended to find the missing population of PNe in our Galaxy. As it has been shown in this thesis, this survey has found some of the missing PNe. Surveys like this can be used to compare the population of PNe in the Galactic Disk with the one in the Galactic Bulge.

From what was found in this thesis, from the sample of PNe analysed towards the Galactic Bulge 70% of them have bipolar/multipolar morphologies, in contrast with what is found in PNe in the Galactic Disk, where no more than 20% of them are found to be bipolar. This discrepancy is not well understood. It could be due to external causes, such as the different environments, metallicity, density of stars. Or internal causes may play a role: morphology, binarity, chemical evolution. Understanding the population of the Bulge would help us to understand its formation, and the formation of our Galaxy.

Comparing new observations of PNe in other satellite galaxies like the LMC, SMC and the Sagittarius Dwarf Spheroidal Galaxy would also be very interesting, and using telescopes like the *HST*, the *VLT* and *ALMA*, we will be able to analyse the relationship between morphology and PAH formation in all of the PNe and compare their different environments. Chemical models would be tested in other galaxies with similar metallicity and age as the Bulge and analyse their similarities (or differences). This will give

## 7: *AFTERTHOUGHTS*

us a better understanding of the physical and chemical processes occurring in these objects. If the CO photodissociation occurring in the very dense tori of these objects is the main PAH formation mechanism, then this will constrain the PAH formation models.

It has been claimed that PAHs may be the most abundant molecules in the interstellar medium (ISM) after  $\text{H}_2$  and CO (Léger et al. 1989a). However, the question of their existence is still open and it is therefore of great interest to study the processes contributing to their formation and growth in astrophysical media. Allain et al. (1997) calculated that the PAH formation rate in circumstellar envelopes is large enough to support the hypothesis that PAHs could constitute the first step in the formation of dust grains. Dust particles have a crucial role in circumstellar envelopes because they partly drive the stellar wind and therefore influence the structure of the shells where PAHs form.

PAHs have been observed in a large variety of astronomical environments including the diffuse ISM, star forming regions, reflection nebulae, T-Tauri stars, Herbig AeBe stars, AGB stars, post-AGB stars, planetary nebulae, WR stars, novae and supernovae remnants. More over, they are wide spread in various types of galaxies up to redshifts of  $\sim 3$  (spectroscopically) and  $\sim 6$  (photometrically). A remarkable 10-15% of the total power output of galaxies is emitted in the PAH bands. Characterising the PAH formation and growth processes is a crucial task to understand all these astronomical objects.

For the “The  $^3\text{He}$  Problem” better observations are needed. The only way to constraint the models is if we observe more PNe and we can determine the  $^3\text{He}$  abundance for a big enough sample of PNe with masses between  $1\text{--}2M_\odot$ . If we are able to show that most of the PNe between this mass range do produce  $^3\text{He}$ , as it is what it has been observed so far, then we need to think on better mechanisms of destroying or depleting this element before it reaches the ISM.

# Appendix A

## IPHAS object classification

Spectroscopic follow-up for the IPHAS candidates. The next set of images shows on the left side, the  $H\alpha$  emission image taken from the IPHAS finder charts<sup>1</sup>, SuperCOSMOS H-alpha Survey<sup>2</sup> and the STScI Digitized Sky Survey<sup>3</sup>. The corresponding spectrum of each source is presented. The PN candidates were observed using the following telescopes:

- The 2.1-m telescope of the Kitt Peak National Observatory (KPNO) which is part of the National Optical Astronomy Observatory (NOAO). The 2.1-m GoldCam spectrometer offers resolutions from 300 to 4500 using a variety of gratings. The settings for these observations used the grating 240, centred at 5500Å that has a coverage of 3040Å with a dispersion of 1.52 (Å/pixel) giving us a resolution of 4.1Å.
- The 1.9m telescope in the South African Astronomical Observatory (SAAO), part of the national centre for optical and infrared astronomy in South Africa. The settings for these observations used two gratings; (1) Grating 7, has a dispersion of 210Å/mm, a coverage of 4200Å with a blaze of 4600Å giving us a resolution of 5Å. (2) Grating 5, has a dispersion of 50Å/mm, a coverage of 800Å with a blaze

---

<sup>1</sup>[http://apm3.ast.cam.ac.uk/iphas\\_finder.html](http://apm3.ast.cam.ac.uk/iphas_finder.html)

<sup>2</sup><http://www-wfau.roe.ac.uk/sss/halpha/habatchfile.html>

<sup>3</sup>[http://archive.stsci.edu/cgi-bin/dss\\_form](http://archive.stsci.edu/cgi-bin/dss_form)

## A: IPHAS OBJECT CLASSIFICATION

of  $6800\text{\AA}$  giving us a resolution of  $1\text{\AA}$ .

They are classified as it is shown in Table 2.7. True PN are presented first, then possible PN, HII regions, Strömgren spheres, SNRs and unclear objects at the end. They all conserved their PNe candidate name, therefore they are labeled PN and then their coordinates.

### A.1 True PNe

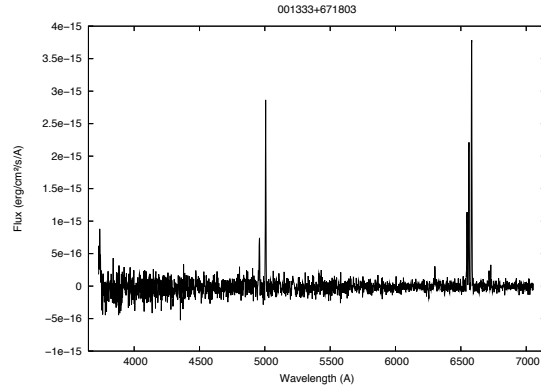


Figure A.1: PN 00:13:33 +67:18:03

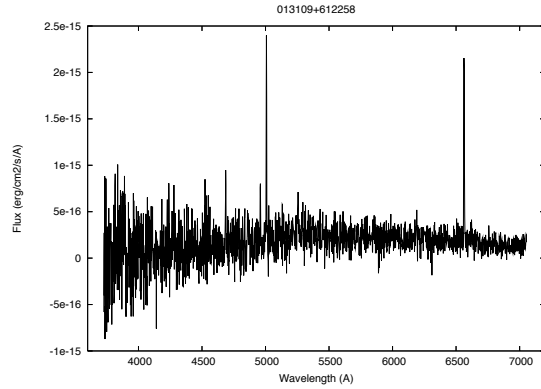
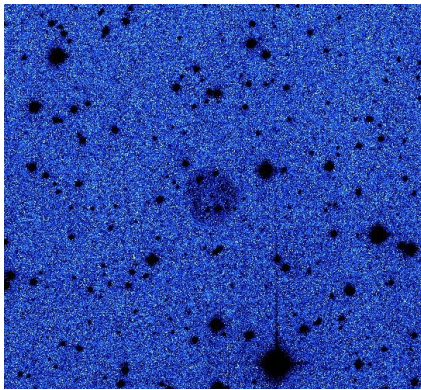


Figure A.2: PN 01:31:09 +61:22:58

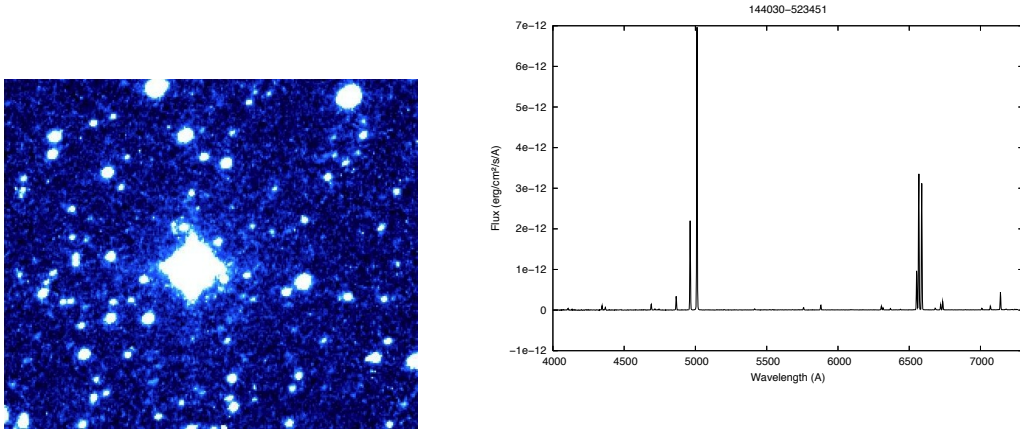


Figure A.3: PN 14:40:30 -52:34:51

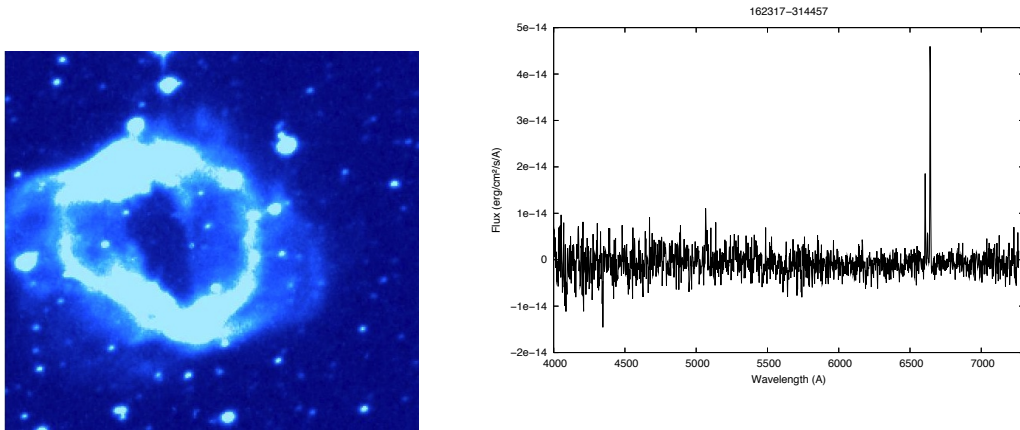


Figure A.4: PN 16:23:17 -31:44:57

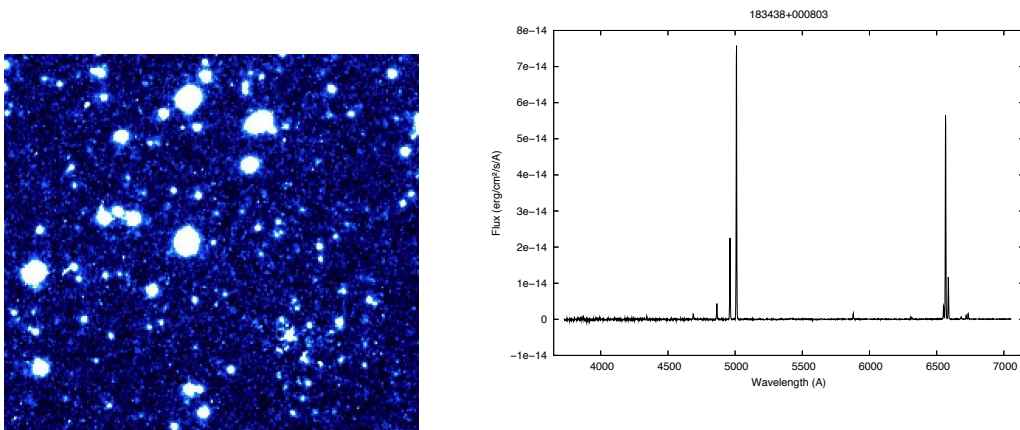


Figure A.5: PN 18:34:38 +00:08:03

## A: IPHAS OBJECT CLASSIFICATION

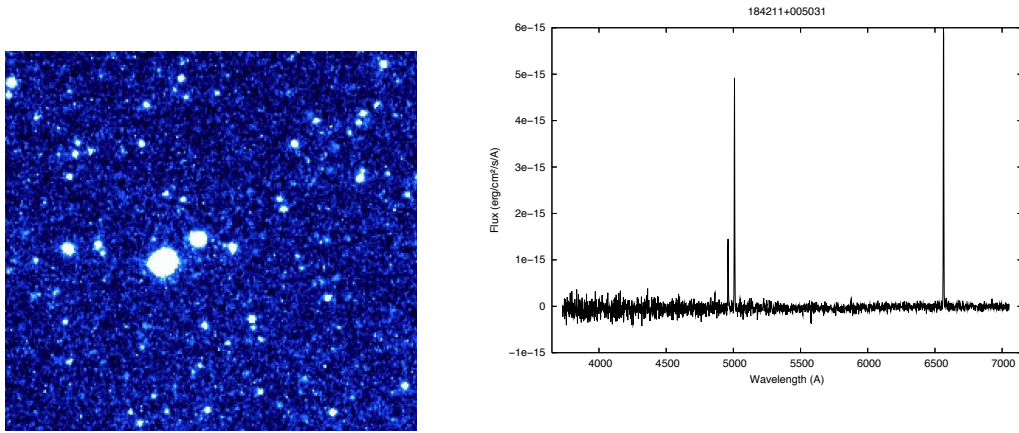


Figure A.6: PN 18:42:11 +00:50:31

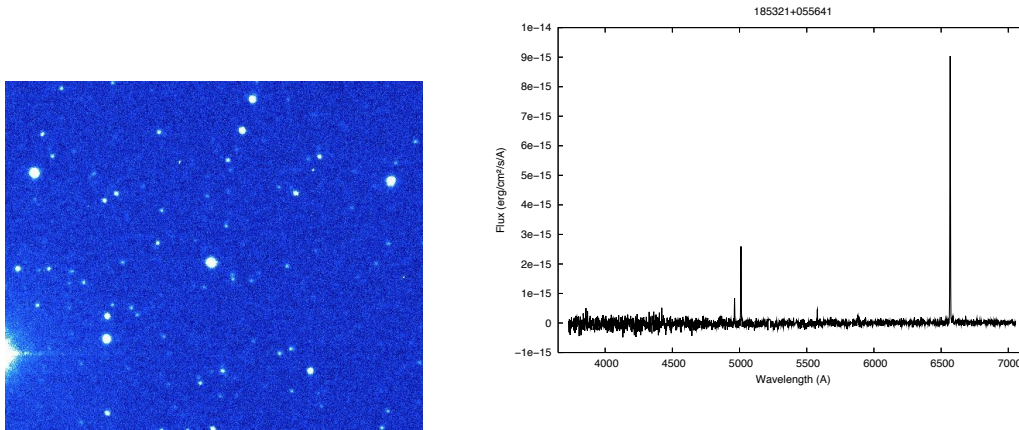


Figure A.7: PN 18:53:21 +05:56:41

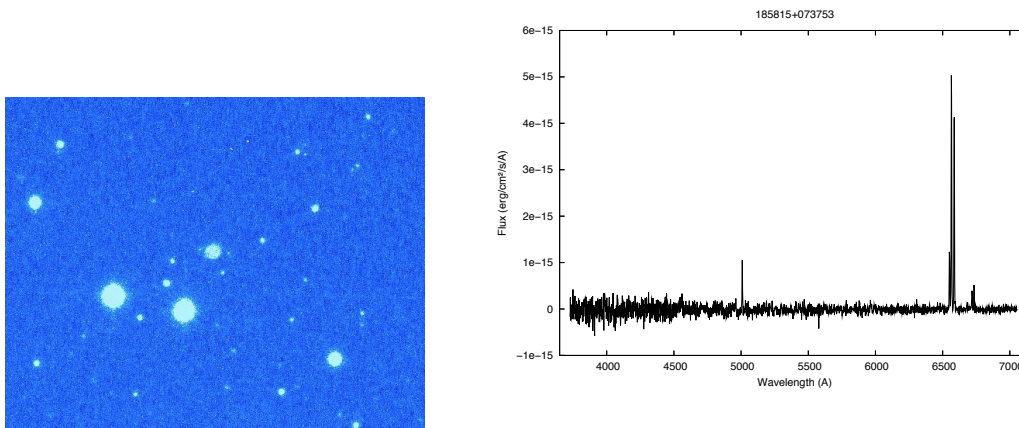


Figure A.8: PN 18:58:15 +07:37:53



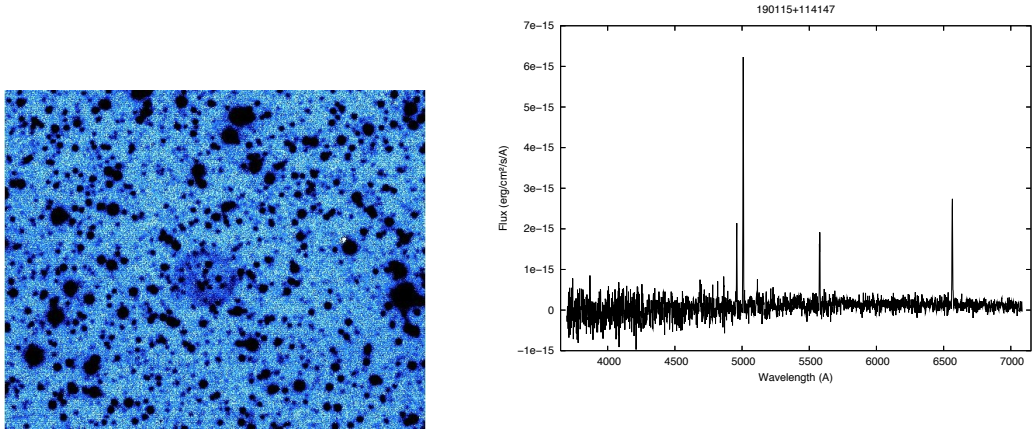


Figure A.9: PN 19:01:15 +11:41:47

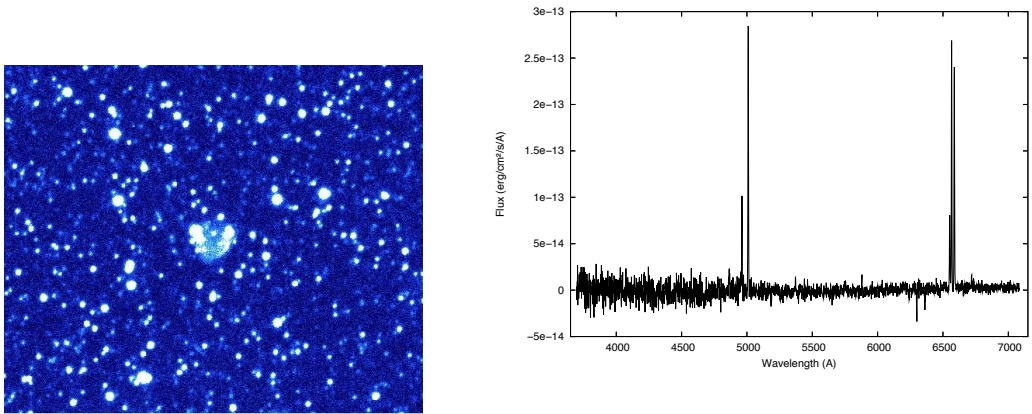


Figure A.10: PN 19:04:54 +10:18:01

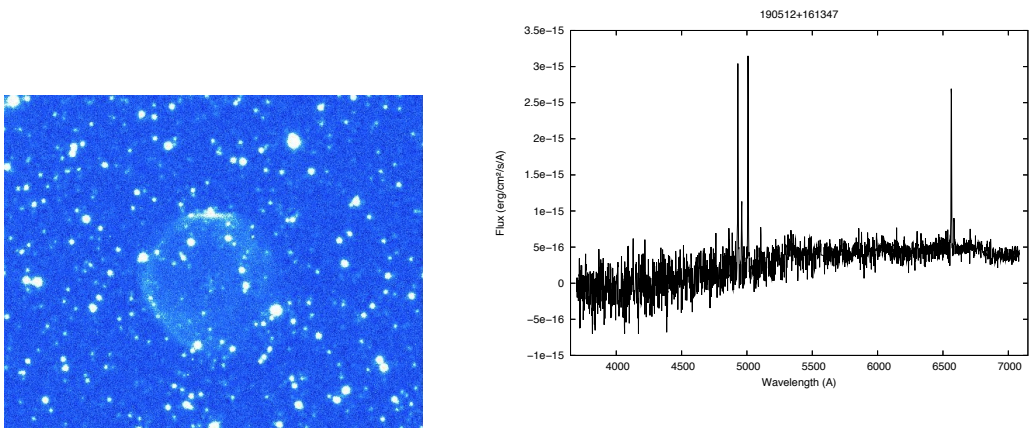


Figure A.11: PN 19:05:12 +16:13:47

## A: IPHAS OBJECT CLASSIFICATION

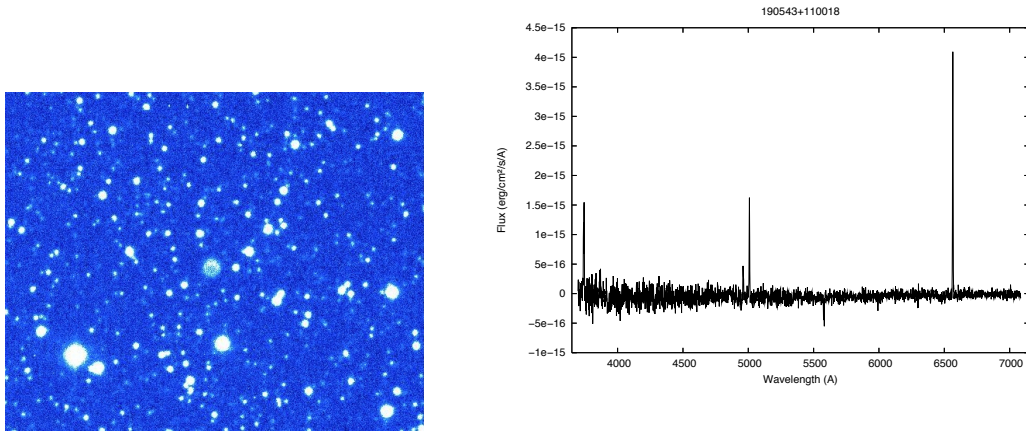


Figure A.12: PN 19:05:43 +11:00:18

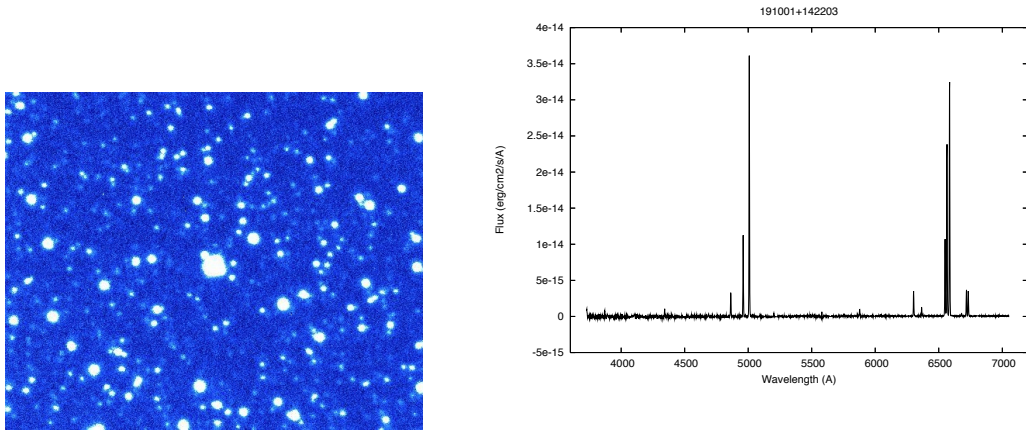


Figure A.13: PN 19:10:01 +14:22:03

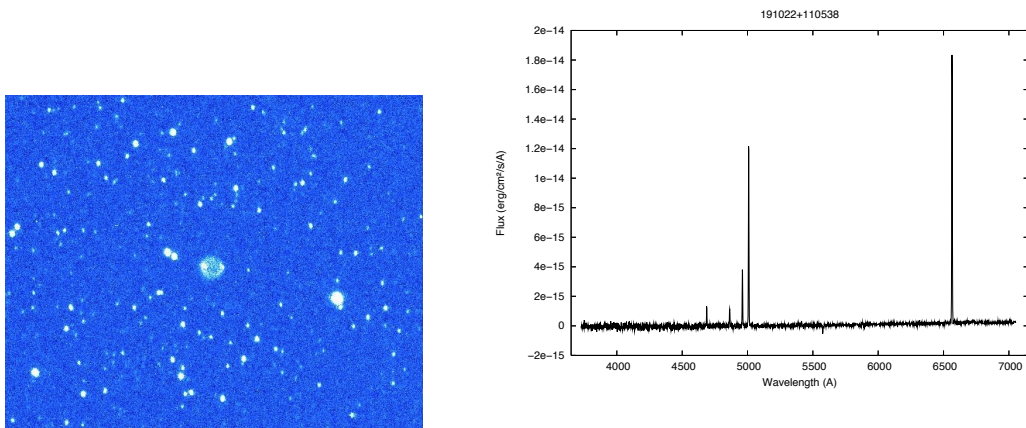


Figure A.14: PN 19:10:22 +11:05:38



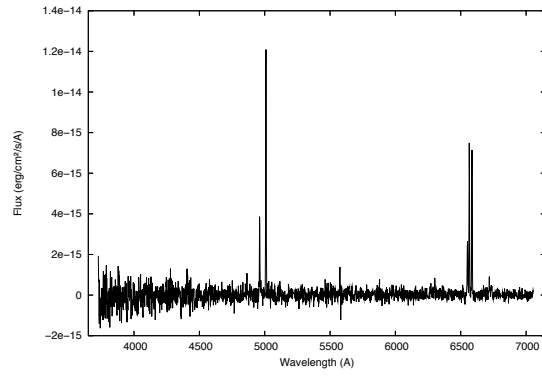
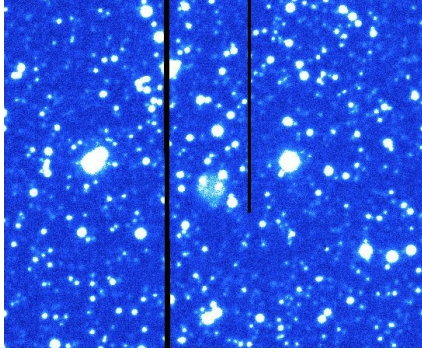


Figure A.15: PN 19:10:27 +03:40:46

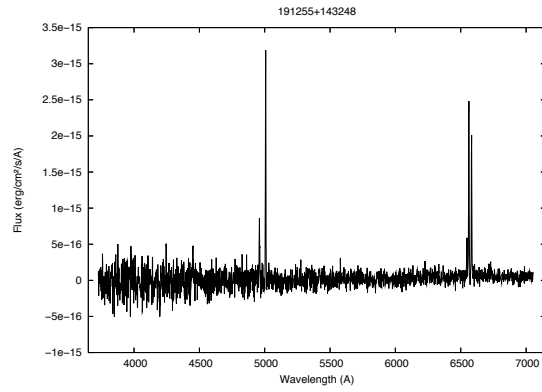
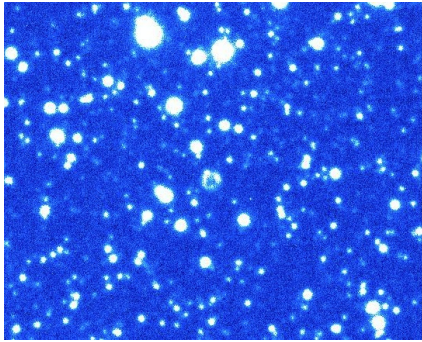


Figure A.16: PN 19:12:55 +14:32:48

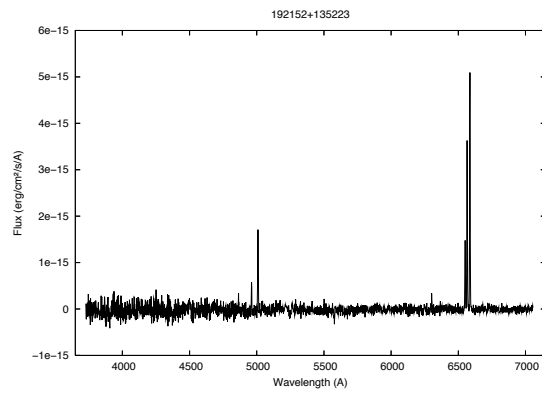
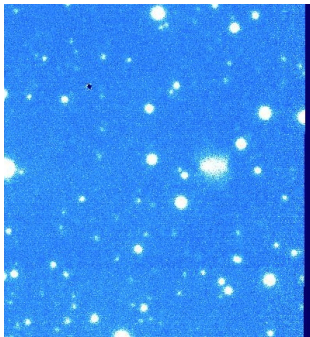


Figure A.17: PN 19:21:52 +13:52:23

## A: IPHAS OBJECT CLASSIFICATION

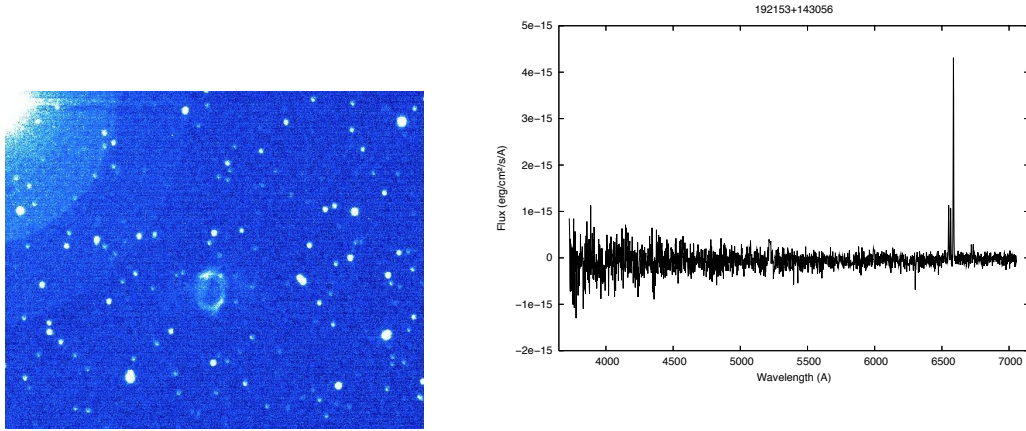


Figure A.18: PN 19:21:53 +14:30:56

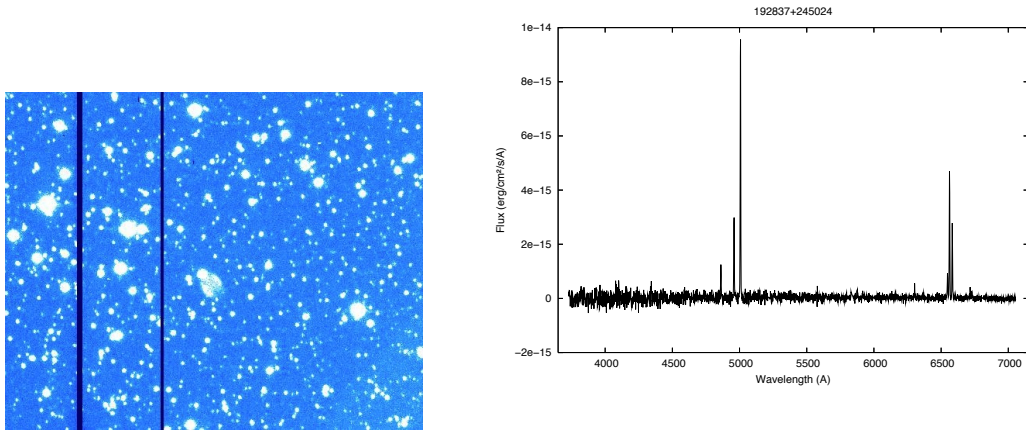


Figure A.19: PN 19:28:37 +24:50:24

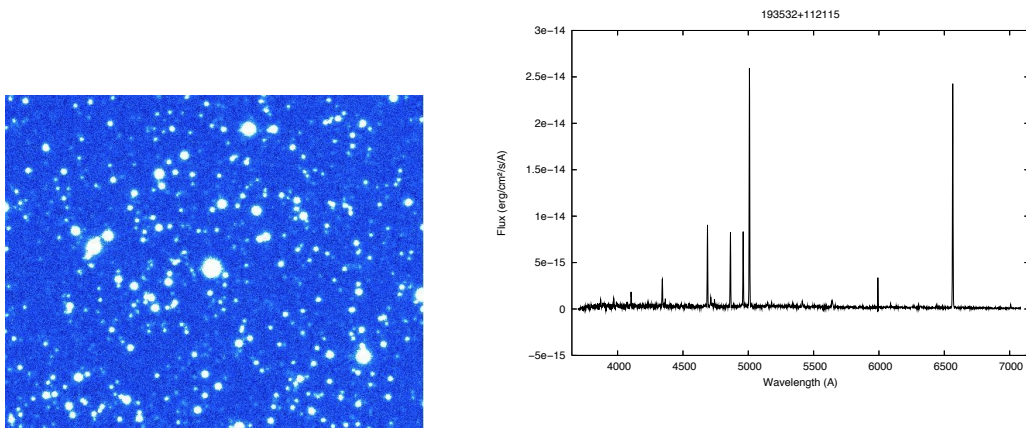


Figure A.20: PN 19:35:32 +11:21:15

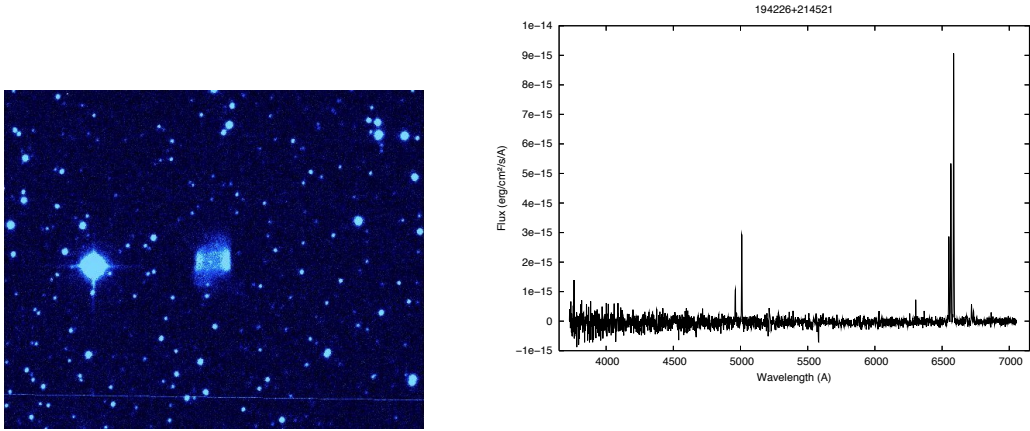


Figure A.21: PN 19:42:26 +21:45:21

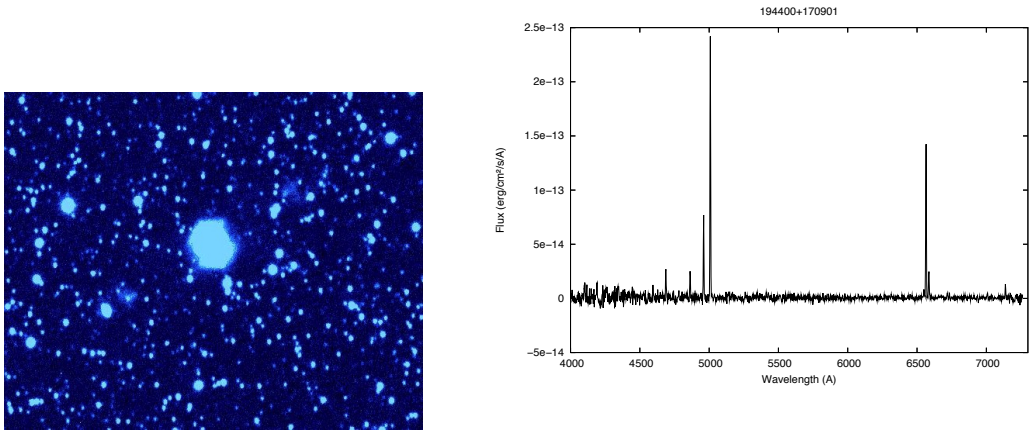


Figure A.22: PN 19:44:00 +17:09:01

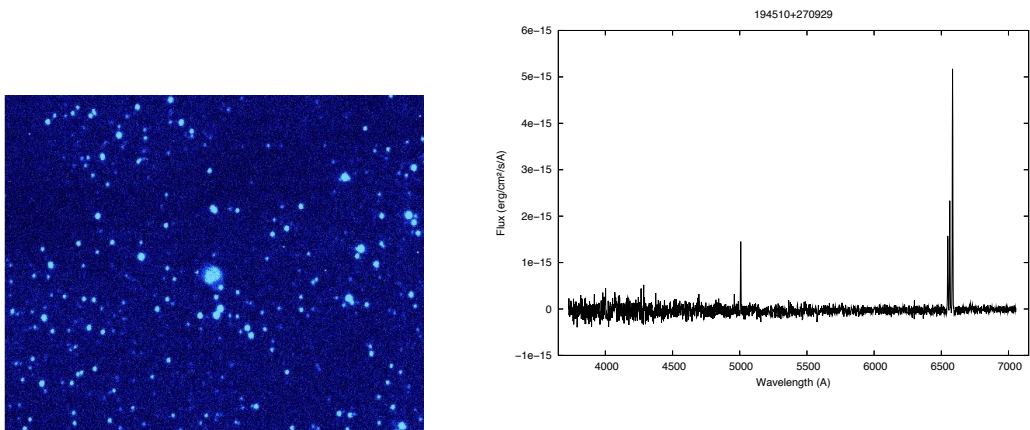


Figure A.23: PN 19:45:10 +27:09:29



## A: IPHAS OBJECT CLASSIFICATION

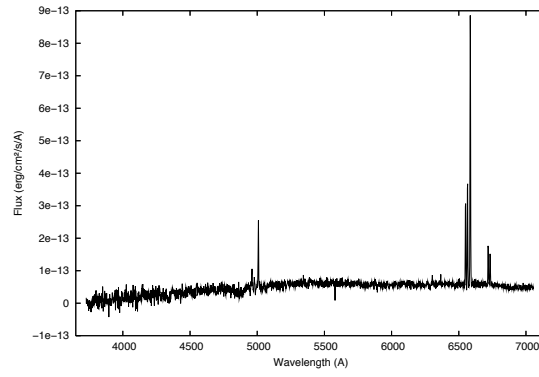
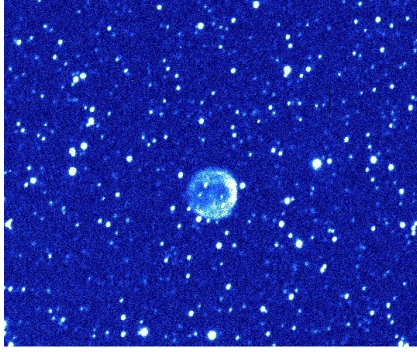


Figure A.24: PN 19:48:52 +22:25:16

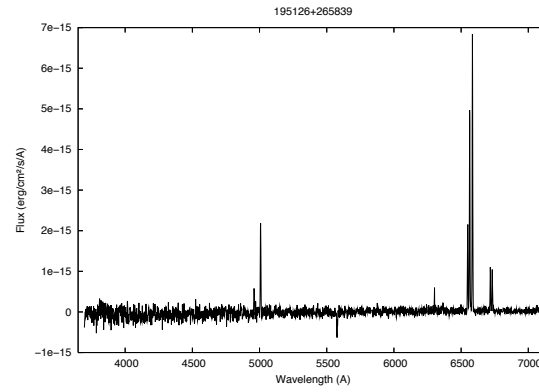
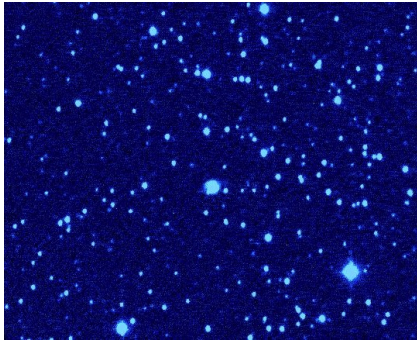


Figure A.25: PN 19:51:26 +26:58:39

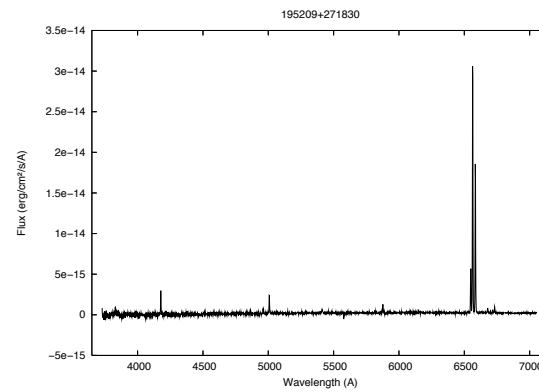
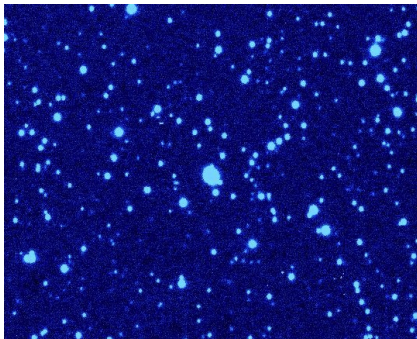


Figure A.26: PN 19:52:09 +27:18:30

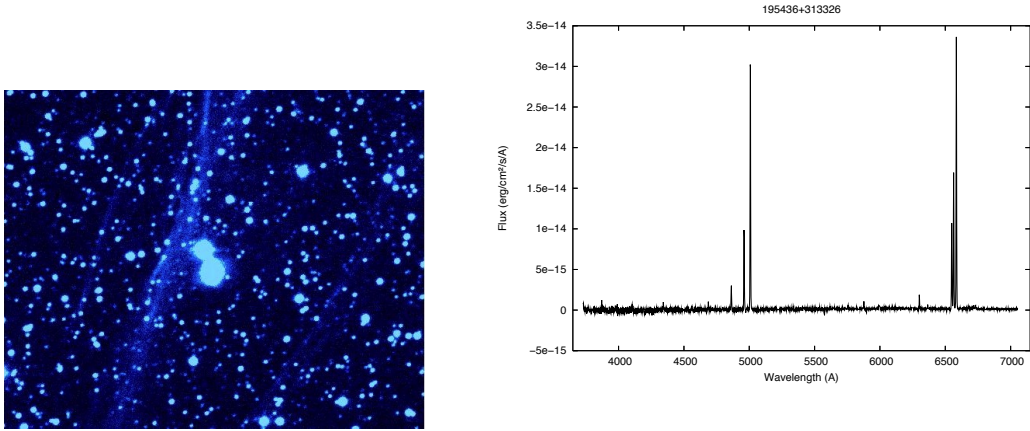


Figure A.27: PN 19:54:36 +31:33:26

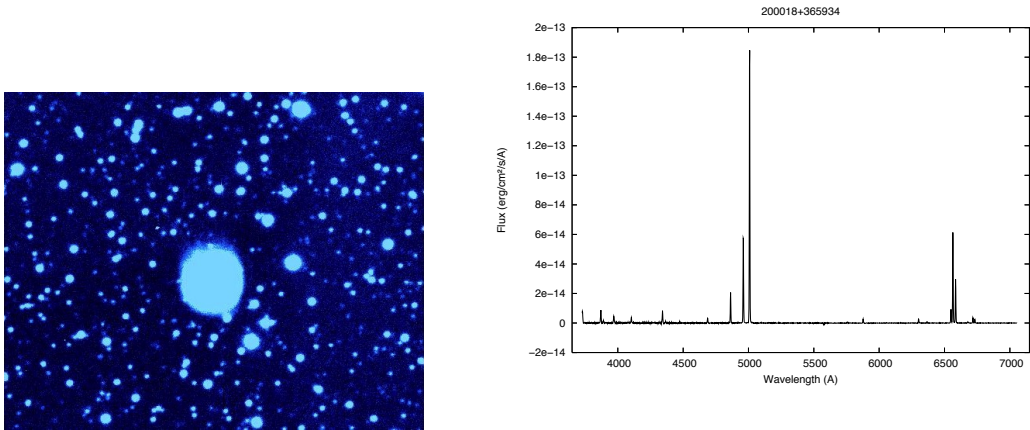


Figure A.28: PN 20:00:18 +36:59:34

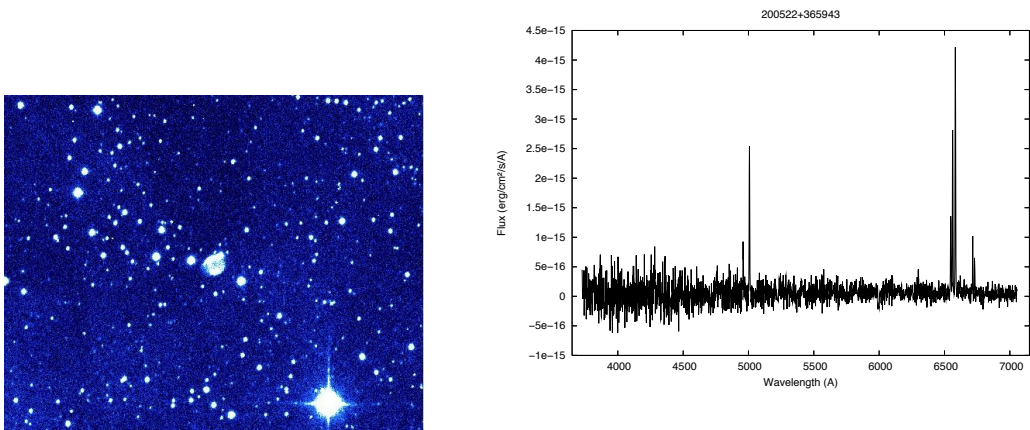


Figure A.29: PN 20:05:22 +36:59:43

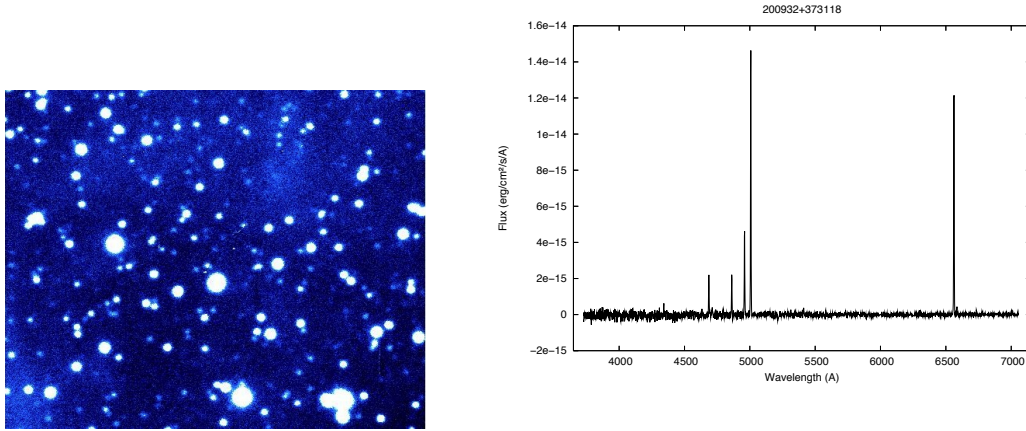


Figure A.30: PN 20:09:32 +37:31:18

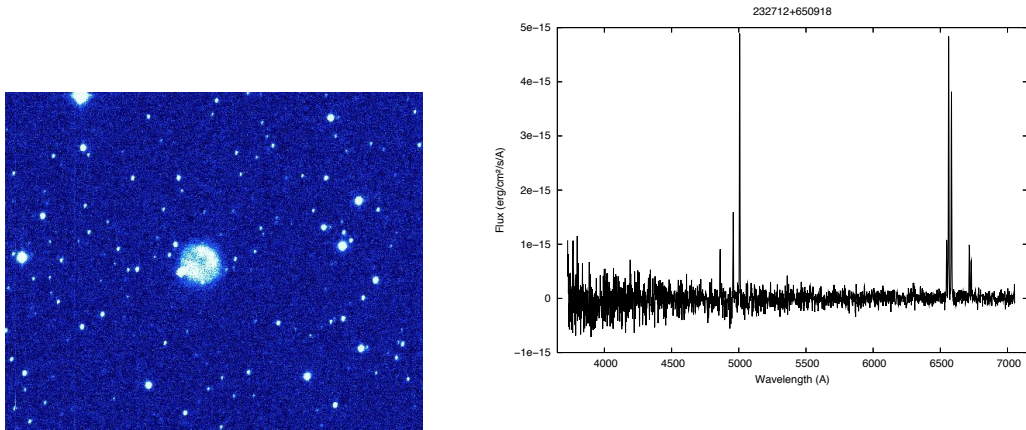


Figure A.31: PN 23:27:12 +65:09:18

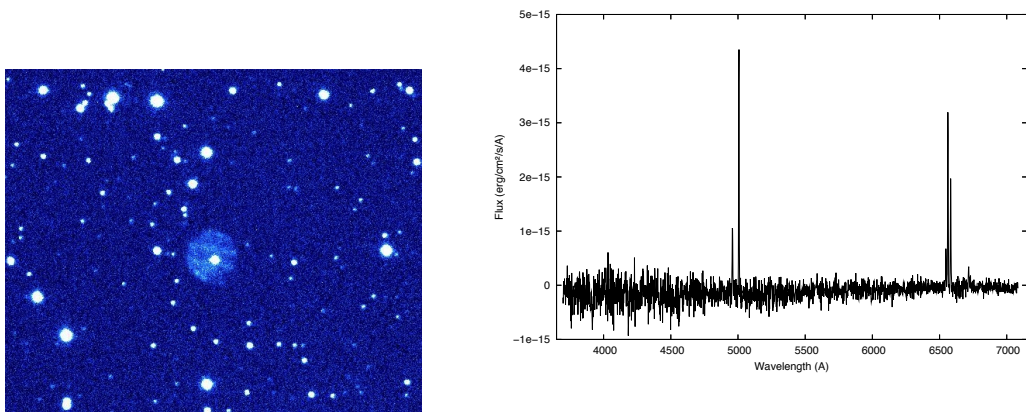


Figure A.32: PN 23:44:03 +60:32:42



## A.2 Possible PNe

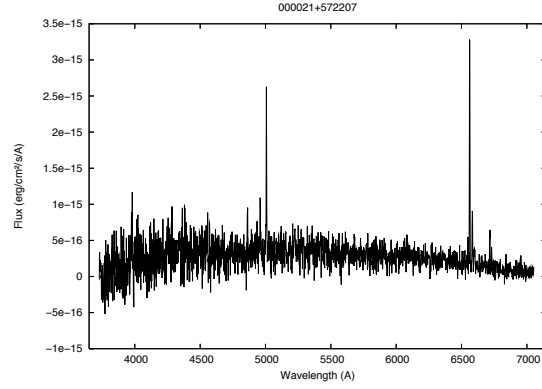
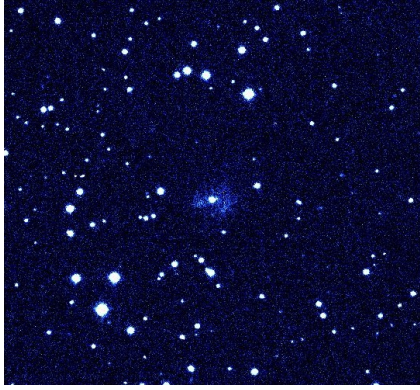


Figure A.33: PN 00:00:21 +57:22:07

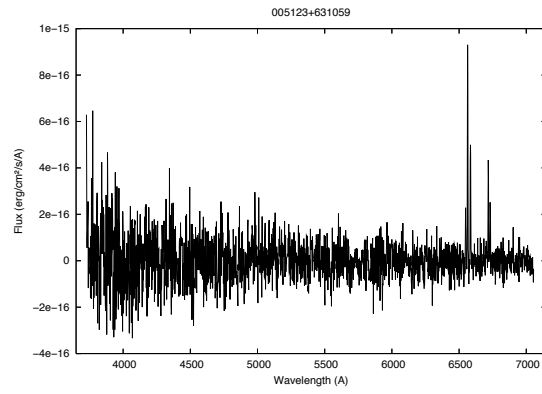
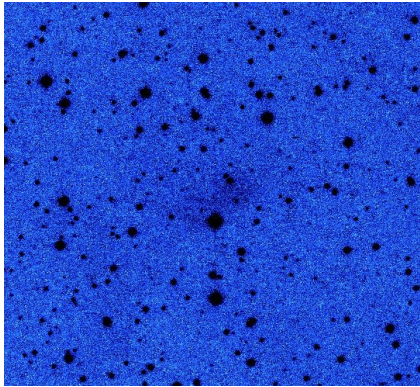


Figure A.34: PN 00:51:23 +63:10:59

## A: IPHAS OBJECT CLASSIFICATION

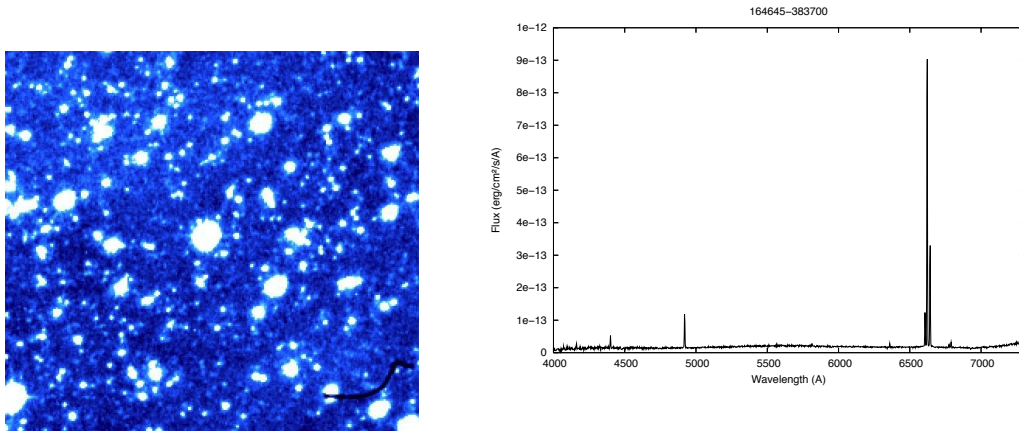


Figure A.35: PN 16:46:45 -38:37:00

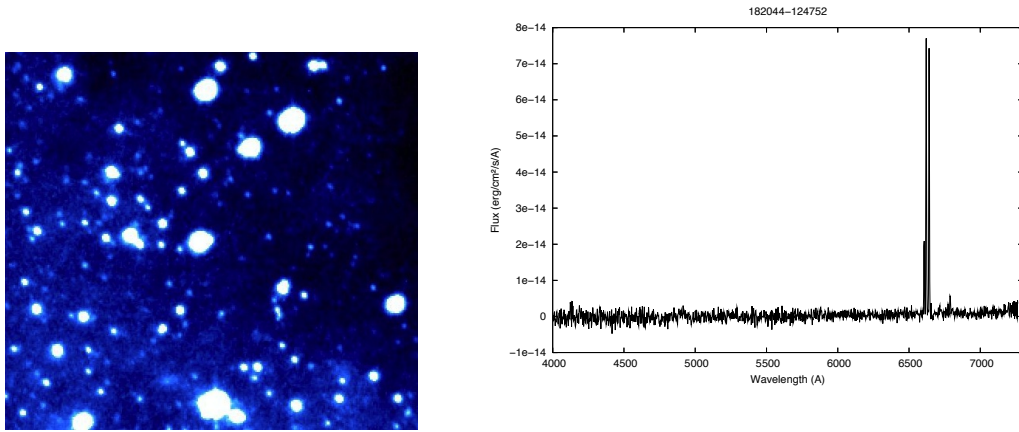


Figure A.36: PN 18:20:44 -12:47:52

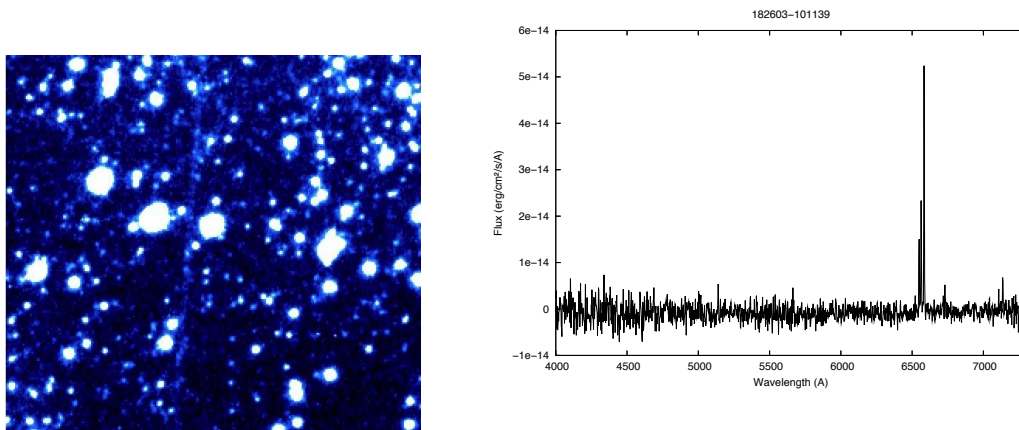


Figure A.37: PN 18:26:03 -10:11:39



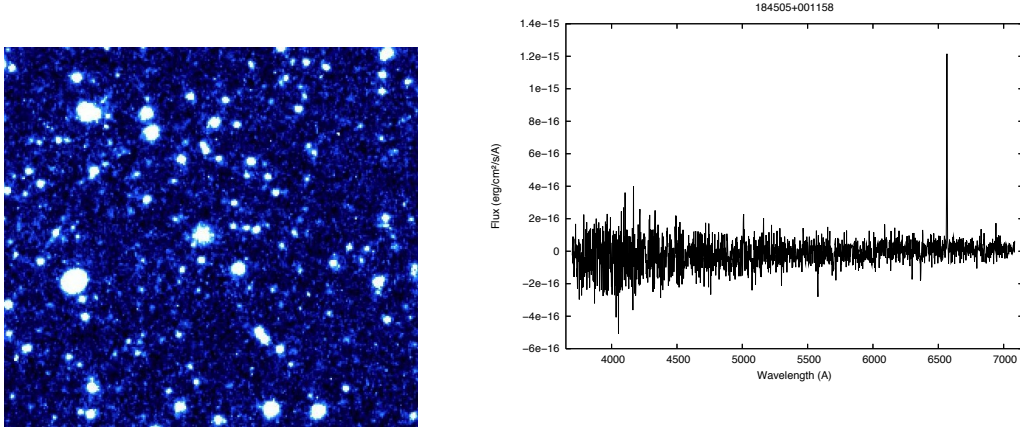


Figure A.38: PN 18:45:05 +00:11:58

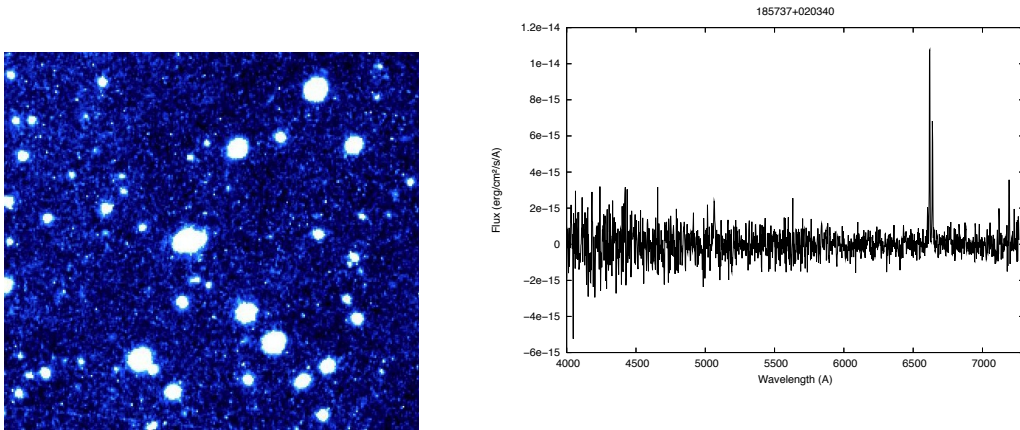


Figure A.39: PN 18:57:37 +02:03:40

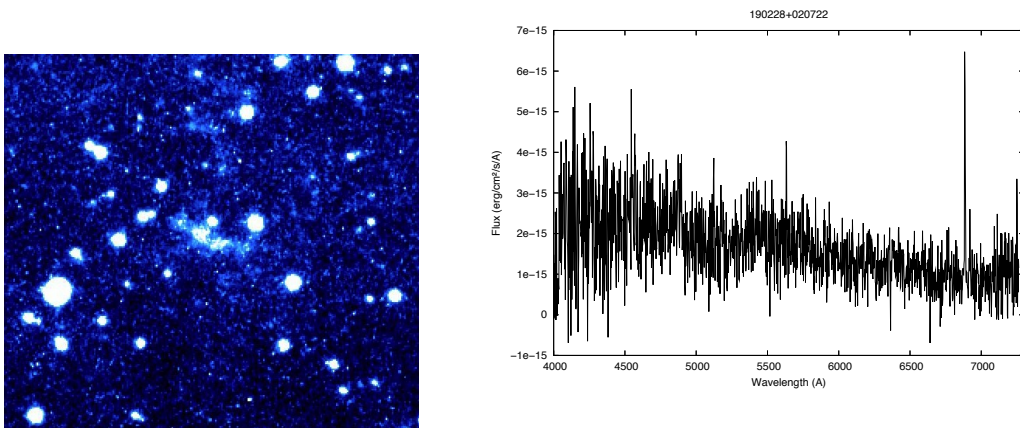


Figure A.40: PN 19:02:28 +02:07:22

## A: IPHAS OBJECT CLASSIFICATION

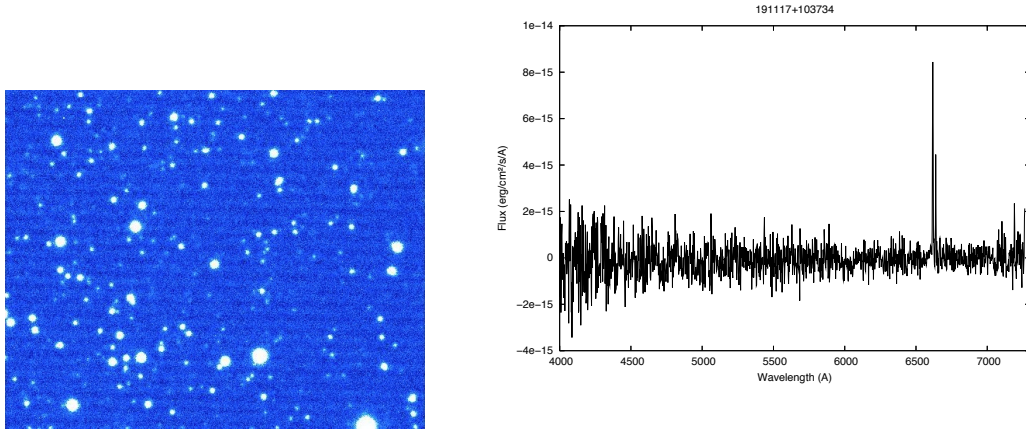


Figure A.41: PN 19:11:17 +10:37:34

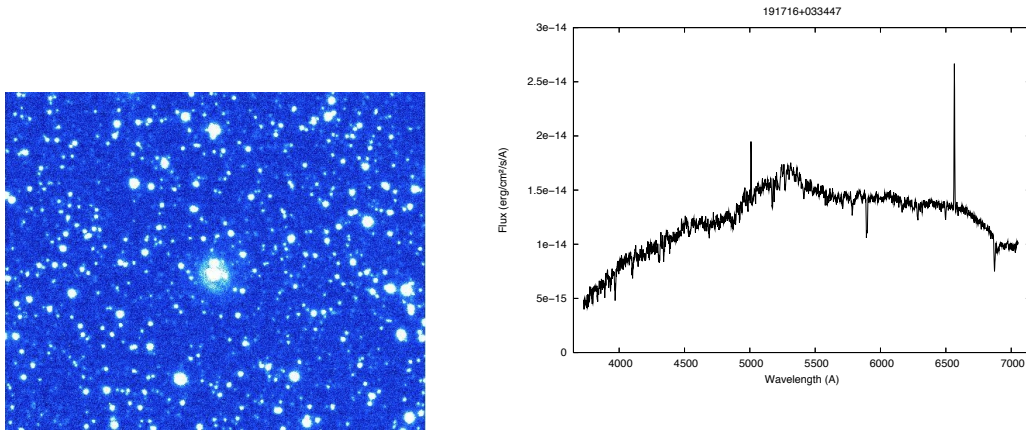


Figure A.42: PN 19:17:16 +03:34:47

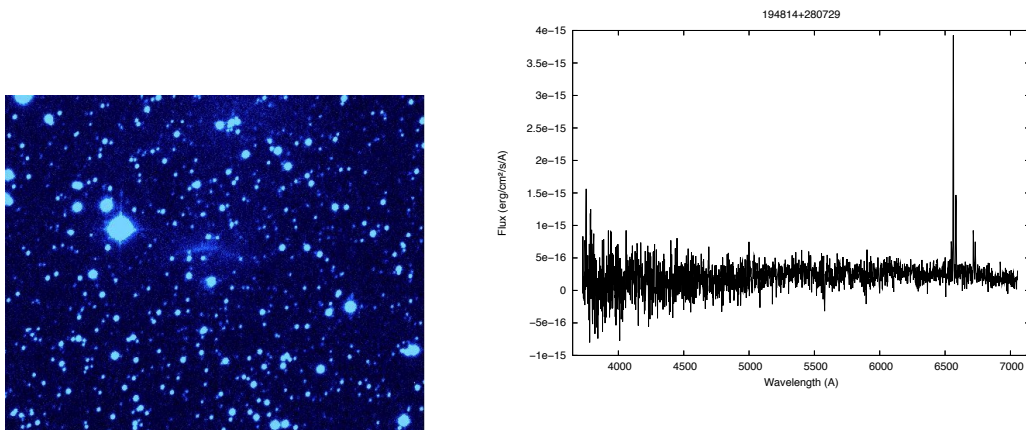


Figure A.43: PN 19:48:14 +28:07:29

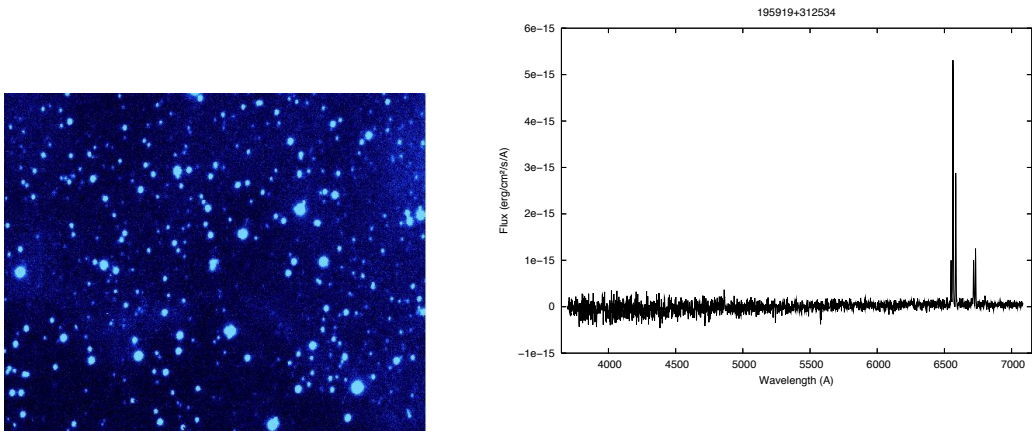


Figure A.44: PN 19:59:19 +31:25:34

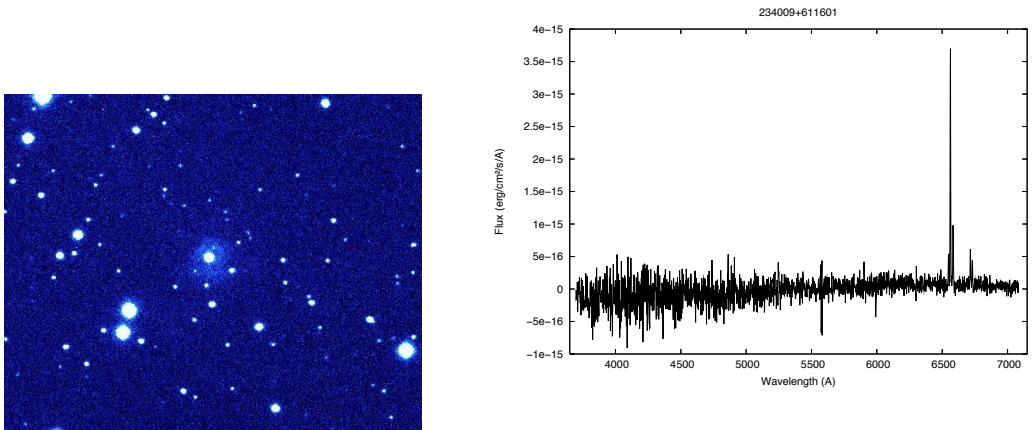


Figure A.45: PN 23:40:09 +61:16:01

### A.3 HII regions

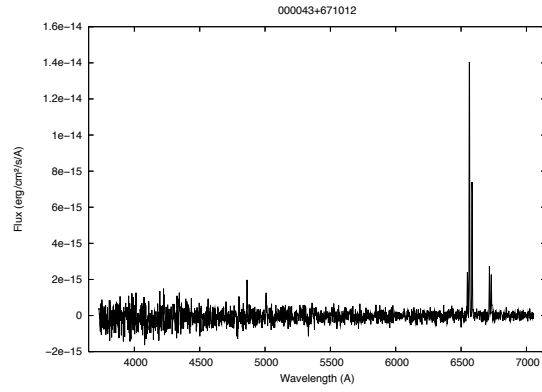
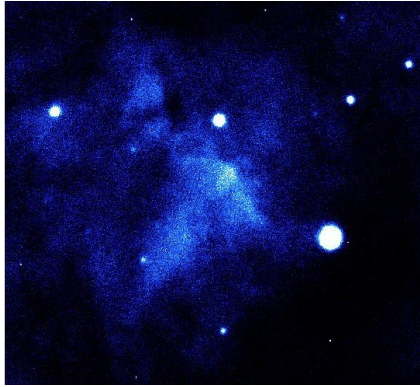


Figure A.46: PN 00:00:43 +67:10:12

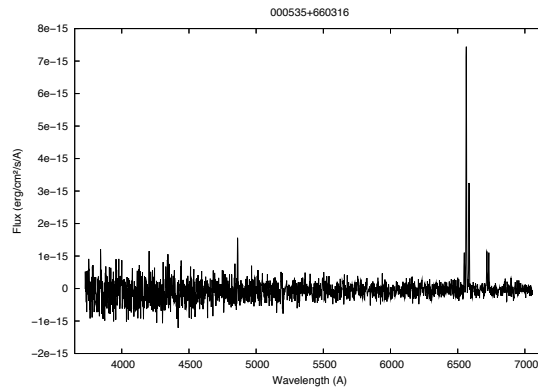
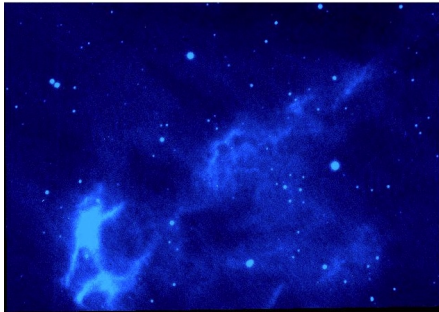


Figure A.47: PN 00:05:35 +66:03:16



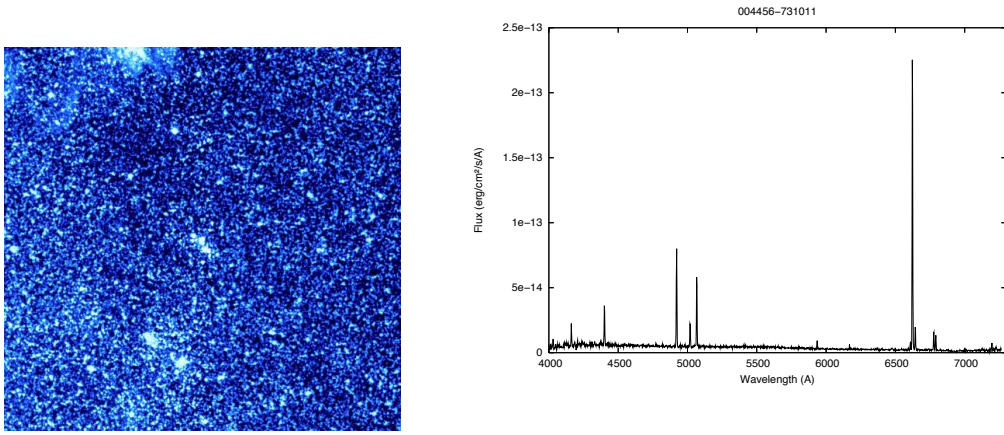


Figure A.48: PN 00:44:56 -73:10:11

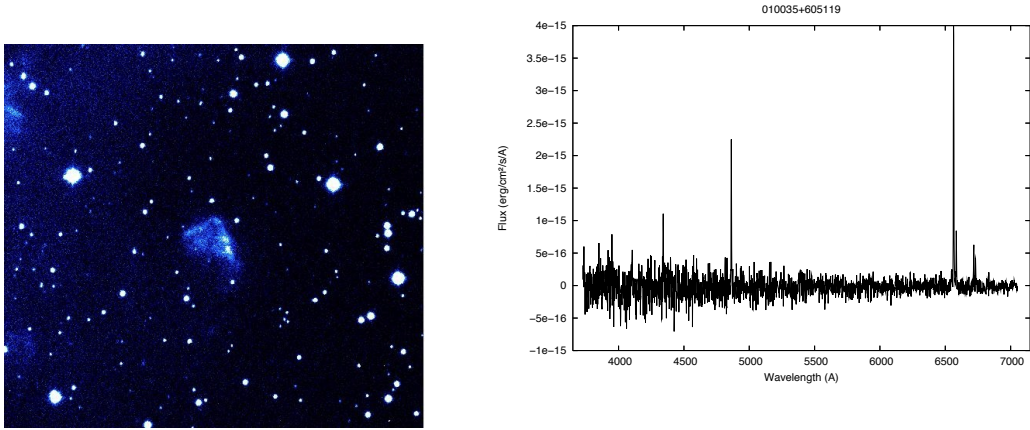


Figure A.49: PN 01:00:35 +60:51:19

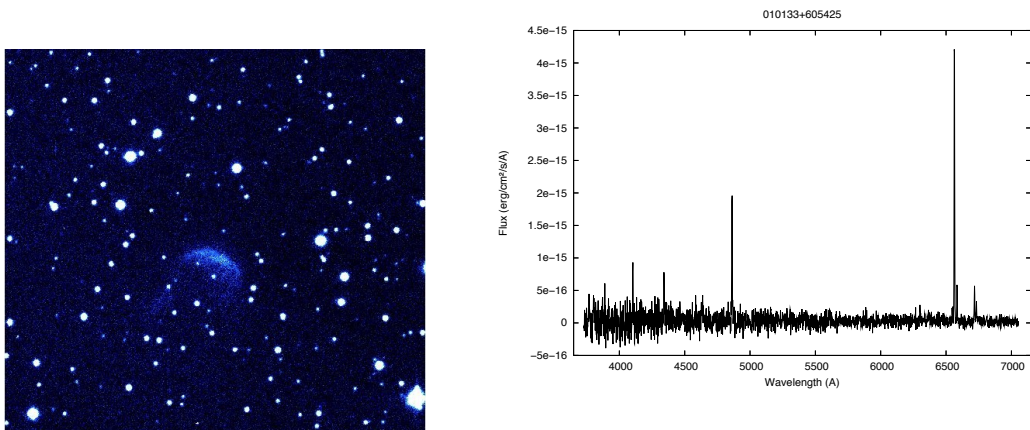


Figure A.50: PN 01:01:33 +60:54:25

## A: IPHAS OBJECT CLASSIFICATION

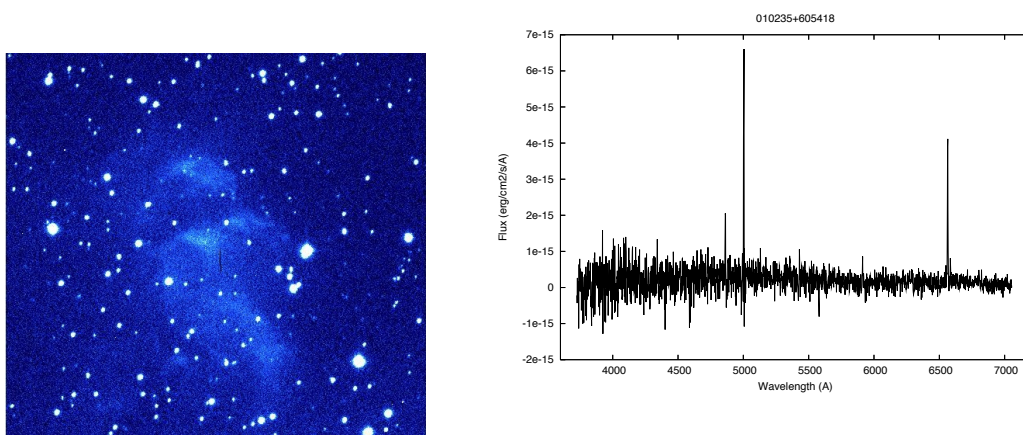


Figure A.51: PN 01:02:35 +60:54:18

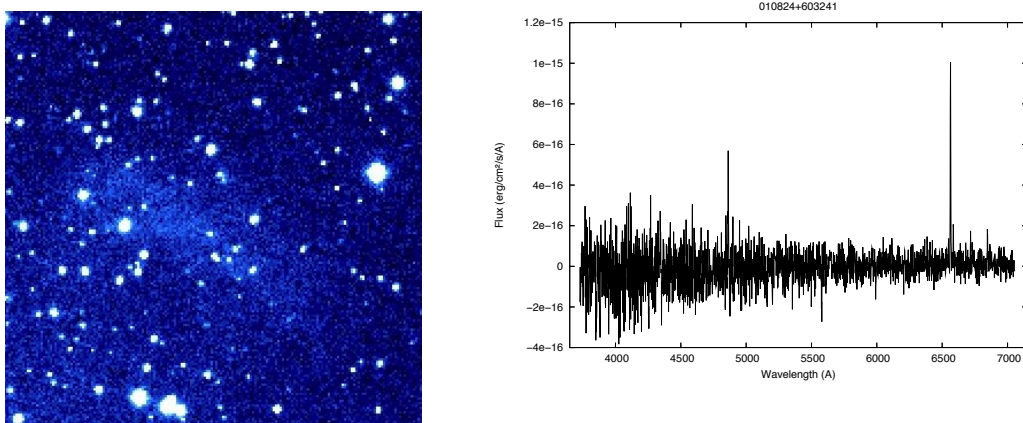


Figure A.52: PN 01:08:24 +60:32:41

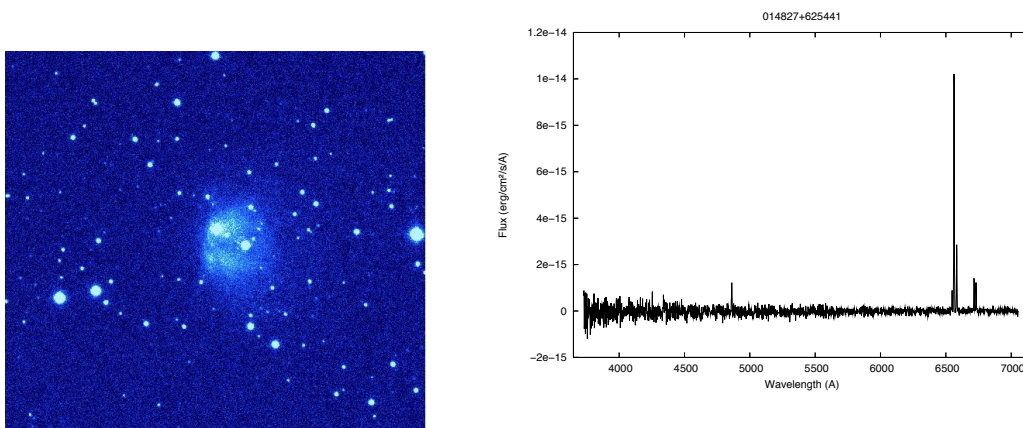


Figure A.53: PN 01:48:27 +62:54:41

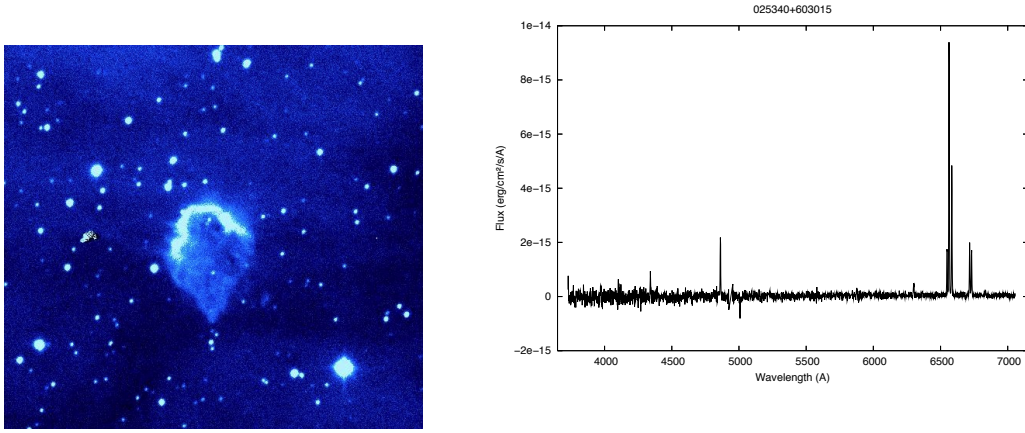


Figure A.54: PN 02:53:40 +60:30:15

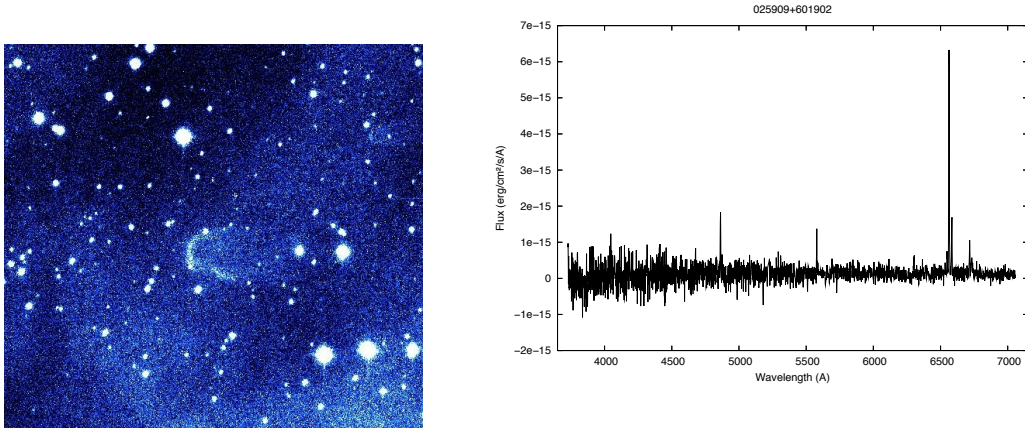


Figure A.55: PN 02:59:09 +60:19:02

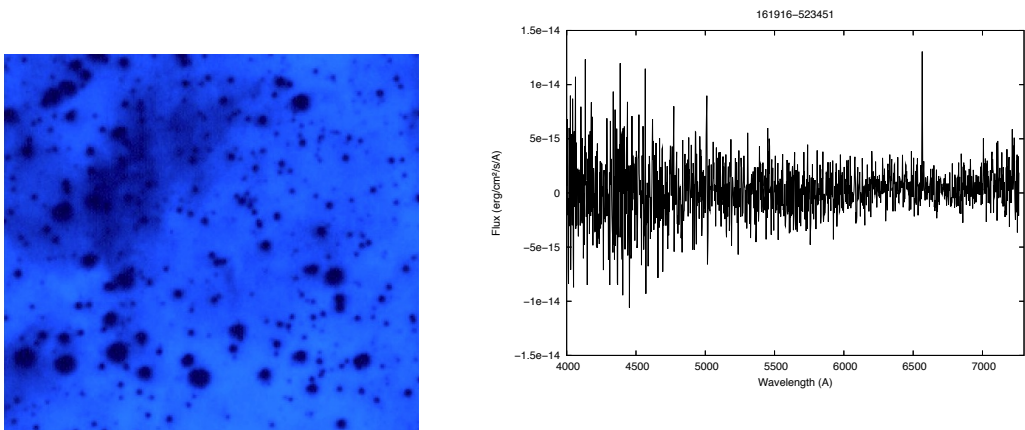


Figure A.56: PN 16:19:16 -52:34:51



## A: IPHAS OBJECT CLASSIFICATION

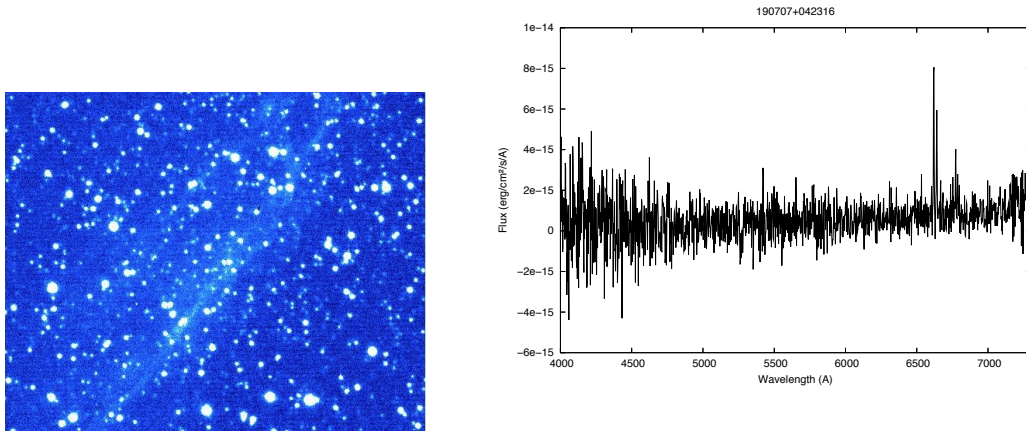


Figure A.57: PN 19:07:07 +04:23:16

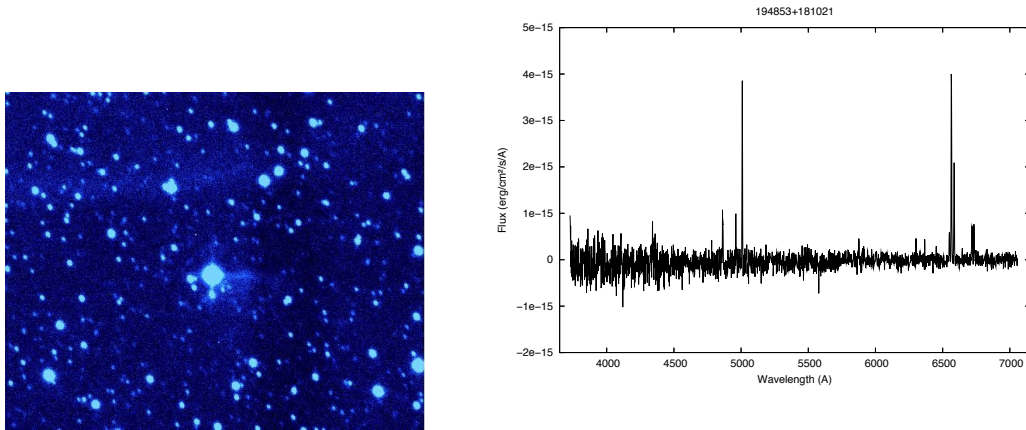


Figure A.58: PN 19:48:53 +18:10:21

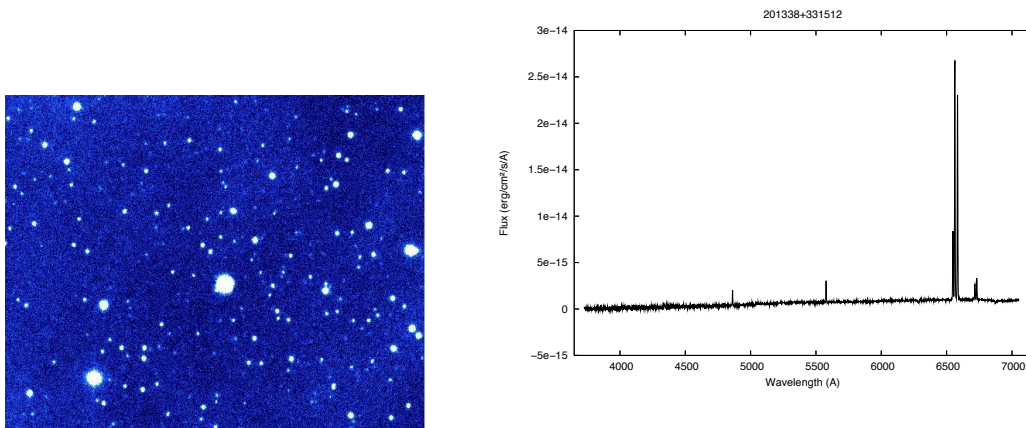


Figure A.59: PN 20:13:38 +33:15:12



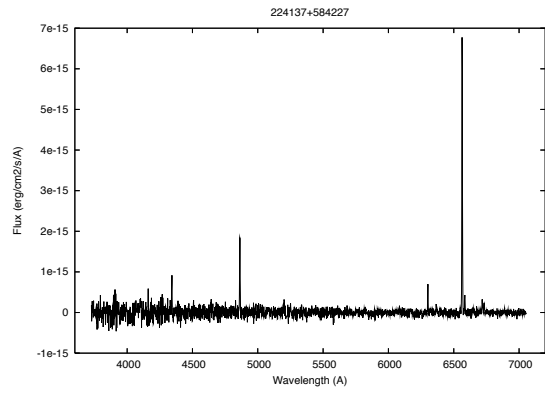
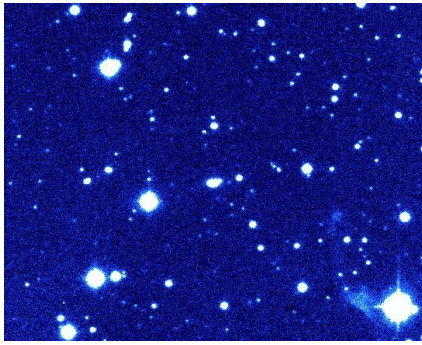


Figure A.60: PN 22:41:37 +58:42:27

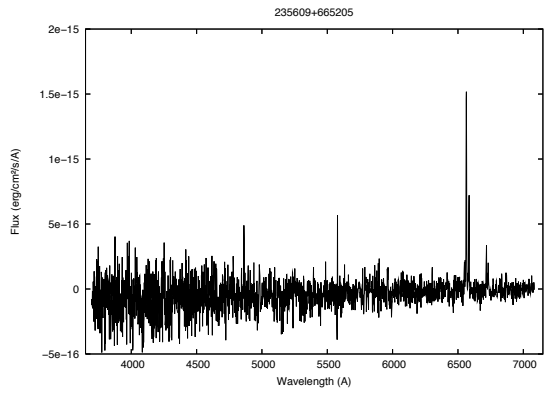
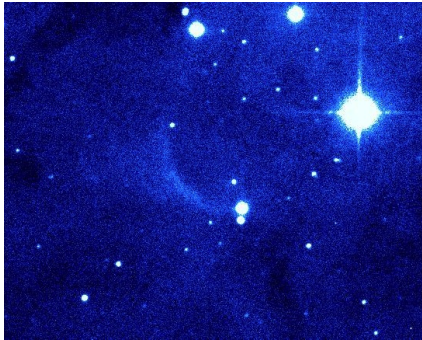


Figure A.61: PN 23:56:09 +66:52:05

## A.4 Strömgren Spheres

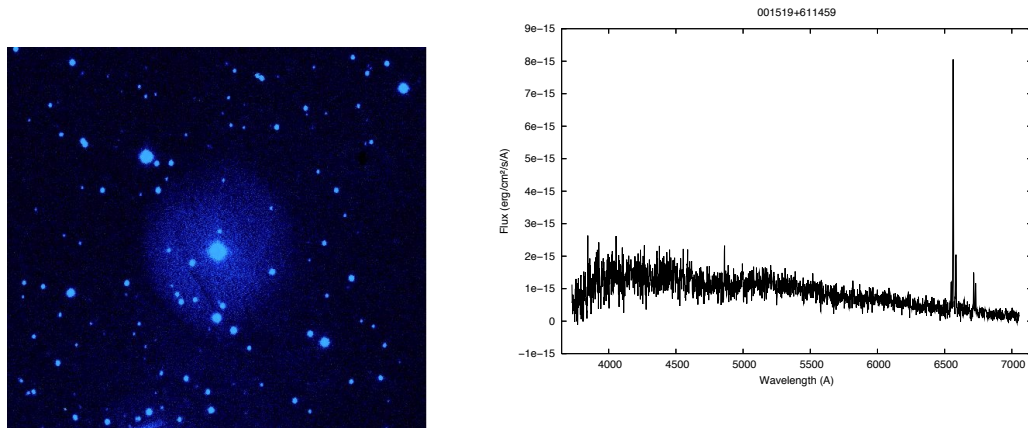


Figure A.62: PN 00:15:19 +61:14:59

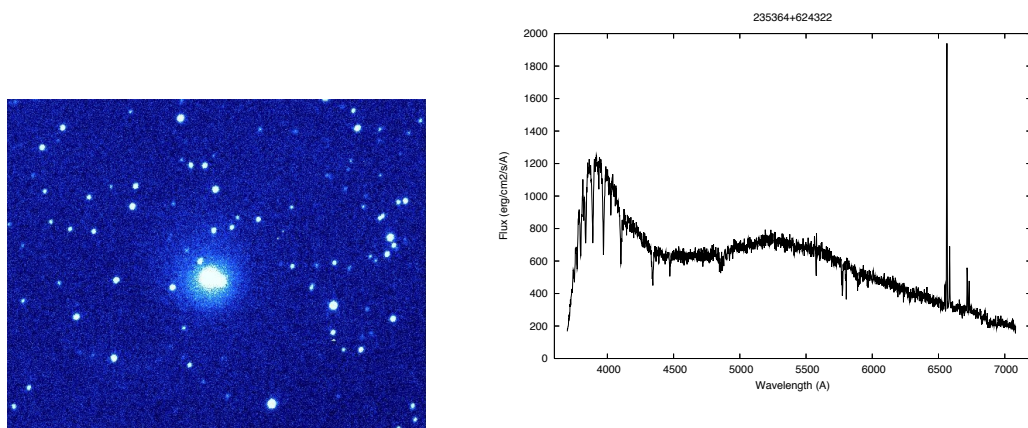


Figure A.63: PN 23:53:04 +62:46:32

## A.5 Supernova Remnants

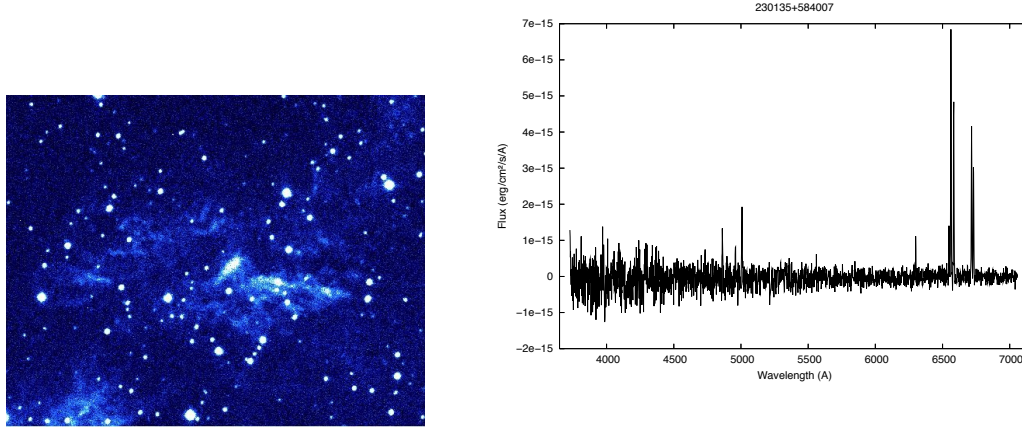


Figure A.64: PN 23:01:35 +58:40:07

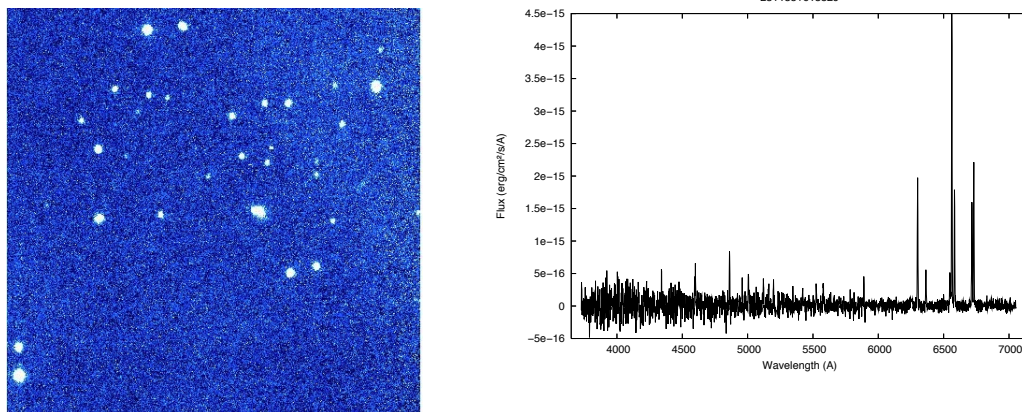


Figure A.65: PN 23:11:35 +61:38:29

## A.6 Unclear objects

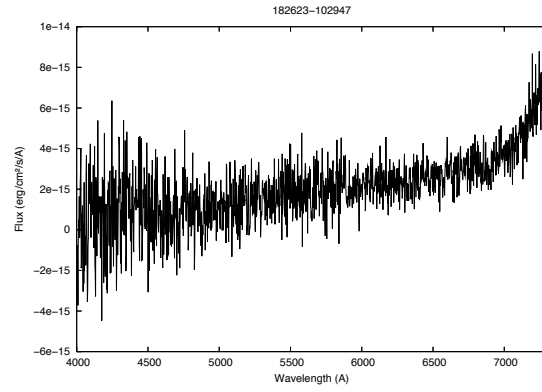
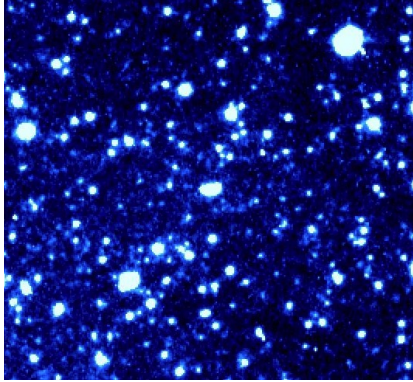


Figure A.66: PN 18:26:23 -10:29:47

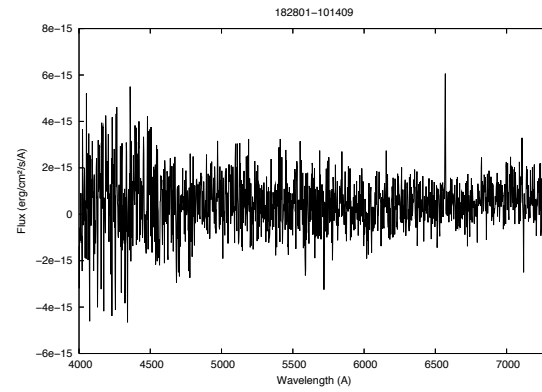
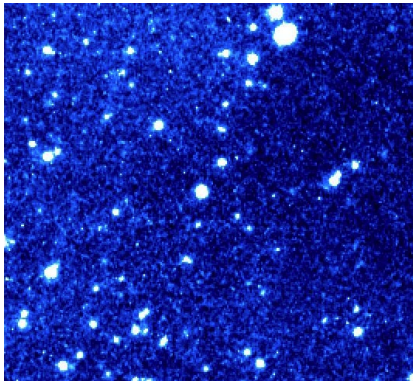


Figure A.67: PN 18:28:01 -10:14:09



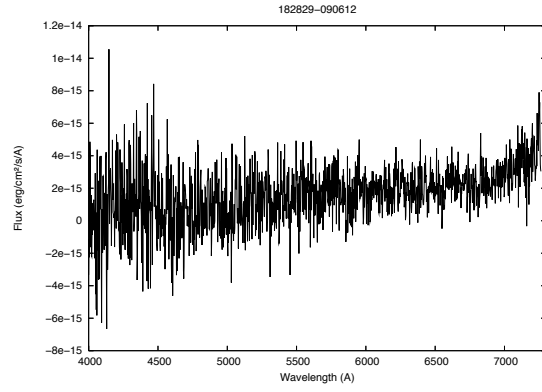
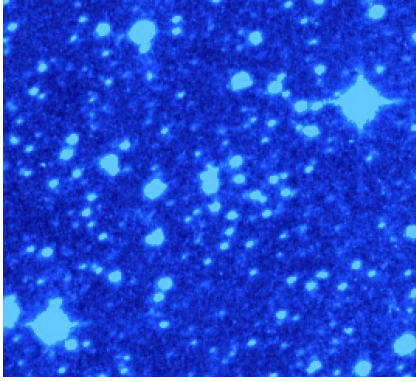


Figure A.68: PN 18:28:29 -09:06:12

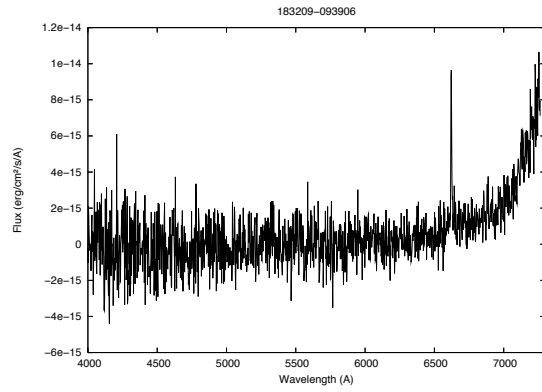
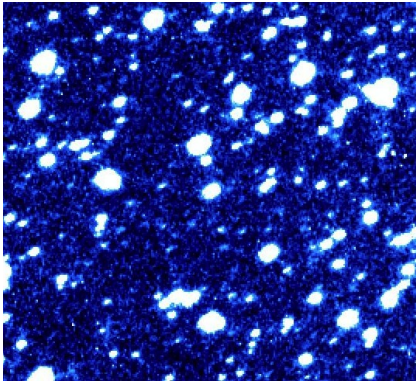


Figure A.69: PN 18:32:09 -09:39:06

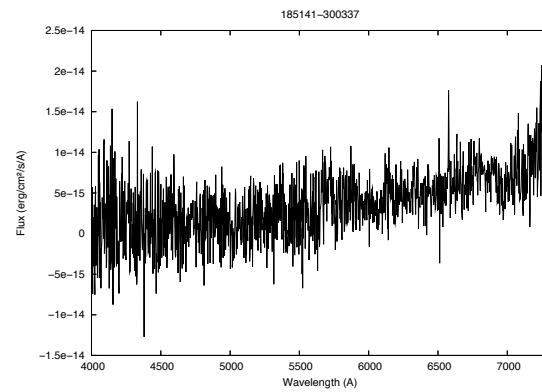
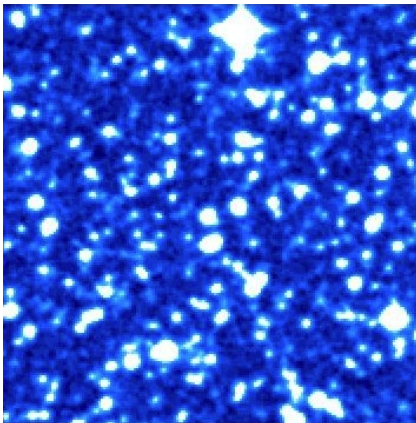


Figure A.70: PN 18:51:41 -30:03:37

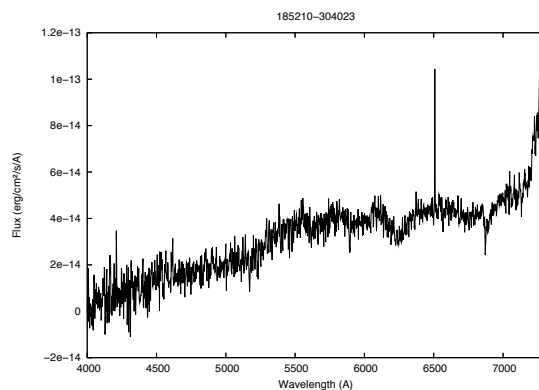
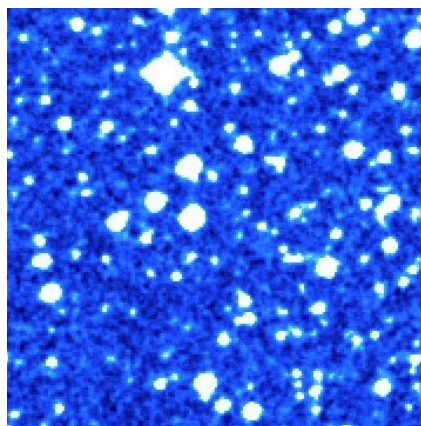


Figure A.71: PN 18:52:10 -30:40:23

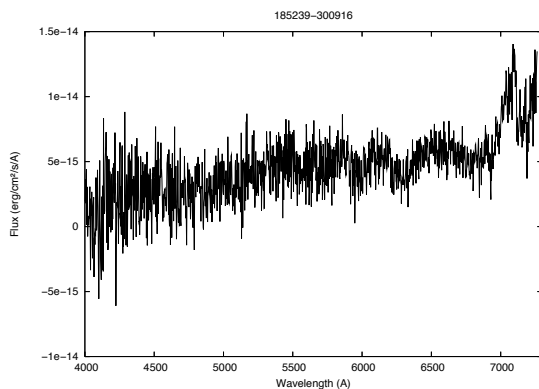
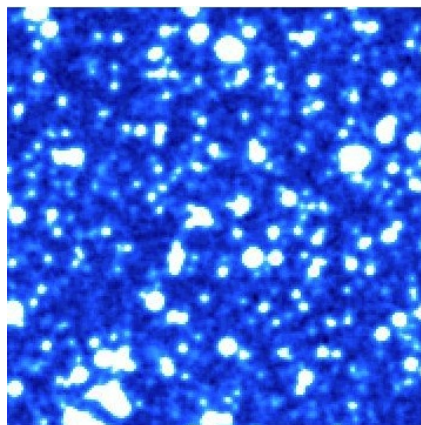


Figure A.72: PN 18:52:39 -30:09:16

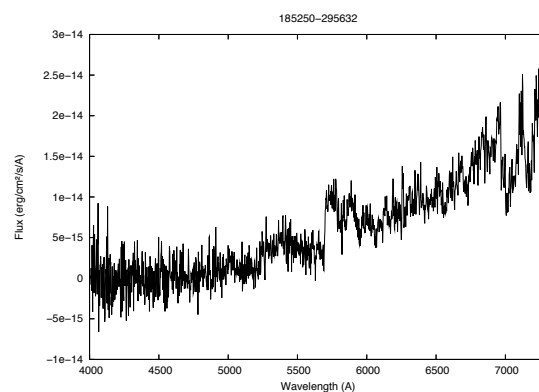
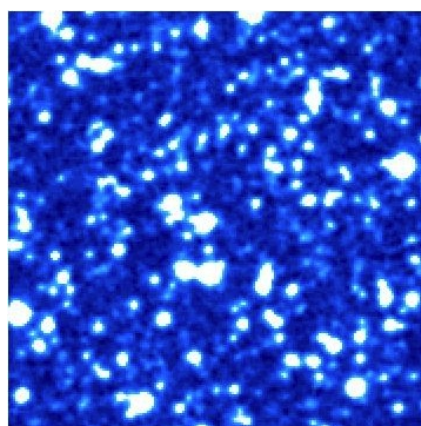


Figure A.73: PN 18:52:50 -29:56:32

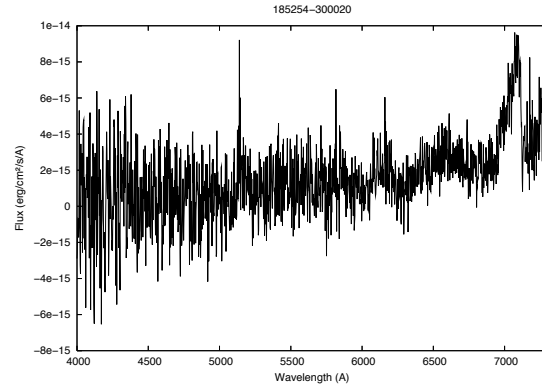
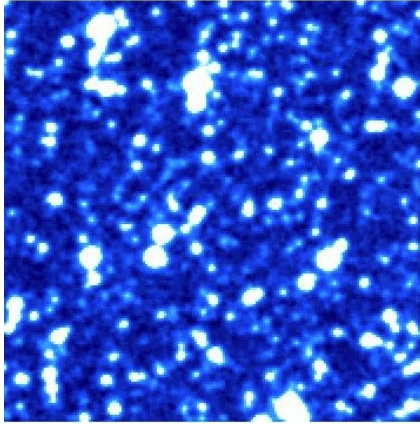


Figure A.74: PN 18:52:54 -30:00:20

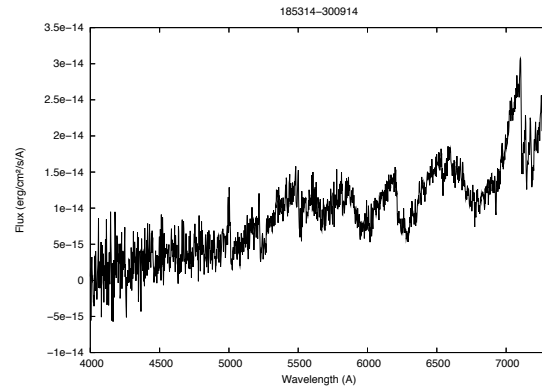
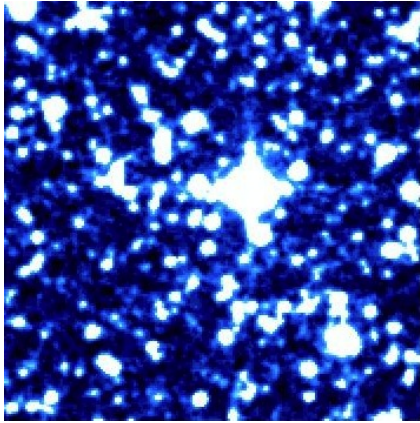


Figure A.75: PN 18:53:14 -30:09:14

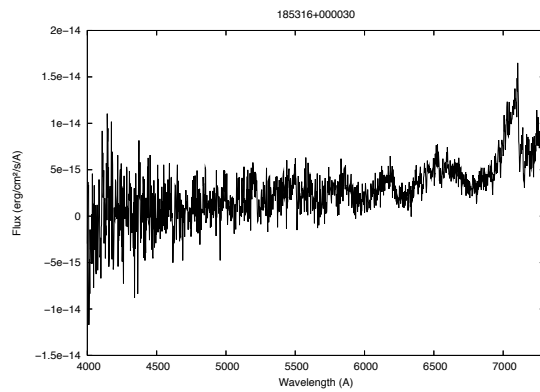
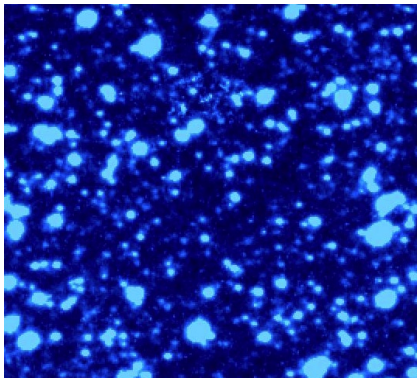


Figure A.76: PN 18:53:16 +00:00:30



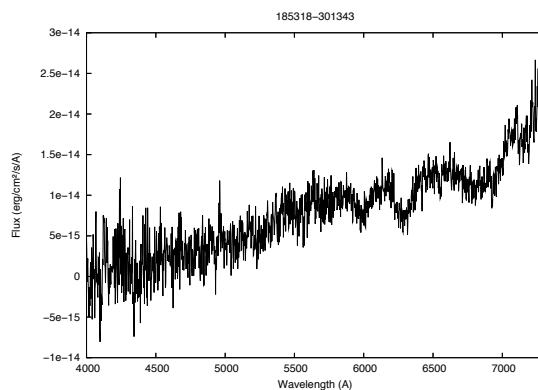
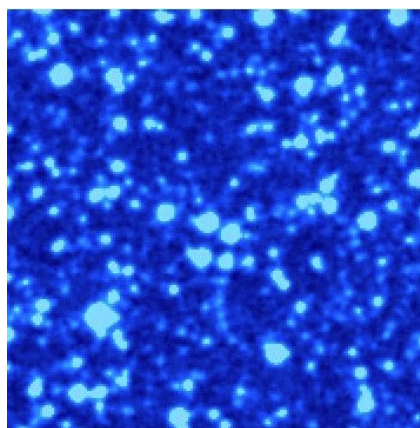


Figure A.77: PN 18:53:18 -30:13:43

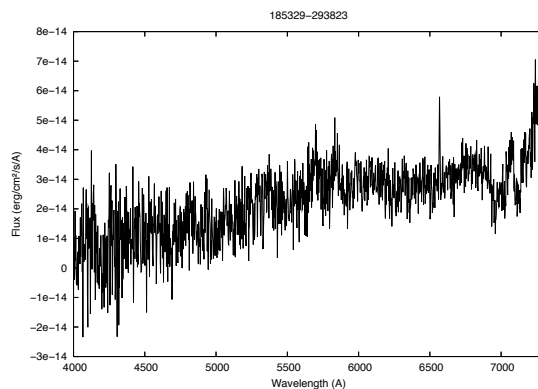
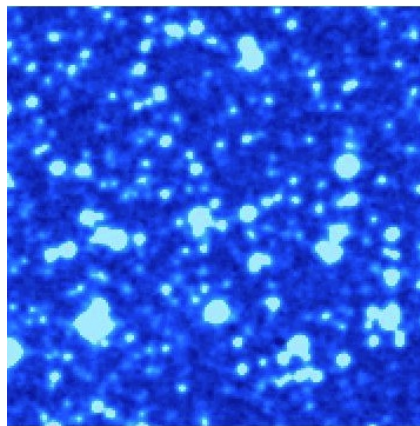


Figure A.78: PN 18:53:29 -29:38:23

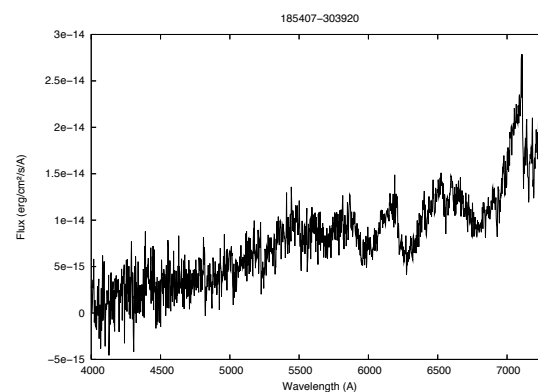
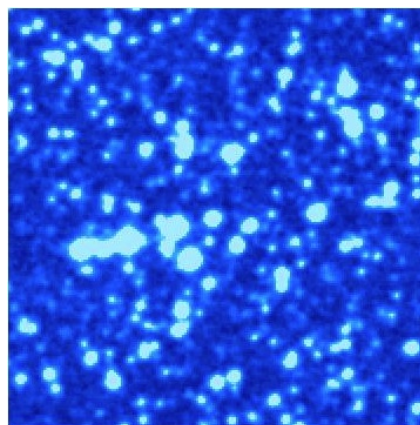


Figure A.79: PN 18:54:07 -30:39:20



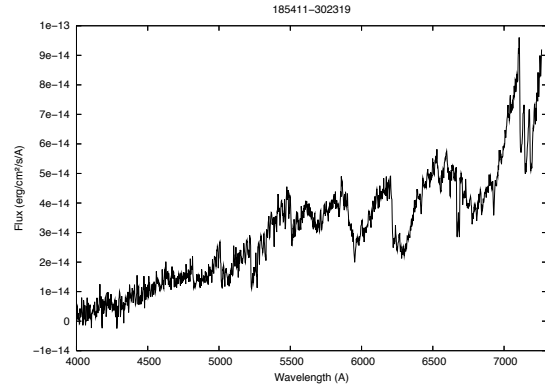
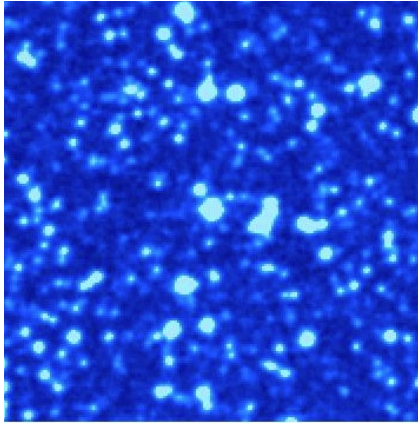


Figure A.80: PN 18:54:11 -30:23:19

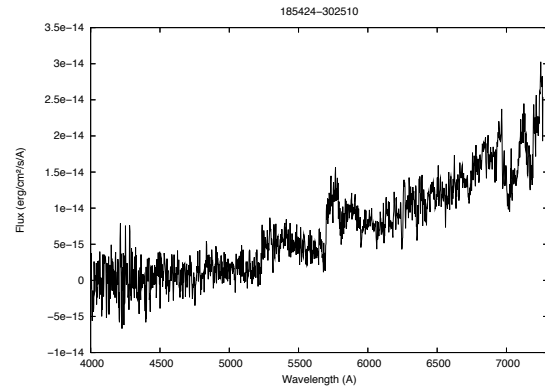
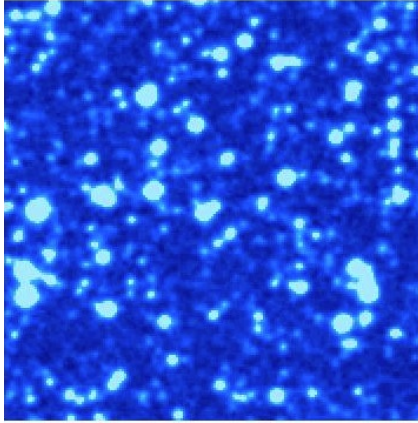


Figure A.81: PN 18:54:24 -30:25:10

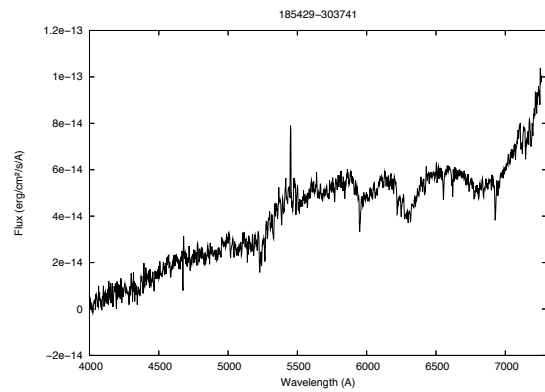
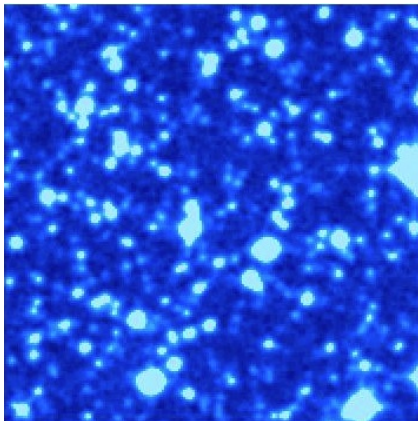


Figure A.82: PN 18:54:29 -30:37:41

## A: IPHAS OBJECT CLASSIFICATION

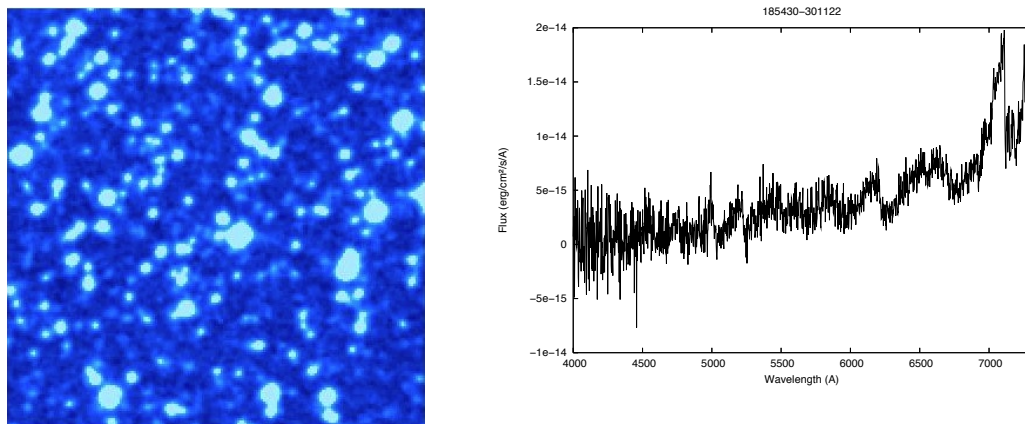


Figure A.83: PN 18:54:30 -30:11:22

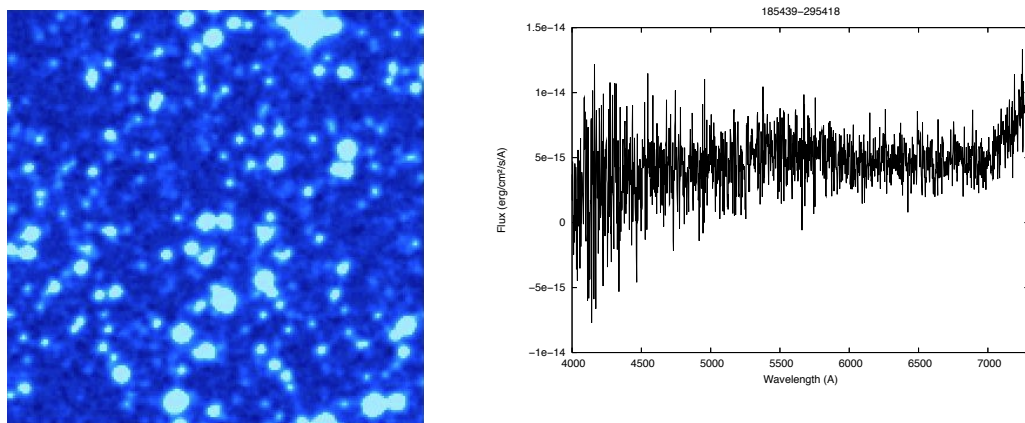


Figure A.84: PN 18:54:39 -29:54:18

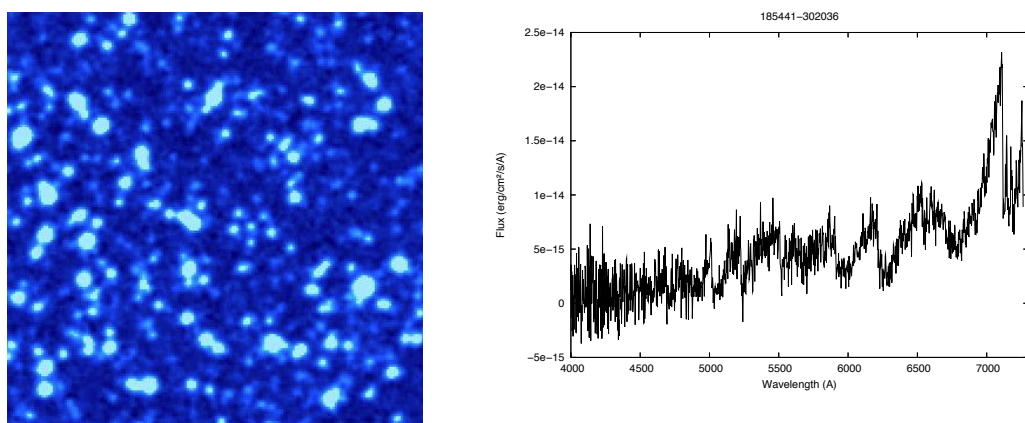


Figure A.85: PN 18:54:41 -30:20:36

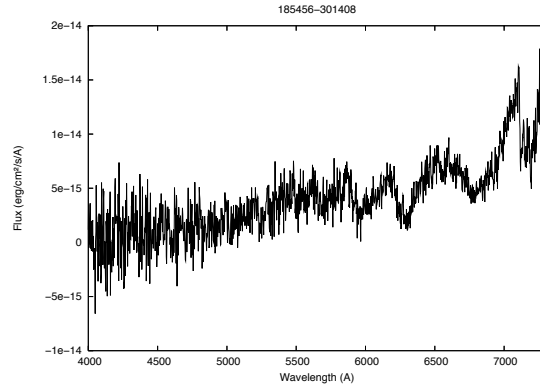
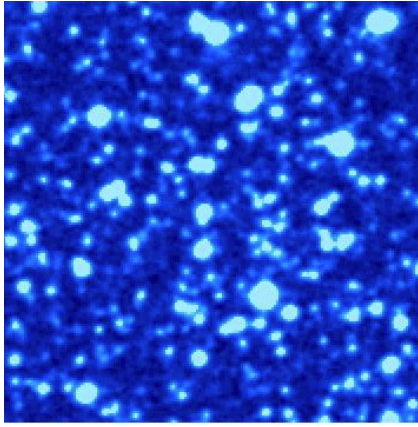


Figure A.86: PN 18:54:56 -30:14:08

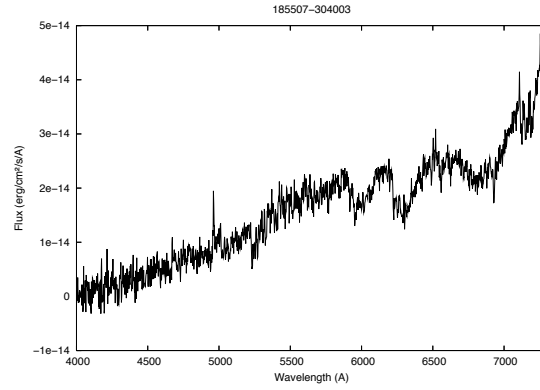
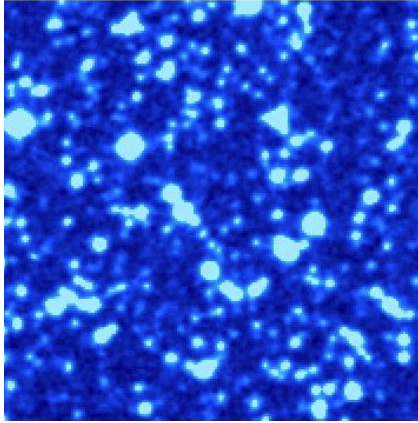


Figure A.87: PN 18:55:07 -30:40:03

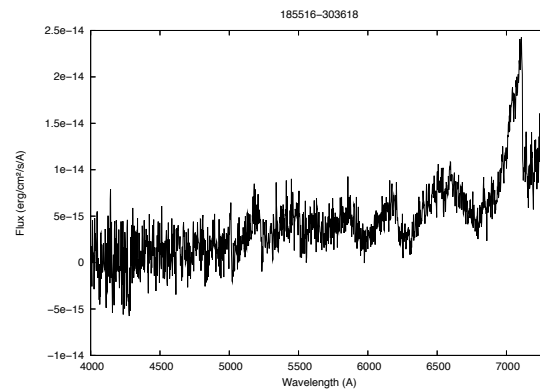
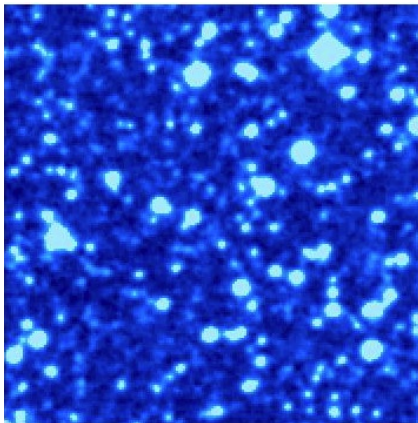


Figure A.88: PN 18:55:16 -30:36:18

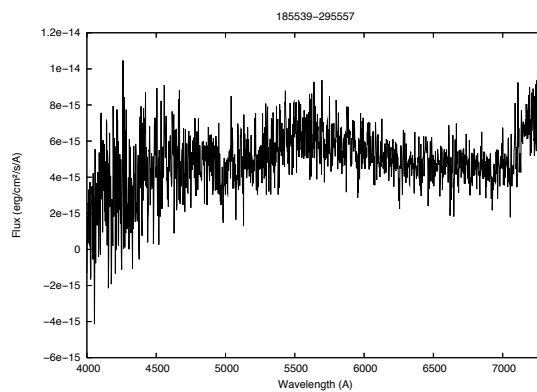
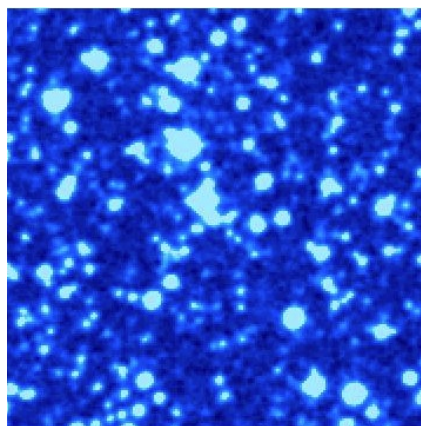


Figure A.89: PN 18:55:39 -29:55:57

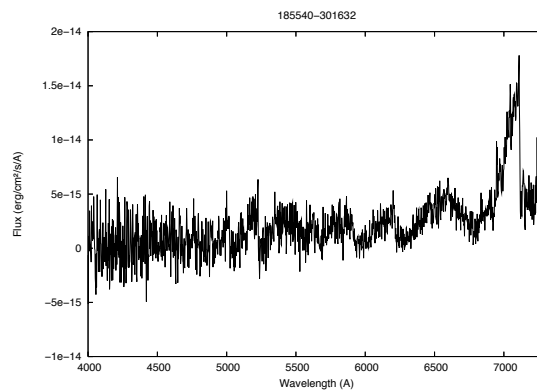
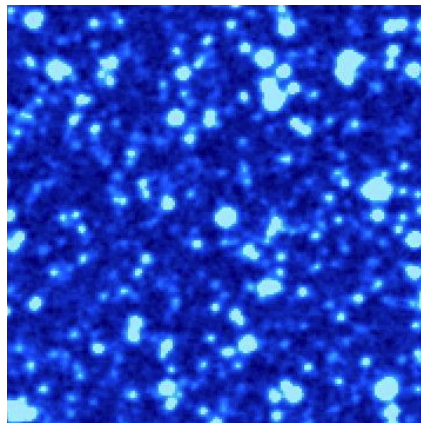


Figure A.90: PN 18:55:40 -30:16:32

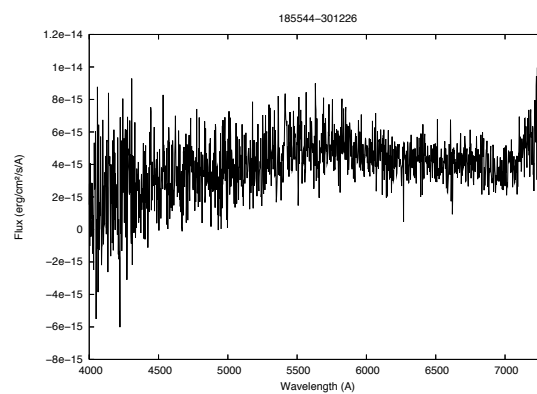
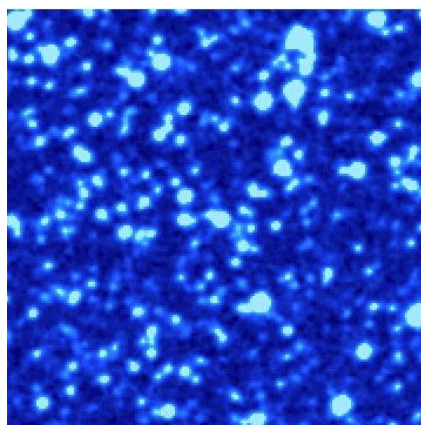


Figure A.91: PN 18:55:44 -30:12:26



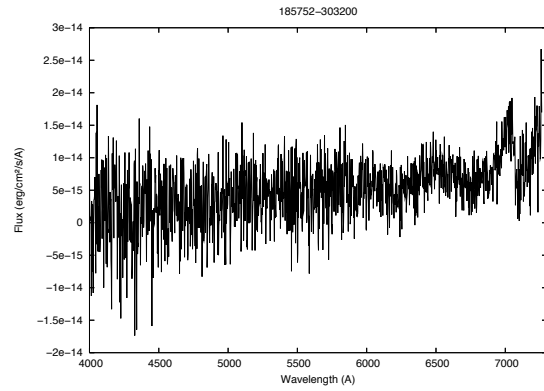
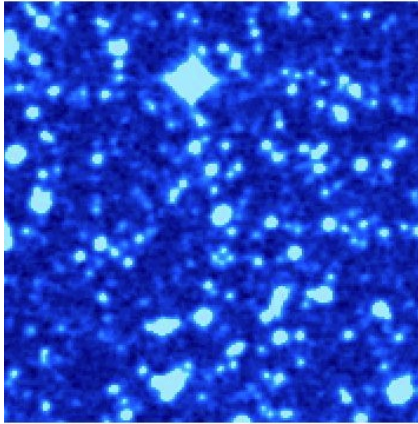


Figure A.92: PN 18:57:52 -30:32:00

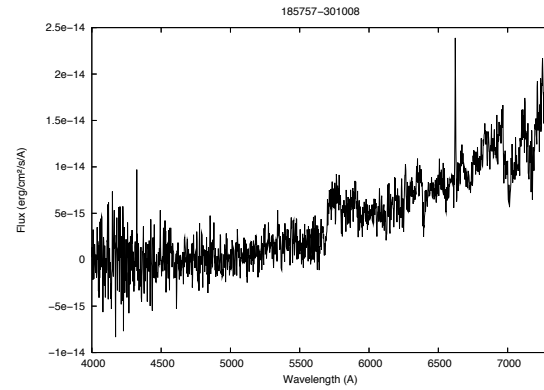
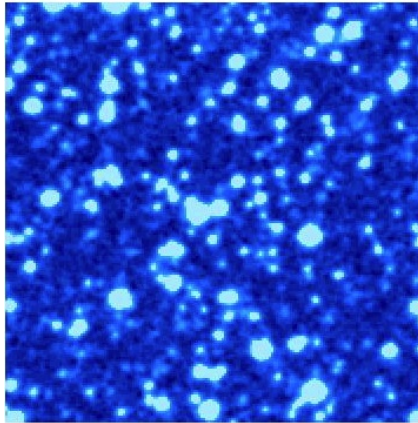


Figure A.93: PN 18:57:57 -30:10:08

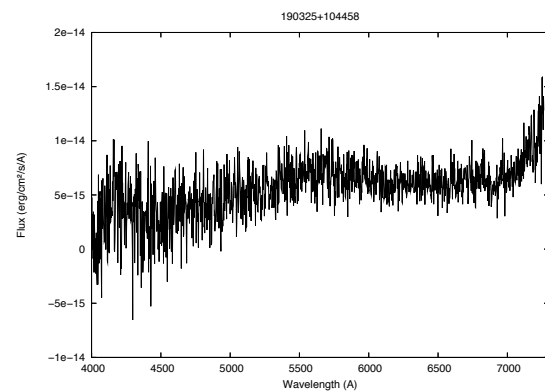
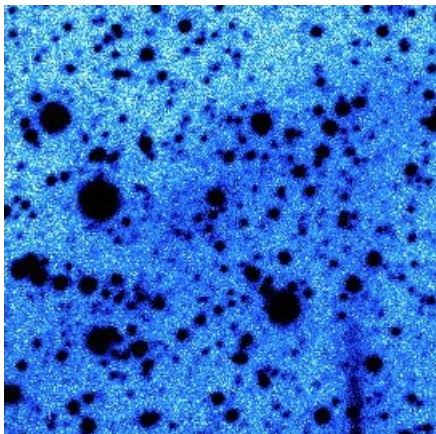


Figure A.94: PN 19:03:25 +10:44:58

## A: IPHAS OBJECT CLASSIFICATION

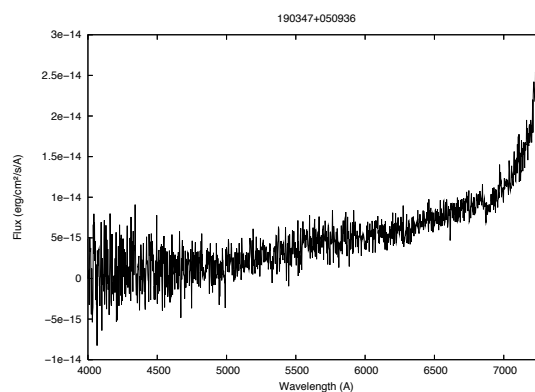
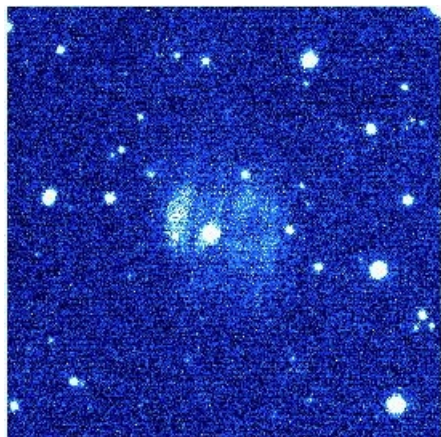


Figure A.95: PN 19:03:47 +05:09:36

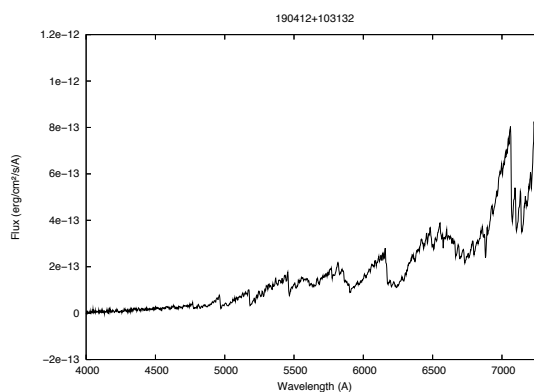
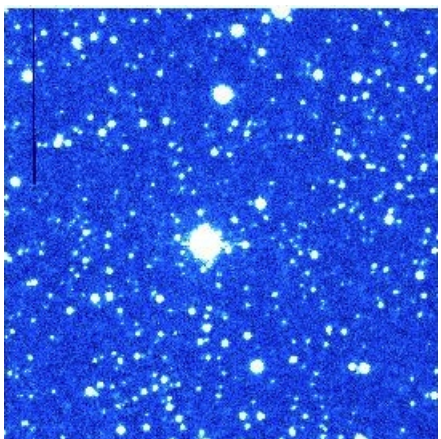


Figure A.96: PN 19:04:12 +10:31:32

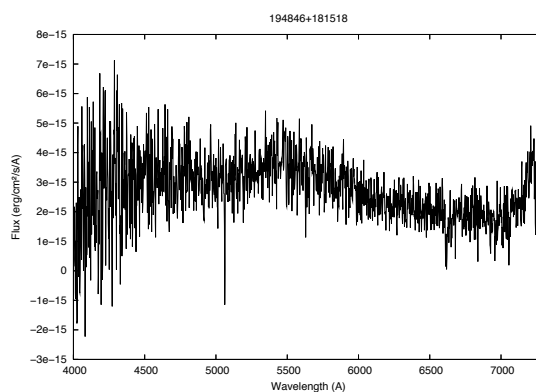


Figure A.97: PN 19:48:46 +18:15:18

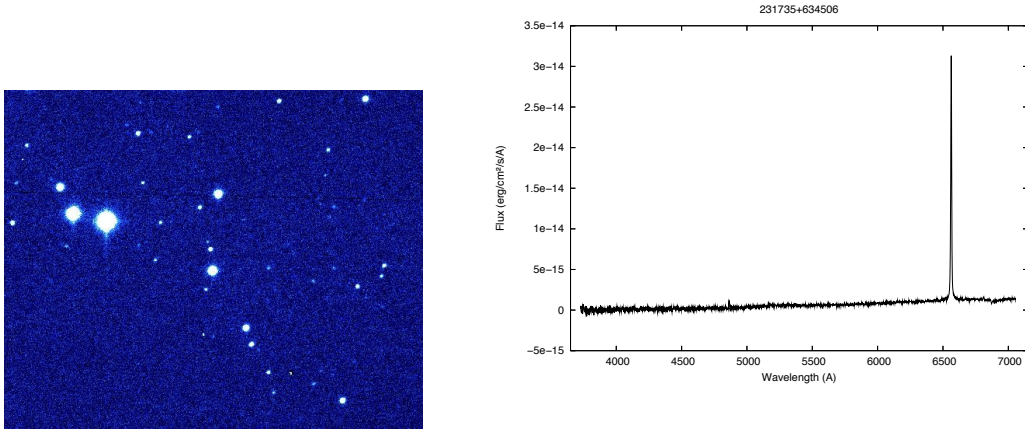


Figure A.98: PN 23:17:35 +63:45:06

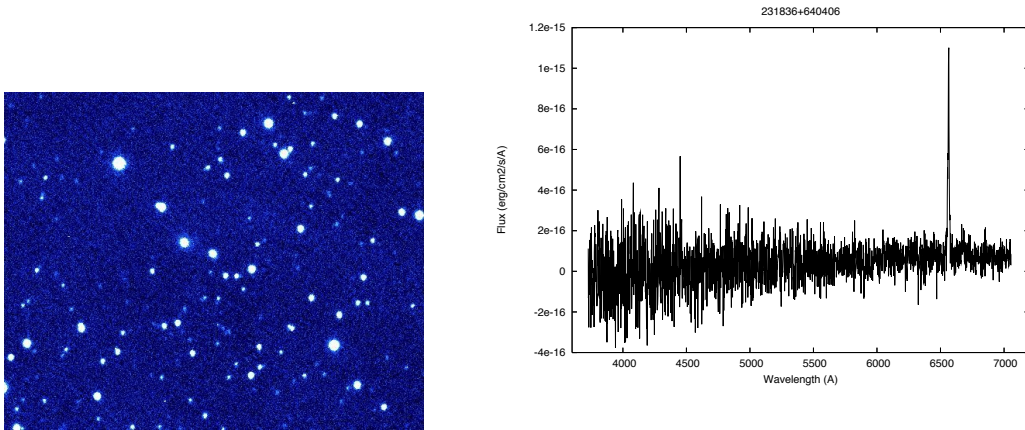


Figure A.99: PN 23:18:36 +64:04:06

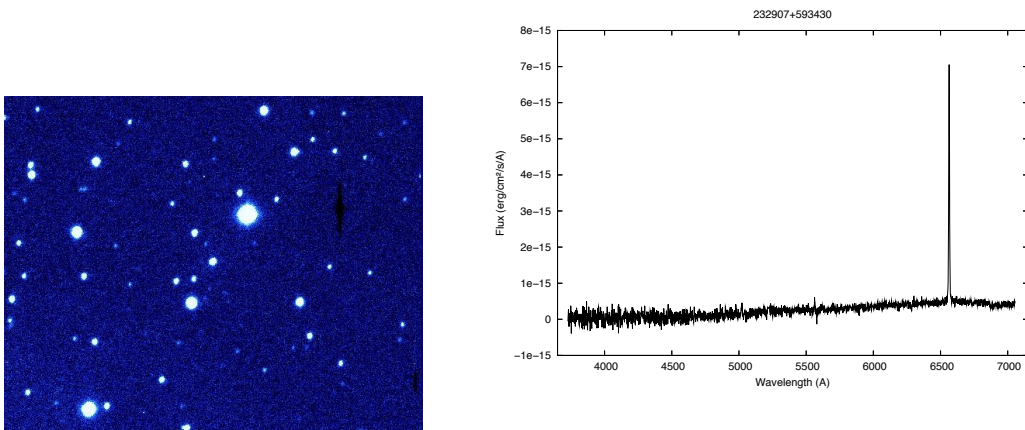


Figure A.100: PN 23:29:07 +59:34:30





# Appendix B

## IRAF data reduction

If you have never used IRAF before, this guide will try to show you how to reduce data, from scratch. This guide is only made to help on the data reduction process. For more information about IRAF and its tasks please see: A User's Guide to CCD Reductions with IRAF ([iraf.noao.edu/iraf/docs/ccduser3.ps.Z](http://iraf.noao.edu/iraf/docs/ccduser3.ps.Z)).

- **Step 1. Make the IRAF directory in your data file**

...example: `/local/scratch/LizData/2.1Obsr/`

...in the terminal write:

```
>mkiraf
```

Enter terminal: `xgterm` (best option for graphs and spectra)

⇒ this creates a `login.cl` file, that you can edit

- **Step 2. Edit the `login.cl` file**

```
>emacs login.cl &
```

Edit the parameters of the file like:

```
>set stdimage = imt4096
```

```
>set imtype = "fits"
```

Edit the packages that you want to open from the start, like:

```
noao
```

imred  
ccdred  
twodspec  
longslit  
!ds9 &  
ctr x+s to save the file

- **Step 3. Start IRAF**

...type in your terminal:

> xgterm & (it will automatically open an other terminal, type cl to start IRAF)

- **Step 4. Start the data reduction**

**Remove the overscan area**

>ls a\*.fits > all.lst (make a list of all the files)

>emacs all.lst (check the list to make sure you have all the data)

...make a new list with all the data but diff name

...we'll use an o at the end of each file referring to overscan

...go to Edit - Search - Replace

...replace:.fits = with: o.fits (make sure you are at the top of the list)

...press shift + 1 (!) so it will do it for all the files

...save the buffer as: allo.lst

>imhead xx.xx (file)

...find the overscan = [2323:2353,1:336]

>epar ccdproc

I R A F

Image Reduction and Analysis Facility

PACKAGE = ccdred

TASK = ccdproc

images = @all.lst List of CCD images to correct

(output = @allo.lst) List of output CCD images

(ccdtype= ) CCD image type to correct

(max\_cac= 0) Maximum image caching memory (in Mbytes)  
 (noprocc = no) List processing steps only?  
 (fixpix = no) Fix bad CCD lines and columns?  
 (oversca= yes) Apply overscan strip correction?  
 (trim = no) Trim the image?  
 (zerocor= no) Apply zero level correction?  
 (darkcor= no) Apply dark count correction?  
 (flatcor= no) Apply flat field correction?  
 (illumco= no) Apply illumination correction?  
 (fringe= no) Apply fringe correction?  
 (readcor= no) Convert zero level image to readout correction?  
 (scancor= no) Convert flat field image to scan correction?  
 (readaxi= ) Read out axis (column—line)  
 (fixfile= ) File describing the bad lines and columns  
 (biassec= [2323:2353,1:336]) Overscan strip image section  
 (trimsec= ) Trim data section  
 (zero = ) Zero level calibration image  
 (dark = ) Dark count calibration image  
 (flat = ) Flat field images  
 (illum = ) Illumination correction images  
 (fringe = ) Fringe correction images  
 (minrepl= 1.) Minimum flat field value  
 (scantyp= shortscan) Scan type (shortscan—longscan)  
 (nscan = 1) Number of short scan lines  
 (interac= yes) Fit overscan interactively?  
 (functio= legendre) Fitting function  
 (order = 1) Number of polynomial terms or spline pieces  
 (sample = \*) Sample points to fit  
 (naverag= 1) Number of sample points to combine  
 (niterat= 1) Number of rejection iterations  
 (low\_rej= 1.) Low sigma rejection factor

## B: IRAF DATA REDUCTION

(high\_re= 1.) High sigma rejection factor

(grow = 0.) Rejection growing radius

(mode = ql)

:wq (write and quit)

:go (to execute the task)

...because we said interac = yes

...it will ask us if we want to do the fit interactively and we will say yes for the first ones to check the fit, then we can assume the same for the others.

...once you said yes, it will open a graph window, with the fit that you choose (Legendre order 1), you can check, if is ok, then just type

:q (quit)

...if not, you can change the order of the polynomial

:order 2

then press f (to do the fit)

...check the fit, if is fine then q, ...and you can change the function as well

:fun chebyshev

f

:order 3

f

...check the fit and when you are satisfied then type q

...IRAF will ask you again for the next image, you can type no (don't show you this image, and then will ask for the next one, or if you don't want to check any other image, type NO)

⇒ will create new files with new names xxo.fits

### • Step 5. Subtract the bias

You need to create a Master bias (average of all the bias) first.

> files bias1.xx,bias2.xx,bias3.xx,bias4.xx,bias5.xx > bias.lst (create a list with all the bias)

```
> epar zerocomb
```

I R A F

Image Reduction and Analysis Facility

PACKAGE = ccdred

TASK = zerocombine

input = @bias.lst List of zero level images to combine

(output = Zero) Output zero level name

(combine= average) Type of combine operation

(reject = avsigclip) Type of rejection

(ccdtype= zero) CCD image type to combine

(process= no) Process images before combining?

(delete = no) Delete input images after combining?

(clobber= no) Clobber existing output image?

(scale = none) Image scaling

(statsec= ) Image section for computing statistics

(nlow = 0) minmax: Number of low pixels to reject

(nhigh = 1) minmax: Number of high pixels to reject

(nkeep = 1) Minimum to keep (pos) or maximum to reject (neg)

(mclip = yes) Use median in sigma clipping algorithms?

(lsigma = 3.) Lower sigma clipping factor

(hsigma = 3.) Upper sigma clipping factor

(rdnoise= 0.) ccdclip: CCD readout noise (electrons)

(gain = 1.) ccdclip: CCD gain (electrons/DN)

(snoise = 0.) ccdclip: Sensitivity noise (fraction)

(pclip = -0.5) pclip: Percentile clipping parameter

(blank = 0.) Value if there are no pixels

(mode = ql)

```
:go
```

⇒ will create a file called Zero.fits with the bias average image

Now you need to make a list of all the images that you want to subtract the bias

(no bias images here)  
>emacs allo.lst  
...edit the list, erase the bias and save it again = allbias.lst  
...then edit again the list for the output list, change the .fits to b.fits  
...and save the list again = allob.lst  
...now your files will have in their name the o (overscan) and a b (bias)

>epar ccdpro

I R A F

Image Reduction and Analysis Facility

PACKAGE = ccdred

TASK = ccdproc

images = @allbias.lst List of CCD images to correct

(output = @allob.lst) List of output CCD images

(ccdtype= ) CCD image type to correct

(max\_cac= 0) Maximum image caching memory (in Mbytes)

(noprocc = no) List processing steps only?

(fixpix = no) Fix bad CCD lines and columns?

(oversca= no) Apply overscan strip correction?

(trim = no) Trim the image?

(zerocor= yes) Apply zero level correction?

(darkcor= no) Apply dark count correction?

(flatcor= no) Apply flat field correction?

(illumco= no) Apply illumination correction?

(fringec= no) Apply fringe correction?

(readcor= no) Convert zero level image to readout correction?

(scancor= no) Convert flat field image to scan correction?

(readaxi= ) Read out axis (column—line)

(fixfile= ) File describing the bad lines and columns

(biassec= ) Overscan strip image section

(trimsec= ) Trim data section

(zero = Zero) Zero level calibration image  
 (dark = ) Dark count calibration image  
 (flat = ) Flat field images  
 (illum = ) Illumination correction images  
 (fringe = ) Fringe correction images  
 (minrepl= 1.) Minimum flat field value  
 (scantyp= shortscan) Scan type (shortscan—longscan)  
 (nscan = 1) Number of short scan lines  
 (interac= yes) Fit overscan interactively?  
 (functio= chebyshev) Fitting function  
 (order = 1) Number of polynomial terms or spline pieces  
 (sample = \*) Sample points to fit  
 (naverag= 1) Number of sample points to combine  
 (niterat= 1) Number of rejection iterations  
 (low\_rej= 1.) Low sigma rejection factor  
 (high\_re= 1.) High sigma rejection factor  
 (grow = 0.) Rejection growing radius  
 (mode = ql)  
 :go  
 ⇒ will create the new files xxob.fits

- **Step 6. Flats**

Make a list of all the flats, to combine them

```
>files xx.xx,xx.xx,xx.xx > domeflats.lst
```

...before you combine them, check every flat image, cause we'll combine them, but if one of several images are not good, then we wont use them, check the values are around 30 000 counts (good image).

```
>imexa @domeflats.lst
```

....check the counts, then press n (next)

## B: IRAF DATA REDUCTION

```
>epar flatcombine
I R A F
Image Reduction and Analysis Facility
PACKAGE = ccdred
TASK = flatcombine
input = @domeflats.lst List of flat field images to combine
(output = DomeFlat) Output flat field root name
(combine= average) Type of combine operation
(reject = avsigclip) Type of rejection
(ccdtype= flat) CCD image type to combine
(process= yes) Process images before combining?
(subsets= yes) Combine images by subset parameter?
(delete = no) Delete input images after combining?
(clobber= no) Clobber existing output image?
(scale = mode) Image scaling
(statsec= ) Image section for computing statistics
(nlow = 1) minmax: Number of low pixels to reject
(nhigh = 1) minmax: Number of high pixels to reject
(nkeep = 1) Minimum to keep (pos) or maximum to reject (neg)
(mclip = yes) Use median in sigma clipping algorithms?
(lsigma = 3.) Lower sigma clipping factor
(hsigma = 3.) Upper sigma clipping factor
(rdnoise= rdnoise) ccdclip: CCD readout noise (electrons)
(gain = gain) ccdclip: CCD gain (electrons/DN)
(snoise = 0.) ccdclip: Sensitivity noise (fraction)
(pclip = -0.5) pclip: Percentile clipping parameter
(blank = 1.) Value if there are no pixels
(mode = ql)
:go
⇒ will create the file DomeFlat.fits
...check the result image
```



```
>display DomeFlat.fits 1
```

...normalisation of the flats (IRAF will divide the flats by a function to normalise the values so you can use the normalised fit and divide the images, to correct pixel to pixel variations)

```
>epar response
```

I R A F

Image Reduction and Analysis Facility

PACKAGE = longslit

TASK = response

calibrat= DomeFlat Longslit calibration images

normaliz= DomeFlat Normalization spectrum images

response= nDomeFlat Response function images

(interac= yes) Fit normalization spectrum interactively?

(thresho= INDEF) Response threshold

(sample = \*) Sample of points to use in fit

(naverag= 1) Number of points in sample averaging

(functio= spline3) Fitting function

(order = 1) Order of fitting function

(low\_rej= 3.) Low rejection in sigma of fit

(high\_re= 3.) High rejection in sigma of fit

(niterat= 1) Number of rejection iterations

(grow = 0.) Rejection growing radius

(graphic= stdgraph) Graphics output device

(cursor = ) Graphics cursor input

(mode = ql)

```
:go
```

...since we said yes to interact, we'll need to check the fit, and change it if we want to

```
:order 2
```

```
f
```

## B: IRAF DATA REDUCTION

```
:order 3
f
...till we're happy with the fit, and then just press q (quit)
⇒ will create the file nDomeFlat.fits
...when it finishes check the nDomeFlat image, just to see if everything is fine
(values around 1)
>display nDomeFlat.fits 2
...then we need to do the Flat-Field division
...make a list of all the images you want to do the flat division (no bias, no flats)
>emacs allo.lst
...edit the list and erase the flats
...save it with a new name = flats.lst
...now use the replace task in emacs to add another letter to the file name
...replace: .fits with: f.fits
....save the list = allobf.lst (now the f stands for flats correction)

>epar ccdproc
I R A F
Image Reduction and Analysis Facility
PACKAGE = ccdred
TASK = ccdproc
images = @flats.lst List of CCD images to correct
(output = @allobf.lst) List of output CCD images
(ccdtype= ) CCD image type to correct
(max_cac= 0) Maximum image caching memory (in Mbytes)
(noproc = no) List processing steps only?
(fixpix = no) Fix bad CCD lines and columns?
(oversca= no) Apply overscan strip correction?
(trim = no) Trim the image?
(zeroacor= no) Apply zero level correction?
(darkcor= no) Apply dark count correction?
```

(flatcor= yes) Apply flat field correction?  
 (illumco= no) Apply illumination correction?  
 (fringe= no) Apply fringe correction?  
 (readcor= no) Convert zero level image to readout correction?  
 (scancor= no) Convert flat field image to scan correction?  
 (readaxi= ) Read out axis (column—line)  
 (fixfile= ) File describing the bad lines and columns  
 (biassec= [2323:2353,1:336]) Overscan strip image section  
 (trimsec= ) Trim data section  
 (zero = Zero) Zero level calibration image  
 (dark = ) Dark count calibration image  
 (flat = nDomeFlat) Flat field images  
 (illum = ) Illumination correction images  
 (fringe = ) Fringe correction images  
 (minrepl= 1.) Minimum flat field value  
 (scantyp= shortscan) Scan type (shortscan—longscan)  
 (nscan = 1) Number of short scan lines  
 (interac= yes) Fit overscan interactively?  
 (functio= chebyshev) Fitting function  
 (order = 1) Number of polynomial terms or spline pieces  
 (sample = \*) Sample points to fit  
 (naverag= 1) Number of sample points to combine  
 (niterat= 1) Number of rejection iterations  
 (low\_rej= 3.) Low sigma rejection factor  
 (high\_re= 3.) High sigma rejection factor  
 (grow = 0.) Rejection growing radius  
 (mode = ql)  
 :go  
 ⇒ will create the new files xxobf.fits

- **Step 7. Remove bad columns**

...make a list of the bad columns that we need to erase  
>emacs fixpix.lst  
...use the flat image to find the bad columns, and play with the scales usign ds9  
...in the file we'll need to put the x1,x2,y1,y2 values of each column  
...x1=203 x2=206 y1=1 y2=336 (this mean erase the column between 203-206 in  
x axis and from 1-336 in the y axis)  
....in the file you only need to put the numbers without the x1,x2,y1,y2...only  
separated by a space.  
...make a new list with the images...edit the allobf.lst  
>emacs allobf.lst  
...replace:.fits with: p.fits (the p is for bad pixels)  
...save = allobfp.lst

>epar ccdproc

I R A F

Image Reduction and Analysis Facility

PACKAGE = ccdred

TASK = ccdproc

images = @allobf.lst List of CCD images to correct

(output = @allobfp.lst) List of output CCD images

(ccdtype= ) CCD image type to correct

(max\_cac= 0) Maximum image caching memory (in Mbytes)

(noprocc = no) List processing steps only?

(fixpix = yes) Fix bad CCD lines and columns?

(oversca= no) Apply overscan strip correction?

(trim = no) Trim the image?

(zerocor= no) Apply zero level correction?

(darkcor= no) Apply dark count correction?

(flatcor= no) Apply flat field correction?

(illumco= no) Apply illumination correction?

(fringec= no) Apply fringe correction?  
 (readcor= no) Convert zero level image to readout correction?  
 (scancor= no) Convert flat field image to scan correction?  
 (readaxi= ) Read out axis (column—line)  
 (fixfile= fixpix.lst) File describing the bad lines and columns  
 (biassec= [2323:2353,1:336]) Overscan strip image section  
 (trimsec= ) Trim data section  
 (zero = Zero) Zero level calibration image  
 (dark = ) Dark count calibration image  
 (flat = nDomeFlat) Flat field images  
 (illum = ) Illumination correction images  
 (fringe = ) Fringe correction images  
 (minrepl= 1.) Minimum flat field value  
 (scantyp= shortscan) Scan type (shortscan—longscan)  
 (nscan = 1) Number of short scan lines  
 (interac= yes) Fit overscan interactively?  
 (functio= chebyshev) Fitting function  
 (order = 1) Number of polynomial terms or spline pieces  
 (sample = \*) Sample points to fit  
 (naverag= 1) Number of sample points to combine  
 (niterat= 1) Number of rejection iterations  
 (low\_rej= 3.) Low sigma rejection factor  
 (high\_re= 3.) High sigma rejection factor  
 (grow = 0.) Rejection growing radius  
 (mode = ql)  
 :go  
 ⇒ will create the new images without the bad columns = xxobfp.fits

- **Step 8. Trim the images**

...to trim the images from the bias and areas that we don't need

```
...make a new list with the new name
>emacs allobfp.lst
...replace: .fits with: t.fits
...save = allobfpt.lst
>display xx.xx (image-source) and check the size you'd prefer = [20:2290,40:310]

>epar ccdproc
I R A F
Image Reduction and Analysis Facility
PACKAGE = ccdred
TASK = ccdproc
images = @allobfp.lst List of CCD images to correct
(output = @allobfpt.lst) List of output CCD images
(ccdtype= ) CCD image type to correct
(max_cac= 0) Maximum image caching memory (in Mbytes)
(noproc = no) List processing steps only?
(fixpix = no) Fix bad CCD lines and columns?
(oversca= no) Apply overscan strip correction?
(trim = yes) Trim the image?
(zero = Zero) Zero level calibration image
(zero = no) Apply zero level correction?
(darkcor= no) Apply dark count correction?
(flatcor= no) Apply flat field correction?
(illumco= no) Apply illumination correction?
(fringec= no) Apply fringe correction?
(readcor= no) Convert zero level image to readout correction?
(scancor= no) Convert flat field image to scan correction?
(readaxi= line) Read out axis (column—line)
(fixfile= fixpix.lst) File describing the bad lines and columns
(biassec= [2323:2353,1:336]) Overscan strip image section
(trimsec= [20:2290,40:310]) Trim data section
(zero = Zero) Zero level calibration image
```

(dark = ) Dark count calibration image  
 (flat = nDomeFlat) Flat field images  
 (illum = ) Illumination correction images  
 (fringe = ) Fringe correction images  
 (minrepl= 1.) Minimum flat field value  
 (scantyp= shortscan) Scan type (shortscan—longscan)  
 (nscan = 1) Number of short scan lines  
 (interac= yes) Fit overscan interactively?  
 (functio= chebyshev) Fitting function  
 (order = 1) Number of polynomial terms or spline pieces  
 (sample = \*) Sample points to fit  
 (naverag= 1) Number of sample points to combine  
 (niterat= 1) Number of rejection iterations  
 (low\_rej= 3.) Low sigma rejection factor  
 (high\_re= 3.) High sigma rejection factor  
 (grow = 0.) Rejection growing radius  
 (mode = ql)  
 :go  
 ⇒ will create the new files xxobfpt.fits (the t stands for trimmed)

- **Step 9. Remove cosmic rays**

...to clean the images from cosmic ray, we need to use a program that we can find on the web

...Google: LA Cosmic

...copy and paste the script and save it with the name = lacos\_spec.cl

...once you have the script in the same directory of the IRAF and your data, go back to the xgterm terminal

...this task can work with a list, but we'll try to use it with each image at a time.

>stsdas

>task lacos\_spec = lacos\_spec.cl

```
>epar lacos_spec
I R A F
Image Reduction and Analysis Facility
PACKAGE = clpackage
TASK = lacos_spec
input = a0030obfpt.fits input spectrum
output = a0030obfptc.fits cosmic ray cleaned output spectrum
outmask = a0030obfptc.pl output bad pixel map (.pl)
(gain = 1.4) gain (electrons/ADU)
(readn = 8.5) read noise (electrons)
(xorder = 0) order of object fit (0=no fit)
(yorder = 0) order of sky line fit (0=no fit)
(sigclip= 2.5) detection limit for cosmic rays (sigma)
(sigfrac= 0.2) fractional detection limit for neighbouring pixels
(objlim = 1.) contrast limit between CR and underlying object
(niter = 2) maximum number of iterations
(verbose= yes)
(mode = ql)
:go
⇒ will make the new file xxobfptc.fits (the c stands for cosmic ray)
...do this for each image (source only)
```

- **Step 10. Wavelength calibration**

...the task we'll use is identify, and to do this we need to load the list of lines that we need, according to the lamp that we use for the arcs observations, in our case we used HeNeAr lamp, so in the IRAF list we'll use the `henear.dat` list, and the task will create a directory (`database=default`) but we'll need to change the name cause we have lots of objects and we don't want to get confused so we'll put the name of the object.

...to do the line identification we first need to plot the arc image and compare



it with the spectrum in which we already have the line identification done (plot that your support astronomer should give you the first day).

>cd linelist (in the cl terminal, will show you all the line lists that IRAF has)

>splot xx.xx (name of the arc file)

...line(150): yes

...to zoom in use a & a

...to fit a function use d & d at each side of the line and then g (to fit a gaussian)

...go to peak of the line and press g

...q (quit)

...s (single)

...s (single)

...check the gfwhm (in our case was 3, we'll use this value in the identify task)

...use - & - on each side of the line to subtract the line and see the fit

...c (clear)

...# (to go to the original spectra)

>epar identify

I R A F

Image Reduction and Analysis Facility

PACKAGE = longslit

TASK = identify

images = a0025obfpt.fits Images containing features to be identified

(section= middle line) Section to apply to two dimensional images

(databas= PN6.2) Database in which to record feature data

(coordli= linelists\$henear.dat) User coordinate list

(units = ) Coordinate units

(nsum = 10) Number of lines/columns/bands to sum in 2D images

(match = 10.) Coordinate list matching limit

(maxfeat= 50) Maximum number of features for automatic identification

(zwidth = 100.) Zoom graph width in user units

(ftype = emission) Feature type  
(fwidth = 3.5) Feature width in pixels  
(cradius= 5.) Centering radius in pixels  
(thresho= 10.) Feature threshold for centering  
(minsep = 2.) Minimum pixel separation  
(functio= spline3) Coordinate function  
(order = 1) Order of coordinate function  
(sample = \*) Coordinate sample regions  
(niterat= 1) Rejection iterations  
(low\_rej= 3.) Lower rejection sigma  
(high\_re= 3.) Upper rejection sigma  
(grow = 0.) Rejection growing radius  
(autowri= no) Automatically write to database  
(graphic= stdgraph) Graphics output device  
(cursor = ) Graphics cursor input  
crval = Approximate coordinate (at reference pixel)  
cdelt = Approximate dispersion  
(aidpars= ) Automatic identification algorithm parameters  
(mode = al)

:go

...the program will show us the arc spectra and we'll need to identify the lines.

...put the cursor in the line press m

...write the wavelength number (if the line is in the `henear.dat` list, it will give you the name of the element)

...then find an other line and do the same m, and write the number

...the same for 4 or 5 lines

...then press f (fit), check the fit is the values for the fit are small (0.2-0.5) is a good fit, if not, change the function and/or the order.

...q if you're happy

...it will give you the same plot but now with wavelength units

...l to identify all the lines

...f to fit again (check again the numbers, and change the order and/or function if needed)

...q (quit)

>yes (it will save the changes, fit and the wavelength units)

>epar reidentify

I R A F

Image Reduction and Analysis Facility

PACKAGE = longslit

TASK = reidentify

referenc= a0025obfpt.fits Reference image

images = a0025obfpt.fits Images to be reidentified

(interac= yes) Interactive fitting?

(section= middle line) Section to apply to two dimensional images

(newaps = yes) Reidentify apertures in images not in reference?

(overrid= yes) Override previous solutions?

(refit = yes) Refit coordinate function?

(trace = no) Trace reference image?

(step = 10) Step in lines/columns/bands for tracing an image

(nsum = 10) Number of lines/columns/bands to sum

(shift = 0.) Shift to add to reference features (INDEF to search)

(search = 0.) Search radius

(nlost = 100) Maximum number of features which may be lost

(cradius= 5.) Centering radius

(thresho= 10.) Feature threshold for centering

(addfeat= no) Add features from a line list?

(coordli= linelists\$henear.dat) User coordinate list

(match = 10.) Coordinate list matching limit

(maxfeat= 50) Maximum number of features for automatic identification

(minsep = 2.) Minimum pixel separation

(databas= PN6.2) Database

## B: IRAF DATA REDUCTION

(logfile= logfile) List of log files  
(plotfil= ) Plot file for residuals  
(verbose= yes) Verbose output?  
(graphic= stdgraph) Graphics output device  
(cursor = ) Graphics cursor input  
answer = NO Fit dispersion function interactively?  
crval = Approximate coordinate (at reference pixel)  
cdelt = Approximate dispersion  
(aidpars= ) Automatic identification algorithm parameters  
(mode = al)  
:go  
...it will show us again the plot and the fit, we should check the fit  
...q  
...q  
>NO (if you don't want the interactive mode anymore)  
...at the end it will give you the number of lines identified.

>epar fitcoords

I R A F

Image Reduction and Analysis Facility

PACKAGE = longslit

TASK = fitcoords

images = a0025obfpt Images whose coordinates are to be fit  
(fitname= a0025obfpt) Name for coordinate fit in the database  
(interac= yes) Fit coordinates interactively?  
(combine= no) Combine input coordinates for a single fit?  
(databas= PN6\_2) Database  
(deletio= deletions.db) Deletion list file (not used if null)  
(functio= chebyshev) Type of fitting function  
(xorder = 6) X order of fitting function  
(yorder = 6) Y order of fitting function

(logfile= STDOUT,logfile) Log files  
 (plotfil= plotfile) Plot log file  
 (graphic= stdgraph) Graphics output device  
 (cursor = ) Graphics cursor input  
 (mode = al)  
 :go  
 ...check the fit, you can erase any point that is really far from the fit (if they are just a few points)  
 ...to erase the point, put the cursor on it  
 ...press d (delete)  
 ...p (point)  
 ...you can plot diff residuals, x vs y, x vs r, y vs r  
 ...to do that press x-x axis and then what you want to be plotted in the x axis (x), y-y axis and whatever you want to plot in the y axis (r-residuals)  
 ...xx, yr (will give you the plot with x vs residuals)  
 >yes (to save the fit)  
 ...next task, transform, we'll use this task twice, first to apply the calibration to the arc image, and then to the real object image  
  
 >epar transform  
 I R A F  
 Image Reduction and Analysis Facility  
 PACKAGE = longslit  
 TASK = transform  
 input = a0025obfptc.fits Input images  
 output = a0025obfptcw Output images  
 (minput = ) Input masks  
 (moutput= ) Output masks  
 fitnames= a0025obfpta0025obfpt Names of coordinate fits in the database  
 (databas= PN6.2) Identify database  
 (interpt= spline3) Interpolation type

## B: IRAF DATA REDUCTION

(x1 = INDEF) Output starting x coordinate  
(x2 = INDEF) Output ending x coordinate  
(dx = INDEF) Output X pixel interval  
(nx = INDEF) Number of output x pixels  
(xlog = no) Logarithmic x coordinate?  
(y1 = INDEF) Output starting y coordinate  
(y2 = INDEF) Output ending y coordinate  
(dy = INDEF) Output Y pixel interval  
(ny = INDEF) Number of output y pixels  
(ylog = no) Logarithmic y coordinate?  
(flux = yes) Conserve flux per pixel?  
(blank = INDEF) Value for out of range pixels  
(logfile= STDOUT,logfile) List of log files  
(mode = al)  
;go  
⇒ will create a new file called xxobfptcw with the w meaning wavelength calibration  
...check the image  
>spplot a0025obfptcw.fits and check two or three lines, in the edges of the plot, and within diff lines, so we can see if they have almost the same wavelength, if everything is fine, then apply the calibration for the object.  
  
>epar transform  
I R A F  
Image Reduction and Analysis Facility  
PACKAGE = longslit  
TASK = transform  
input = a0024obfptc.fits Input images  
output = a0024obfptcw Output images  
(minput = ) Input masks  
(moutput= ) Output masks

```

fitnames= a0025obfpta0025obfpt Names of coordinate fits in the database
(databas= PN6.2) Identify database
(interpt= spline3) Interpolation type
(x1 = INDEF) Output starting x coordinate
(x2 = INDEF) Output ending x coordinate
(dx = INDEF) Output X pixel interval
(nx = INDEF) Number of output x pixels
(xlog = no) Logarithmic x coordinate?
(y1 = INDEF) Output starting y coordinate
(y2 = INDEF) Output ending y coordinate
(dy = INDEF) Output Y pixel interval
(ny = INDEF) Number of output y pixels
(ylog = no) Logarithmic y coordinate?
(flux = yes) Conserve flux per pixel?
(blank = INDEF) Value for out of range pixels
(logfile= STDOUT,logfile) List of log files
(mode = al)
:go
⇒ will create a spectrum that is wavelength calibrated (happy times).
>splot a0024obfptcw.fits
...plot the line in which the object has the emission (ei. 135): yes
...analyse the lines

```

- **Step 11. Background subtraction**

...we first need to check in the object image the background parts without any kind of emission, parts completely clean from star, sky or some kind of emission, parts with a flat background, and then write them, lines on the y axis. The task will make an average image of the background and then it will subtract it from the real image.

...this is an example of the lines clean from my first image:

## B: IRAF DATA REDUCTION

1:20,27:40,64:86,170:181,219:230,237:255

>epar background

I R A F

Image Reduction and Analysis Facility

PACKAGE = longslit

TASK = background

input = a0024obfptcw.fits Input images to be background subtracted

output = a0024obfptcwg.fits Output background subtracted images

(axis = 2) Axis along which background is fit and subtracted

(interac= yes) Set fitting parameters interactively?

(sample = \*) Sample of points to use in fit

(naverag= 1) Number of points in sample averaging

(functio= chebyshev) Fitting function

(order = 1) Order of fitting function

(low\_rej= 0.) Low rejection in sigma of fit

(high\_re= 0.) High rejection in sigma of fit

(niterat= 1) Number of rejection iterations

(grow = 0.) Rejection growing radius

(graphic= stdgraph) Graphics output device

(cursor = ) Graphics cursor input

(mode = al)

:wq

...we need to put the numbers outside the epar commands cause we have a long line, so we can do that outside the window

>background sample="1:20,27:40,64:86,170:181,219:230,237:255"

...it will show us the plot and the fit that is using, we can change it if we want to.

...:order 2

...f

...:fun chebyshev



...f

...q (when we're happy with the fit)

⇒ it will create the new image `xxobfptcwg.fits` (g from background).

- **Step 12. Flux Calibration**

>onedstds

>cd onedstds...open the README file and look for the file that has the standard star.

...in this case we used `eg274` as a standard star, is in the directory:

`onedstds$ctiocal/`

>epar airmass

I R A F

Image Reduction and Analysis Facility

PACKAGE = onedspec

TASK = setairmass

images = a0065obfptcwg.fits Input images

(observa= )\_observatory) Observatory for images

(intype = beginning) Input keyword time stamp

(outtype= effective) Output airmass time stamp

(ra = ra) Right ascension keyword (hours)

(dec = dec) Declination keyword (degrees)

(equinox= epoch) Equinox keyword (years)

(st = st) Local sidereal time keyword (hours)

(ut = ut) Universal time keyword (hours)

(date = date-obs) Observation date keyword

(exposur= exptime) Exposure time keyword (seconds)

(airmass= airmass) Airmass keyword (output)

(utmiddl= utmiddle) Mid-observation UT keyword (output)

(scale = 750.) The atmospheric scale height

## B: IRAF DATA REDUCTION

```
(show = yes) Print the airmasses and mid-UT?
(update = yes) Update the image header?
(override= yes) Override previous assignments?
(mode = ql)
:go
⇒ IRAF will return this messages:
...Image UT middle effective begin middle end updated
...SETAIRMAS: Observatory parameters for Kitt Peak National Observatory
...latitude = 31:57.8
...a0065obfptcwg.fits 6:42:15.7 1.1169 1.0977 1.1161 1.1395 yes

>epar kpnoslit
I R A F
Image Reduction and Analysis Facility
PACKAGE = imred
TASK = kpnoslit
(extinct= onedstdskpnoextinct.dat)Extinctionfile
(caldir = onedstdsoke1990/) Standard star calibration directory
(observa= observatory) Observatory of data
(interp = poly5) Interpolation type
(dispxi= 2) Image axis for 2D/3D images
(nsum = 1) Number of lines/columns/bands to sum for 2D/3D images
(databas= database) Database
(verbose= no) Verbose output?
(logfile= logfile) Log file
(plotfil= ) Plot file
(records= ) Record number extensions
(version= KPNOSLIT V3: January 1992)
(mode = ql)
:go
```

```

>epar standard
I R A F
Image Reduction and Analysis Facility
PACKAGE = longslit
TASK = standard
input = Input image file root name
output = std Output flux file (used by SENSFUNC)
(samesta= yes) Same star in all apertures?
(beam_sw= no) Beam switch spectra?
(apertur= ) Aperture selection list
(bandwid= INDEF) Bandpass widths
(bandsep= INDEF) Bandpass separation
(fnuzero= 3.6800000000000E-20) Absolute flux zero point
(extinct= onedstdskpnoextinct.dat)..extinction)Extinction file
(caldir = onedstdsoke1990/)..caldir) Directory containing calibration data
(observa= )..observatory) Observatory for data
(interac= yes) Graphic interaction to define new bandpasses
(graphic= stdgraph) Graphics output device
(cursor = ) Graphics cursor input
star_nam= eg274 Star name in calibration list
airmass = Airmass
exptime = Exposure time (seconds)
mag = Magnitude of star
magband = Magnitude type
teff = Effective temperature or spectral type
answer = no (no—yes—NO—YES—NO!—YES!)
(mode = ql)
:go
⇒ will create the std file.

>epar sensfunc

```

## B: IRAF DATA REDUCTION

I R A F

Image Reduction and Analysis Facility

PACKAGE = longslit

TASK = sensfunc

standard= std Input standard star data file (from STANDARD)

sensitiv= sens Output root sensitivity function imagename

(apertur= ) Aperture selection list

(ignorea= yes) Ignore apertures and make one sensitivity function?

(logfile= logfile) Output log for statistics information

(extinct= onedstds\$kpnoextinct.dat )\_extinction) Extinction file

(newexti= extinct.dat) Output revised extinction file

(observa= )\_observatory) Observatory of data

(functio= spline3) Fitting function

(order = 6) Order of fit

(interac= yes) Determine sensitivity function interactively?

(graphs = sr) Graphs per frame

(marks = plus cross box) Data mark types (marks deleted added)

(colors = 2 1 3 4) Colors (lines marks deleted added)

(cursor = ) Graphics cursor input

(device = stdgraph) Graphics output device

answer = yes (no—yes—NO—YES)

(mode = ql)

:go

⇒ will create the sens file.

...make a list of all the images you want to flux calibrate

>files xxg.fits > examples

>epar calibrate

I R A F

Image Reduction and Analysis Facility

PACKAGE = longslit

```

TASK = calibrate
input = @examples Input spectra to calibrate
output = c//@examples Output calibrated spectra
(extinct= yes) Apply extinction correction?
(flux = yes) Apply flux calibration?
(extinct= onedstds$kpnoextinct.dat) Extinction file
(observa= )..observatory) Observatory of observation
(ignorea= yes) Ignore aperture numbers in flux calibration?
(sensiti= sens) Image root name for sensitivity spectra
(fnu = no) Create spectra having units of FNU?
(mode = ql)
:go
⇒ will give you a flux calibrated image. This files will have a c (calibrated) in
front of the name file.

```

- **Extra commands that you may use:**

...in case you have done some of the tasks wrong, IRAF won't let you do the task again, until you change the header, so to do that you need:

```
>epar hedit
```

```
I R A F
```

```
Image Reduction and Analysis Facility
```

```
PACKAGE = imutil
```

```
TASK = hedit
```

```
images = @allobfp.lst images to be edited
```

```
fields = TRIM fields to be edited
```

```
value = value expression
```

```
(add = no) add rather than edit fields
```

```
(addonly= no) add only if field does not exist
```

```
(delete = no) delete rather than edit fields
```

```
(verify = yes) verify each edit operation
```

```
(show = yes) print record of each edit operation
```

```
(update = yes) enable updating of the image header
```

```
(mode = al)
```

```
:go
```

...it will change the trim section and you can do now a new trim if you need it

...it will also work for other fields = overscan, zero, flats, etc.

```
cp -r = to copy all the files
```

```
logout = logout from IRAF
```

```
>twospec
```

```
...apextract. longslit. (gives you all the packages you can use)
```

```
>longslit (gives you all the task you can use)
```

```
>epar splot (to execute a task)
```

```
:wq (write and quit)
```

```
:go (do the task)
```

```
>ls (list all the files in the directory)
```

```
>display xxx.fits 1 (use ds9 to display the images in the frame no.1..ds9 has 16
```

frames)  
...in ds9 you can match different frames  
...go to FRAME - Match Frames - Image  
...FRAME - Match colorbars  
>imexa (you can examine the flux (median) of your data)  
...select the region you want to measure and then press m (main)  
...you can press n (next) or p (previous) and then m again, and it will give you  
the flux in each frame, so you can compare  
...q (quit)  
>imhead xx.fits (to see the header of the file, short version)  
>imhea xx.fits lo+ —page (to see the header long version)  
>implot xx.xx 171 (line for the cut)  
...use a & a again to zoom in in some region  
...c to clear





# Appendix C

## *Spitzer* spectra of GBPNe

In here the complete sample of spectra of all the GBPNe observed by *Spitzer* is presented. All the spectra were taken with the Infrared Spectrograph (IRS) (Houck et al. 2004). The spectra cover a range between 5.2-37.2 $\mu$ m by using the Short-Low (SL: 5.2-14.5 $\mu$ m;  $64 < R < 128$ ), Short-High (SH: 9.9-19.6 $\mu$ m;  $R \sim 600$ ) and Long-High (LH: 18.7-37.2 $\mu$ m;  $R \sim 600$ ) modules. The data were retrieved from the *Spitzer* Science Centre Data Archive using Leopard. The *Spitzer* IRS Custom Extractor (SPICE) was used to do the extraction of the spectra for each nod position from the 2D images. All spectra were cleaned for bad data points, spurious jumps and glitches, and then they were combined and merged to create a single 5–37 $\mu$ m spectrum. We did not correct for flux offsets between different wavelengths ranges but these are minor. Offsets can be caused by the fact that the different wavelength ranges use different slits, and our objects have sizes similar to or larger than the slit widths.

On the left side the complete 5–37 $\mu$ m spectra is presented and in the right side the short wavelength spectra is presented, this is for a clearer view of the PAHs bands. The short wavelength spectra was created using only the SL settings of the IRS.

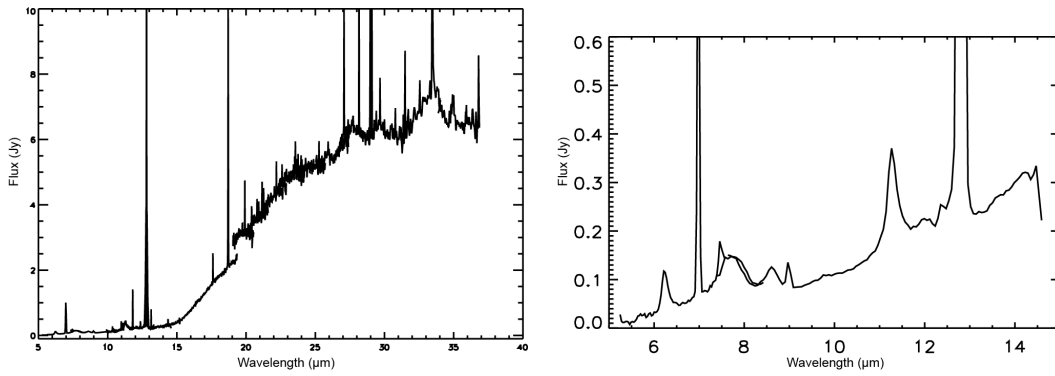


Figure C.1: PN G000.0 -06.8

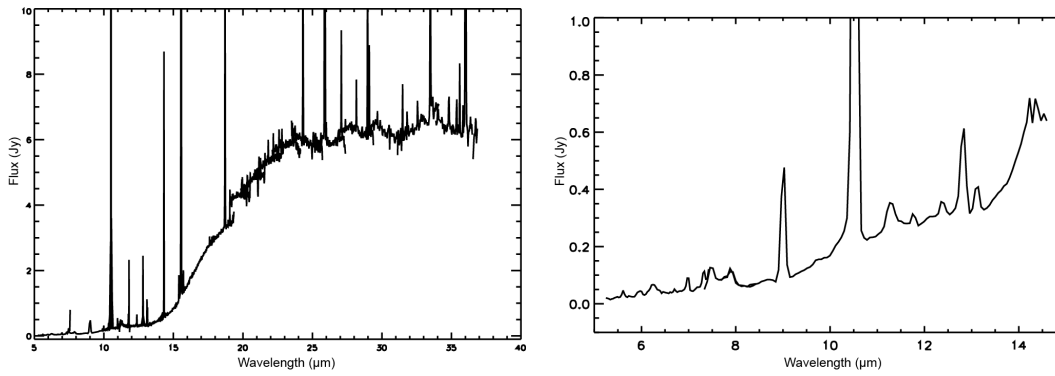


Figure C.2: PN G000.1 +04.3

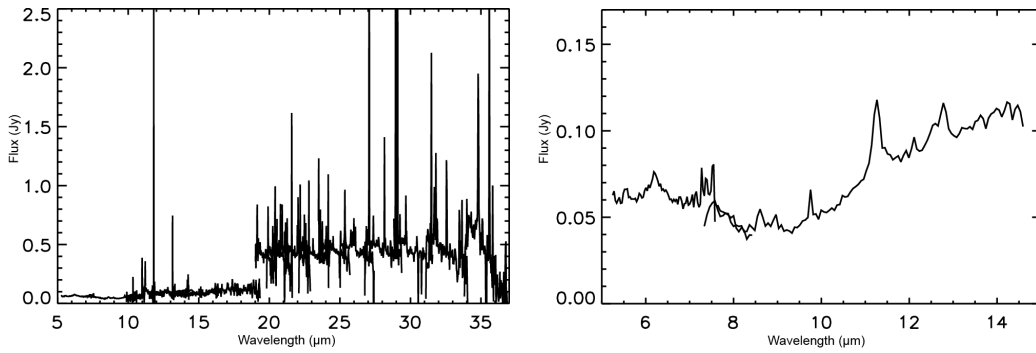


Figure C.3: PN G000.3 +01.5

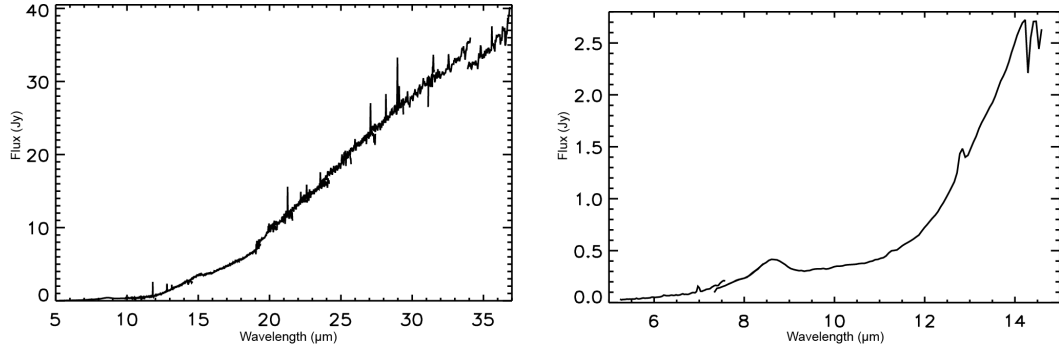


Figure C.4: PN G000.8 +01.3

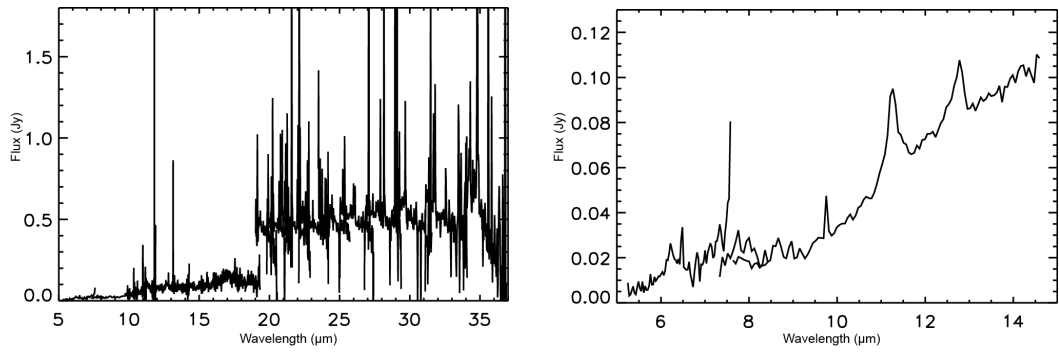


Figure C.5: PN G001.2 +01.2

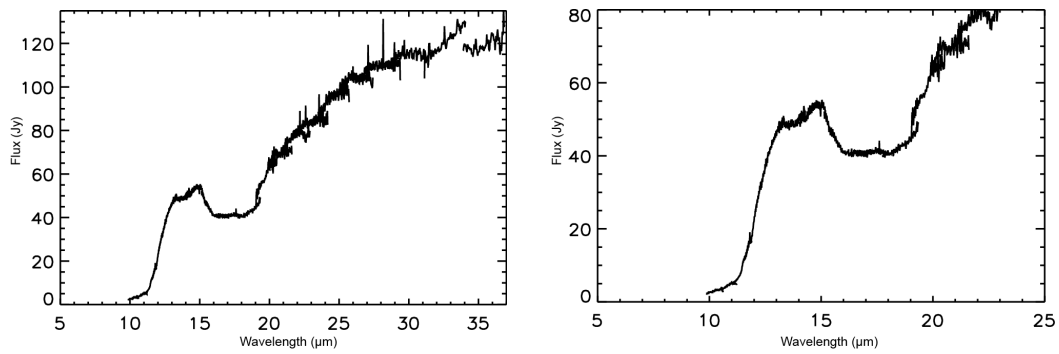


Figure C.6: PN G001.3 +00.9

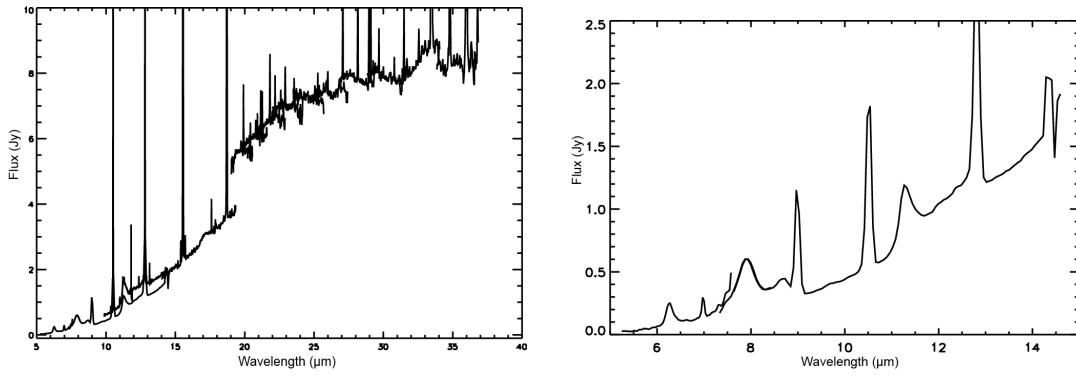


Figure C.7: PN G002.2 -09.4

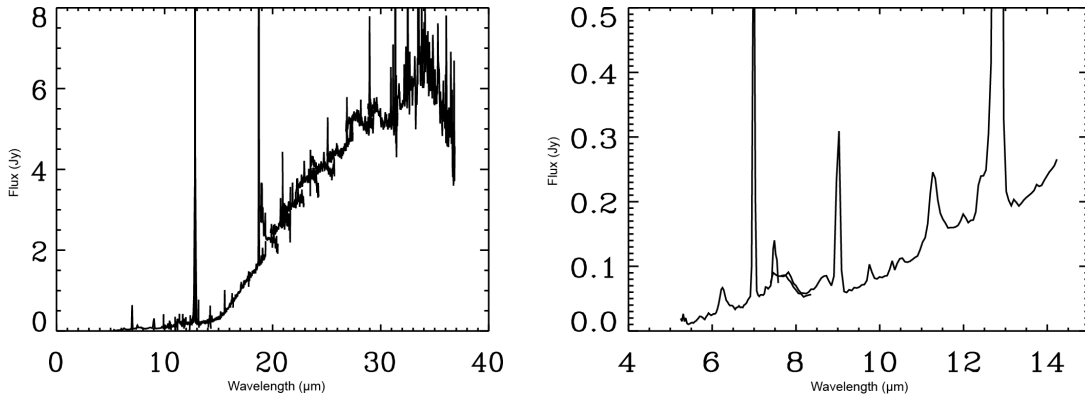


Figure C.8: PN G002.8 +01.7

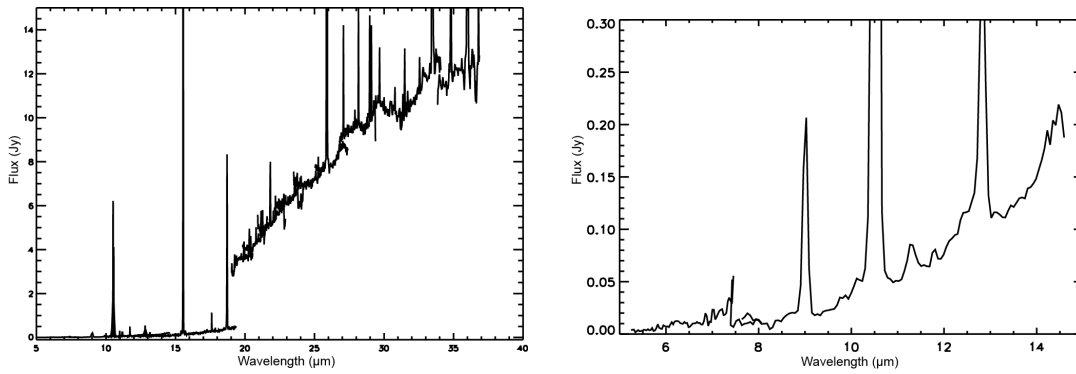


Figure C.9: PN G003.1 +02.9

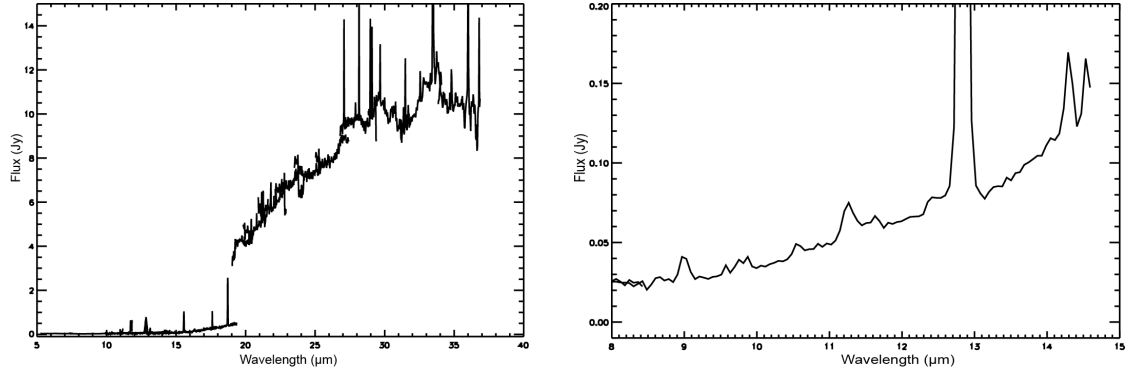


Figure C.10: PN G003.6 +03.1

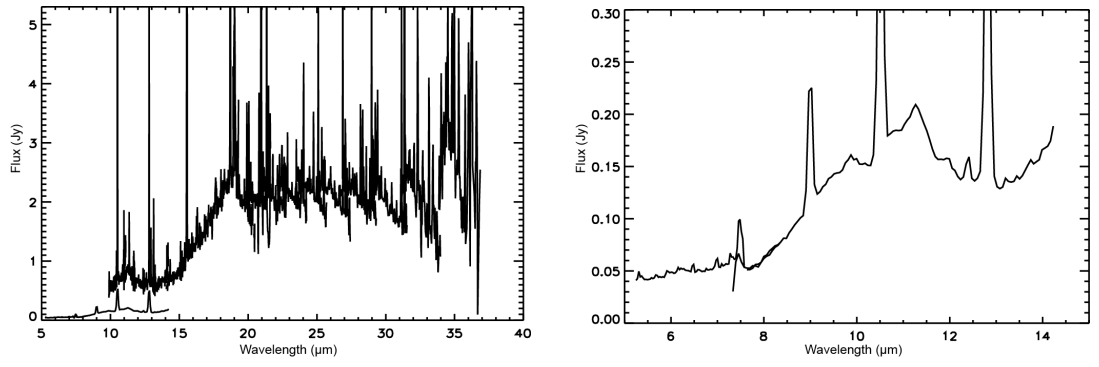


Figure C.11: PN G004.0 -03.0

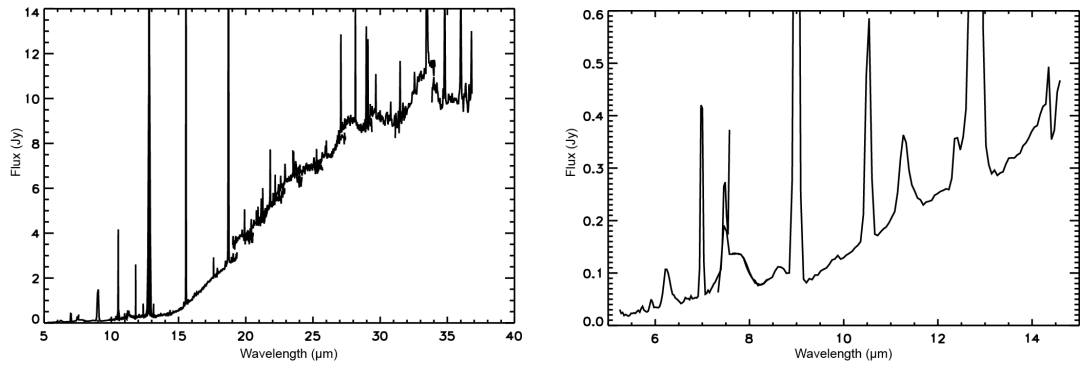


Figure C.12: PN G004.9 +04.9

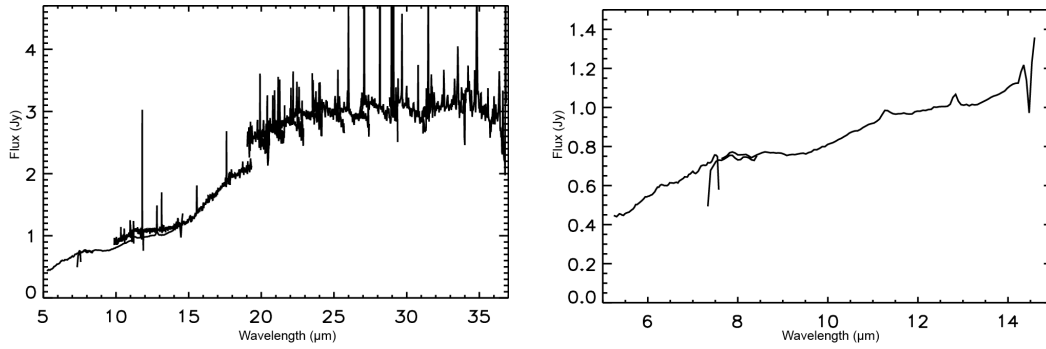


Figure C.13: PN G005.2 +04.2

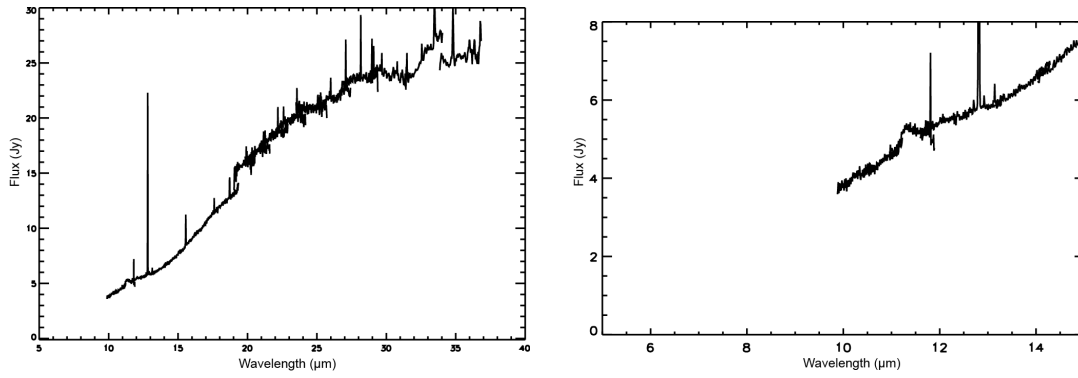


Figure C.14: PN G005.9 -02.6

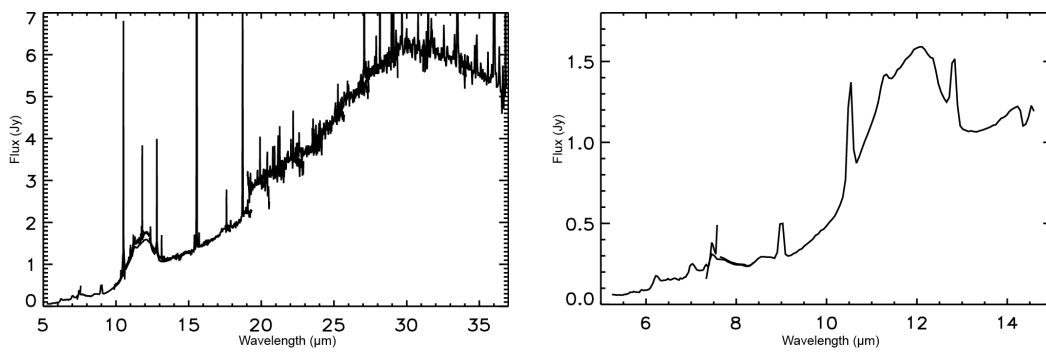


Figure C.15: PN G006.1 +08.3

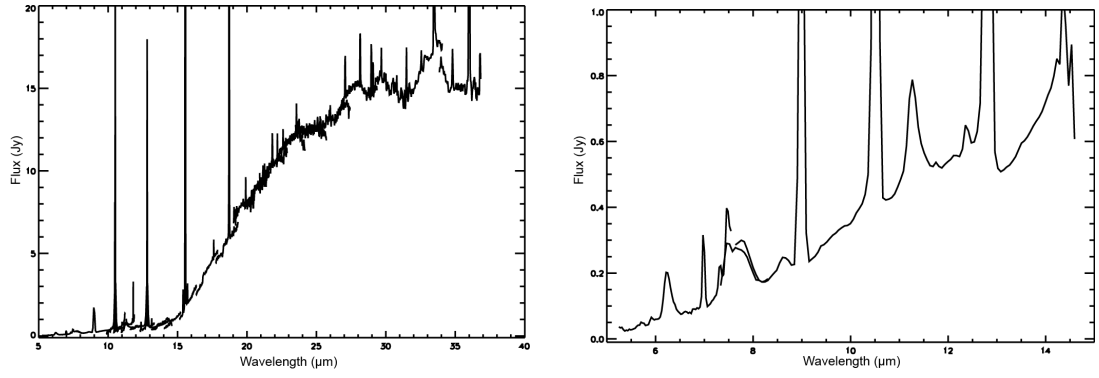


Figure C.16: PN G006.4 +02.0

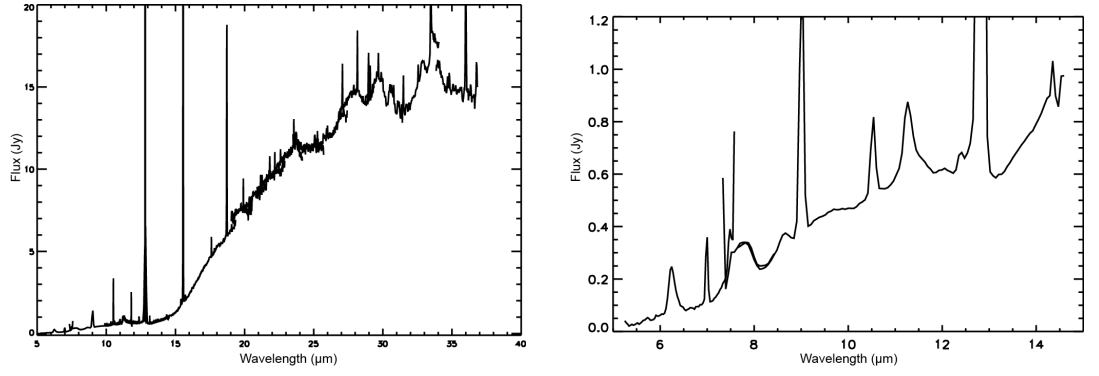


Figure C.17: PN G006.5 -03.1

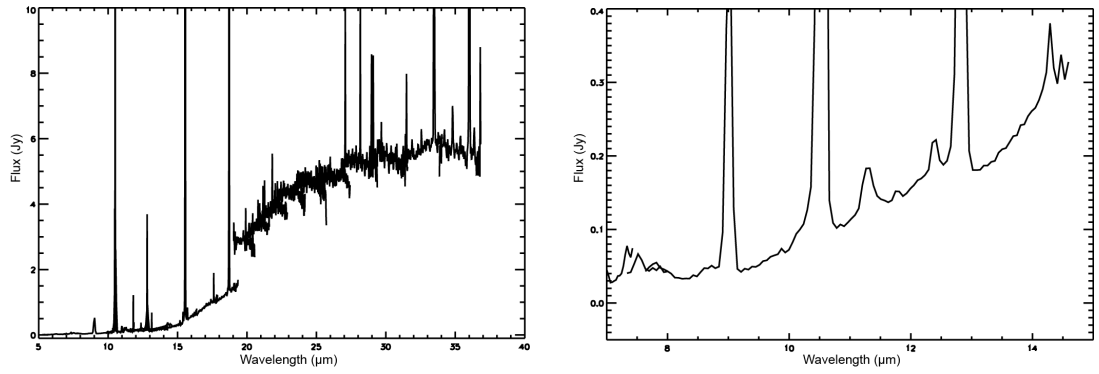


Figure C.18: PN G006.8 +04.1

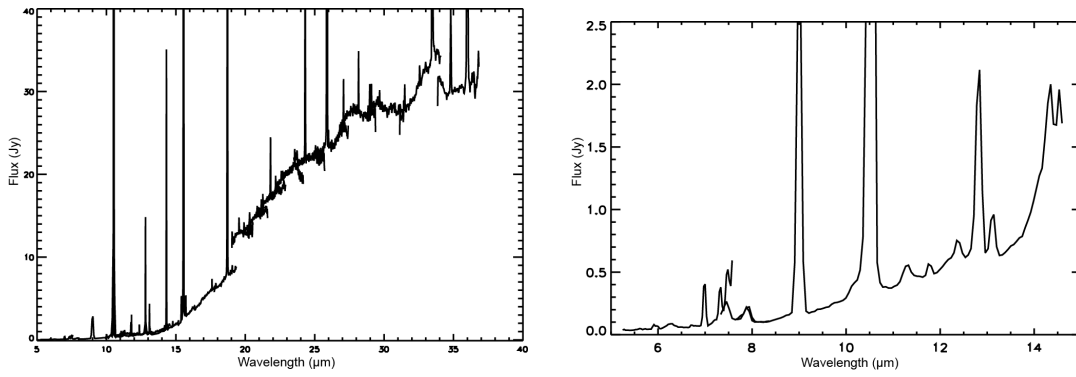


Figure C.19: PN G007.2 +01.8

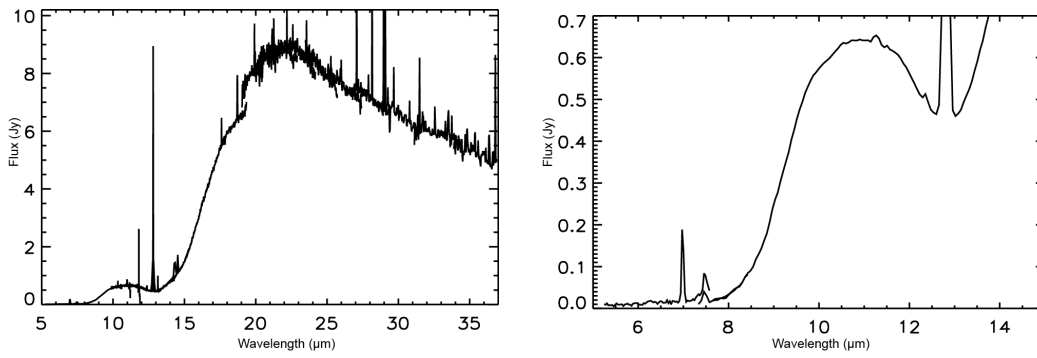


Figure C.20: PN G008.2 +06.8

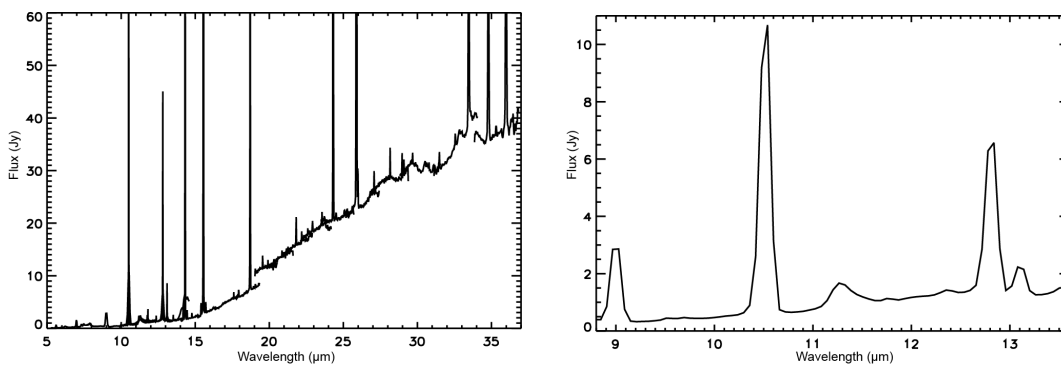


Figure C.21: PN G008.3 +01.1



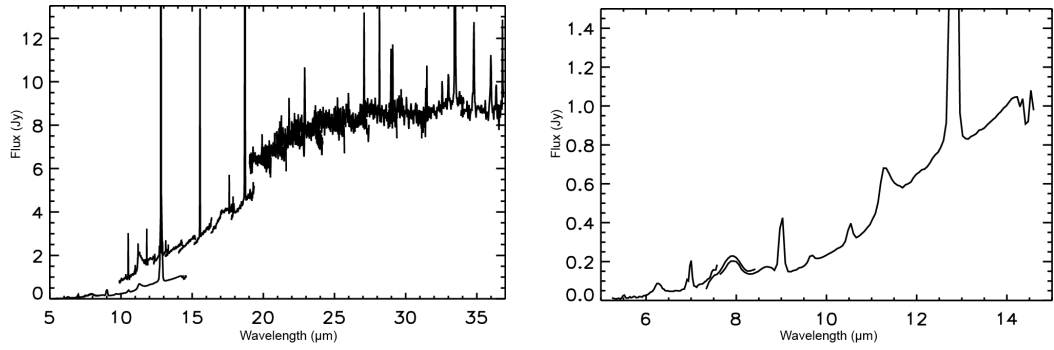


Figure C.22: PN G011.9 +04.2

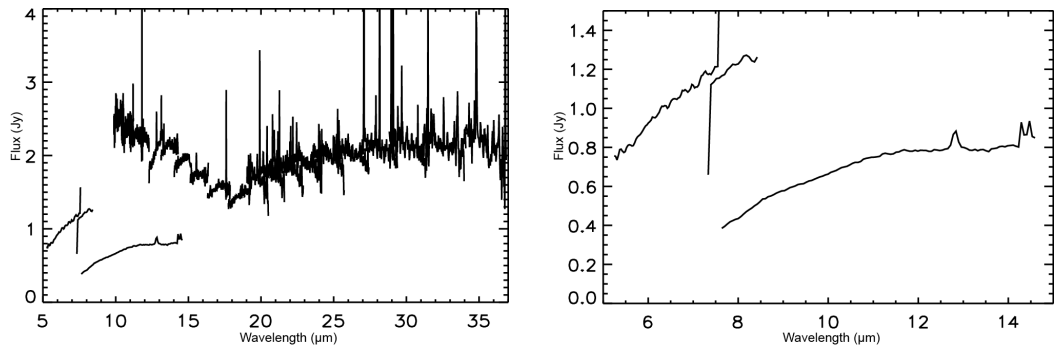


Figure C.23: PN G012.2 +04.9

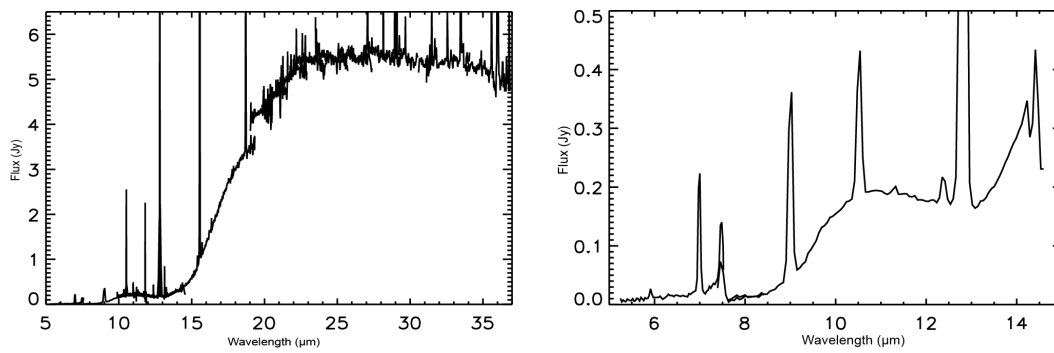


Figure C.24: PN G331.3 -12.1

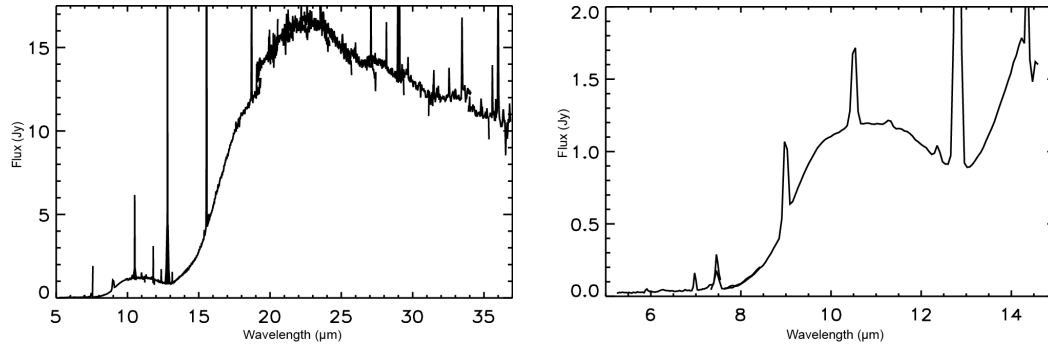


Figure C.25: PN G345.0 -04.9

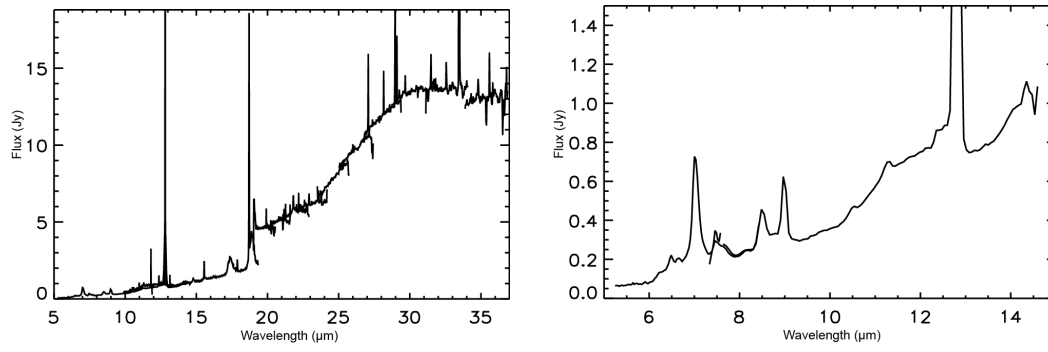


Figure C.26: PN G345.2 -08.8

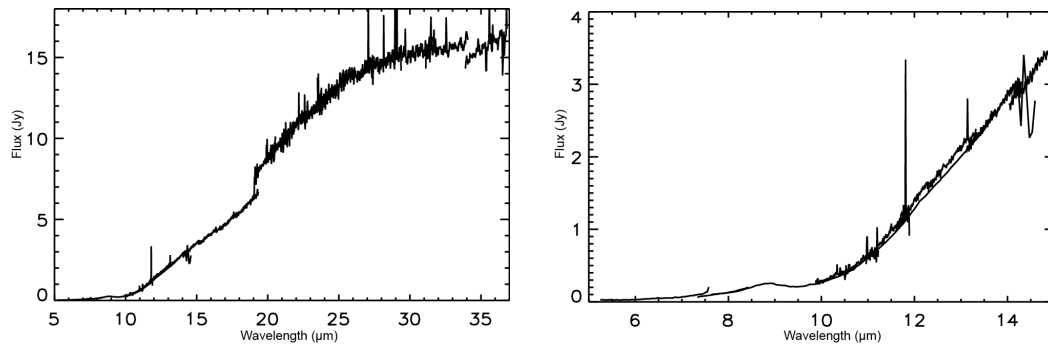


Figure C.27: PN G348.4 -02.8

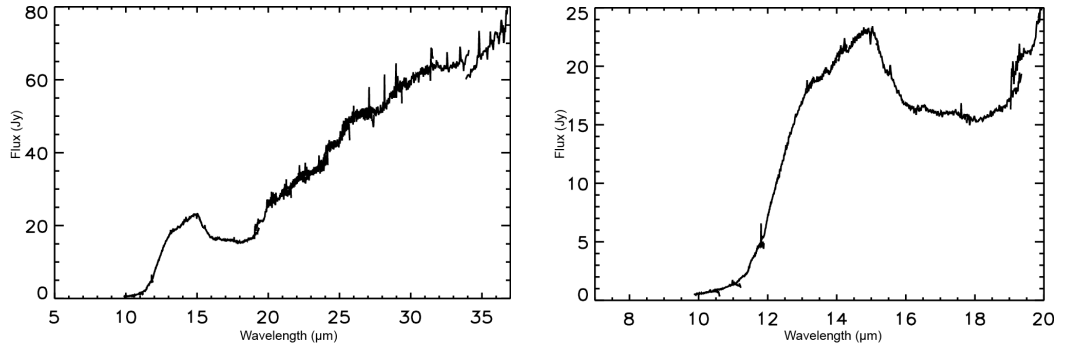


Figure C.28: PN G349.8 -00.3

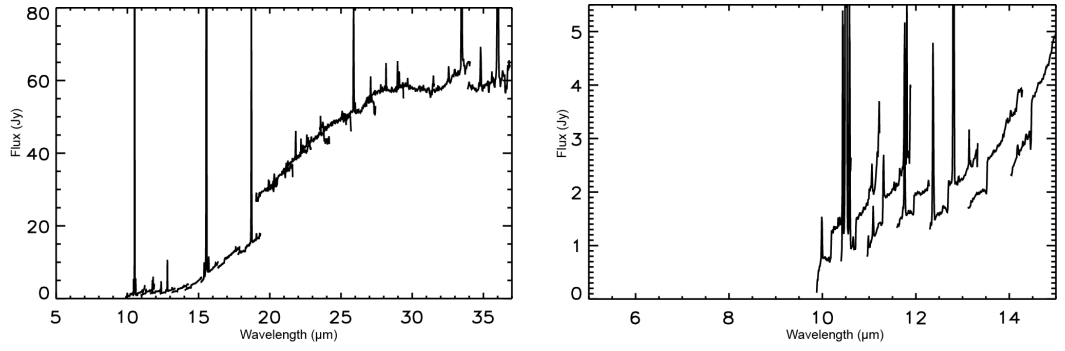


Figure C.29: PN G352.6 +00.1

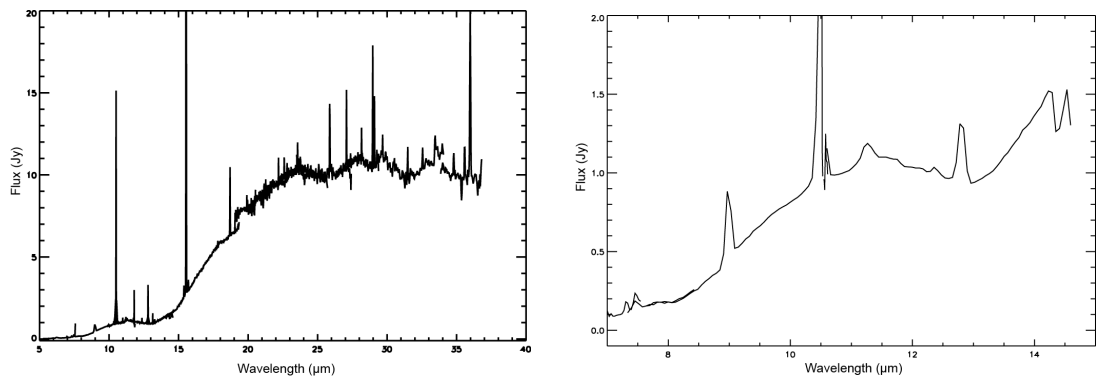


Figure C.30: PN G354.5 +03.3

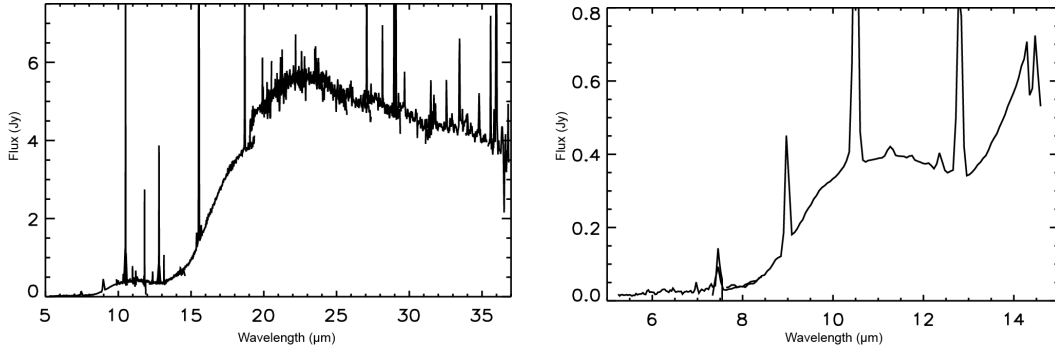


Figure C.31: PN G355.6 -02.7

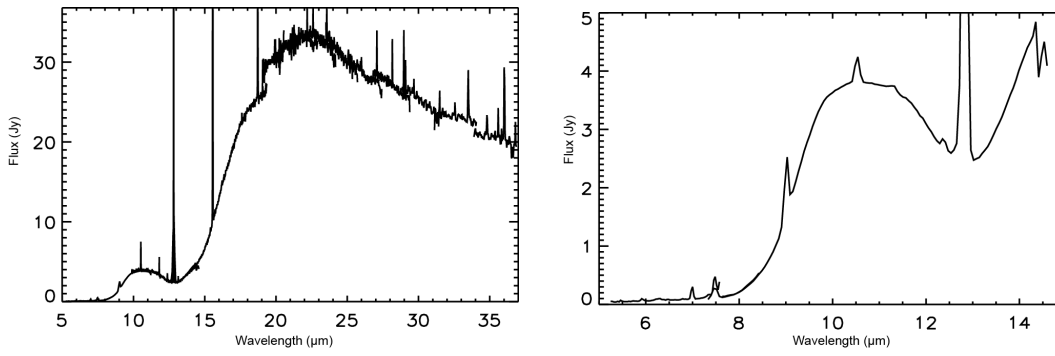


Figure C.32: PN G355.7 -03.5

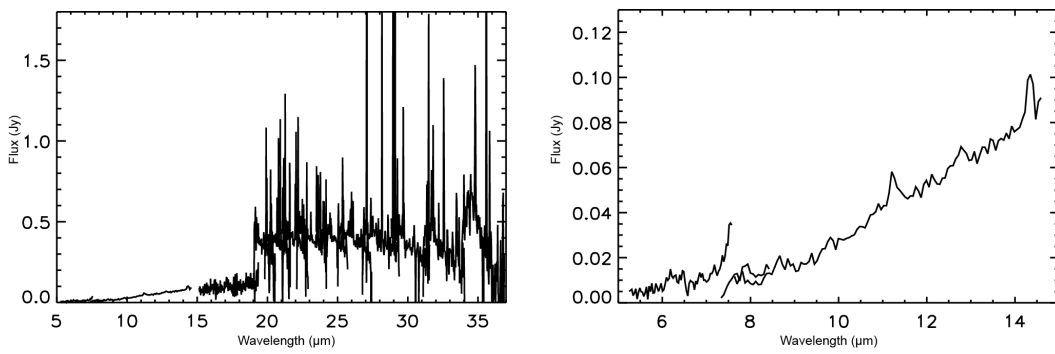


Figure C.33: PN G355.9 -02.3

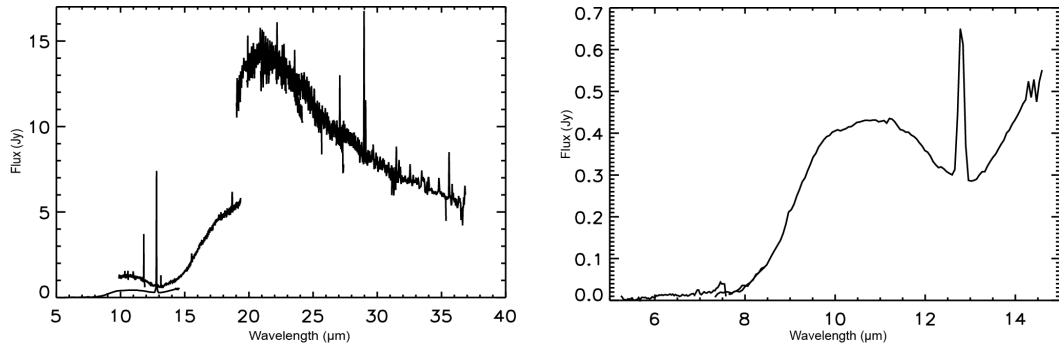


Figure C.34: PN G355.9 +03.6

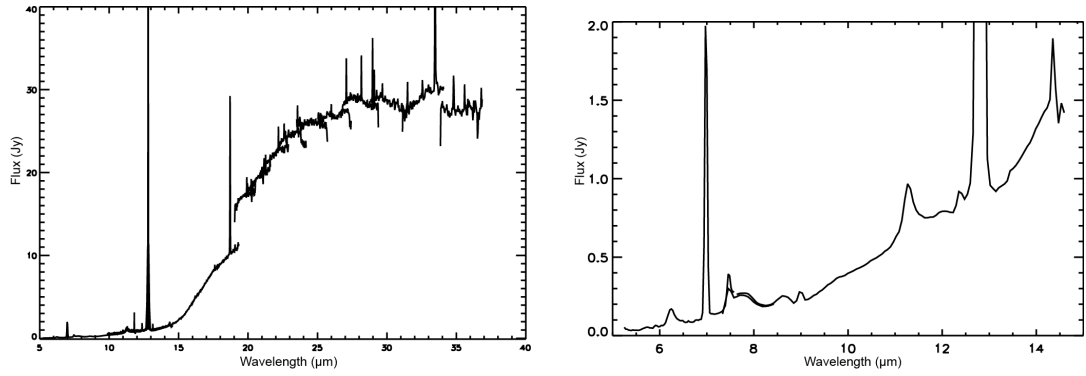


Figure C.35: PN G356.5 -02.3

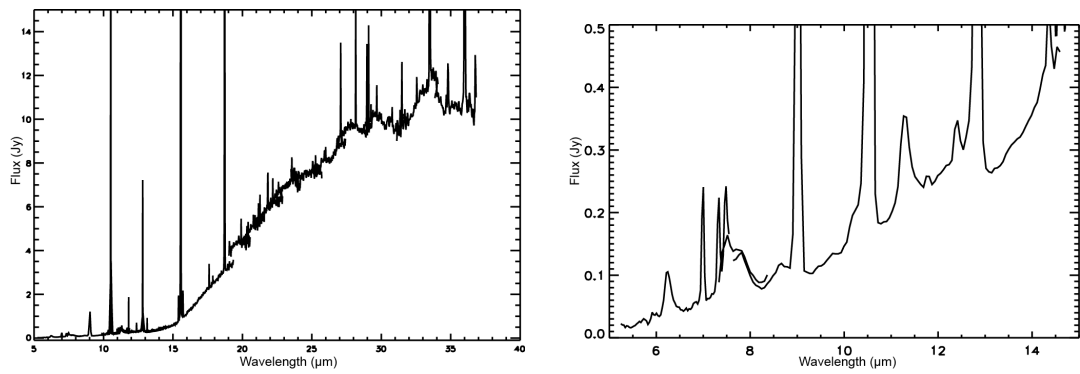


Figure C.36: PN G356.5 -03.6

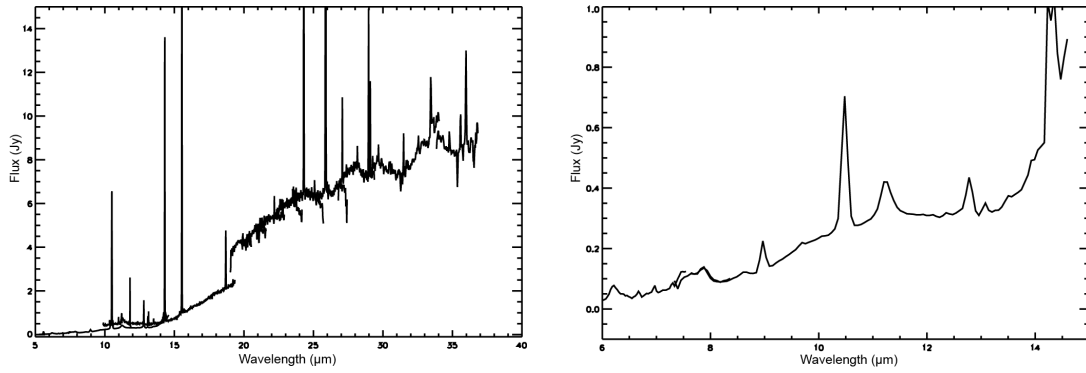


Figure C.37: PN G356.9 +04.4

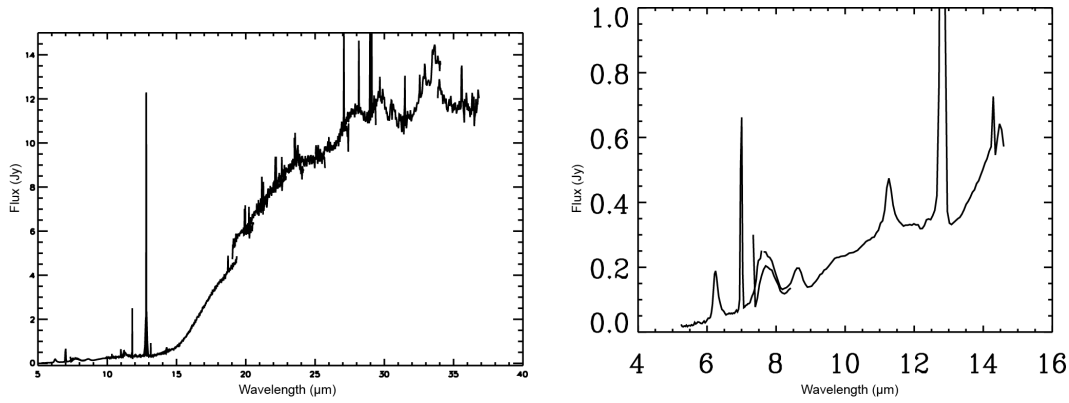


Figure C.38: PN G357.6 +01.7

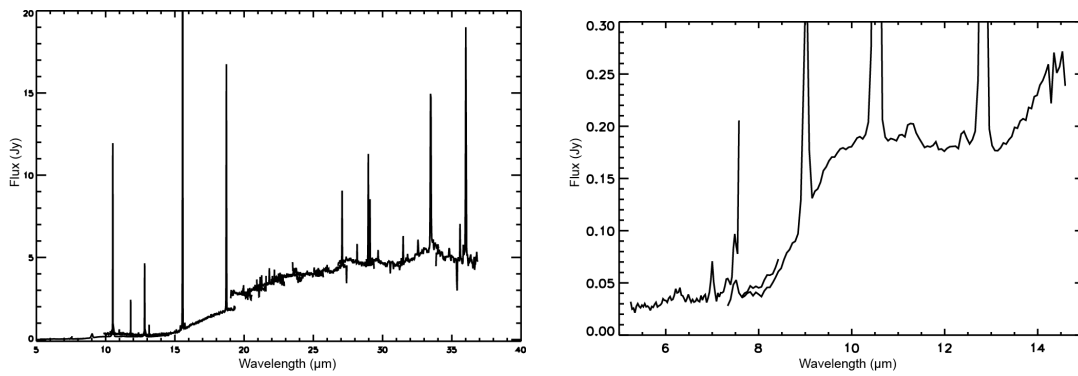


Figure C.39: PN G358.2 +04.2

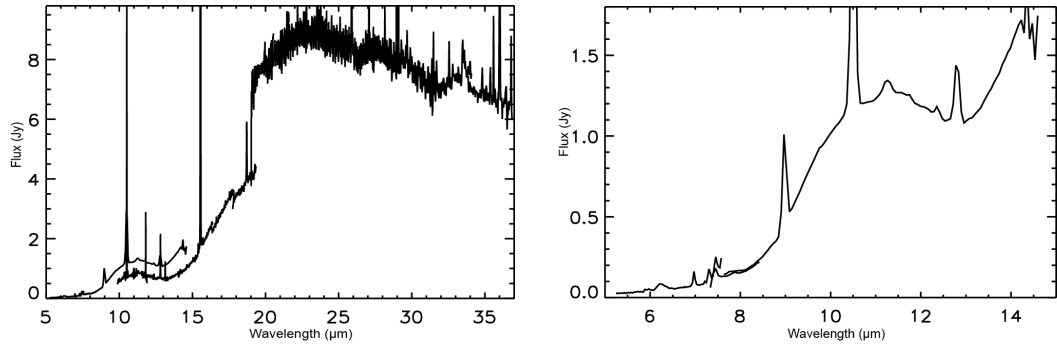


Figure C.40: PN G358.3 +03.0

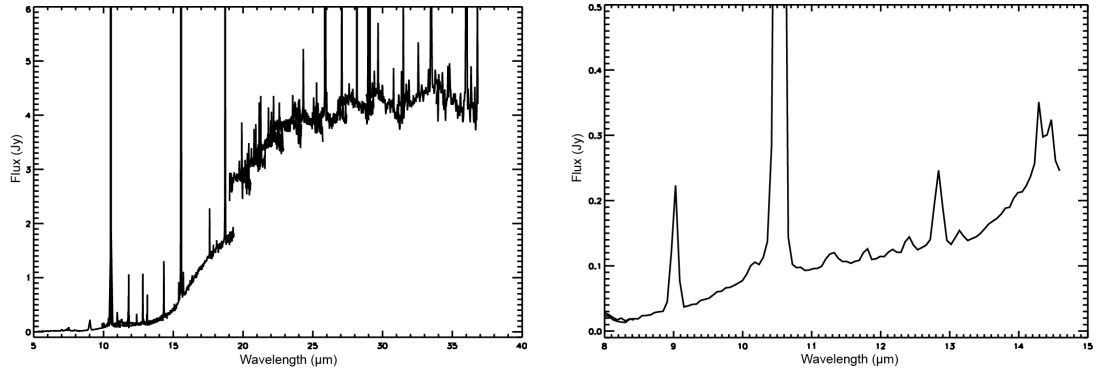


Figure C.41: PN G358.7 -05.2

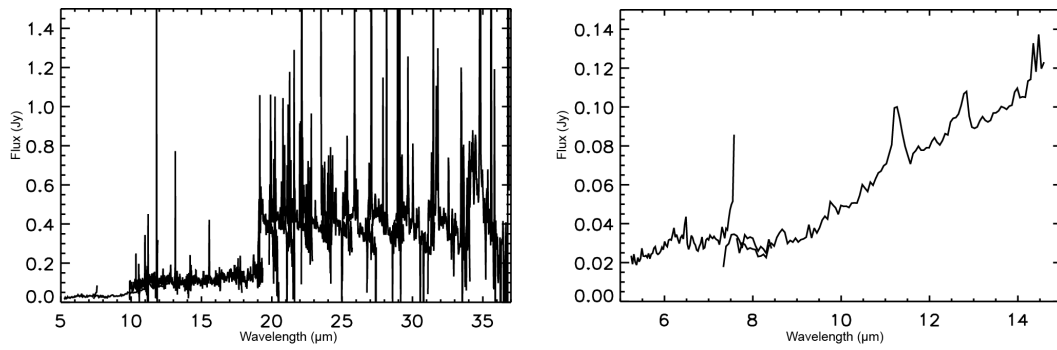


Figure C.42: PN G359.1 -01.7

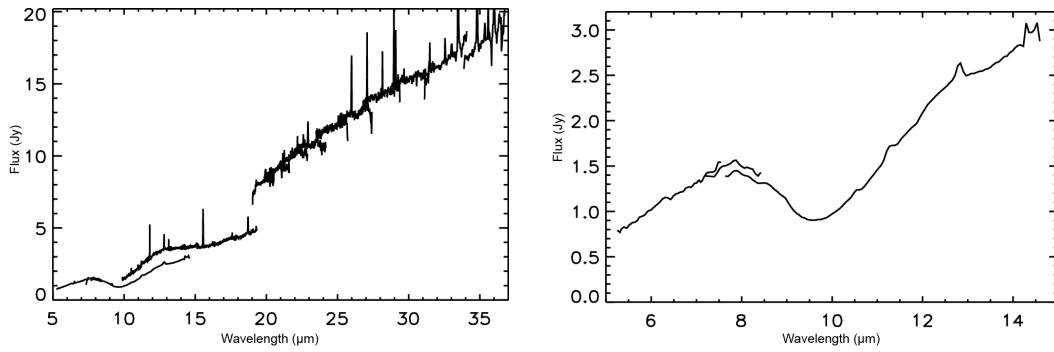


Figure C.43: PN G359.2 +01.2

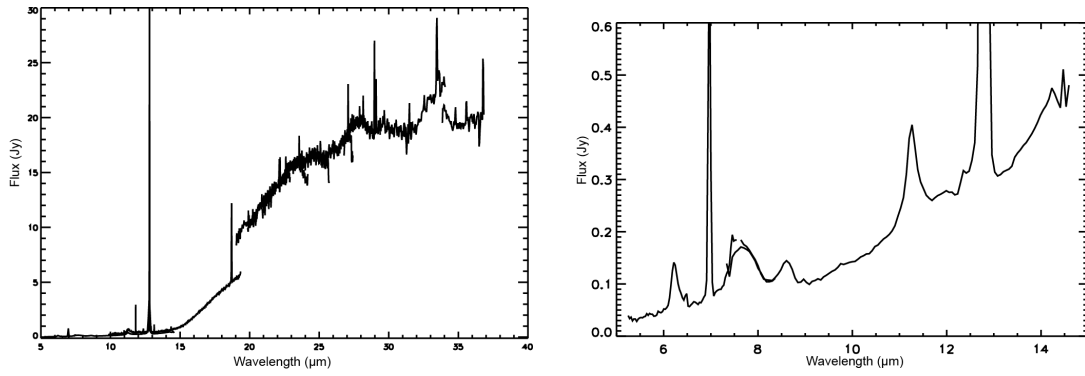


Figure C.44: PN G359.3 -01.8

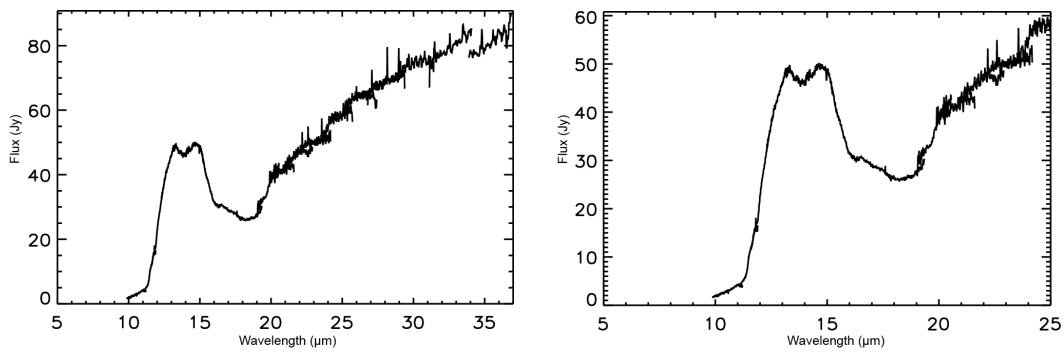


Figure C.45: PN G359.4 -00.8



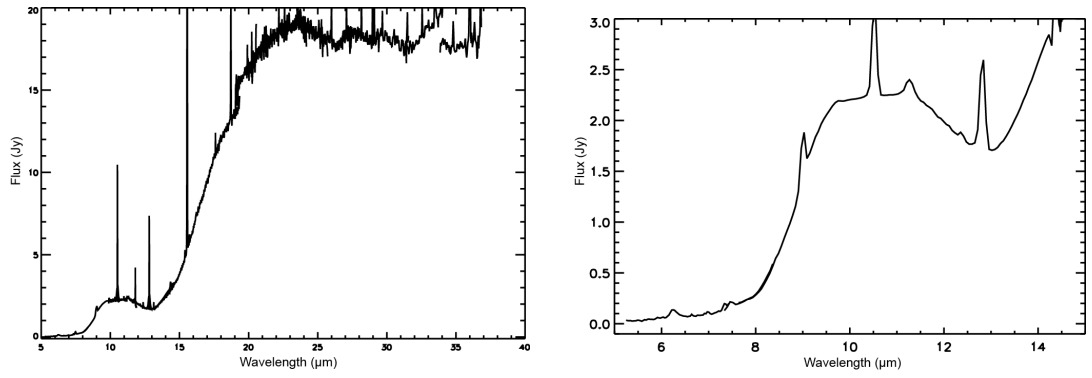


Figure C.46: PN G359.7 -02.6

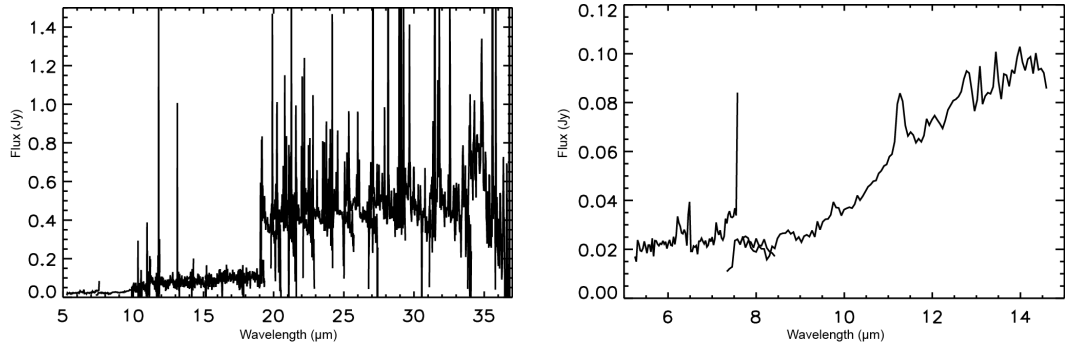


Figure C.47: PN G359.8 +02.4



# References

- Aaquist O. B., Kwok S., 1990a, A&AS, 84, 229
- Aaquist O. B., Kwok S., 1990b, A&AS, 84, 229
- Aaquist O. B., Kwok S., 1991, ApJ, 378, 599
- Acker A., Marcout J., Ochsenbein F., Stenholm B., Tylanda R., Schohn C., 1992, The Strasbourg-ESO Catalogue of Galactic Planetary Nebulae. Parts I, II.
- Acker A., Neiner C., 2003, A&A, 403, 659
- Acker A., Stenholm B., Veron P., 1991, A&AS, 87, 499
- Agundez M., Cernicharo J., Guelin M., 2010a, ArXiv e-prints
- Agundez M., Cernicharo J., Guelin M., 2010b, ArXiv e-prints
- Allamandola L. J., Tielens A. G. G. M., Barker J. R., 1989, ApJS, 71, 733
- Azzopardi M., Lequeux J., Rebeiro E., 1988, A&A, 202, L27
- Balick B., 2007, in Asymmetrical Planetary Nebulae IV The Planetary Nebula Image Catalogue (PNIC)
- Balick B., Frank A., 2002, ARA&A, 40, 439
- Balser D. S., Bania T. M., Brockway C. J., Rood R. T., Wilson T. L., 1994, ApJ, 430, 667
- Balser D. S., Bania T. M., Rood R. T., Wilson T. L., 1997, ApJ, 483, 320
- Balser D. S., Goss W. M., Bania T. M., Rood R. T., 2006, ApJ, 640, 360
- Bania T. M., Balser D. S., Rood R. T., Wilson T. L., LaRocque J. M., 2007, ApJ, 664, 915
- Bania T. M., Rood R. T., Balser D. S., 2010, in Charbonnel C., Tosi M., Primas F., Chiappini C., eds, IAU Symposium Vol. 268 of IAU Symposium, Measurements of  $^3\text{He}$  in Galactic HII regions and planetary nebulae. pp 81–90

## REFERENCES

- Barnbaum C., Kastner J. H., Morris M., Likkell L., 1991, *A&A*, 251, 79
- Bensby T., Feltzing S., Johnson J. A., Gould A., Adén D., Asplund M., Meléndez J., Gal-Yam A., Lucatello S., Sana H., Sumi T., Miyake N., Suzuki D., Han C., Bond I., Udalski A., 2010, *A&A*, 512, A41+
- Boothroyd A. I., Sackmann I.-J., 1999, *ApJ*, 510, 232
- Calvet N., Peimbert M., 1983, *Rev. Mex. Astronomy and Astrophysics*, 5, 319
- Cami J., Bernard-Salas J., Peeters E., Malek S. E., 2010, *Science*, 329, 1180
- Cernicharo J., Agúndez M., Kahane C., Guélin M., Goicoechea J. R., Marcelino N., De Beck E., Decin L., 2011, *A&A*, 529, L3
- Cherchneff I., 1995, *Ap&SS*, 224, 379
- Cherchneff I., Barker J. R., Tielens A. G. G. M., 1992, *ApJ*, 401, 269
- Chesneau O., Lykou F., Balick B., Lagadec E., Matsuura M., Smith N., Spang A., Wolf S., Zijlstra A. A., 2007, *ArXiv e-prints*
- Cohen M., Barlow M. J., 2005, *MNRAS*, 362, 1199
- Cohen M., Barlow M. J., Liu X., Jones A. F., 2002, *MNRAS*, 332, 879
- Cohen M., Barlow M. J., Sylvester R. J., Liu X., Cox P., Lim T., Schmitt B., Speck A. K., 1999, *ApJL*, 513, L135
- Corradi R. L. M., Schönberner D., Steffen M., Perinotto M., 2003, *MNRAS*, 340, 417
- Corradi R. L. M., Schwarz H. E., 1995a, *A&A*, 293, 871
- Corradi R. L. M., Schwarz H. E., 1995b, *A&A*, 293, 871
- Cutri R. M., IPAC/WISE Science Data Center Team 2012, in *American Astronomical Society Meeting Abstracts #219 Vol. 219 of American Astronomical Society Meeting Abstracts, WISE Final Data Release Preview*. p. #401.06
- Daltabuit E., Dodorico S., Sabbadin F., 1976, *A&A*, 52, 93
- De Marco O., Soker N., 2002, *PASP*, 114, 602
- Dearborn D. S. P., Schramm D. N., Steigman G., 1986, *ApJ*, 302, 35
- Decin L., Justtanont K., de Beck E., Lombaert R., de Koter A., Waters L. B. F. M., Marston A. P., Teyssier D., Schöier F. L., Bujarrabal V., Alcolea J., Cernicharo J., Dominik C., Melnick G., Menten K., 2010, *A&A*, 521, L4+

- Dopita M. A., 1976, *ApJ*, 209, 395
- Drew J. E., Greimel R., Irwin M. J., et al., 2005, *MNRAS*, 362, 753
- Duari D., Cherchneff I., Willacy K., 1998, in *IAU Symposium Vol. 191 of IAU Symposium, Carbon-bearing species in the inner wind of oxygen-rich Miras.* pp 232P–+
- Eggleton P. P., Dearborn D. S. P., Lattanzio J. C., 2006, *Science*, 314, 1580
- Feast M., 2007, in F. Kerschbaum, C. Charbonnel, & R. F. Wing ed., *Why Galaxies Care About AGB Stars: Their Importance as Actors and Probes Vol. 378 of Astronomical Society of the Pacific Conference Series, C– and O– Rich Miras and Galactic Structure.* pp 479–+
- Frew D. J., Parker Q. A., 2006, in Barlow M. J., Méndez R. H., eds, *Planetary Nebulae in our Galaxy and Beyond Vol. 234 of IAU Symposium, Towards a New Distance Scale and Luminosity Function for Nearby Planetary Nebulae.* pp 49–54
- Galli D., 2004, *ArXiv Astrophysics e-prints*
- Galli D., Palla F., Ferrini F., Penco U., 1995, *ApJ*, 443, 536
- Galli D., Stanghellini L., Tosi M., Palla F., 1997, *ApJ*, 477, 218
- Gathier R., Pottasch S. R., Goss W. M., van Gorkom J. H., 1983, *A&A*, 128, 325
- Geiss J., 1993, in Prantzos N., Vangioni-Flam E., Casse M., eds, *Origin and Evolution of the Elements Primordial abundances of hydrogen and helium isotopes..* pp 89–106
- Gesicki K., Zijlstra A. A., 2000, *A&A*, 358, 1058
- Gesicki K., Zijlstra A. A., 2007, in R. Napiwotzki & M. R. Burleigh ed., *15th European Workshop on White Dwarfs Vol. 372 of Astronomical Society of the Pacific Conference Series, Central Stars of Planetary Nebulae.* pp 41–+
- Gesicki K., Zijlstra A. A., Acker A., Górny S. K., Goździewski K., Walsh J. R., 2006, *A&A*, 451, 925
- Giesen J., 1994, *ArXiv High Energy Physics - Theory e-prints*
- Gloeckler G., Geiss J., 1996, *Nature*, 381, 210
- González-Solares E. A., et al. 2008, *MNRAS*, 388, 89
- Górny S. K., Perea-Calderón J. V., García-Hernández D. A., García-Lario P., Szczerba R., 2010, *A&A*, 516, A39+

## REFERENCES

- Górny S. K., Stasińska G., Escudero A. V., Costa R. D. D., 2004, *A&A*, 427, 231
- Gould R. J., 1994, *ApJ*, 423, 522
- Groves B., Nefs B., Brandl B., 2008, *MNRAS*, 391, L113
- Guerrero M. A., Chu Y.-H., Gruendl R. A., 2004, in Meixner M., Kastner J. H., Balick B., Soker N., eds, *Asymmetrical Planetary Nebulae III: Winds, Structure and the Thunderbird Vol. 313 of Astronomical Society of the Pacific Conference Series, X-Ray Observations of Planetary Nebulae*. p. 259
- Gutenkunst S., Bernard-Salas J., Pottasch S. R., Sloan G. C., Houck J. R., 2008, *ApJ*, 680, 1206
- Guzmán L., Loinard L., Gómez Y., Morisset C., 2009, *AJ*, 138, 46
- Guzman-Ramirez L., Zijlstra A. A., Níchuimín R., Gesicki K., Lagadec E., Millar T. J., Woods P. M., 2011, *MNRAS*, 414, 1667
- Habing H. J., 1996, in Blitz L., Teuben P. J., eds, *Unsolved Problems of the Milky Way Vol. 169 of IAU Symposium, Stellar Populations in the Galactic Bulge*. p. 317
- Hajian A. R., Terzian Y., Bignell C., 1995, *AJ*, 109, 2600
- Herwig F., 2005, *ARA&A*, 43, 435
- Houck J. R., Roellig T. L., van Cleve J., Forrest W. J., Herter T., Lawrence C. R., Matthews K., Reitsema H. J., Soifer B. T., Watson D. M., Weedman D., Huisjen M., Troeltzsch J., 2004, *ApJS*, 154, 18
- Irwin M., Lewis J., 2001, *New Astronomy Reviews*, 45, 105
- Jamiet P. A., Danchi W. C., Sandell G., Sutton E. C., 1992, *ApJ*, 400, 535
- Jeffries R. D., Stevens I. R., 1996, *MNRAS*, 279, 180
- Joblin C., Pilleri P., Montillaud J., Fuente A., Gerin M., Berné O., Ossenkopf V., Le Bourlot J., Teyssier D., Goicoechea J. R., Le Petit F., Röllig M., Akyilmaz M., Benz A. O., Boulanger F., 2010, *A&A*, 521, L25+
- Kaler J. B., 1976, *ApJS*, 31, 517
- Kaschinski C. B., Pauldrach A. W. A., Hoffmann T. L., 2012, *A&A*, 542, A45
- Kashiyama K., Ioka K., 2010, in Kawai N., Nagataki S., eds, *American Institute of Physics Conference Series Vol. 1279 of American Institute of Physics Conference Series, White Dwarf Model for PAMELA Positron Excess*. pp 352–354
- Kassis M., Adams J. D., Campbell M. F., Deutsch L. K., Hora J. L., Jackson

- J. M., Tollestrup E. V., 2006, *ApJ*, 637, 823
- Kastner J. H., 2007, in *Asymmetrical Planetary Nebulae IV X-ray Emission from Planetary Nebulae and their Central Stars: a Status Report*
- Kastner J. H., Montez Jr. R., Balick B., Frew D. J. e., 2012, *AJ*, 144, 58
- Kastner J. H., Soker N., 2003, in *American Astronomical Society Meeting Abstracts Vol. 35 of Bulletin of the American Astronomical Society, X-ray Observations of AGB Stars with XMM-Newton*. p. 1253
- Kennicutt Jr. R. C., Bresolin F., French H., Martin P., 2000, *ApJ*, 537, 589
- Kimura R. K., Gruenwald R., Aleman I., 2012, *A&A*, 541, A112
- Kohoutek L., 2001, *VizieR Online Data Catalog*, 4024, 0
- Kwok S., 1985, *AJ*, 90, 49
- Kwok S., 2000, *The Origin and Evolution of Planetary Nebulae*. Cambridge University Press
- Kwok S., Aaquist O. B., 1993, *PASP*, 105, 1456
- Lagage P. O., Pel J. W., Authier M., et al., 2004, *The Messenger*, 117, 12
- Lagarde N., Romano D., Charbonnel C., Tosi M., Chiappini C., Matteucci F., 2012, *A&A*, 542, A62
- Lattanzio J., Frost C., Cannon R., Wood P. R., 1996, *Mem. Soc. Astron. Italiana*, 67, 729
- Le Bertre T., Tanaka M., Yamamura I., Murakami H., 2003, *A&A*, 403, 943
- Le Petit F., Nehmé C., Le Boulrot J., Roueff E., 2006, *ApJS*, 164, 506
- Le Teuff Y. H., Millar T. J., Markwick A. J., 2000, *A&AS*, 146, 157
- Liebert J., Bergeron P., Holberg J. B., 2005, *ApJS*, 156, 47
- Manchado A., 2004, in *Meixner M., Kastner J. H., Balick B., Soker N., eds, Asymmetrical Planetary Nebulae III: Winds, Structure and the Thunderbird Vol. 313 of Astronomical Society of the Pacific Conference Series, Correlation of PN Morphologies and Nebular Parameters*. p. 3
- Manchado A., Guerrero M. A., Stanghellini L., Serra-Ricart M., 1996, *The IAC morphological catalog of northern Galactic planetary nebulae*
- McDonald I., White J. R., Zijlstra A. A., Guzman Ramirez L., Szyszka C., van Loon J. T., Lagadec E., Jones O. C., 2012, *ArXiv e-prints*

## REFERENCES

- McEwan M. J., Scott G. B. I., Adams N. G., Babcock L. M., Terzieva R., Herbst E., 1999, *ApJ*, 513, 287
- Millar T. J., Flores J. R., Markwick A. J., 2001, *MNRAS*, 327, 1173
- Millar T. J., Walsh C., Cordiner M. A., Ní Chuimín R., Herbst E., 2007, *ApJL*, 662, L87
- Miszalski B., Parker Q. A., Acker A., Birkby J. L., Frew D. J., Kovacevic A., 2008, *MNRAS*, 384, 525
- Moe M., De Marco O., 2006, *ApJ*, 650, 916
- Morisset C., 2006, in Barlow M. J., Méndez R. H., eds, *Planetary Nebulae in our Galaxy and Beyond Vol. 234 of IAU Symposium*, Cloudy\_3D, a new pseudo-3D photoionization code. pp 467–468
- Morisset C., Georgiev L., 2009, *A&A*, 507, 1517
- Neufeld D. A., González-Alfonso E., Melnick G. J., Szczerba R., Schmidt M., Decin L., de Koter A., Schöier F., Cernicharo J., 2011, *ApJL*, 727, L28
- Ní Chuimín R., 2009, *Carbon Chain Species in Photo-Dominated Regions* (PhD Thesis). University of Manchester
- Osterbrock D. E., O'dell C. R., eds, 1968, *Planetary nebulae, proceedings from IAU Symposium no. 34*. Vol. 34 of *IAU Symposium*
- Parker Q. A., Acker A., Frew D. J., Hartley M., Peyaud A. E. J., Ochsenbein F., Phillipps S., Russel D., Beaulieu S. F., Cohen M., Köppen J., Miszalski B., Morgan D. H., Morris R. A. H., Pierce M. J., Vaughan A. E., 2006, *MNRAS*, 373, 79
- Peimbert M., 1978, in Terzian Y., ed., *Planetary Nebulae Vol. 76 of IAU Symposium*, Chemical abundances in planetary nebulae. pp 215–223
- Peimbert M., Serrano A., 1980, *Rev. Mex. Astronomy and Astrophysics*, 5, 9
- Perea-Calderón J. V., García-Hernández D. A., García-Lario P., Szczerba R., Bobrowsky M., 2009, *A&A*, 495, L5
- Perinotto M., 1991, *ApJS*, 76, 687
- Perrine C. D., 1929, *Astronomische Nachrichten*, 237, 89
- Phillips J. P., 2003, *A&A*, 412, 791
- Phillips J. P., Cuesta L. C., Ramos-Larios G., 2010, *MNRAS*, pp 1448–+
- Phillips J. P., Márquez-Lugo R. A., 2011, *Rev. Mex. Astronomy and Astrophysics*,



- 47, 83
- Pottasch S. R., ed. 1984, Planetary nebulae - A study of late stages of stellar evolution Vol. 107 of Astrophysics and Space Science Library
- Redman M. P., Viti S., Cau P., Williams D. A., 2003, MNRAS, 345, 1291
- Richardson W. H., 1972, Journal of the Optical Society of America (1917-1983), 62, 55
- Riesgo H., López J. A., 2006, Rev. Mex. Astronomy and Astrophysics, 42, 47
- Rood R. T., Bania T. M., Wilson T. L., Balser D. S., 1995, in Crane P., ed., The Light Element Abundances The Quest for the Cosmic Abundance of  $^3\text{He}$ . p. 201
- Rood R. T., Wilson T. L., Steigman G., 1979, ApJL, 227, L97
- Sabbadin F., D'Odorico S., 1976, A&A, 49, 119
- Sabbadin F., Minello S., Bianchini A., 1977, A&A, 60, 147
- Sahai R., Morris M., Sánchez Contreras C., Claussen M., 2007, AJ, 134, 2200
- Savage B. D., Sembach K. R., 1996, ARA&A, 34, 279
- Schlegel D. J., Finkbeiner D. P., Davis M., 1998, ApJ, 500, 525
- Schneider S. E., Buckley D., 1996, ApJ, 459, 606
- Schwarz H. E., Corradi R. L. M., Melnick J., 1992, A&AS, 96, 23
- Shklovsky I. S., 1957, in Herbig G. H., ed., Non-stable stars Vol. 3 of IAU Symposium, On the nature of planetary nebulae Discussion. p. 83
- Sloan G. C., Price S. D., 1998, ApJS, 119, 141
- Smiljanic R., Gauderon R., North P., Barbuy B., Charbonnel C., Mowlavi N., 2009, A&A, 502, 267
- Smolders K., Acke B., Verhoelst T., Blommaert J. A. D. L., Decin L., Hony S., Sloan G. C., Neyskens P., van Eck S., Zijlstra A. A., van Winckel H., 2010, A&A, 514, L1+
- Soker N., 2006, ApJL, 645, L57
- Stanton L., 1973, Journal of Raman Spectroscopy, 1, 53
- Terzian Y., 1966, AJ, 71, 182
- Tielens A. G. G. M., 2005, The Physics and Chemistry of the Interstellar Medium
- Uttenthaler S., Blommaert J. A. D. L., Lebzelter T., Ryde N., Wood P. R.,

## REFERENCES

- Schultheis M., Aringer B., 2012, in European Physical Journal Web of Conferences Vol. 19 of European Physical Journal Web of Conferences, Elemental abundances in AGB stars and the formation of the Galactic bulge. p. 6009
- Uttenthaler S., Hron J., Lebzelter T., Busso M., Palmerini S., Schultheis M., Käußl H. U., Lederer M. T., Aringer B., 2008, *A&A*, 478, 527
- Vangioni-Flam E., Olive K. A., Prantzos N., 1994, *ApJ*, 427, 618
- Vassiliadis E., Wood P. R., 1993, *ApJ*, 413, 641
- Wang H., Frenklach M., 1994, *Journal of Physical Chemistry*, 98, 11465
- Wareing C. J., Zijlstra A. A., O'Brien T. J., 2007, *MNRAS*, 382, 1233
- Waters L. B. F. M., Beintema D. A., Zijlstra A. A., de Koter A., Molster F. J., Bouwman J., de Jong T., Pottasch S. R., de Graauw T., 1998, *A&A*, 331, L61
- Waters L. B. F. M., Cami J., de Jong T., Molster F. J., van Loon J. T., Bouwman J., de Koter A., Waelkens C., Van Winckel H., Morris P. W., Cami J., Bouwman J., de Koter A., de Jong T., de Graauw T., 1998, *Nature*, 391, 868
- Weiss A., Wagenhuber J., Denissenkov P. A., 1996, *A&A*, 313, 581
- Wilson T. L., Rood R., 1994, *ARA&A*, 32, 191
- Wolf S., Henning T., Stecklum B., 1999, *A&A*, 349, 839
- Wood K., Kenyon S. J., Whitney B., Turnbull M., 1998, *ApJ*, 497, 404
- Woodall J., Agúndez M., Markwick-Kemper A. J., Millar T. J., 2007, *A&A*, 466, 1197
- Woods P. M., Millar T. J., Herbst E., Zijlstra A. A., 2003, *A&A*, 402, 189
- Woods P. M., Millar T. J., Zijlstra A. A., Herbst E., 2002, *ApJL*, 574, L167
- Woods P. M., Nyman L.-Å., Schöier F. L., Zijlstra A. A., Millar T. J., Olofsson H., 2005, *A&A*, 429, 977
- Woods P. M., Willacy K., 2007, *ApJL*, 655, L49
- Woon D. E., Herbst E., 1996, *ApJ*, 465, 795
- Zijlstra A. A., 2007, *Baltic Astronomy*, 16, 79
- Zijlstra A. A., Chapman J. M., te Lintel Hekkert P., Likkell L., Comeron F., Norris R. P., Molster F. J., Cohen R. J., 2001, *MNRAS*, 322, 280
- Zijlstra A. A., Gaylard M. J., te Lintel Hekkert P., Menzies J., Nyman L., Schwarz H. E., 1991, *A&A*, 243, L9

## REFERENCES

- Zijlstra A. A., Pottasch S. R., 1991, *A&A*, 243, 478
- Zijlstra A. A., Pottasch S. R., Bignell C., 1989, *A&AS*, 79, 329
- Zoccali M., Minniti D., 2009, in *Revista Mexicana de Astronomia y Astrofisica Conference Series Vol. 35 of Revista Mexicana de Astronomia y Astrofisica Conference Series, Formation and Evolution of the Galactic Bulge*. pp 85–90
- Zoccali M., Renzini A., Ortolani S., Greggio L., Saviane I., Cassisi S., Rejkuba M., Barbuy B., Rich R. M., Bica E., 2003a, *A&A*, 399, 931
- Zoccali M., Renzini A., Ortolani S., Greggio L., Saviane I., Cassisi S., Rejkuba M., Barbuy B., Rich R. M., Bica E., 2003b, *A&A*, 399, 931